

# **Nanotechnology for the treatment of industrial-scale effluents – particularly the removal of organic contaminants from textile effluents using nano-TiO<sub>2</sub>**

Report to the  
Water Research Commission

by

**CJ Greyling<sup>1</sup>, VG Fester<sup>2</sup>, JC Ngila<sup>3</sup>, EFC Chaúque<sup>3</sup> and  
W Edwards<sup>4</sup>**

<sup>1</sup> Technology Station in Clothing and Textiles, Cape Peninsula University of Technology.

<sup>2</sup> Department of Civil Engineering, Cape Peninsula University of Technology

<sup>3</sup> Department of Applied Chemistry, University of Johannesburg

<sup>4</sup> ATL Hydro Pty Ltd

With contributions by:

S Krause<sup>1</sup>, A Munnik<sup>1</sup>, E Nortjie<sup>1</sup>, M Chowdhury<sup>2</sup>, S Ntiribinyange<sup>2</sup>, B Kriedmann<sup>2</sup>, J Lind<sup>2</sup>, NL Dlamini<sup>3</sup>,  
LF Tichagwa<sup>4</sup>, I Chickurunhe<sup>4</sup>, S Tapiwanashe<sup>4</sup>, Y Salie<sup>5</sup>, C Muanda<sup>6</sup>.

<sup>1</sup> Technology Station in Clothing and Textiles, Cape Peninsula University of Technology.

<sup>2</sup> Department of Civil Engineering, Flow Process and Rheology Centre, Cape Peninsula University of Technology.

<sup>3</sup> Applied Chemistry Department, University of Johannesburg.

<sup>4</sup> Department of Polymer Technology and Engineering, Harare Institute of Technology.

<sup>5</sup> ATL-Hydro.

<sup>6</sup> CWSS, Cape Peninsula University of Technology.

**WRC Report no. 2386/1/17**

**ISBN 978-1-4312-0901-9**

**June 2017**

**Obtainable from:**

**Water Research Commission  
Private Bag X03  
Gezina 0031  
South Africa**

[orders@wrc.org.za](mailto:orders@wrc.org.za) or download from [www.wrc.org.za](http://www.wrc.org.za)

#### **DISCLAIMER**

This report has been reviewed by the Water Research Commission (WRC) and approved for publication. Approval does not signify that the contents necessarily reflect the views and policies of the WRC, nor does mention of trade names or commercial products constitute endorsement or recommendation for use.

# EXECUTIVE SUMMARY

---

## BACKGROUND

Suitable quality water is essential for life and industrial productivity. The only two options available are to purify available seawater on the planet to produce more potable water but ideally, to conserve and reuse the available water. The textile industry is one of the most chemically intensive industries on earth, using more than 100 000 types of chemicals and is the number one polluter of potentially potable water internationally.

This project was conducted in collaboration with Falke Eurosocks, a major textile company, which has a factory in Cape Town. Falke uses a range of dyes as part of the production of its leg wear. Wastewater is generated at the factory which is channelled to a primary effluent settling tank and then an overflow sump before it is discharged into the municipal sewer line. Falke Eurosocks was motivated to investigate the potential installation of a treatment plant at its factory out of a commitment to improve environmental performance, minimise and recycle waste, increase water supply security, and lower municipal discharge tariffs.

The aim of this project was to assess the application of one of the emerging nanotechnologies for water treatment, namely, nanofiltration and nanophotocatalytic treatment of the nanofilter retentate.

Nanoparticles (NPs), especially titanium dioxide,  $\text{TiO}_2$ , also known as titania, have photocatalytic properties. A commercial  $\text{TiO}_2$  nanoparticle, Evonik P25®, is a 21 nm  $\text{TiO}_2$  round particle, which is composed of approximately 25% rutile and 75% anatase phases. It is used in many studies of photocatalytic degradation, and also commercially. Titania is non-toxic, widely available, has a large surface area, is chemically stable and has a low cost. P25 titania has been used for more than 35 years to break down organics and sterilise water using UV light. Titania is an effective catalyst to generate a strong oxidising agent, a hydroxyl radical which is much stronger than chlorine, ozone and peroxide oxidising agents. The anatase phase of  $\text{TiO}_2$  has a lower band gap than the rutile phase, and is thus more efficient as a nanophotocatalyst. Over the past decades, metal-, nitrogen- or carbon-doped  $\text{TiO}_2$  have been widely studied for improved photocatalytic performance in degrading various organic pollutants under visible light. Generally accepted is that there are two essential paths to making  $\text{TiO}_2$  NPs active under daylight. One path is to reduce the particle size to less than 10 nm; the second path is to dope the  $\text{TiO}_2$  NPs with metals such as silver or gold. The use of non-metallic elements such as sulphur, nitrogen and carbon has been evaluated to reduce the cost of enhancing photocatalytic activity significantly due to a lower band gap.

There are many synthesis routes to prepare anatase and rutile phase nano- $\text{TiO}_2$ , such as precipitation, solvothermal, sol-gel, micelle and inverse micelle, hydrothermal, combustion synthesis, direct oxidation, microwave, and chemical and physical vapour deposition methods. The sol-gel synthesis method, although it has high yields, typically has long periods of ageing time or requires elevated temperatures. Continuous hydrothermal synthesis (CHS) has been identified as a scalable and effective method for producing reproducible nanoparticles. The anatase phase  $\text{TiO}_2$  is preferred, due to the lower band gap and thus higher potential to be active under daylight. The major factors affecting the photocatalysis process are the initial organic load, the amount of catalyst, reactor design, ultraviolet (UV) radiation time, temperature, solution pH, light intensity and presence of ionic species.  $\text{TiO}_2$  photocatalysts require photon energy to initiate the degradation reaction. Daylight has a lower energy than UV light but can potentially have sufficient energy to purify water if the catalyst activity can be increased to be operational under daylight (420 to 760 nm).

The nanophotocatalytic reactor would require vast surfaces exposed to sunlight. Typical textile treatment plants have a large roof surface area or ground space on the property where such systems could be installed. A trickle-bed reactor using simulated daylight lamps was therefore selected as a model system to determine the efficiency of photocatalysis in the treatment of textile effluents.

The objectives of this work were as follows:

- To conduct a stream segregation scoping assessment a cleaner production effluent audit for a proposed wastewater treatment process at Falke Eurosocks.
- To design, build and evaluate a pilot-scale rig for the treatment of textile effluent using pre-filtration, ultrafiltration (UF) and nanofiltration (NF).
- To develop synthesis strategies for the production of controlled-sized  $\text{TiO}_2$  nanophotocatalyst powders.
- To develop and optimise technology to treat effluent using  $\text{TiO}_2$  NPs immobilised on carbonised electrospun polyacrylonitrile (PAN) under daylight in a trickle-bed reactor.
- To evaluate the performance of the nanofiltration and photocatalysis of real textile effluent.

This report presents results for the treatment of commercial textile effluents using nanofiltration and photocatalysis using nano- $\text{TiO}_2$ .

## METHODOLOGY

An assessment of the Falke Eurosocks textile plant was conducted to identify possible solutions for a cleaner production system. Since the focus was on using nanotechnology and nano- $\text{TiO}_2$ , synthesis strategies for the controlled growth of  $\text{TiO}_2$  nanopowders were investigated in order to develop photocatalysis systems that can be up-scaled, immobilisation of nanopowders in electrospun scaffolds and subsequent treatment in a fixed-bed, trickle-bed reactor using simulated daylight and UV lamps.

The nanophotocatalysts were prepared using a sol-gel and hydrothermal treatment procedure and a CHS technique. To reduce the synthesis time, the effect of acid concentration (3, 4 and 5 M) and gel formation time (72, 24, and 12 hours) on the particle characteristics were evaluated. The work was conducted in a 1 L pressure vessel. The powders were characterised using HR-TEM to determine particle size and shape and XRD for polymorph quantification. The photocatalytic performance of the catalyst was evaluated using methylene blue solutions.

A CHS pilot plant was used to produce sub-10 nm  $\text{TiO}_2$  particles. A 3-level Box-Behnken factorial trial design was used to evaluate the correlations and interaction between operating parameters such as temperature, concentration and flow rate and particle characteristics. The powders were characterised using HR-TEM to determine particle size and shape and XRD for polymorph quantification.

A  $\beta\text{-FeOOH}/\text{TiO}_2$  heterojunction structure was synthesised from ultra-small  $\beta\text{-FeOOH}$  nanorods (2–6 nm diameter) and spherical anatase phase of  $\text{TiO}_2$  nanoparticles to improve photocatalysis in daylight. Three different  $\beta\text{-FeOOH}$  mol% of (2, 5 and 10%)  $\beta\text{-FeOOH}/\text{TiO}_2$  composite was prepared, and X-ray diffraction spectroscopy, Fourier transform infrared spectroscopy, transmission electron microscopy and UV-visible light spectroscopy diffuse reflectance spectra were used to characterise the prepared catalyst. The nanophotocatalysts were evaluated on laboratory-prepared model dyes, including methyl orange and acid black, and their performance compared to pure anatase and P25.

The P25  $\text{TiO}_2$  nanoparticles, sol-gel formed nanoparticles and  $\beta\text{-FeOOH}/\text{TiO}_2$  were immobilised in and on polyacrylonitrile electrospun scaffolds, stabilised for sol-gel conversion into  $\text{TiO}_2$ , and evaluated in a fixed-bed, trickle-bed reactor with UV-A, UV-B, UV-C and daylight lamps. The decolourisation of the model dyes and industrial dye samples was measured mainly by scanning UV-VIS spectroscopy but also by colorimetry and chemical oxygen demand (COD).

An UF/NF pilot plant was constructed and installed at the Falke factory. Its performance was evaluated by treating several reactive dye drop effluents. A mass balance was conducted primarily because wastewater management strategies in industry are increasingly relevant given the rising costs of potable water and risk

aspects of water security. The integration of water and mass balance models supports the development of water management plans and is critical for developing strategies aligned with water recycling and the objectives of achieving closed-loop water and wastewater usage, or for minimisation strategies. These models are frequently used to assess water management alternatives, key infrastructure changes or requirements, and any uncertainty underlying current and future water management scenarios. Model inputs include volumetric flows as well as physical inputs such as pH, total dissolved solids and temperature. Model outputs include the range of flows, water volumes, constituent concentrations at selected locations within the plant infrastructure, release points and the receiving environment.

One of the critical risk aspects of developing water and mass balance models in the textile industry relates specifically to sensitivity and uncertainty analyses due to the variable nature of the inputs associated with the variance in textile polymer types and associated variations in specific 'recipes' required to dye the various polymer types—variations in pre-treatment and scouring, salt type and concentration, dye chemicals, post-dyeing rinse cycles, softening, etc.

The effluent was obtained immediately after it was dropped and mixed in the main sump. The brine was collected and treated using the  $\beta$ -FeOOH/TiO<sub>2</sub> catalyst. Chemical analyses were conducted on the effluent samples before and after treatment.

## KEY FINDINGS AND CONCLUSIONS

The **stream segregation audit** revealed that the installation of 3-way valves into the existing piping systems can easily facilitate separation of waste streams for treatment and reuse purposes. In addition to the valve installation, the incorporation of a programmable timed event log system to the existing dye vat PLC-based control system is required. Boiler water and condensate as well as from the heat exchanger can be treated and separated from the dye vat effluents. This will reduce the footprint of the final effluent treatment plant.

Several strategies were developed for the local **production of nano-TiO<sub>2</sub> powders** for use in photocatalysis. Existing sol-gel methods were improved by reducing the synthesis time from 72 hours to 18 hours. It was shown that acid concentration can be used as a means to control polymorph composition at shorter gel formation times. Robust process conditions were established for the production of sub-10 nm particles using CHS to produce multi-polymorph anatase-rich TiO<sub>2</sub>. A heterojunction  $\beta$ -FeOOH/TiO<sub>2</sub>Anatase was produced and showed improved photocatalytic properties over anatase and P25 (anatase and rutile mixture). The CHS TiO<sub>2</sub> was also combined in a heterojunction with  $\beta$ -FeOOH and showed similar to improved photocatalytic performance. These results are very encouraging, showing the possibilities for locally manufactured photocatalysts to be used in the treatment of textile effluents.

Various methods of **immobilising TiO<sub>2</sub>** inside and outside of electrospun PAN fibres were evaluated, using commercial P25, titanium precursors as well as methods to carbonise these mats to be used in a trickle-bed reactor. Both model dye solutions (acid black and navy blue) and real effluent were degraded by up to 60% over a period of 9 hours in the trickle-bed reactor using the electrospun fibre mats with immobilised TiO<sub>2</sub>. The industrial potential for the utilisation of the TiO<sub>2</sub> immobilisation techniques developed in this work is great since there is a nanofibre spinning company in Cape Town (Stellenbosch Nanofibre Company) that is able to produce mats of up to two metres wide. These larger mats could be incorporated in a multistage, thin-film, fixed-bed photocatalytic reactor for upscaling of the process, using artificial and/or natural sunlight.

PAN nanofibres were further developed by the electrospinning technique and modified with EDTA-EDA chelating agents. After the chelation of Ti<sup>4+</sup> ions with surface carboxylic and amine groups of the EDTA-EDA chemically immobilised on PAN nanofibres (following self-growth of TiO<sub>2</sub> nanoparticles during the incubation process), additional changes to the properties of the modified PAN nanofibres were observed. The **fabricated composite nanofibres** exhibited the combined advantages of the two-phase materials such as unique catalytic and optical properties of TiO<sub>2</sub> nanoparticles, along with the excellent thermal stability, chemical inertness and high mechanical strength of PAN nanofibres.

An **UF/NF pilot plant was designed** and installed at the Falke factory to treat the effluent from the sump. Unfortunately, the effluent from the dye drop could not be pumped directly to the UF/NF pilot plant because it would require significant changes. Under the current conditions, 50% of water could be recovered as the nanofiltration permeate. The **colour was successfully removed from the NF brine** during treatment using standard conditions as determined during the development of a visible light active  $\beta$ -FeOOH/TiO<sub>2</sub> nanophotocatalyst. The sample was only treated for 90 minutes and if treatment time is increased, further reduction of COD and total organic carbon (TOC) could be achieved. The amounts of inorganic ions can be recovered during a further treatment step.

## RECOMMENDATIONS

- The effluent system pipeline should be modified to allow dye drop effluent to be directly fed to the UF/NF pilot plant to facilitate easy redirection of the reactive dye drops to the UF/NF pilot plant sump. The drops happened mainly in the early morning hours, making it very difficult for the research team to collect it for testing. Large-scale treatment systems will treat the concentrated dye drop effluent and not that of the mixed effluent in the sump. The efficiency of the UF/NF pilot plant to handle concentrated effluents should be evaluated.
- The industrial potential for the utilisation of the TiO<sub>2</sub> immobilisation techniques developed in this work is great since there is a nanofibre spinning company in Cape Town (Stellenbosch Nanofibre Company) that is able to produce mats of up to two metres wide methods of immobilising nanoparticles developed in this work. These larger mats should be incorporated in a multistage, thin-film, fixed-bed photocatalytic reactor for upscaling of the process, using artificial and/or natural sunlight.
- The intermediate complex organic compounds formed during degradation of the dyes should be monitored using high performance liquid chromatography (HPLC) coupled with a diode array detector followed by mass spectrometry (HPLC-DAD-MS). This is an extremely important part of the degradation study as it was shown in previous studies that over-treatment could lead to more toxic clear water than the actual dyestuff in the original effluent.
- The actual cost and saving of the proposed two-phase strategy treatment be conducted based on larger-scale treatment trials to confirm the current projection that it will lead to lower CAPEX investment requirements and the ability to recycle a larger volume of effluent once treated.
- Future studies should focus on the stability of the fabricated composite nanofibres in order to reduce the self-degradation of the support nanopolymer and consequently minimise the leaching of the metal oxide.

## KEYWORDS

Photocatalysis, titanium dioxide, photodegradation, sol-gel, continuous hydrothermal synthesis, electrospinning, sol-gel, immobilisation, polyacrylonitrile, textile effluent, slurry reactor, trickle-bed reactor, band gap, nanotechnology, nanoparticles.

# ACKNOWLEDGEMENTS

The project team wishes to thank the following people for their contributions to the project.

<b>Reference Group</b>	
Dr Jo Burgess	Water Research Commission
Prof Sabelo Mhlanga	University of South Africa
Dr Chris Buckley	University of KwaZulu-Natal.
Prof Rui Krause	Rhodes University
Mr Chris Fennemore	eThekweni Municipality
Prof Ochieng Aoyi	Vaal University of Technology
Dr Jessica Chamier	University of Cape Town
<b>Others</b>	
Mr Jesko Serrer	Falke, Technical Manager
Mr Reynald Gelderblom	Falke, Dyehouse Manager
Mr Shamil Isaacs	TSCT, CPUT, Manager
Mr Dave Mason	Independent consultant to the TSCT and Falke
Technology Innovation Agency (TIA)	Funders of the TSCT, CPUT and original scoping project in 2013.
Prof Daniel Iku-Omoregbe	CPUT, Chemical Engineering
Dr Langehlile Ndlamini	UJ, Department of Chemistry
Prof Lilian Tichagwa	Department of Polymer Engineering, Harare Institute of Technology
Ms Andiswa Dumayi	TSCT, CPUT, for analytical chemistry expertise.
Mr Rushdeen Rose	TSCT, CPUT, for assisting with project administration
Mr Nangamso Nyangiwe	Previously TSCT, now CSIR, NRE
Mr Anton Munnik	TSCT, CPUT for UV-VIS analyses
Prof Alvin Lagardien	TSCT, CWSS, HOD
Mr Christophe Muanda	TSCT, CWSS, water treatment expert
Mr Manuel Jackson	TSCT, CWSS, laboratory manager
Ms Miranda Waldron	UCT, Microscopy Unit for SEM and EDS analyses
Mr Steve Amos	BlueStar Fibres, for supply of correct grade PAN polymer
Mr Yaseem Salie	ATL-Hydro, training on Falke rig operation.
Prof Leslie Petrik	UWC, ENS, use of tube furnace for carbonisation.

# CONTENTS

<b>EXECUTIVE SUMMARY .....</b>	<b>ii</b>
<b>ACKNOWLEDGEMENTS .....</b>	<b>vii</b>
<b>CONTENTS .....</b>	<b>viii</b>
<b>LIST OF FIGURES .....</b>	<b>xiii</b>
<b>LIST OF TABLES.....</b>	<b>xvii</b>
<b>ACRONYMS and ABBREVIATIONS .....</b>	<b>xviii</b>
<b>GLOSSARY.....</b>	<b>xx</b>
<b>CHAPTER 1: BACKGROUND .....</b>	<b>1</b>
1.1 PROJECT AIMS .....	3
1.2 SCOPE AND LIMITATIONS .....	4
<b>CHAPTER 2: LITERATURE REVIEW.....</b>	<b>5</b>
2.1 NANOTECHNOLOGIES FOR WATER TREATMENT .....	5
2.2 TEXTILE EFFLUENT: TYPICAL POLLUTANTS.....	5
2.3 REVIEW OF REPORTS ON TREATMENT OF TEXTILE EFFLUENTS.....	7
2.4 COMMERCIAL / INDUSTRIAL TEXTILE EFFLUENT TREATMENT AND AOP'S.....	8
2.4.1 Industrial textile effluent treatment.....	8
2.4.2 Advanced oxidation processes, AOP's, for colour removal from textile effluents .....	8
2.5 SOUTH AFRICAN INDUSTRIAL EFFLUENT STANDARDS .....	10
2.6 NANOPHOTOCATALYSTS.....	11
2.6.1 Mechanism of photocatalysis.....	11
2.6.2 Theory of the photodegradation of organic dyes .....	12
2.6.3 Nano titania particles for photocatalysis .....	15
2.6.4 Enhancement of photocatalytic efficiency of nano-TiO <sub>2</sub> .....	15
2.6.4.1 Carbon and nitrogen modification of the TiO <sub>2</sub> photocatalyst (Anion doped TiO <sub>2</sub> ) ..	16
2.6.4.2 Metal modification of the TiO <sub>2</sub> photocatalyst (Cation doped TiO <sub>2</sub> ) .....	17
2.6.4.3 Co-catalyst modification of the TiO <sub>2</sub> photocatalyst by coupled / composite TiO <sub>2</sub> ..	17
2.6.5 The effect of the catalyst support on the TiO <sub>2</sub> photocatalyst .....	18
2.6.6 Conclusions on doped nano-TiO <sub>2</sub> .....	18
2.7 REMOVAL OF TEXTILE DYES WITH PHOTOCATALYSTS.....	19
2.7.1 Examples of the photodegradation of organics, including dyes .....	19
2.7.2 Effect of reaction parameters and conditions on the photocatalysis of textile effluents .....	23
2.7.2.1 Introduction to evaluation of reaction conditions on photocatalysts of textile effluents	23
2.7.2.2 Effect of light intensity and wavelength on the efficiency of photocatalysts of textile dyes	23
2.7.2.3 Effect of pH on the efficiency of photocatalysts of textile effluents .....	23
2.7.2.4 Effect of catalyst load on the efficiency of photocatalysts of textile effluents .....	25
2.7.2.5 Effect of catalyst type on the efficiency of photocatalysts of textile effluents .....	25
2.7.2.6 Effect of peroxide concentration on the efficiency of photocatalysts of effluents ..	25
2.7.2.7 Conclusions on the effect of reaction conditions on photocatalysts of textile effluents	26



2.8	PRODUCTION OF NANOPHOTOCATALYSTS .....	26
2.8.1	Introduction .....	26
2.8.2	Synthesis of TiO <sub>2</sub> nanoparticles using bench-scale laboratory conditions .....	26
2.8.2.1	Review of methods for the synthesis of TiO <sub>2</sub> nanoparticles .....	26
	Sol-gel synthesis .....	26
2.8.2.2	Synthesis of doped TiO <sub>2</sub> nanoparticles modified with nitrogen and carbon .....	29
2.8.2.3	Synthesis of doped TiO <sub>2</sub> nanoparticles using a hetero-junction structure.....	31
2.8.3	Large-scale production of nanoparticles using CHS.....	31
2.9	IMMOBILISATION OF NANOPHOTOCATALYSTS .....	32
2.9.1	Types of catalyst supports .....	32
2.9.2	Electrospun catalyst supports using polyacrylonitrile, PAN .....	35
2.9.2.1	Electrospinning process .....	35
2.9.2.2	Polyacrylonitrile and carbon fibre catalyst supports .....	36
2.10	DESIGN OF LARGE SCALE PHOTOCATALYTIC REACTORS .....	38
2.10.1	Photocatalyst reactors .....	38
2.11	TOXICITY OF PHOTOCATALYSTS .....	40
<b>CHAPTER 3: STREAM SEGREGATION SCOPING ASSESSMENT FOR A PROPOSED WASTEWATER TREATMENT PROCESS AT THE FALKE EUROSOCKS .....</b>		<b>42</b>
3.1	INTRODUCTION .....	42
3.2	DESCRIPTION OF CURRENT WASTEWATER DISCHARGE INFRASTRUCTURE AT FALKE .....	42
3.3	STREAM SEGREGATION EVALUATION.....	44
3.3.1	Process design and strategy.....	44
3.3.2	Piping and Instrumentation diagram .....	44
3.4	THE DYES AND DYEING EFFLUENTS FROM FALKE .....	49
3.4.1.1	Dye-stuffs and additives .....	49
3.4.1.2	Analyses of Falke sump samples .....	50
3.5	CONCLUSIONS.....	51
<b>CHAPTER 4: CATALYST DEVELOPMENT AND EVALUATION IN A SLURRY REACTOR .....</b>		<b>53</b>
4.1	PREPARATION OF TiO <sub>2</sub> NP'S CONSISTING OF VARIOUS POLYMORPHS USING SOL-GEL/HYDROTHERMAL SYNTHESIS.....	53
4.1.1	Experimental method for sol-gel synthesis and hydrothermal treatment.....	54
4.1.1.1	Synthesis of the sol .....	54
4.1.1.2	Synthesis of the gel .....	54
4.1.1.3	Hydrothermal treatment procedure .....	55
4.1.1.4	Particle Characterisation .....	55
4.1.2	Results and discussion of TiO <sub>2</sub> nanoparticles using a sol-gel/hydrothermal .....	55
4.1.3	Photocatalytic properties of batch produced TiO <sub>2</sub> multi-polymorph powders .....	59
4.2	CONTINUOUS HYDROTHERMAL SYNTHESIS (CHS) OF TiO <sub>2</sub> NANOPARTICLES.....	61
4.2.1	CHS pilot plant and experimental methods .....	61
4.2.1.1	Overview of CHS pilot plant.....	61
4.2.1.2	Chemicals used .....	63
4.2.1.3	CHS procedure .....	63
4.2.1.4	Box-Behnken factorial design for CHS optimisation.....	63
4.2.1.5	Particle Characterisation .....	64
4.2.2	Results and discussion of continuous hydrothermal synthesis (CHS) of TiO <sub>2</sub> .....	64
4.2.3	Conclusion from factorial trial.....	68
4.3	SYNTHESIS OF ULTRA-SMALL B-FE(OH)/TiO <sub>2</sub> HETERO-JUNCTION NP .....	69
4.3.1	Experimental methods for synthesis of $\beta$ -FeOOH/TiO <sub>2</sub> hetero-junction NP .....	69

4.3.1.1	Preparation of $\beta$ -FeOOH nanoparticles .....	69
4.3.1.2	Preparation of $\beta$ -FeOOH/TiO <sub>2</sub> hetero-junction structures.....	69
4.3.1.3	Characterization .....	70
4.3.2	Results and discussion of the preparation of $\beta$ -FeOOH/TiO <sub>2</sub> .....	70
4.3.2.1	Evaluation of the photocatalytic performance of $\beta$ -FeOOH/TiO <sub>2</sub> .....	71
4.3.2.2	Photocatalysis of methyl orange (MO) using $\beta$ -FeOOH/TiO <sub>2</sub> in slurry system .....	72
4.3.3	Comparison of catalyst performance of ultra-small $\beta$ -FeOOH/TiO <sub>2</sub> hetero-junction.....	73
4.4	CONCLUSIONS.....	74

## **CHAPTER 5: CATALYST IMMOBILISATION AND EVALUATION IN A TRICKLE BED REACTOR .....76**

5.1	PREPARATION OF IMMOBILISED NANO-TiO <sub>2</sub> PARTICLES .....	76
5.1.1	Experimental method for electrospinning PAN, stabilisation and carbonisation .....	76
5.1.1.1	Materials used for electrospinning.....	76
5.1.1.2	Preparation of the electrospinning dope.....	76
5.1.1.3	Electrospinning equipment .....	76
5.1.1.4	Electrospinning parameters.....	76
5.1.1.5	PAN stabilisation and carbonisation in a furnace .....	77
5.1.2	Experimental method for electrospinning with TiO <sub>2</sub> and TiO <sub>2</sub> precursors.....	77
5.1.2.1	TiO <sub>2</sub> nanoparticles inside the electrospun fibres .....	77
5.1.2.1	Ti precursors inside the electrospun fibres.....	78
5.1.2.2	Immobilisation of titanium precursors outside fibres through dip-coating .....	78
5.1.2.3	Characterisation of the immobilised TiO <sub>2</sub> in and on PAN.....	79
5.2	CHARACTERISATION OF PAN ELECTROSPUN FIBRES AND MATS.....	79
5.2.1	PAN electrospun fibres – the role of electrospinning (ES) parameters on fibre formation .....	79
5.2.2	Immobilisation of nanophotocatalyst particles in and on PAN fibres .....	80
5.2.3	Results and discussion for ES PAN mats with TiO <sub>2</sub> pre-cursors in the spinning dope .....	81
5.2.3.1	TTIP, titanium based, pre-cursor in the electrospinning dope.....	81
5.2.3.2	TiCl <sub>4</sub> pre-cursor in the electrospinning dope .....	82
5.2.4	Results and discussion for carbon and PAN mats dipped into TiO <sub>2</sub> pre-cursor solutions.....	82
5.2.5	Stabilisation and carbonisation of fibres .....	83
5.3	EXPERIMENTAL METHOD OF CATALYST EFFICIENCY IN A TRICKLE-BED REACTOR (TBR).....	84
5.3.1	Description of trickle bed reactor and light sources used in the TBR experiments .....	84
5.3.1.1	The laboratory scale trickle-bed reactor .....	84
5.3.1.2	The characterization of light sources.....	85
5.3.1.3	Mats with immobilised TiO <sub>2</sub> used in the TBR experiments.....	86
5.3.1.4	Experimental method for evaluating model dyes .....	87
5.3.1.5	Plant sampling points of real textile effluent.....	87
5.4	RESULTS AND DISCUSSION OF THE TREATMENT OF MODEL DYES IN THE TRICKLE-BED REACTOR .....	87
5.4.1.1	Calibration curves for Methyl orange, Acid black and Navy Blue.....	87
5.4.1.2	Methyl orange degradation in the TBR using different lamps on P25 TiO <sub>2</sub> mats.....	88
5.4.1.3	Methyl orange degradation in the TBR using UVC lamp .....	89
5.4.1.4	Acid black degradation in the TBR using UVC lamp.....	90
5.5	DEGRADATION OF THE FALKE EFFLUENT FROM DIFFERENT SAMPLING POINTS.....	90
5.5.1	Degradation of Falke AB sump sample in the TBR .....	90
5.5.1.1	Treatment of Falke NB sump sample in the TBR.....	91
5.5.2	Degradation of NF brine after treatment in the TBR .....	91
5.6	CONCLUSIONS.....	92

## **CHAPTER 6: CATALYST IMMOBILISATION USING CHELATING LINKERS AND EVALUATION IN A COMMERCIAL PHOTOCATALYTIC REACTOR.....94**

6.1	INTRODUCTION .....	94
6.2	MATERIALS AND METHODS .....	95
6.2.1	Reagents .....	95
6.2.2	Preparation and modification of PAN nanofibres .....	95
6.2.3	Preparation of composite nanofibres .....	96
6.2.4	Photocatalytic test .....	96
6.2.5	Characterization techniques .....	96
6.3	RESULTS AND DISCUSSION .....	97
6.3.1	Surface morphology of the nanofibres .....	97
6.3.2	Surface chemistry of the nanofibres .....	99
6.3.3	Photodegradation of dyes .....	105
6.4	CONCLUSIONS .....	106

## **CHAPTER 7: SURFACE MODIFICATION OF PAN NANOFIBRES USING CHELATING LINKERS FOR THE REMOVAL OF DYES.....107**

7.1	INTRODUCTION .....	107
7.2	MATERIALS AND METHODS .....	108
7.2.1	Reagents .....	108
7.2.2	Functionalization reactions of PAN nanofibres .....	108
7.2.3	Instrumentation .....	108
7.2.4	Adsorption experiments .....	108
7.2.5	Reusability of EDTA-EDA-PAN nanofibres .....	109
7.3	RESULTS AND DISCUSSION .....	109
7.3.1	Textural analysis .....	109
7.3.2	Surface imaging .....	109
7.3.3	Thermal properties .....	110
7.3.4	Surface chemistry .....	111
7.3.5	Electrostatic properties of nanofibres .....	112
7.3.6	Adsorption studies .....	113
7.3.6.1	Effect of pH .....	113
7.3.6.2	Effect of contact time .....	113
7.3.6.3	Effect of initial concentration .....	114
7.3.7	Adsorption isotherms .....	114
7.3.8	Adsorption kinetics .....	116
7.4	CONCLUSIONS .....	117

## **CHAPTER 8: DESIGN, INSTALLATION AND EVALUATION OF UF/NF PILOT PLANT AND PHOTOCATALYTIC TREATMENT OF NF BRINE .....118**

8.1	DESIGN CONSIDERATIONS .....	118
8.2	P&ID .....	118
8.3	PILOT PLANT LAYOUT .....	119
8.4	COMMISSIONING AND OPERATION .....	121
8.5	MASS BALANCE ANALYSIS .....	123
8.5.1	Dye drop mass balance analysis after pre-treatment, UF and NF treatment .....	123
8.6	NANOFILTER BRINE TREATMENT USING PHOTOCATALYSIS .....	130
8.6.1	Olive effluent .....	131
8.6.2	Black effluent .....	133
8.6.3	Bell Blue effluent .....	134
8.7	CHARACTERISTICS OF FALKE EFFLUENT BEFORE AND AFTER TREATMENT .....	136
8.8	CONCLUSIONS .....	138

<b>CHAPTER 9: CONCLUSIONS AND RECOMMENDATIONS .....</b>	<b>139</b>
9.1 CONCLUSIONS.....	139
9.2 RECOMMENDATIONS.....	140
<b>CHAPTER 10: REFERENCES.....</b>	<b>142</b>

# LIST OF FIGURES

Figure 2.1 Schematic illustrating the photocatalytic processes.....	12
Figure 2.2 UV/VIS reflectance spectra of size-quantised TiO <sub>2</sub> (Hoffmann et al., 1995) .....	14
Figure 2.3 Electron and holes transfer between Fe <sub>2</sub> O <sub>3</sub> and TiO <sub>2</sub> under visible light (A) and UV light (B) irradiation (Zhang et al., 2014) .....	18
Figure 2.4 pH dependence of the rate of degradation of trichloroacetate (●) and chloroethylammonium (○) ions where [CCl <sub>3</sub> CO <sub>2</sub> <sup>-</sup> ] = [Cl(CH <sub>2</sub> ) <sub>2</sub> NH <sub>2</sub> ] <sub>0</sub> = 10 mM, [TiO <sub>2</sub> ] = 0.5 g/ L, [O <sub>2</sub> ] <sub>0</sub> = 0.25 mM, and I <sub>a</sub> (310 to 380 nm) = 2.5 x 10 <sup>-4</sup> Einstein/L/min (Hoffmann et al., 1995). .....	24
Figure 2.5 Different morphologies produced via CHS (Einarsrud and Grande, 2012).....	27
Figure 2.6 Morphology-dependant photocatalytic activity (Mingshan et al., 2011) .....	28
Figure 2.7 Schematic of the electrospinning process (Ke et al., 2014).....	35
Figure 2.8 Chemical reaction of the stabilisation and carbonisation of PAN (McGann et al., 2012).....	37
Figure 2.9 Packed bed photocatalyst reactor (Feitz et al., 2009).....	38
Figure 2.10 Packed bed photocatalytic reactor (Saien et al., 2009) .....	38
Figure 2.11 Thin film photocatalytic reactor (Feitz et al., 2000) .....	39
Figure 2.12 Thin film photocatalytic reactor (Bahnemann, 2004).....	39
Figure 2.13 Pilot plant using sunlight as a light source (Bahnemann, 2004) .....	39
Figure 3.1 Process flow diagram of Falke's existing discharge infrastructure .....	43
Figure 3.2 Schematic diagram of the factory layout at Falke before the incorporation of WPYD .....	43
Figure 3.3 Schematic diagram of the current factory layout at Falke after the incorporation of WPYD.....	44
Figure 3.4 P&ID schematics indicating relationships between dye process streams, heat exchanger infrastructure and the water softening plant .....	45
Figure 3.5 Stream segregation audit for acrylics, nylon, polyester, and cotton.....	48
Figure 3.6 Photograph of examples of Falke powder dyes .....	49
Figure 3.7 Photograph of Falke cotton and polyester dye bath drop samples.....	51
Figure 4.1 Amorphous TiO <sub>2</sub> gel before hydrothermal treatment .....	54
Figure 4.2 Hydrothermal reactor used for the conversion of amorphous TiO <sub>2</sub> nanoparticles to crystalline TiO <sub>2</sub> nanoparticles .....	55
Figure 4.3 Evolution of TiO <sub>2</sub> nanoparticle shape for a 3, 4 and 5 M HCl concentration and gel formation time of 72 (A), 48 (B), 24 (C), and 12 (D) hours .....	56
Figure 4.4 Effect of gel formation time and concentration of HCl acid on particle size .....	56
Figure 4.5 XRD patterns of TiO <sub>2</sub> nanoparticles for various gel formation times for 3, 4 and 5 M HCl .....	57
Figure 4.6 Percentage rutile formed for increasing HCl concentration and gel formation time.....	57
Figure 4.7 Phase transformation of TiO <sub>2</sub> for with HCl concentration at gel formation times of 24 and 12 hours .....	58
Figure 4.8 Degradation of methylene blue in the presence of various catalysts.....	59
Figure 4.9 Process flow design of the CHS pilot plant used in this study .....	62

Figure 4.10 (A) 3D design of CHS pilot plant (B) CHS plant in lab at Cape Peninsula University of Technology .....	63
Figure 4.11 3D quadratic plot of temperature versus acid addition on the effect of APS at (a) low pressure (20 MPa) and (b) high pressure (30 MPa) .....	65
Figure 4.12 TEM images showing the effect of temperature on APS .....	66
Figure 4.13 A 3D quadratic plot of temperature versus acid addition on the effect of PSD at (a) low pressure (20 MPa) and (b) high pressure (30 MPa) .....	67
Figure 4.14 A 3D quadratic plot of temperature versus acid addition on the effect of PY at (a) low pressure (20 MPa) and (b) high pressure (30 MPa) .....	67
Figure 4.15 Quantitative analysis of XRD results .....	68
Figure 4.16 a) XRD patterns of the different materials b) TEM image of 5% $\beta$ -FeOOH rod-like particle (inset shows PSD) c) Heterojunction structure of $\beta$ -FeOOH/TiO <sub>2</sub> d) HRTEM image of $\beta$ -FeOOH/TiO <sub>2</sub> heterojunction and e) High temperature XRD of the $\beta$ -FeOOH particles .....	71
Figure 4.17 Role of H <sub>2</sub> O <sub>2</sub> concentration on MO degradation in the absence of catalysts .....	72
Figure 4.18 MO degradation using various catalysts .....	73
Figure 4.19 Repeatability tests of MO degradation using $\beta$ -FeOOH/TiO <sub>2</sub> anatase .....	74
Figure 4.20 Comparison of MO degradation using $\beta$ -FeOOH/TiO <sub>2</sub> Anatase and $\beta$ -FeOOH/TiO <sub>2</sub> CHS .....	74
Figure 5.1 Programmable furnace used for the thermal treatment of electrospun PAN mats (stabilisation and carbonisation) .....	77
Figure 5.2 Micrographs of 8% PAN/DMSO, as spun and after stabilisation .....	79
Figure 5.3 Micrographs of 12% PAN/DMF, as spun and after stabilisation .....	80
Figure 5.4 Micrographs of 6% P25 in 6% PAN/DMF, as spun and after stabilisation .....	80
Figure 5.5 Micrographs of 1% and 3% P25 in 6% PAN/DMF, after carbonisation .....	81
Figure 5.6 TTIP in 6% PAN/DMSO as spun and stabilised .....	81
Figure 5.7 EDS elemental mapping for titanium in TTIP in 6% PAN/DMSO as spun and stabilised .....	81
Figure 5.8 Micrographs of TiCl <sub>4</sub> in 8% PAN/DMF .....	82
Figure 5.9 Micrographs of carbon fibre mat and ES PAN dipped in TTIP .....	83
Figure 5.10 PAN and PAN composites before and after stabilisation .....	83
Figure 5.11 Degree of shrinkage of ES PAN mats during stabilisation and carbonisation .....	84
Figure 5.12 The laboratory-scale trickle-bed reactor .....	85
Figure 5.13 Spectral output of lamps used in the TBR experiments .....	86
Figure 5.14 Falke Synoset® acid black and Everzol® navy blue samples .....	87
Figure 5.15 Calibration curves for laboratory-prepared dye samples of MO, AB and NB .....	88
Figure 5.16 Reduction in colour of MO in the TBR with UVC lamp for P25/8% PAN mats .....	88
Figure 5.17 Reduction in colour of MO in the TBR with UVB and daylight on 3% P25/8% PAN mat .....	89
Figure 5.18 Reduction in colour of MO in the TBR with UVC on 3% TiO <sub>2</sub> anatase 8% PAN mat .....	89
Figure 5.19 Degradation of laboratory prepared 50 ppm AB in the TBR with UVC .....	90
Figure 5.20 UV/VIS spectra for the degradation of AB sump with UVC on 3% P25/8%PAN .....	91

Figure 5.21 UV/VIS spectra for the degradation of NB sump with UVC on 3% P25/8% PAN .....	91
Figure 5.22 UV/VIS spectra for the degradation of NB sump in the TBR with UVC and a catalyst mat of 3% P25/8%PAN stabilised over time till 5 hours' treatment .....	92
Figure 5.23 Degradation of NB sump in the TBR with daylight mat of 3% $\beta$ -FeOOH/TiO <sub>2</sub> /8%PAN .....	92
Figure 6.1 SEM micrographs of (a) pristine PNFs (b) EDTA-EDA-PNFs. (c) TiO <sub>2</sub> -EDTA-EDA-PNFs .....	98
Figure 6.2 EDS spectra of TiO <sub>2</sub> -EDTA-EDA-PNFs composite.....	98
Figure 6.3 FT-IR spectra of (a) PNFs (b) EDA-PNFs (c) EDTA-EDA-PNFs and (d) TiO <sub>2</sub> -EDTA-EDA-PNFs.....	99
Figure 6.4 Proposed chemical reaction pathways for the modification of PNFs by EDTA-EDA chelating agent .....	100
Figure 6.5 XPS spectra of EDTA-EDA-PNFs and TiO <sub>2</sub> -EDTA-EDA-PNF composites .....	101
Figure 6.6 XPS spectra for the Ti 2p states of TiO <sub>2</sub> -EDTA-EDA-PNF composite.....	101
Figure 6.7 XPS spectra for the O 1s states of TiO <sub>2</sub> -EDTA-EDA-PNFs .....	102
Figure 6.8 XPS C 1s spectra of (a) EDTA-EDA-PNFs and (b) TiO <sub>2</sub> -EDTA-EDA-PNFs.....	103
Figure 6.9 XPS spectra for the N 1s states of (a) EDTA-EDA-PNFs and (b) TiO <sub>2</sub> -EDTA-EDA-PNFs.....	104
Figure 6.10 Comparison of the surface composition of EDTA-EDA-PNFs and TiO <sub>2</sub> - EDTA-EDA-PNF composites given by C 1s and N 1s peaks.....	104
Figure 6.11 XRD spectra of (a) EDTA-EDA-PNF and (b) TiO <sub>2</sub> -EDTA-EDA-PNF composites. ....	105
Figure 6.12 Photocatalytic degradation of MO (a) and MB (b) using TiO <sub>2</sub> -EDTA-EDA-PAN and commercial TiO <sub>2</sub> P25 (mass of catalyst 0.10 g, volume of solution 100 mL, and an initial concentration of 30 mgL <sup>-1</sup> MO and 10 mgL <sup>-1</sup> MB.....	106
Figure 7.1 SE micrographs of the (a) electrospun PAN (b) EDA-PAN and (c) EDTA-EDA-PAN nanofibres at $\times 10,000$ magnification .....	110
Figure 7.2 TGA patterns of PAN, EDA-PAN and EDTA-EDA-PAN nanofibres.....	111
Figure 7.3 FT-IR spectra of the as-prepared and modified electrospun PAN nanofibres .....	112
Figure 7.4 Chemical reactions for the modification of PAN nanofibres (where EDA is ethylenediamine, EDTA is ethylenediaminetetraacetic acid dianhydride (EDTAD), THF is tetrahydrofuran, Nt3 is triethyleamine). The monomers <i>l</i> , <i>k</i> and <i>m</i> correspond to 93, 6 and 1%. respectively) .....	112
Figure 7.5 Effect of pH on the adsorption of dyes on EDTA-EDA-PAN nanofibres using 0.05 g nanofibres in 25 mL 50 mgL <sup>-1</sup> dye solutions.....	113
Figure 7.6 Effect of contact time for the adsorption of dyes on EDTA-EDA-PAN nanofibres .....	114
Figure 7.7 Effect of initial concentration for the adsorption of dyes on EDTA-EDA-PAN nanofibres.....	114
Figure 7.8 Langmuir model for the adsorption of MB, MO and RR onto EDTA-EDA-PAN nanofibres .....	115
Figure 7.9 Freundlich model for the adsorption of MB, MO and RR onto EDTA-EDA-PAN nanofibres .....	116
Figure 7.10 Temkin model for the adsorption of MB, MO and RR onto EDTA-EDA-PAN nanofibres .....	116
Figure 7.11 Adsorption kinetic of MB, MO and RR onto the EDTA-EDA-PAN nanofibres using pseudo-first-order kinetic model .....	117
Figure 7.12 Adsorption kinetic of MB, MO and RR onto the EDTA-EDA-PAN nanofibres using pseudo-second-order models, Pseudo-second-order kinetic model.....	117
Figure 8.1 Process flow diagram of UF/NF pilot plant.....	119
Figure 8.2 Process flow diagram of UF/NF pilot plant.....	120

Figure 8.3 UF/NF pilot plant set up at Falke.....	121
Figure 8.4 Volumetric and mass input analysis for Olive dye sequences. ....	124
Figure 8.5 Volumetric and mass input analysis for Bell Blue dye sequences. ....	125
Figure 8.6 Volumetric and mass input analysis for Black cotton reactive dye sequences. ....	126
Figure 8.7 Cotton reactive Olive UF and NF mass balances. ....	127
Figure 8.8 Cotton reactive Bell Blue UF and NF mass balances. ....	128
Figure 8.9 Cotton reactive Black pre-treatment UF and NF mass balances. ....	129
Figure 8.10 Representative dye fraction at various pre- and post-treatment stages indicating complete colour retention by NF treatment. ....	130
Figure 8.11 UV-Vis spectra for NF brine and treated NF brine .....	131
Figure 8.12 Photodegradation of Olive NF Brine at $\lambda_{\text{max}}$ of 418.5 nm for Synozol Yellow, 541.4 nm for Synozol Red and 614.4 nm for Synozol Navy.....	132
Figure 8.13 Photodegradation of Black NF brine .....	133
Figure 8.14 Photodegradation of Bell Blue NF brine.....	134
Figure 8.15 Colour comparison of brine and treated brine of Olive. Black and Bell Blue effluents.....	135
Figure 8.16 Colour comparison of effluent from dye bath to final treated product .....	135
Figure 8.17 pH .....	136
Figure 8.18 Conductivity .....	136
Figure 8.19 TDS .....	137
Figure 8.20 TOC .....	137
Figure 8.21 Sulphate .....	138
Figure 8.22 Phosphates.....	138



## LIST OF TABLES

Table 2.1 Dye types used on specific polymer fibre types .....	6
Table 2.2 Standards for effluent discharge into natural water resources .....	10
Table 2.3 TiO <sub>2</sub> photocatalyst optimisation process and the optimisation mechanisms .....	19
Table 2.4 Examples of scientific articles using doped TiO <sub>2</sub> and ZnO photocatalysts: Type of catalyst and organic dye contaminant .....	19
Table 2.5 Examples of scientific articles using doped TiO <sub>2</sub> and ZnO photocatalysts; B: Photocatalytic treatment condition .....	21
Table 2.6 Examples of scientific articles using doped TiO <sub>2</sub> and ZnO photocatalysts: Photocatalytic performance. ....	22
Table 2.7 Common TiO <sub>2</sub> , C-TiO <sub>2</sub> , N-TiO <sub>2</sub> and C-N-TiO <sub>2</sub> synthesis techniques and precursors .....	30
Table 2.8 The immobilization of nanoparticles .....	33
Table 2.9 TBR flow rates .....	40
Table 3.1 Selected Dyestuffs from Falke.....	49
Table 3.2 Selected additives from Falke .....	49
Table 3.3 Physicochemical parameters of industrial dyeing effluents.....	52
Table 4.1: Catalyst size, phase and photocatalytic activity .....	60
Table 4.2: Variables in Box-Behnken design.....	64
Table 4.3 Factorial trial sample matrix - Operating parameters and their respective particle characteristics. ....	65
Table 4.4: Correlation factors of operating parameters on particle size.....	65
Table 4.5 Correlation factor of operating parameters on particle size distribution .....	66
Table 4.6 Correlation factor of operating parameters on product yield .....	67
Table 4.7 Summary of correlation factors.....	69
Table 5.1 Trick bed reactor parameters from literature .....	85
Table 5.2 Lux and lumen values of lamps used in the TBR experiments at 1 cm from the lamp surface .....	86
Table 5.3 Measurement of the daylight lamp intensity at different distances above the catalyst .....	86
Table 8.1 Specification for the ATL-HYDRO UF/NF rig at Falke.....	122

## ACRONYMS and ABBREVIATIONS

AB	Acid black
AOPs	Advanced oxidation processes
APS	Average particle size
ASTM	American Standard Test Methods
BET	Brunauer – Emmett - Teller
BMO	Bi-metallic metal oxide
BOD	Biological oxygen demand
CAPEX	Capital expenditure
CHS	Continuous hydrothermal synthesis
CIP	Clean in place
COD	Chemical oxygen demand
Conc.	Concentration
CPUT	Cape Peninsula University of Technology
CSIR	Council for Scientific and Industrial Research
CVD	Chemical vapour deposition
CWSS	Community Water and Sanitation Services
DMF	Dimethyl formamide
DMSO	Dimethyl-sulphoxide
DRS	Diffuse Reflectance Spectroscopy
DST	Department of Science and Technology, RSA
EDA	Ethylenediamine
EDTA	Ethylenediaminetetraacetic acid
EDTAD	Ethylenediaminetetraacetic acid dianhydride
ENNSATOX	Engineered Nanoparticle Impact on Aquatic environments: Structure, Activity and Toxicology
ENP	Engineered nanoparticle
ES	Electrospinning
eV	Electron volt
FP7	7 <sup>th</sup> Framework programme
FTIR	Fourier Transform Infrared Spectroscopy
GAC	Granular Activated Carbon
GC-MS	Gas Chromatography coupled with Mass Spectroscopy
GDNP	Global Dialogue on Nanotechnology and the Poor: Opportunities and Risks
HPLC	High performance liquid chromatography
IC	Ion chromatography
ICP-OES	Inductively coupled plasma – optical emission spectroscopy
LC-MS	Liquid chromatography coupled with mass spectroscopy
LOX	Liquid oxygen
MB	Methylene blue dye
MC	Metal complex

MO	Metal oxide
MO	Methyl orange
NB	Navy blue
NF	Nanofiltration
NMP	FP7 Nanomaterials Programme
NP	Nanoparticle
NRE	Natural Resources and the Environment, CSIR, South Africa
NRF	National Research Foundation, South Africa
OECD	Organisation for Economic Cooperation and Development
P&ID	Piping and instrumentation diagram
PAN	Polyacrylonitrile
PFD	Process flow diagram
PNF	PAN nanofibres
POC	Persistent Organic Compounds
POU	Point-of-use
ppm	Concentration in parts per million or alternatively mg/litre
PSD	Particle size distribution
PY	Product yield
R and D	Research and development
REL	Recommended Exposure Limit
RO	Reverse Osmosis
RR	Reactive red dye
RSA	Republic of South Africa
SEM	Scanning electron microscopy
TBR	Trickle-bed reactor
TDS	Total dissolved solids
TEM	Transmission electron microscopy
TNP	TiO <sub>2</sub> nanoparticles
TOC	Total organic carbon
TSCT	Technology Station in Clothing and Textiles
TTIP	Titanium tetra-isopropoxide
UF	Ultrafiltration
UCT	University of Cape Town
UJ	University of Johannesburg
UNESCO	The United Nations Educational, Scientific and Cultural Organization
UV	Ultraviolet
UV-VIS	Ultraviolet and visible light spectroscopy
WHO	World Health Organisation
W/O	Water in oil
WPYD	Western Province Yarn Dyers
XPS	X-ray photoelectron spectroscopy
XRD	X-ray Diffraction Spectroscopy

# GLOSSARY

---

- Decolourisation:** The reduction in colour visible by the human eye.
- Effluent degradation:** The UV-VIS results showing dye degradation and concentration of chromophores.
- P25:** A commercial, round, titania nanoparticle, with a particle size of 21 nm, with 75% anatase phase and 21% rutile phase. Supplied by Evonik Industries, South Africa, Mr Selwyn Lee Fong, [selwyn.leefong@evonik.com](mailto:selwyn.leefong@evonik.com). Sample previously supplied by Degussa who have now merged with other companies to form Evonik. Sample referred to as P25® by Evonik.  
<http://coranoparticlesporate.evonik.com/en/Pages/default.aspx>.
- Falke:** Falke Eurosocks (Pty) Ltd, Hosiery Manufacturers. Address: Cnr. Fabriek and Oop St, Bellville South, 7530, South Africa.  
Tel: +27 (021) 951 2137. A factory belonging to FALKE KGaA, Schmallenberg, Germany.
- Spinning dope:** Solution of a polymer in a solvent used for spinning fibres.
- Doped nanoparticles:** Metal oxide nanoparticles where either some of the metal atoms or the oxygen atoms are replaced by other metals, nitrogen or carbon or combined in heterojunctions with other metal oxides.



# CHAPTER 1: BACKGROUND

---

Suitable quality water is essential for life and industrial productivity. The only two options available are to purify available seawater on the planet to produce more potable water, or, ideally, to conserve and reuse the available water. The textile industry is one of the most chemically intensive industries on earth, using more than 100 000 types of chemicals and is the number one polluter of potentially potable water internationally. It takes about 2000 litres of water to produce enough fabric to cover one sofa (Slater, 2003). The textile finishers are comprised of a diverse, fragmented group of establishments that produce, and/or process, textile-related products (fibre, yarn, fabric) for further processing into apparel, home furnishings, and industrial textiles. As much as 50 to 100 L of wastewater per kg of finished textile product is produced by the dyeing and finishing industry (Manu and Chaudhari, 2002). The World Bank estimates that the textile industry in most countries contributes 17 to 20% of global industrial water pollution. Dyes prevent sunlight from reaching into water bodies causing damage to aquatic life. Colour is also an obvious polluted water indicator (Asghar et al., 2014; Ghoreishian et al., 2014).

The availability of water impacts on food, energy, biodiversity and mining. South Africa is a water scarce country with a developing economy. The emerging nanotechnologies for water treatment, nanophotocatalysis, can potentially contribute in water and energy savings in industry for sustainable growth in southern Africa. The use of nanotechnology for industrial textile effluent clean-up, removing harmful by-products from the textile finishing process, has promise. Such harmful substances include organic dyestuffs such as azo dyes, hydrophobic finishing agents, which are composed of fluorocarbons and silicones, and flame retardants which are halogenated or phosphonated compounds. All these compounds are carcinogenic, making the water dangerous to all living species. There are many structural varieties of dyes, such as azo, anthraquinone, phthalocyanine, direct, reactive, disperse, acid, basic, neutral and metal complexed. Reactive dyes are the most often used in the dyeing process, for reasons such as good stability during washing, and allowing relatively simple dyeing procedures. Reactive dyes are used for dyeing wool and cellulosic fibres such as cotton. Reactive dyes have good water solubility and are easily hydrolysed, but approximately 20 to 40% of these dyes remain in the effluent (Radovic et al., 2014).

The requirements to remove colour from textile effluent on site prior to discharge to sewers have been progressively tightened. The removal of the colouration of textile dyes has been a topic of numerous research articles since the 1960s and several review articles on the topic have been published (Joshi et al., 2004; Gupta and Suhas, 2009; Forgacs et al., 2004; Singh and Arora, 2011). Reviews of the use of low-cost biosorbents have been authored by Crini (2006) and Bharathi and Ramesh (2013). They argue that the use of granular activated carbon (GAC) as an absorbent of textile effluent organics cannot be cost effective and that the use of agricultural waste may be financially viable.

Reactive dyes have been estimated to contribute the most to those dyes that are discharged into wastewater, due to their low fixation rate (Pearce et al., 2003). Quantitative dye bath exhaustion is not possible with most systems. Most current practices for wastewater decolourisation treatment fall into the following four main classes:

- Physical or physicochemical techniques, i.e. precipitation, coagulation/flocculation, ion exchange, adsorption, and membrane separation. These remove or separate the colour physically and result in need for solid waste disposal;
- Chemical techniques, i.e. ozonolysis, chemical oxidation/reduction, etc. These technologies remove the colour from the effluent by breaking down the dye into simpler fragments and destroy the chromophores responsible for colour;
- Biological techniques, i.e. aerobic and anaerobic digestion, whereby decolourization takes place either by adsorption of dyes on activated sludge or by biological degradation of dye molecules;

- Electrochemical techniques, i.e. electro dialysis ion oxidation. It combines the oxidation of the dye and the other polluting contaminants by means of the electrolytic process with the physicochemical precipitation of the sludge.

Each technique has a specific application and distinct advantages and disadvantages. As a result, each method has to be evaluated according to cost, application and performance relative to the desired goal. No treatment technology has universal application; a combination of one or two is generally employed, depending on wastewater characteristics (Joshi et al., 2004).

The treatment of textile effluents has received attention in previous Water Research Commission (WRC) research projects and a review of the literature revealed at least 16 WRC research reports listed on the WRC website. These research thrusts can be briefly summarised as consisting of membranes and anaerobic baffled reactors and other chemical (advanced oxidation) processes, biological and physical methods all of which reduce the level of organics and colour but not to sufficient levels to comply with effluent discharge standards. In addition, the processes typically take up to 20 days, or at best 72 hours.

The development of new materials is an area of water quality engineering where nanotechnology is expected to make a critical impact (Tarabara, 2009). Nanotechnologies for wastewater treatment immobilised in robust industrial-scale systems are an emerging technology with international attention only since 2005. Research in relation to drinking water treatment in small point-of-use (POU) devices has already received impetus since the mid-1990s.

Photocatalytic processes for water and waste water treatment are a new area having vast applications (Velhal et al., 2012). Titanium dioxide, ( $\text{TiO}_2$ ), also called titania, is an effective catalyst for generating a strong oxidising agent, a hydroxyl radical which is much stronger than chlorine, ozone and peroxide oxidising agents (Velhal et al., 2012). Evonik (formerly Degussa) P25® is a commercially available spherical 21 nm  $\text{TiO}_2$  which consists of approximately 25% rutile and 75% anatase crystal phases. Titanium dioxide, due to its relative non-toxicity, widespread availability, large surface area, chemical stability and low cost, has been used in studies regarding the photocatalytic degradation of organic wastewater contaminants from the textile and allied industries. Moreover,  $\text{TiO}_2$  has been found to be relatively stable in aqueous media, to have fairly good tolerance for acidic and alkaline conditions and is more readily synthesised in nanostructure form than other photocatalysts (Chong et al., 2010; Bahnemann, 2004).

Recent research on  $\text{TiO}_2$  showed that photocatalytic ability is dependent on shape. Shaped nanomaterials such as nanobelts, nanowires and nanotubes have been shown to have higher photocatalytic activity than spherical particles, and especially when there is preferential growth in the 101 plane (Wu et al., 2010a). Testino et al. (2007) observed a correlation between the photocatalytic activity in the UV photodegradation of phenol solutions and the particle size, and further, that prismatic rutile particles with length around 5 nm and breadth of 60-100 nm showed the highest activity. This is of interest as anatase is usually more reactive than rutile. None of these studies were scaled up to real industrial textile effluents, which requires ability to scale up the reproducible production of these novel-shaped nanoparticles (NPs).

There are many ways to synthesise  $\text{TiO}_2$ , either pure or as a mixture of anatase and rutile with or without brookite, such as precipitation, solvothermal, sol-gel, micelle and inverse micelle, hydrothermal, combustion synthesis, direct oxidation, microwave, and chemical and physical vapour deposition methods. The sol-gel synthesis method, although it has high yields, suffers from long periods of ageing time. If the ageing time can be reduced, the method can be effective in producing large quantities in a batched synthesis process.

Continuous hydrothermal synthesis (CHS) has been identified as a scalable and effective method for producing high-quality spherical nanoparticles. The effect of process conditions on the particle properties needs to be evaluated to develop robust process conditions for production of uniform powders.

Generally,  $\text{TiO}_2$  catalysts are applied in the form of powder in suspension. Difficulties during recovery of the catalyst after treatment in a large-scale approach can be solved by immobilising the catalyst on an inert surface such as glass, quartz, concrete, ceramics or carbonised polymeric polyacrylonitrile (PAN) fibres.

The major factors affecting the photocatalysis process are the initial organic load, amount of catalyst, reactor design, UV radiation time, temperature, solution pH, light intensity and presence of ionic species. Over the past decades, metal such as silver and gold, nitrogen or carbon-doped  $\text{TiO}_2$  have been widely studied for improved photocatalytic performance on degradation of various organic pollutants under visible light. A significant shift of the absorption edge to a longer wavelength (lower energy) from 420 nm to 456 nm and 420 nm to 428 nm was observed for the carbon-doped and nitrogen-doped  $\text{TiO}_2$  respectively. The photocatalytic activity of the catalyst was tested using methyl orange as a model pollutant in a trickle-bed reactor outdoors under daylight and was based on the decolourization of the dye as it was degraded. The doped  $\text{TiO}_2$  exhibited higher photocatalytic activity than the undoped  $\text{TiO}_2$  (Nyamukamba et al., 2012).

This project was conducted in collaboration with a major textile company in Cape Town. Falke Eurosocks is an international clothing and lifestyle brand and leg wear market leader. Headquartered in Germany, Falke South Africa exports more than 90% of its socks to more than 30 countries, but mostly to the USA. Falke dyeing batches are made up of 80% disperse dyes on polyester, 15% reactive dyes on cotton and the remaining 5% acidic dyes on nylon. Falke Eurosocks' processing plant in Bellville historically consumed an average of 1 920 kL/month of potable water and discharged 95% (1 820 kL/month) of this as effluent to the municipal sewer. (The municipal effluent discharge tariff is based on a percentage, as opposed to direct volumetric measurement). Since 2008, municipal effluent discharge and potable water costs have increased by 84% (from R5.65/kL to R10.39/kL) and 95% (from R6.95/kL to R13.51/kL) respectively. Falke currently discharges a single combined effluent stream to the Bellville municipal wastewater treatment works located in Sacks Circle, via a discharge sump located on the Falke premises. Wastewater is generated at the Falke Eurosocks factory from water utilised in dye house processes, washing and drying of product, machine cleaning, precipitation and wash-water run-off from process areas. The wastewater is currently channelled to a primary effluent settling tank from where it is transferred via gravity separation into an overflow sump before it is discharged into the municipal sewer line.

It is believed that Falke can save a considerable amount of money by treating the most polluted streams with the appropriate technology as opposed to treating the entire outflow with a technology intervention tailored to 10% of the actual stream. This allows 90% to be recycled at a much lower cost than just decreasing the pollutant load and relying on the savings to pay for the capital expenditure (CAPEX).

## 1.1 PROJECT AIMS

The objectives of this work were as follows:

1. To conduct a stream segregation scoping assessment a cleaner production effluent audit for a proposed wastewater treatment process at Falke Eurosocks.
2. To design, build and evaluate a pilot-scale rig for the treatment of textile effluent using pre-filtration, ultrafiltration (UF) and nanofiltration (NF).
3. To develop synthesis strategies for the production of controlled sized  $\text{TiO}_2$  and doped- $\text{TiO}_2$  nanophotocatalyst particles.
4. To develop and optimise technology to treat NF brine using nanophotocatalysts based on  $\text{TiO}_2$  NPs immobilised on various types of electrospun PAN.
5. To evaluate the performance of the NF and photocatalysis of real textile effluent.



## 1.2 SCOPE AND LIMITATIONS

The WRC, as well as the South African strategic plan for nanotechnology development, both highlight the local development of intellectual property (IP) and innovative processes for industrial implementation. The true success of the use of nanotechnology in the treatment of textile effluents depends on the ability to locally produce technology and know-how. This project therefore aimed to develop local expertise in nanotechnology for the treatment of textile effluent.

Model dyes used were methyl orange, methylene blue and/or acid black for the  $\text{TiO}_2$  photocatalytic discolouration evaluations of the  $\text{TiO}_2$  powders developed in a slurry reactor and the electrospun fibre mats developed in either a trickle-bed reactor (TBR) or a commercial photoreactor.

Industrial dye samples from Falke included the dye bath drop, the sump from reactive dye bath drops of Olive, Black and Bell Blue. The samples were taken as the dye bath drops were fed to the mixed sump (directly after a requested bath drop) and from the NF plant (concentrate and permeate) with subsequent treatment of the NF brine using photocatalysis in a slurry reactor.

Effluent samples were tested only for pH, chemical oxygen demand (COD), conductivity, total dissolved solids (TDS), total organic carbon (TOC), nitrates and phosphates.

## CHAPTER 2: LITERATURE REVIEW

---

This chapter presents a review of scientific articles related to the role of nanotechnology in water treatment, dyeing processes, nanophotocatalyst preparation and mechanisms in organic dye removal.

### 2.1 NANOTECHNOLOGIES FOR WATER TREATMENT

A brief overview of the technologies is provided here and classified according to the predominant field of application. Excellent review articles and reference books on the application of nanotechnologies for water treatment are available. Just a few examples of which the first seven are listed here, of which the first five listed below, have origin in the Republic of South Africa (RSA).

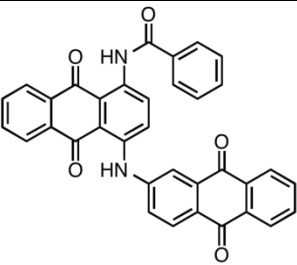
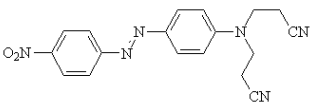
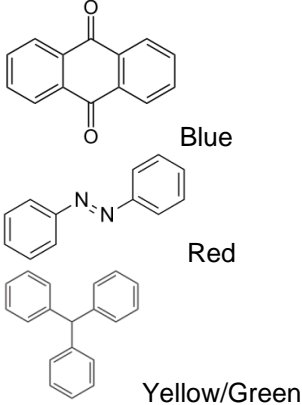
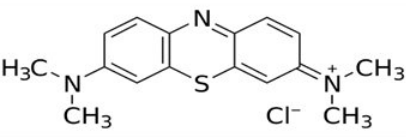
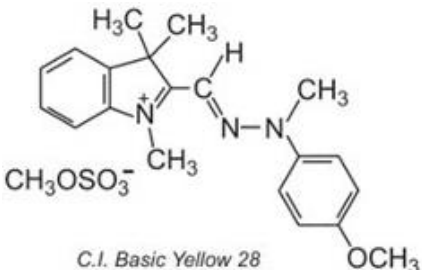
1. The Meridian Institute have published a 44-page review article entitled “Nanotechnology, Water and Development” (Hille et al., 2006) as commissioned by the Global Dialogue on Nanotechnology and the Poor: Opportunities and Risks. The review article is co-authored by researchers from Sri Lanka and the CSIR in South Africa. It compares conventional and nanotechnology-based water treatment for POU drinking water devices.
2. A South African, WRC-commissioned, 28-page report by the University of Pretoria’s Department of Chemical Engineering, entitled “Evaluation of Nanotechnology for Application in Water and Wastewater Treatment and Related Aspects in South Africa” (Schutte and Focke, 2007).
3. A 27-page review article by the University of Pretoria’s Department of Microbiology and Plant Pathology, entitled “Nanotechnology and Water Treatment: Application and Emerging Opportunities” (Theron et al., 2008).
4. A 38-page review, published by the Meridian Institute entitled “An Overview and Comparison of Conventional and Nano-based Water Treatment Technologies” (Meridian 2009).
5. A 200-page book published by Caister Academic Press in June 2010 entitled; “Nanotechnology in Water Treatment Applications” (Cloete et al., 2010).
6. A 700-page book, published by Elsevier in 2009, entitled: “Nanotechnology Applications for Clean Water” (Diallo et al., 2009).
7. Frost and Sullivan Market Surveys. Topics in these technical publications relate more to international industrial trends in wastewater treatment recycling, NF, nanotechnology for chemical free water treatment and industrial challenges for the application of nanotechnology-related water treatment (Frost and Sullivan, 2006).

### 2.2 TEXTILE EFFLUENT: TYPICAL POLLUTANTS

The textile industry has received increased attention worldwide due to the generation of contaminated effluents to the environment (Nguyen and Juang, 2013; Riu et al., 1997). There are several industry-specific contaminants in textile waste waters, including dyes, chemicals, colours, fats, and oil. The textile industry is currently facing severe pressure to reduce colour in wastewater from dyeing and finishing operations.

Dyes may be classified according to parameters such as chemical structure, colour, application, fastness, manufacturer, synthesis route, date invented, etc. (Clark, 2011). Table 2.1 presents a classification related to the type of fibre dyed and the characteristics of the major dye-classes for each fibre type, as used at Falke, the test factory for this project. It is noted that the structures are all aromatic and contain groups with nitrogen atoms.

**Table 2.1 Dye types used on specific polymer fibre types**

Fibre	Dye Type	Description	Dye structure
Cotton	Reactive	Reactive dyes form a covalent bond between the dye and fibre. They contain a reactive group, that, when applied to a fibre in an alkaline dye bath, forms a chemical bond with a hydroxyl group on the cellulosic fibre. In a reactive dye, a chromophore contains a substituent that reacts to the surface of the fibre.	
Polyester	Dispersive	Dispersive dyes tend to be fairly hydrophobic. The polymer chains in polyester are highly crystalline and thus molecularly tightly packed, and, as such, polyester fibres have low affinity for large ionic dye molecules. Dispersive dyes are small, planar and non-ionic molecules with attached polar functional groups. The dye is generally applied under pressure, at temperatures of about 130°C.	
Nylon/ polyamide	Acid	The chemistry of acid dyes is relatively complex. Acid dyes are normally very large aromatic molecules consisting of many linked aromatic rings. Acid dyes are soluble in acidic aqueous solutions. Acid dyes are generally divided into three classes which depend on fastness requirements, level dyeing properties and economy.	
Nylon / polyamide	Metal Complex (MC)	MC dyes are a sub-class of acid dyes that require an acidic aqueous medium. In MC dyes, one or two dye molecules are coordinated with a metal ion. The dye molecule is typically a monoazo structure, which is capable of forming a strong co-ordination complex with transition metal ions such as chromium, cobalt, nickel and copper.	
Acrylic	Basic	Basic dye is a stain that is cationic so it will react with fibres that are negatively charged. This dye is usually a base, which is actually an aniline dye. Their chromophore is not water soluble but can be made so by converting the base into a salt. The basic dyes, while having strong colour and brightness, are not generally light-fast. A few examples of basic dyes are: methylene blue, crystal violet, basic fuchsin safranin, etc.	 <i>C.I. Basic Yellow 28</i> <a href="http://www.dyes-pigments.com/reactive-dyes.html">http://www.dyes-pigments.com/reactive-dyes.html</a>

Textile wastewater contains organic compounds, mainly azo dyes, from the dyeing process. The presence of the dyes in effluent streams causes environmental pollution as they are highly toxic and could be carcinogenic (Xu et al., 2013). Due to their complex aromatic structure and stability, dyes are hardly removed by physical, chemical or biological treatment processes (Falah and Thekra, 2010).

Currently, more than 280 000 tons of textile dyes are discharged into industrial effluents per annum (Jin et al., 2007). These effluents possess adverse impacts in terms of organic matter content, suspended solids, salinity, colour, a large pH range (i.e. pH 2 to 12) and organic compounds including dyes (Savin and Butnaru, 2008). Furthermore, the anaerobic degradation of dyes generates aromatic amines, which are very toxic, carcinogenic and mutagenic to human beings (Nguyen and Juang, 2013; Riu et al., 1997). This fact has significant relevance to a country like South Africa where the majority of wastewater treatment plants are employing biological processes.

## 2.3 REVIEW OF REPORTS ON TREATMENT OF TEXTILE EFFLUENTS

This section reviews related WRC reports and comments on local and international effluent discharge standards.

In recent years, numerous technical reports have been funded and published by the WRC regarding the treatment of textile effluents — Barclay and Buckley (1990, 2002 and 2004); Binda et al. (2008); Classens (2004); Cronje et al. (2005); Mutambanengwe et al. (2008); Swartz et al. (2004) and more.

These technical reports provide limited reference to scientific data on nanoparticles for the treatment of industrial-scale effluents, particularly the removal of organic contaminants from textile effluents using nano-TiO<sub>2</sub>.

The textile effluent treatment technologies studied have included enzymes, nanoporous polymers, membranes, anaerobic baffled reactors, electrolysis, immobilising titania on carbon nanotubes and a holistic approach to using combined methods.

The degree of decolouration of the effluents was never reported as 100% but as a maximum of 96%, for example:

- Decolourisation of 72% to 93% for an effluent dye mixture and the dye mixture plus silicate salts, using SRB-BioSURE process sludge over a five-day period (Mutambanengwe et al., 2008).
- Decolourisation of 70% to 90% for 18 reactive dyes (14 azo dyes, 3 phthalocyanine dyes and a dye based on the anthraquinone chromophore) using an anaerobic process. It was shown that the phthalocyanine dyes tested gave a wide spread of results with decolourisation efficiencies ranging from 25% to 90%, and the anthraquinone dye showed little decolourisation. The decolourisation was conducted over five months (Barclay and Buckley, 2004).
- Removal of up to 75% of organics was reported using a proton exchange membrane system to sterilise water and remove organics, using an electrolysis system. The organic phenol and *Escherichia coli* were treated within 4 hours. The process requires high energy input and expensive membranes (Cronje et al., 2005).
- Removal efficiencies of up to 92% on methylene blue within 6 hours were achieved using nanotechnology. Titania and doped titania were immobilised on carbon nanotubes. The highest removal efficiency was obtained with silver doped titania (Petric and Ndungu, 2012). It was proposed that silver nanoparticles deposited on the TiO<sub>2</sub> act as electron acceptors, thereby enhancing the

charge separation of the electrons and holes, and that leads to a transfer of the trapped electrons to the adsorbed oxygen during UV radiation.

The promotion of biodegradable chemicals in the textile industry was discussed by Binda et al. (2008). A scoring system was assessed at 16 textile factories as a tool to assist in the prevention of pollution and the replacement of potentially toxic chemicals with less harmful alternatives. The score system was based on four parameters deemed important for characterising the impact of chemicals and dyestuffs on the environment. These are discharged amount of substance, biodegradability, bioaccumulation, and toxicity.

In summary, the novel treatment methods were effective in the removal/reduction of organic pollutants but require further verification and optimisation.

## **2.4 COMMERCIAL/INDUSTRIAL TEXTILE EFFLUENT TREATMENT AND ADVANCED OXIDATION PROCESSES**

This section presents the conventional methods for textile effluent treatment, briefly addresses some of the more unique methods and discusses advanced oxidation processes (AOPs).

### **2.4.1 Industrial textile effluent treatment**

Conventional disposal of wastewater from textile and dye mills is to discharge it into local wastewater treatment plants with maybe minimum treatment such as pH neutralisation. To meet the ever more stringent water discharge criteria, enhanced treatment is critical in the mills to prevent environmental pollution. Chemicals, heavy metals, oils, wax, pigments, chromium and inorganic salts are the most common and the most difficult matters to remove from wastewater.

There is an array of established water treatment technologies including aeration, filtration, ultraviolet (UV) radiation, chemical treatment, distillation and desalination. Flocculation and coagulation can be used to separate dispersive dyes which will be removed in the sludge at a conventional waste water treatment plant. Liquid phase adsorption has been one of the most popular methods of removing pollutants from wastewater. Ion exchange and adsorption are valuable in removing colour but this depends on many factors such as physicochemical factors like active surface area of the adsorbent, time, particle size and pH, and thermal factors. Adsorption has been a preferred technique because it does not generate harmful substances but such processes, including the use of activated carbon in the adsorption process, have proved to be far too expensive and pose a regeneration challenge. Various filtration methods such as membrane filtration processes (microfiltration, ultrafiltration, nanofiltration and reverse osmosis) have been used extensively in wastewater treatment (Shon et al., 2013) but removal of carcinogenic organic products may still be a challenge if treated water has to be recycled.

Challenges of colour elimination and total organic degradation are often not met due to the complexity of the chemical structure and synthetic nature of the dyes. Proponents suggest that nanotechnology-based materials could lead to cheaper, more durable, and more efficient water treatment technologies that will meet the needs of developing countries (Hill, 2010).

### **2.4.2 Advanced oxidation processes for colour removal from textile effluents**

Advanced oxidation processes (AOPs) are treatment procedures designed to remove organic (and sometimes inorganic) materials in water, by oxidation through reactions with hydroxyl radicals. This term usually refers more specifically to a subset of such chemical processes that employs ozone ( $O_3$ ), hydrogen peroxide ( $H_2O_2$ ) and/or UV light. A well-known example of an AOP is the use of a Fenton's reagent. AOPs involve the two stages of oxidation: 1) the formation of strong oxidants (e.g. hydroxyl radicals) and 2) the reaction of these oxidants with organic contaminants in water.

AOPs are particularly useful for cleaning biologically toxic or non-degradable materials such as aromatics, pesticides, petroleum constituents, and volatile organic compounds in wastewater. The contaminant materials are converted to a large extent into stable inorganic compounds such as water, carbon dioxide and salts, i.e. they undergo mineralisation. A goal of wastewater purification by means of AOPs is the reduction of the chemical contaminants and the toxicity to such an extent that the cleaned wastewater may be reintroduced into receiving streams or, at least, into a conventional sewage treatment.

Oxidation reactions that produce radicals tend to be followed by additional oxidation reactions between the radical oxidants and other reactants (both organic and inorganic) until thermodynamically stable oxidation products are formed. The ability of an oxidant to initiate chemical reactions is measured in terms of its oxidation potential. The most powerful oxidants are fluorine, hydroxyl radicals ( $\bullet\text{OH}$ ), ozone, and chlorine with oxidation potentials of 2.85, 2.70, 2.07 and 1.49 electron volts, respectively. Violet-based systems break down organic molecules and kill bacteria and viruses, and can be used in conjunction with other water treatment systems. Ozone is also used to oxidise iron and other metals for easier removal by filtration. AOPs are replacing the use of harmful oxidants such as chlorine, hypochlorite and peroxides.

Ozone can be used prior to a biological process (Takahashi et al., 2007) since ozone will convert organic molecules into smaller, more biodegradable species. This benefit is well known in the literature. In textile wastewater processes, a 20 to 30% improvement in the action of the biological system has been observed.

Ozone can improve biodegradability and thereby reduce toxicity. Where the treated water is tested for toxicity, the impact of the treatment process must be considered. Destroying one organic molecule, but creating more toxic ones in a treatment process has been observed; for example, the ozonation of MTBE (methyl ethyl ketones), without any additional agents or treatment processes, can result in a more toxic wastewater (Takahashi et al., 2007). Another consideration is the presence of surfactants and the need to remove these compounds from the water. In some locales surfactant concentrations are tightly controlled and must be kept under 1 mg/L. This creates an additional demand for oxidant. Some textile wastewaters contain both colour and surfactants.

Ozone is effective in removing the colour from all dyes used in textile processing. The amount of ozone can vary depending on a number of factors: how much colour was removed in the biological process, the type of dye used, where ozone is applied in the process, etc. Knowing the proper amount of ozone required to meet the colour removal objective for the receiving water body is critical to the economics of the ozone system. In general, it is not easy to predict the amount of ozone required, so, in virtually all cases where specific previous experience is not available, pilot testing is employed. Most industrial ozone generators convert oxygen to ozone using the corona discharge method. The oxygen can come from dry air, oxygen concentrated from air or liquid oxygen. Tosik (2005) has shown that about 1 mg ozone/mg dye is required to achieve 95% colour removal, although this ratio varies by dye type. The ratio increases to about 1.5 mg ozone for 100% removal. Reaction times measured are about 10 minutes. In the textile industry, a typical dosage might be 15 mg/L post biological treatment, but the levels could easily reach 25 mg/L. It is important to note that the ozone dose only needs to make the dye compound uncoloured and not necessarily completely mineralise the material.

Oxidation processes, such as biological, chemical or physical, are one of the major steps during water treatment. Despite the feasibility and wide applicability of biological oxidation processes, the presence of toxic organic pollutant makes the application of this process impractical (Amoth et al., 1992). Physical separation processes like thermal destruction of chemicals at elevated temperatures is effective but not economically feasible; more so, the generation of toxins during thermal destruction poses environmental risk. Advanced oxidation processes, i.e.  $\text{O}_3/\text{H}_2\text{O}_2$ ,  $\text{UV}/\text{O}_3$ ,  $\text{UV}/\text{H}_2\text{O}_2$ , Fenton,  $\text{UV}/\text{Fenton}$ , photocatalytic oxidation, wet air oxidation, wet peroxide oxidation, electron beam and catalytic ozonation, have been used to optimise both process and economic efficiency (Kasprzyk-Hordern et al., 2003).

Photocatalysis is a promising alternative among the various advanced oxidation methods. However, the difficulty in separation of the photocatalyst from the solution hinders the application of photocatalysis in

environmental remediation. Immobilisation of the photocatalyst in a solid support has been proposed as a solution to bypass the aforementioned problem. There are several other advantages, i.e. higher surface area, enhanced adsorption and reduced charge recombination (Lazar et al., 2012).

## 2.5 SOUTH AFRICAN INDUSTRIAL EFFLUENT STANDARDS

Effluent standards are specifications of the physical, biological, and chemical quality of the effluent to be produced by the treatment. These usually include allowable concentrations of BOD, COD, suspended solids (SS), nitrogen, phosphorus, etc. Most such concentrations are expressed in mg/L or ppm.

The standards for discharge into natural water resources in South Africa are provided in Table 2.2. For example, the effluent should have a COD in the range of 30 to 75 mg/L. Despite these stringent guidelines, many municipalities are not complying as their effluents have a high level of BOD, nutrients and other pollutants that are harming the general environment. This lack of compliance has been attributed to the inadequacy of the treatment processes, lack of knowledge and expertise among process controllers and poor monitoring of influent quality.

**Table 2.2 Standards for effluent discharge into natural water resources**

Parameters	South Africa DWAF (1998)	
	General limit	Special limit
pH	5.5 - 9.5	5.5 - 7.5
Ammonia s N (mg/L)	3	2
Nitrate as N (mg/L)	15	1.5
Oil and Grease (mg/L)	2.5	0
BOD <sub>5</sub> (mg/L)		
COD (mg/L)	75	30
TSS (mg/L)	25	10
TP (mg/L)		
Orthophosphate (mg/L)	10	1 - 2.5
TN (mg/L)		
FC (cfu/100ml)	1,000	0
Electrical conductivity	7 - 150	50 - 100
Phenols (microgram/l)		
Chlorine (mg/l) residual		
Chlorine (as free chlorine)	0.25	0
Fluoride (mg/L)	1	1
Dissolved Arsenic (mg/L)	0.02	0.01
Dissolved Cadmium (mg/L)	0.005	0.001
Dissolved Chromium (mg/L)	0.05	0.02
Dissolved Copper (mg/L)	0.01	0.002
Dissolved Cyanide (mg/L)	0.02	0.01
Dissolved Iron (mg/L)	0.3	0.3
Dissolved Lead (mg/L)	0.01	0.006
Dissolved Manganese (mg/L)	0.1	0.1
Mercury and its compounds (mg/l)	0.005	0.001
Dissolved Selenium (mg/L)	0.02	0.02
Dissolved Zinc (mg/L)	0.1	0.04
Boron (mg/L)	1	0.5

With regard to the level of treatment of municipal effluent prior to discharge, the main objective applied internationally is to reduce waste loads, particularly those of suspended solids and biochemical oxygen demand. Municipal effluent has characteristic loads of these two substances that are easy to measure and, by reducing these, it is also possible to markedly decrease the loads of other potentially harmful substances, e.g. nutrients and toxins such as trace metals.

Treatment levels of municipal effluent (sewage) can broadly be categorised into stages, namely preliminary treatment, primary treatment, secondary treatment and tertiary treatment which includes disinfection.

The first stage of the treatment process uses screens to remove the larger solid inorganic material such as paper and plastics. This is followed by the removal of particles such as grit and silt which are abrasive to plant equipment. Following preliminary treatment, wastewater is passed through a primary sedimentation tank where solid particles of organic material are removed from the suspension by gravity settling. The resultant settled primary sludge is raked to the centre of the tank where it is concentrated and pumped away for further treatment.

This next stage is a biological process which breaks down dissolved and suspended organic solids by using naturally occurring micro-organisms. It is called the activated sludge process. The settled wastewater enters aeration tanks where air is blown into the liquid to provide oxygen for mixing and to promote the growth of micro-organisms. The active biomass uses the oxygen and consumes organic pollutants and nutrients in the wastewater to grow and reproduce. From the aeration tanks, the mixture of wastewater and micro-organisms passes into a secondary sedimentation tank (also known as a clarifier) where the biomass settles under gravity to the bottom of the tank and is concentrated as sludge. Some of this sludge is recycled to the inlet of the aeration tank to maintain the biomass, hence the name for the process – activated sludge. The remainder is pumped to anaerobic digesters for further treatment. The clarified wastewater is discharged from the secondary clarifier and passes through for tertiary treatment.

All wastewater treatment plants use disinfection for tertiary treatment to reduce pathogens, which are micro-organisms which can pose a risk to human health. Chlorine is usually dosed into the treated wastewater stream for disinfection. However, some plants use large ponds in which sunlight and other micro-organisms reduce the pathogens. Additional treatment may be required if the treated wastewater is reused for purposes such as irrigation of food crops or where close human contact may result.

Despite the use of these stages, conventional wastewater treatment in South Africa does not adequately address the removal of organics. This is due to the fact that many wastewater treatment plants are designed for domestic wastewater and to some extent industrial effluent. With the growth of industries (including textiles) in South Africa, different types of effluent containing high levels of organics are being discharged into municipal wastewater streams, thus making the treatment process difficult. Municipal wastewater systems designed for the treatment of domestic wastewater cannot treat these effluents to acceptable standards unless a pre-treatment process is performed at the source of generation.

## **2.6 NANOPHOTOCATALYSTS**

In this section of the report the mechanism of photocatalysis is discussed and then more specific information on titania and doped titania mechanisms of photocatalysis is presented.

### **2.6.1 Mechanism of photocatalysis**

Heterogeneous photocatalysis by light activated  $\text{TiO}_2$  particles has proven to be a successful technique for the degradation and mineralisation of persistent organic pollutants (Bandara et al., 2007). It has been reported by Xu et al. (2013) and Jinhui et al. (2012) that the process is environmentally friendly as no other harsh chemicals are required to make the process efficient.

When a semiconductor such as  $\text{TiO}_2$ ,  $\text{ZnO}$ ,  $\text{Fe}_2\text{O}_3$ ,  $\text{CdS}$  etc. is irradiated with a beam of light, a portion of the photons is absorbed. If the energy of the photon matches or exceeds the band gap energy of the semiconductor, an electron is liberated from the valence band into the conduction band, leaving an electron hole behind (Inagaki et al., 2014; Daghrir et al., 2013; Leary and Westwood, 2011). The photogenerated electrons induce reduction reactions on the conduction band while the holes induce oxidation reactions on the valence band. Materials which can generate electron-hole ( $e^-h^+$ ) pairs are classified as photocatalysts (Daghrir et al., 2013; Leary and Westwood, 2011).



The photogenerated electron-hole ( $e^-h^+$ ) pairs can decompose pollutants adsorbed onto the photocatalyst's surface. For photocatalyst reuse, it is desirable that their surface remain unchanged during the photocatalytic process due to unmodified surface active sites. This is achieved when the oxidation-reduction reactions occur at similar rates (Leary and Westwood, 2011). Figure 2.1 illustrates the photocatalytic process, where the main processes in semiconductor photocatalysis are: (i) photon absorption and electron-hole pair generation; (ii) charge separation and migration – (a) to surface reaction sites or (b) to recombination sites; (iii) surface chemical reaction at active sites (Leary and Westwood, 2011).

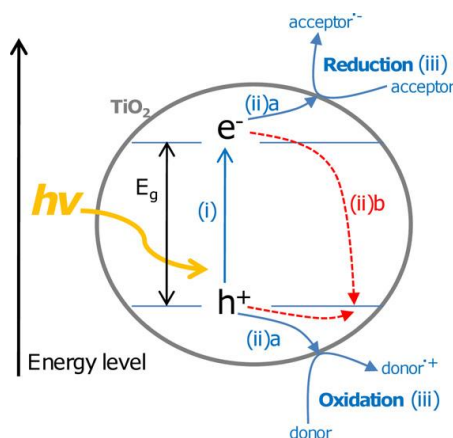


**Figure 2.1 Schematic illustrating the photocatalytic processes**

The excited state conduction band electrons and valence band holes can recombine and dissipate the input energy as heat, get trapped in metastable surface states, or react with electron donors and electron acceptors adsorbed on the semiconductor surface or within the surrounding electrical double layer of the charged particles.

### 2.6.2 Theory of the photodegradation of organic dyes

In principle, when  $\text{TiO}_2$  is irradiated with UV light of a band gap energy equal to or greater than  $\lambda < 380 \text{ nm}$ , electrons from the valence band  $\text{TiO}_2 (h^{+vb})$  migrate to the conduction band  $\text{TiO}_2 (e^{-cb})$ . By so doing, positively charged holes ( $h^{+vb}$ ) and negatively charged electrons ( $e^{-cb}$ ) are created (Mills et al., 1993).



The holes ( $\text{TiO}_2 (h^{+vb})$ ) and the electrons  $\{\text{TiO}_2 (e^{-cb})\}$  migrate to the surface of the photocatalyst where they initiate redox reactions with the organic contaminants adsorbed at the surface of the photocatalyst.

The oxidisable species are the adsorbed organic dyes ( $D_{\text{ads}}$ ), hydroxyl ions ( $\text{OH}^-_{\text{ads}}$ ) and water molecules ( $\text{H}_2\text{O}_{\text{ads}}$ ). Water molecules and hydroxyl ions are both oxidised to very reactive hydroxyl radicals ( $\text{OH}^\bullet$ ) with the help of  $\text{TiO}_2 (h^{+vb})$  as follows:



Dissolved oxygen molecules are reduced to reactive superoxide radicals ( $\text{O}_2^{\cdot-}$ ) by conduction band electrons ( $\text{TiO}_2 (e^{-cb})$ ).





The hydroxyl radicals and the superoxide radicals are both involved in the photo-oxidation of the organic molecules. Conduction band electrons  $\{\text{TiO}_2(\text{e}^{-\text{cb}})\}$  alone can also reduce organic contaminants like dyes and many other species in the wastewater (Minero et al., 1995).

The recombination of holes  $\{\text{TiO}_2(\text{h}^{+\text{vb}})\}$  and conduction band electrons  $\{\text{TiO}_2(\text{e}^{-\text{cb}})\}$  has the effect of reducing their availability for participation in the redox reactions.



The rate at which the holes ( $\text{TiO}_2(\text{h}^{+\text{vb}})$ ) and electrons ( $\text{TiO}_2(\text{e}^{-\text{cb}})$ ) are channelled into the redox reactions prior to recombination determines the extent to which the photocatalytic reaction can efficiently proceed. Titanium dioxide would be easily the best material for catalytic photodegradation, were it not for this recombination which reduces productivity. There is therefore need to improve the residence and reactivity time of holes and electrons before recombination can occur. Achieving this implies that  $\text{TiO}_2$  can easily be used for industrial-scale applications (Wold, 1993). In order to improve the effectiveness of titanium dioxide as a photocatalytic material, doping has been used as a method of enhancing reactivity (Choi et al., 1994; Litter, 1999 and Tayade et al., 2006).

Doping is a process of incorporating a guest atom (metal or non-metal) into a host material ( $\text{TiO}_2$ ). Vacant sites and defects present in the structure of  $\text{TiO}_2$  are utilised during the doping process. Such a modification improves the properties of  $\text{TiO}_2$ . Doping of metal into  $\text{TiO}_2$  is seen as accelerating the removal of conducting electrons ( $\text{TiO}_2(\text{e}^{-\text{cb}})$ ) from  $\text{TiO}_2$  particles and their subsequent transfer to molecular oxygen. The rate limiting step in photocatalytic oxidation of organics is the reduction of oxygen to superoxide radicals as suggested by Gerischer and Heller (1991).

In its undoped state,  $\text{TiO}_2$  electrons  $\{\text{TiO}_2(\text{e}^{-\text{cb}})\}$  and holes  $\{\text{TiO}_2(\text{h}^{+\text{vb}})\}$  quickly recombine, thus reducing the reactivity of the photocatalyst. The efficiency of the photocatalytic reactions is increased by improving the separation of charge carriers and the rate of oxygen reduction. Major factors influencing the characteristics and properties of photocatalysts include the method of doping used, the  $\text{TiO}_2$  used, concentration of dopant, band gap, surface area, particle size and thermal property, among other factors.

In the absence of suitable electron and hole scavengers, the stored energy is dissipated within a few nanoseconds by recombination. If a suitable scavenger or surface defect state is available to trap the electron or hole, recombination is prevented and subsequent redox reactions may occur. The valence band holes are powerful oxidants (+1.0 to +3.5 V) depending on the semiconductor and pH, while the conduction band electrons are good reductants (+0.5 to -1.5 V). Most organic photodegradation reactions utilise the oxidising power of the holes either directly or indirectly by the formation of activated oxygen species from water. To prevent a build up of charge, one must also provide a reducible species to react with the electrons. In contrast, on bulk semiconductor electrodes, only one species, either the hole or electron, is available for reaction due to band bending. However, in very small semiconductor particle suspensions, both species are present on the surface.

Photocatalytic activity can be increased by the following five approaches:

- (i) The use of photosensitizers for band-gap tuning
- (ii) Minimisation of charge carrier recombination
- (iii) Promotion of the forward reaction and adsorbance of reactants through provision of adequate quality and quantity of active sites (Inagaki et al., 2014; Leary and Westwood, 2011)
- (iv) Reduction in the nanoparticle size below 10 nm

- (v) Extension of the excitation wavelength into the UV range.

The ( $e^-$ - $h^+$ ) recombination process usually occurs at the boundaries and defects of the photocatalyst surface.

When the crystallite dimension of a semiconductor particle falls below a critical radius of approximately 10 nm, the charge carriers appear to behave quantum mechanically (Hoffmann et al., 1995). As a result of this confinement, the band gap increases and the band edges shift, as shown in Figure 2.2, to yield larger redox potentials. When the photocatalyst particle size is reduced, the distance the photogenerated  $e^-$ - $h^+$  would require in reaching the surface reaction sites decreases, lowering the recombination likelihood that favours the photocatalytic process (Inagaki et al., 2014; Daghrir et al., 2013; Leary and Westwood, 2011). Hence there has been increased attention to using nanomaterials as photocatalysts, though there is no consensus on the minimum particle size due to deviations in photocatalytic efficiency as too small particulates present onset quantum size effects (Inagaki et al., 2014; Daghrir et al., 2013; Leary and Westwood, 2011).

The use of size-quantised semiconductors to increase photo efficiencies is supported by several studies (Hoffmann et al., 1995). However, size-quantised semiconductors have been found to be less photoactive than their bulk-phase counterparts. In the latter cases surface speciation and surface defect density appear to control the photocatalytic activity.

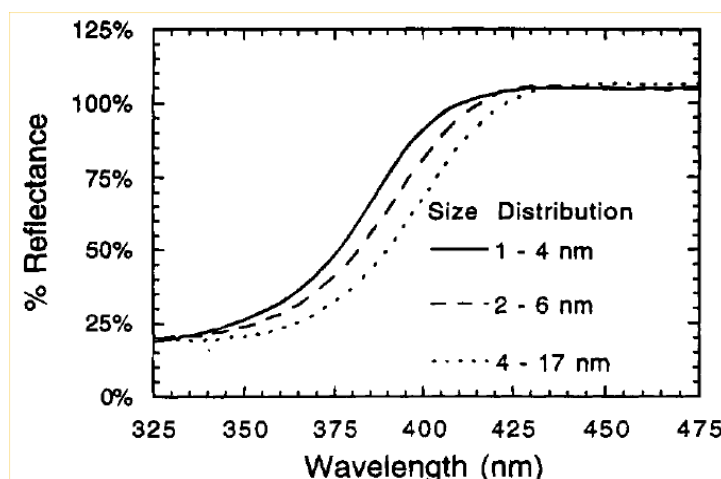


**Figure 2.2 UV/VIS reflectance spectra of size-quantised  $\text{TiO}_2$  (Hoffmann et al., 1995)**

On the other hand, the quantity of active sites determines the rate of chemical reactions on the catalyst surface provided they possess low susceptibility for facilitating the reverse reaction. The number of active sites being directly proportional to the catalyst surface area, photocatalysis is enhanced using porous nanosized materials (Leary and Westwood, 2011). Concurrently, co-catalysts can be used to increase suitable active sites in the photocatalyst surface (Leary and Westwood, 2011). In addition, narrow band gap photosensitizers can be employed to transfer electrons to the photocatalyst conduction band. The surface modification of photocatalysts with suitable chelating agents can also be used to increase the propensity for trapping or adsorbing reactants, and therefore facilitating their transfer to the active sites (Daghrir et al., 2013; Leary and Westwood, 2011; Qu et al., 2010).

Overall, an ideal photocatalytic material should be non-toxic, biologically and chemically inert, stable, readily available and easily processable with a high efficiency of solar energy conversion. The applications of photocatalysis include water splitting, water and wastewater treatment, carbon dioxide remediation, self-cleaning activity and air purification (Dolat et al., 2012; Roy et al., 2010).

### 2.6.3 Nano titania particles for photocatalysis

TiO<sub>2</sub> is a well-known photocatalytic material, naturally occurring in three crystallographic phases, namely anatase, brookite, and rutile. TiO<sub>2</sub> has been used commercially as a photocatalyst under UV light for water purification (destruction of organic contaminants) and sterilisation for more than 30 years. Among the three crystalline polymorphs, anatase possesses the highest photocatalytic activity, though the large band gap (3.2 eV) limits its application to the ultraviolet range (< 380 nm), which covers around 5% of the solar spectrum (Leary and Westwood, 2011). Anatase titania and rutile titania have a band gap of 3.2 eV and 3.0 eV respectively. These are the most common crystalline titania structures that occur naturally but have also been synthesised (Junghanel, 2010). Brookite titania is not synthesised due to the difficulty in obtaining brookite in a pure phase (Di Poula, 2013). Thus, a number of studies place increased attention in tailoring the electronic and optical properties of these nanosized materials in order to extend their optical absorption edge into the visible light range and improve their photocatalytic properties (Daghrir et al., 2013; Leary and Westwood, 2011; Qu et al., 2010).

Currently, TiO<sub>2</sub> constitutes the cheapest photocatalytic material with the highest photocatalytic activity and stability, and lowest toxicity (Fujishima et al., 2008; Hashimoto et al., 2005) and is widely applied in water and wastewater treatment, air purification, as an antibacterial, and in deodourisation, self-cleaning, coating and anti-stain applications (Dolat et al., 2012; Roy et al., 2010).

Evonik P25 TiO<sub>2</sub> has set the standard for photoreactivity in environmental applications, although TiO<sub>2</sub> produced by Sachtleben (Germany) and Kimera (Finland) show comparable reactivity. Degussa P25 is a non-porous 75:25% anatase to rutile mixture with a BET surface area of  $55 \pm 15 \text{ m}^2\text{g}^{-1}$  and crystallite sizes of 30 nm to 0.1  $\mu\text{m}$  diameter aggregates.

Many researchers claim that rutile is a catalytically inactive or much less active form of TiO<sub>2</sub>, while others find that rutile has selective activity towards certain substrates. Highly annealed rutile ( $T \geq 800^\circ\text{C}$ ) appears to be photoinactive. However, Reral and Domenech (1992) have shown that TiO<sub>2</sub> in rutile form is a substantially better photocatalyst for the oxidation of CN<sup>-</sup> than is the anatase form; on the other hand, he also showed that Evonik P25 was a better catalyst than rutile for the photoreduction of HCrO<sub>4</sub><sup>-</sup>.

### 2.6.4 Enhancement of photocatalytic efficiency of nano-TiO<sub>2</sub>

Over the years, progress has been made by modifying the properties of titanium dioxide photocatalyst by way of doping with metals or non-metals in order to improve its photocatalytic degradation properties. The use of dopants has had significant influence in altering the band gap, surface area, particle size and thermal properties of titania to an extent that even visible light is able to activate doped titania during photodegradation of organic compounds such as dyes. According to Di Paola et al. (2012) doping of TiO<sub>2</sub> is used to enhance visible light and improves the lifetime of photo-induced electron-hole pairs. The produced photocatalyst promotes the separation and prevents the recombination of photogenerated electron-hole pairs, thus improving photocatalytic efficiency (Saravanan et al., 2009). A variety of methods have been attempted to enhance TiO<sub>2</sub> photocatalytic activity including metal particle loading (i.e. Pt, Au, Ag, Cu, Fe), metallic (i.e. Fe, Cr, Mo, Ca, Sr, Ba, La, Ce, and Er) and non-metallic (i.e. N, C, S, B, P and F) doping, co-catalysts, dye sensitisation, and surface functionalisation with organic materials (Inagaki et al., 2014; Daghrir et al., 2013; Dolat et al., 2012). Several doping approaches for the development of visible light active TiO<sub>2</sub> photocatalysts are currently in use but nitrogen doping is by far the most commonly employed, as compared to carbon, fluorine, sulphur, boron, metals and rare-earth transition metals (Presti et al., 2014). Co-catalysts such as Pt, NiO and RuO<sub>2</sub> are also used to introduce suitable active sites to TiO<sub>2</sub> (Leary and Westwood, 2011).

Gupta and Tripathi (2011) reported that it is much more effective to replace Ti<sup>4+</sup> in TiO<sub>2</sub> structure with a cation than to substitute O<sup>2-</sup> with another anion because of their difference in the charge states and their ionic radii. For example, Zhang et al. (2014) reported that doping TiO<sub>2</sub> with Fe<sup>3+</sup> inhibits e<sup>-</sup>/h<sup>+</sup> pair recombination which resulted in high photocatalytic performance.

TiO<sub>2</sub>, individually or simultaneously doped with carbon and nitrogen, has been widely investigated due to the low costs and band-gap narrowing, with significant improvement in the visible light absorption edge (Liu and Syu, 2013; Cheng et al., 2012; Dolat et al., 2012).

In nitrogen doping TiO<sub>2</sub> (N-TiO<sub>2</sub>), nitrogen atoms can exist at substitutional and interstitial sites in the TiO<sub>2</sub> lattice, causing band gap narrowing due to hybridisation of O 2p and N 2p orbitals (Cheng et al., 2012; Sun et al., 2012; Katoh et al., 2010). In addition, the photo-excitation of N 2p to Ti 3d (Ti 3d ← N 2p transition) also provides visible light-induced photocatalysis. However, although the isolated N 2p state is essential to induce efficient photocatalytic activity, higher N concentration can suppress photoactivity due to increased oxygen vacancies that act as recombination sites (Katoh et al., 2010). The nitrogen substitutional forms include N, N-O, N-Ti-O and Ti-O-N (Liu and Syu, 2013; Cheng et al., 2012; Katoh et al., 2010; Dong et al., 2009). Lee and co-workers (2010) suggested effective enhancement of the photocatalytic activity to substitutional nitrogen under visible light radiation compared to nitrogen in the interstitial sites. Sathish and collaborators (2005) observed light absorption shifts from 380 nm for pure TiO<sub>2</sub> to the visible region at 550 nm for N-TiO<sub>2</sub>. Choi et al. (2007) fabricated mesoporous nitrogen-doped TiO<sub>2</sub> photocatalysts and observed red shift in light absorbance up to 468 nm, 0.9 eV lower binding energy of electrons in the Ti 2p state, and reduced interplanar distance of crystal lattices. However, though several findings support higher photocatalytic activity of N-TiO<sub>2</sub> compared to Degussa P25 under visible light, Sun and co-workers (2008) observed opposite behaviour during degradation experiments of azo dyes (i.e. Orange G) under sunlight radiation.

In carbon-doped TiO<sub>2</sub>, (C-TiO<sub>2</sub>), carbon atoms can replace oxygen or titanium in the crystal lattice or deposit at the grain boundary (Inagaki et al., 2014; Wang et al., 2011; Yang et al., 2009; Yang et al., 2008; Treschev et al., 2008; and Kuo et al., 2007). The former enables TiO<sub>2</sub> particles' visible light sensitivity and the latter acts as a photosensitizer transferring electrons to the TiO<sub>2</sub> conduction band (Inagaki et al., 2014; Yang et al., 2009). This mechanism is supported by the existence of Ti-C, O-Ti-C, O-C-O, and C-C bonds, and oxygen vacancy mid-gap states or, as is more widely suggested, the existence of mid-gap states caused by mixing of the C 2p and O 2p states (Yang et al., 2009; Matsunaga and Inagaki, 2006; Hashimoto et al., 2005). However, other researchers argue that co-doping would be necessary to achieve mixing of C 2p or N 2p with O 2p states (Yang et al., 2009; Matsunaga and Inagaki, 2006; Hashimoto et al., 2005; and Sathish et al., 2005). Theoretical studies suggest that formation of oxygen vacancies and substitution of oxygen by carbon occurs under oxygen-poor conditions and that interstitial and/or carbon replacing Ti occurs under oxygen-rich conditions (Leary and Westwood, 2011).

In co-doping of TiO<sub>2</sub> with nitrogen and carbon (C-N-TiO<sub>2</sub>), nitrogen atoms can be incorporated in the TiO<sub>2</sub> lattice, substituting oxygen atoms, while the carbon atoms are deposited at the grain boundary of the crystal (Wang et al., 2011; Yang et al., 2008; Chen et al., 2007; Li et al., 2007). This is the reason why Wang and collaborators (2011) attributed photosensitising effects to carbonaceous materials and red shift absorption edge to nitrogen doping in the C-N-TiO<sub>2</sub> nanomaterials. Chen et al. (2007) also suggested higher photocatalytic activity for the degradation of methylene blue for C-N-TiO<sub>2</sub> compared to C-TiO<sub>2</sub>, N-TiO<sub>2</sub> and undoped TiO<sub>2</sub> and attributed the improvement to a synergistic effect resulting from band-gap narrowing caused by nitrogen substituting for oxygen, and surface carbon species acting as a photosensitizer. Li et al. (2007) also supported the narrowing effect of the band gap and a photosensitising effect of C in C-N-TiO<sub>2</sub> applied to the disinfection of *Escherichia coli*. Dai et al., (2013), incorporating carbon and nitrogen atoms into the lattice of TiO<sub>2</sub> *in situ*, obtained C-N-TiO<sub>2</sub> nanosheets exhibiting strong absorption in the UV-Vis range. Li et al. (2007), carrying out disinfection experiments on *Escherichia coli*, found C-N-TiO<sub>2</sub> to possess higher photocatalytic activity, compared to N-TiO<sub>2</sub> photocatalyst, under visible light illumination. On the other hand, Tachikawa et al. (2004) observed a complete loss in photocatalytic activity for C-S-TiO<sub>2</sub> as compared to the pure or individually doped forms (whose activity increased in the order TiO<sub>2</sub> < S-TiO<sub>2</sub> < C-TiO<sub>2</sub>), when investigating the degradation of methanol. However, Cheng et al. (2012) observed opposite behaviour when incorporating nitrogen in C-N-S-

tridoped TiO<sub>2</sub>. They suggested higher sunlight photocatalytic activity in phenol degradation than Degussa P25 (Cheng et al., 2012).

#### Metal modification of the TiO<sub>2</sub> photocatalyst (cation-doped TiO<sub>2</sub>)

According to Han et al. (2009), noble metals have received much attention in terms of doping into TiO<sub>2</sub> nanoparticles to increase photocatalytic efficiency. Noble metal doping has been reported to facilitate e<sup>-</sup>/h<sup>+</sup> pairs separation, to decrease TiO<sub>2</sub> band gap and to increase surface properties of TiO<sub>2</sub> photocatalysts. However, higher dosage levels during combination has been reported to have a negative effect of lower photoactivity due to created e<sup>-</sup>/h<sup>+</sup> pair recombination centres. However, it has been reported that 2% Ag/TiO<sub>2</sub> promotes optimum photo-efficiency in the degradation of rhodamine B.

Han et al. (2009) has reported that the modification of TiO<sub>2</sub> with transitional metal provides a successful and cost-effective visible light photocatalysts, while the use of noble metals is limited and even restricted because they are very expensive. Transition metal ions are used to add extra energy levels within the TiO<sub>2</sub> semiconductor's band gap so that exciting electrons from these additional levels to conduction band will require less absorption of photo-energy than the energy that would be required for unmodified TiO<sub>2</sub> (Gupta and Triphati, 2011).

Studies have examined the photochemical properties of cation doping of powdered TiO<sub>2</sub>, and many groups have examined how cation doping shifts the TiO<sub>2</sub> absorption properties into the visible light region (Gupta and Triphati, 2011). A variety of metals on TiO<sub>2</sub> have been explored, including: Fe, Cr, V, Mo, Ni, Nb, Mn, Cu and Co (Henderson, 2011). Doping TiO<sub>2</sub> with metal ions such as Fe(III), Mo(V), Ru(III), So(III), Re(V) and V(V) have resulted in an improved trapping-to-recombination rate ratio, improving photocatalytic efficiency in the photo-oxidation and reduction of CHCl<sub>3</sub> and CCl<sub>4</sub> respectively (Gupta and Triphati, 2011).

It was reported in a recent review of Han et al. (2009) that interest in modification of TiO<sub>2</sub> with lanthanides (Eu, Ce, Er, Pr and La) was due to their scarcity and following physical and electronic properties. Lanthanides have an effective adsorb ability of organic compounds on the surface of TiO<sub>2</sub> due to their f-orbital interaction with other structures. When lanthanides are confined to the TiO<sub>2</sub> surface, they can trap conduction band electrons. Lanthanides have a special electronic structure of 4f<sup>x</sup>5d<sup>y</sup> which favours different optical properties and combination with other structures, enhancing photocatalytic efficiency.

#### Co-catalyst modification of the TiO<sub>2</sub> photocatalyst by coupled/composite TiO<sub>2</sub>

In this system, TiO<sub>2</sub> is coupled with a narrower band gap semiconductor to form a composite structure. A heterojunction structure is formed within the composite as an interface between different semiconductors in such a way that visible light irradiation of a narrower band gap semiconductor produces a response in the TiO<sub>2</sub> semiconductor resulting in charge carriers with a long lifetime and effective separation (Gupta and Triphati, 2011).

It was reported and approved by Zhang et al. (2014) that formation of a heterostructure by coupling is the proper approach to form a visible light photocatalyst. The use of coupling with binary compound such as Fe<sub>2</sub>O<sub>3</sub>, ZnO, WO<sub>3</sub>, V<sub>2</sub>O<sub>5</sub>, Bi<sub>2</sub>O<sub>3</sub>, NiO, Nb<sub>2</sub>O<sub>5</sub>, Ta<sub>2</sub>O<sub>5</sub>, ZrO<sub>2</sub>, CeO<sub>2</sub>, Ga<sub>2</sub>O<sub>3</sub> and Cu<sub>2</sub>O was reported by Di Paola et al. (2012) to improve the visible light photo-efficiency of TiO<sub>2</sub>.

It can be deduced, since Rawal et al. (2011) until recently, that the combination of visible light harvesting semiconductors and TiO<sub>2</sub> is the most facile way used to enhance the photocatalytic performance of TiO<sub>2</sub> by inhibiting the electron hole recombination, but dosing is always a crucial factor to restrict creation of e<sup>-</sup>/h<sup>+</sup> recombination centres, as in the concept shown in Figure 2.3.

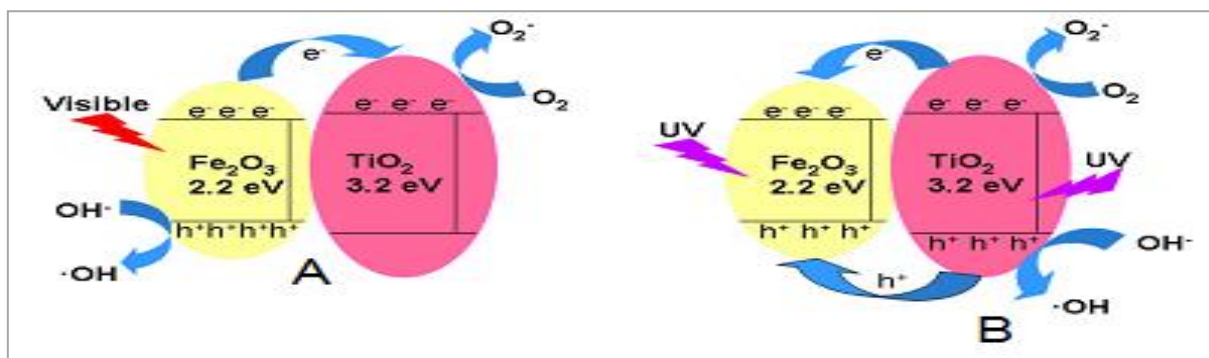


**Figure 2.3 Electron and holes transfer between  $\text{Fe}_2\text{O}_3$  and  $\text{TiO}_2$  under visible light (A) and UV light (B) irradiation (Zhang et al., 2014)**

For example, in the case shown in Figure 2.3, of  $\text{TiO}_2$  doped with  $\text{Fe}_2\text{O}_3$  upon UV light irradiation, electrons are excited from both the VB of  $\text{TiO}_2$  and  $\text{Fe}_2\text{O}_3$  to the CB of  $\text{Fe}_2\text{O}_3$  then the holes of  $\text{TiO}_2$  will be transferred to  $\text{Fe}_2\text{O}_3$  making  $\text{Fe}_2\text{O}_3$  the recombination centre of photogenerated  $e^-/h^+$  pairs (Zhang et al., 2014). While under visible light illumination, at the heterojunction interface, their Fermi levels are in equilibrium so that electrons are excited from VB of  $\text{Fe}_2\text{O}_3$  to its CB then transferred to the CB of  $\text{TiO}_2$  by electric field and the concentration gradient (Zhang et al., 2014). In this system, photogenerated holes accumulate to the VB of  $\text{Fe}_2\text{O}_3$  as shown by Figure 2.3.

Gupta and Tripathi (2011) reported that coupled semiconductor photocatalysts enhance high photocatalytic performance by increasing charge carrier separation and extending the energy range of photo-excitation. Zhang et al. (2014) reported that photosensitisation of  $\text{TiO}_2$  using a lower band gap energy semiconductor is an effective approach which creates heterogeneous structure suitable for visible light absorption and which promote the separation of and prevents  $e^-/h^+$  pair recombination.

### 2.6.5 The effect of the catalyst support on the $\text{TiO}_2$ photocatalyst

The use of  $\text{TiO}_2$  nano-photocatalyst as a powder has been experimentally proved and used for the degradation of most organic compounds and removal of heavy metal ions on a small scale (Vohra and Davis, 1997; Colon et al., 2001). However, there is a problem of filtration to remove and recycle the catalyst after use. To avoid this difficult and costly problem of filtration, many methods and different supports have been proposed and used to immobilise  $\text{TiO}_2$ . Possible supports for  $\text{TiO}_2$  photocatalyst include glass, quartz, stainless steel (Fernandez et al., 1995; Brezová et al., 1995), zeolites (Torimoto et al., 1996), silicon carbide (Nishida et al., 2007), organic fibres and pumice stone (Rao et al., 2004). Silicon carbide is a useful photocatalyst support for use in the liquid phase and has the advantage of high thermal stability, high mechanical strength and high electrical conductivity, and can be easily moulded into a filter (Nishida et al., 2007).

Fernandez et al. (1995) investigated the effects of different supports on the photocatalytic activity of  $\text{TiO}_2$  in the degradation of maleic acid and they found that the photocatalytic activity followed the order:  $\text{TiO}_2/\text{quartz} > \text{TiO}_2/\text{steel} \approx \text{TiO}_2/\text{glass}$ . Silica gel is another promising support since it has been widely used in the industry and it possesses good light transmission and adsorption of pollutants (Wang et al., 2006). Cheaper support materials are preferentially used, for cost effectiveness, in some cases.

The use of supporting materials for N-doped  $\text{TiO}_2$  such as strontium ferrite ( $\text{SrFe}_{12}\text{O}_{19}$ ) has been shown to improve the stability and strength of ferromagnetic properties, resulting in reduced band gap (2.8 eV) and better visible light absorption compared to unsupported N-doped  $\text{TiO}_2$  (Aziz et al., 2012).

### 2.6.6 Conclusions on doped nano- $\text{TiO}_2$

The discussion provided above can be very briefly summarised by the information supplied in Table 2.3.

**Table 2.3 TiO<sub>2</sub> photocatalyst optimisation process and the optimisation mechanisms**

Optimisation objectives	Optimisation approaches	Optimisation mechanisms	Wastewater applications
Enhance photocatalytic reaction kinetics	Size	More surface reactive sites, higher reactant adsorption, lower e <sup>-</sup> /h <sup>+</sup> recombination	High performance UV-activated photocatalytic reaction
	Nano-tube morphology	Shorter carrier diffusion in the tube walls, higher reactant mass transfer rate towards tube surface.	
	Noble metal doping	Better e <sup>-</sup> /h <sup>+</sup> separation, lower e <sup>-</sup> /h <sup>+</sup> recombination	
	Reactive crystallographic facets	Higher reactant sorption, better e <sup>-</sup> /h <sup>+</sup> recombination	
Expend photo-activity range	Metal impurity doping Anion doping Dye sensitizer doping Narrow band gap Semiconductor doping	Separation, lower e <sup>-</sup> /h <sup>+</sup> recombination Impurity energy levels, Band gap narrowing Electron injection Electron injection	Low energy cost for solar, visible light photocatalytic reactors

## 2.7 REMOVAL OF TEXTILE DYES WITH PHOTOCATALYSTS

It is the photocatalytic reactivity, chemical stability, inertness, low cost, thermal property and availability that make nano-TiO<sub>2</sub> the most desired photocatalyst for organic wastewater treatment for a green environment (Chen et al., 2000). The general mechanism of photocatalysis and the specific mechanisms of nano-TiO<sub>2</sub> and doped nano-TiO<sub>2</sub> with textile dyestuffs, are discussed in this section. Examples from literature of experiments with TiO<sub>2</sub> and TiO<sub>2</sub>-ZnO to remove dyes and micro-organisms by other research groups are presented and discussed. Finally, the effect of various reaction variables on the results of the photocatalytic dye-decolourisation experiments is presented and discussed.

### 2.7.1 Examples of the photodegradation of organics, including dyes

There have been literally hundreds of publications in refereed journals regarding the application of TiO<sub>2</sub> and doped TiO<sub>2</sub> as photocatalysts for dye removal. Table 2.4 to Table 2.6 provide the core details of certain of these publications which specifically used TiO<sub>2</sub> and TiO<sub>2</sub>/ZnO co-catalysts. The tables include comments on the description of the catalyst and the dye contaminant, given in Table 2.4, on the photocatalytic reaction conditions, given in Table 2.5, and on the dye removal efficiencies, given in Table 2.6.

**Table 2.4 Examples of scientific articles using doped TiO<sub>2</sub> and ZnO photocatalysts: Type of catalyst and organic dye contaminant**

Reference	Type of catalyst (ZnO / TiO <sub>2</sub> )	Particle size (nm)	Contaminant	Production method	Ratio
Aal et al., 2008	Wurtzite ZnO and anatase TiO <sub>2</sub>	350	2-chlorophenol	Hydrothermal	1:1
Arsana et al., 2012	Wurtzite	Not given	C.I acid red 142	Photodeposition	0.5 to 1.5% Ag
Bai et al., 2012	Hierarchical 3D dendritic TiO <sub>2</sub> P25	2 to 3	Acid orange	Hydrothermal	Not given
Barakat et al., 2004	TiO <sub>2</sub>		Cyanide and Cu(II) Ions	Commercial	



Reference	Type of catalyst (ZnO / TiO <sub>2</sub> )	Particle size (nm)	Contaminant	Production method	Ratio
Bauer, et al., 1999	TiO <sub>2</sub>	Commercial	4-Chlorophenol	Commercial	Not specified
Chen, et al., 2011	Rutile TiO <sub>2</sub>	61 to 32	Methylene blue	Hydrothermal	Not given
Ede et al., 2012	TiO <sub>2</sub> (Degussa P25), 25% rutile and 75% anatase	Not given	Bacterial pollutants	Not given	25% rutile and 75% anatase
Ge et al., 2009	Wurtzite (ZnO) and anatase(TiO <sub>2</sub> )	1000	Methyl orange	Solvothermal, ultrasonic precipitation and heat treatment	01:01
Habib et al., 2013	Wurtzite(ZnO) and anatase, rutile(TiO <sub>2</sub> )	500	Brilliant golden yellow	Heating (600 to 900°C)	1:1 or 1:3
Hashimoto, et al., 2005	TiO <sub>2</sub> (rutile)	415	E. coli	Not specified	Not given
Jiang et al., 2007	Wurtzite(ZnO) anatase (TiO <sub>2</sub> ) and rutile	270	Textile industrial waste water	None, the catalysts were bought	None
Jiemsiriliers et al., 2011	Anatase and zincite	44.1	C.I Basic Blue	Ultrasonic precipitation followed by heat treatment	1:1
Lee and Park, 2013	ZnO		Textile effluent	Hydrothermal	
Li et al., 2013	P 25	27	Not given	Not given	Not given
Hussien et al., 2010	Wurtzite	45	Methyl orange	Parallel flow co-precipitation	1% Sn
Ochiai et al., 2009	P25 TiO <sub>2</sub>	Not given	Phenol	Commercial	Not given
Peralta-zamora, et al., 1998	TiO <sub>2</sub> and ZnO	Not given	Black liquor,	Commercial	Not given
Ryu and Choi, 2007	TiO <sub>2</sub> –graphene	4	Methylene blue	Solvothermal	Not given
Subash et al., 2012	Wurtzite ZnO	5.3	Reactive red 120	Precipitation– thermal decomposition	4% Zr and 2-10wt% Ag
Xuejing et al., 2009	Pure ZnO and carbon nanotubes	50 to 60	Methyl red	Sol-gel	60% CNT
Yun et al., 2010	Anatase TiO <sub>2</sub>	600 ± 150	Acidic waste water (MB)	Sol-gel electrospinning	Not given
Zhaung and Zeng et al., 2010	Wurtzite ZnO	30 to 70	Methylene blue	Sol-gel	Not given
Zhaung et al., 2012	Sheets of anatase TiO <sub>2</sub> -AgS	Not given	Wastewater	Heating	5% TiO <sub>2</sub> -AgS

**Table 2.5 Examples of scientific articles using doped TiO<sub>2</sub> and ZnO photocatalysts; B: Photocatalytic treatment condition.**

Reference	Light source	Distance	Power of the light/ temperature	Batch/continuous reactor	Efficiency
Aal et al., 2008	Mercury lamp	1 m	100 W	Batch photocatalytic reactor	97.3%
Arsana et al., 2012	Sunlight	150 x 10 <sup>9</sup> m	1000 W/m <sup>2</sup>	Batch reactor	65%
Bai et al., 2012	UV lamp	254 nm, 40 mW cm <sup>-2</sup>	Not given	Continuous	Not specified
Barakat et al., 2004	UV lamp	Not specified	100 W	Batch	74.4%
Bauer, et al., 1999	UV lamp	Not specified	400 W	Batch	51%
Chen, et al., 2011	UV lamp	Not given	300 W	Batch 50 mL borosilicate glass	
Ede et al., 2012	UV lamp	Not given	9 W	Batch	30%
Ge, et al., 2009	UV mercury lamp	Not given	300 W	Batch 200 mL photoreactor	98.3%
Habib et al., 2013	Sunlight	150 x 10 <sup>9</sup> m	Sunny day	50 mL borosilicate batch reactor	98%
Hashimoto, et al., 2005	UV lamp	Not given	700 mW/cm <sup>2</sup>	Batch	Not specified
Jiang et al., 2007	UV mercury lamp	Not given	1. 319.15 K ZnO 2. 298.15 K TiO <sub>2</sub>	Batch reactor	1. 95% ZnO 2. 56% TiO <sub>2</sub>
Jiemsiriliers et al., 2011	Sunlight	150 x 10 <sup>9</sup> m	Sunny day	Batch reactor 100 mL borosilicate	Nearly 100%
Lee and Park, 2013	Not given	Not given	Not given	Not given	93%
Li et al., 2013	UV light or solar	Not given	Not given	Not given	Not given
Hussien et al., 2010	Mercury lamp	10 cm	300 W	Batch photochemical reactor	68%
Ochiai et al., 2009	Sunlight	Not given	Not given	Batch	Not specified
Peralta-zamora et al., 1998	UV lamp	Not given	50 W	Batch	60%
Ryu and Choi, 2007	UV lamp	Not given	400 W	Batch	98%
Subash et al., 2012	Sunlight	150 x 10 <sup>9</sup> m	Sunny day	Batch 50 mL borosilicate glass	94.40%
Xuejing et al., 2009	Sunlight	150 x 10 <sup>9</sup> m	Not given	Batch photocatalytic reactor	60%
Yun et al., 2010	UV lamp		800 W	Batch	90%
Zhaung and Zeng et al., 2010	Halogen tungsten lamp	10 cm	500 W	Batch quartz photoreactor	80%
Zhaung et al., 2012	Sunlight	150 x 10 <sup>9</sup> m	15 to 22°C	Batch	Not given

**Table 2.6 Examples of scientific articles using doped TiO<sub>2</sub> and ZnO photocatalysts: Photocatalytic performance.**

Reference	Catalyst loading	Dye loading	Dye concentration	pH	Time taken
Aal et al., 2008	30 g/L	12.5 to 50 mg/L	12.5 to 50 mg/L	9	180 min
Arsana et al., 2012	1 g	1 ppm	1 ppm	Acid medium	60 min
Bai et al., 2012	0.5 g/L	50 mg/L	Not given	Not given	2 h
Barakat et al., 2004	1 g/L	Not given	10 <sup>-3</sup> M	11	4 h
Bauer, et al., 1999	2 g/L	10 <sup>-3</sup> mol/L	Not given	Not specified	24 h
Chen, et al., 2011	TiO <sub>2</sub> electrode	Not given	5 × 10 <sup>-5</sup> mol/ L	3.87	7 h
Ede et al., 2012	0.15 g.dm <sup>-3</sup>	Not given	4.5 mol/lL	Not given	360 min
Ge, et al., 2009	60 mg	5x10 <sup>-5</sup> mol/L	5x10 <sup>-5</sup> mol/L	11	60 min
Habib et al., 2013	6 g/L	20 mg/L	20 mg/L	7	2hr
Hashimoto, et al., 2005	Not given	Not given	Not given	Not given	20 min
Jiang et al., 2007	1. 350 mg ZnO 2. 175 mg TiO <sub>2</sub>	1000 cm <sup>3</sup>	1000 cm <sup>3</sup>	Not given	60 min
Jiemsirilers, et al., 2011	6 to 10 g/L	20 mg/L	20 mg/L	6.21	1hr
Lee and Park, 2013	Not given	Not given	Not given	Not given	10 h
Li et al., 2013	Not given	Not given	Not given	Not given	Not given
Hussien et al., 2010	50 mg	50 mL	10 mg/L	6	60 min
Ochiai et al., 2009	Not given	Not given	250 to 1000 mmol dm <sup>-3</sup>	Not given	30 to 20 min
Peralta-zamora et al., 1998	25 mg TiO <sub>2</sub> and 150 mg ZnO	57.1 mg/L	Not given	7.6	1 h
Ryu and Choi, 2007	Not given	200 mL 2.0 x 10 <sup>-5</sup> M	Not given	Not given	12 min
Subash, et al., 2012	3 g/L	50mL	2x10 <sup>-5</sup> M	7	20 min
Xuejing et al., 2009	0.3 g/L	20 mg/L	20 mg/L	9	30 min
Yun et al., 2010	1.0 g	50 mg/L	Not given	03>10	
Zhaung and Zeng et al., 2010	0.04 g/L	10 mg/L	10 mg/L	5	3.5 h
Zhaung et al., 2012	30 mg	50 mL	Not given	Acidic	7 h

It is noted that none of the studies use the same conditions in terms of dye type and concentration, light type, (i.e. UVA, UVB UVC or daylight/simulated daylight) and intensity, reactor type and reaction conditions. As such, benchmarking of the results is difficult (if not impossible) but attempted in the discussion of the results of this study.

## 2.7.2 Effect of reaction parameters and conditions on the photocatalysis of textile effluents

### Introduction to evaluation of reaction conditions on photocatalysts of textile effluents

During photodecomposition of pollutants from wastewater, it is very important to understand the impact of various parameters on photocatalytic performance of the system since these parameters are the optimisation of the photoreactor design and operation to produce the highest photo-efficiency.

According to Ahmed et al. (2011), the parameters which have the greatest effect on photocatalytic performance are: catalyst load, initial dye concentration, light intensity, solution pH, initial substrate concentration, ionic components in the solution, solvent types, calcination temperature, oxidising agents/electron acceptors and catalyst application mode.

### Effect of light intensity and wavelength on the efficiency of photocatalysts of textile dyes

As discussed previously, photoreaction of  $\text{TiO}_2$  is activated by UV light irradiation but when one adjusts the optical properties of  $\text{TiO}_2$ , the photo response can be a shift to activity in the visible light wavelength range. According to Ahmed et al. (2011), light intensity determines the extent of light absorption by the photocatalyst at a given wavelength and determines the overall degree of pollutant mineralisation and degradation efficiency.

According to Behnajady et al. (2007), the overall light intensity and wavelength, increases proportionally with photodegradation rate. In the decolonization of azo dye AR27 using P-25 the removal percentage is steadily increased with an increase in the light intensity. With low light intensity, (i.e.  $18.8 \text{ Wm}^{-2}$ ), the photoreaction rate increases linearly with light intensity according to first order kinetics, at medium light intensity the kinetic rate is half the order, based on the square root of the light intensity, then for higher light intensities the reaction rate was shown to be independent of the light intensity.

An increase in light intensity increases the photocatalytic reaction, although the nature, or form, of the light has no effect on the pathway of the reaction (Stylidi et al., 2004). Of total natural light, only 5% has enough energy to cause effective photosensitisation (Wilke and Breuer, 1999).

Metal oxides such as  $\text{TiO}_2$  in a heterogeneous system cannot absorb all incident light due to refraction and this makes it quite difficult to determine the quantum yield experimentally.

The rate of reaction varies with the wavelength and it follows the absorption spectrum of the photocatalyst and generally decreases with an increase in wavelength (Herrmann, 1999). The threshold should correspond to the band gap; for instance  $\text{TiO}_2$ , which has a band gap of 3.02 eV, requires light of  $\lambda \leq 400 \text{ nm}$ .

### Effect of pH on the efficiency of photocatalysts of textile effluents

Solution pH affects the ionisation state of the surface of the catalyst and dye surface. It influences adsorption of dye molecules onto the  $\text{TiO}_2$  surface (Akpan and Hameed, 2009). Also, the hydroxyl radical can be formed by reaction between hydroxyl ions and positive holes. According to Akpan and Hameed (2009) the holes are considered the predominant oxidation species at a low pH of solution. Hydroxyl radicals are considered dominant at neutral and high pH.

In alkaline solutions, hydroxyl radicals are easily generated from oxidising hydroxide ions available on the surface of  $\text{TiO}_2$ . As results, the overall photocatalytic performance of the photoreactor is increased (Akpan and Hameed, 2009). It was also noted that within alkaline solution there is a Coulombic repulsion between negative charge and the surface of photocatalyst and hydroxide ions which will prevent formation of hydroxyl radicals to give a low photo-oxidation yield (Akpan and Hameed, 2009b).

In acidic solution, the surface area available for dye and photon absorption is decreased due to  $\text{TiO}_2$  particle agglomeration, but for some dyes, photodegradation increases in acidic solution. Photoactivity is influenced by the charge of the dye particles which depends on the solution pH and the nature of the particles (Akpan and Hameed, 2009).

A clear example of the effect of pH on photocatalytic degradation of organics on  $\text{TiO}_2$  is provided by Hoffmann et al. (1995); the explanation is provided in Figure 2.4.

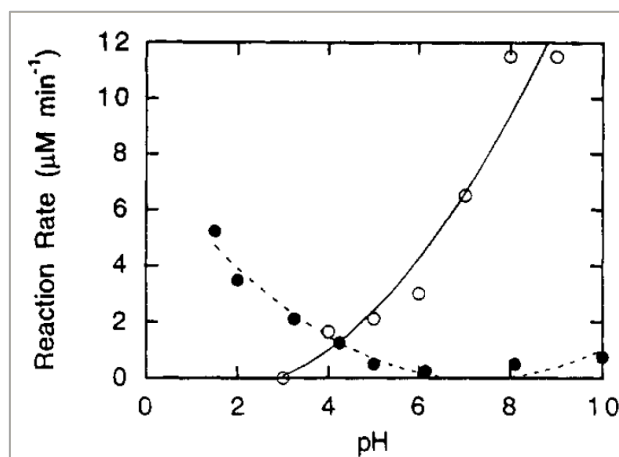


**Figure 2.4 pH dependence of the rate of degradation of trichloroacetate (●) and chloroethylammonium (○) ions where  $[\text{CCl}_3\text{CO}_2^-] = [\text{Cl}(\text{CH}_2)_2\text{NH}_2]_0 = 10 \text{ mM}$ ,  $[\text{TiO}_2] = 0.5 \text{ g/L}$ ,  $[\text{O}_2]_0 = 0.25 \text{ mM}$ , and  $I_a$  (310 to 380 nm) =  $2.5 \times 10^{-4} \text{ Einstein/L/min}$  (Hoffmann et al., 1995).**

In the case of Evonik P25, the corresponding surface acidity constants were found to be  $\text{pK}_{\text{a}1}^{\text{s}} = 4.5$ , which yields a  $\text{pH}_{\text{zpc}} = 6.25$ . The surface proton exchange capacity of P25 is  $0.46 \text{ mol.g}^{-1}$  with a specific surface area of  $50 \text{ m}^2.\text{g}^{-1}$ .

In simple terms,  $\text{pH}_{\text{zpc}} = 6.25$  for  $\text{TiO}_2$  implies that interactions with cationic electron donors and electron acceptors will be favoured for heterogeneous photocatalytic activity at high pH under conditions in which the  $\text{pH} > \text{pH}_{\text{zpc}} = 6.25$  while anionic electron donors and acceptors will be favoured at low pH under conditions in which  $\text{pH} < \text{pH}_{\text{zpc}}$  (Hoffmann et al., 1995). Note that the definition of  $\text{pH}_{\text{zpc}}$  is the point of zero charge (pzc), described as the pH when the electrical charge density on a surface is zero. It is usually determined in relation to an electrolyte's pH, and the pzc value is assigned to a given substrate or colloidal particle.

The implication of this with respect to textile effluents is as follows: the ionic charges of textile dyestuffs, surfactants (soaps) and other additives and finishing agents differ widely and thus the ability of the  $\text{TiO}_2$  nanoparticle to demineralise organic effluents to operate at a given pH of the actual effluent will affect the rate and degree of degradation of each type of organic will differ.

Photocatalytic systems do not require heating—they operate at room temperature. In general, high temperatures favour recombination of charge carriers and desorption of adsorbed reactant species, resulting in a decrease in photocatalytic activity. In the temperature range  $20^\circ\text{C}$  to  $80^\circ\text{C}$ , the true activation energy ( $E_t$ ) is zero while the apparent activation energy ( $E_a$ ) is usually very small. At temperatures below  $0^\circ\text{C}$ ,  $E_a$  increases and desorption of the final product becomes the rate limiting step. At temperatures above  $80^\circ\text{C}$ ,  $E_a$  becomes negative and the exothermic adsorption of a reactant will not be favoured and tends to be the rate limiting step (Herrmann, 1999).

### Effect of catalyst load on the efficiency of photocatalysts of textile effluents

According to Affam and Chaudhuri (2013), the amount of catalyst used is an important factor in photoreactor design. An increase in catalyst load will speed up organic compound removal until a certain point when it will result in lower removal because of catalyst particle aggregation at high concentration. Ahmed et al. (2011) reported that high catalyst concentration reduces the interfacial area between the reaction mixture and the photocatalyst, reducing light penetration.

The rate of the reaction was found to be directly proportional to the mass of a catalyst, but above a certain value of mass, the reaction rate was found to level off and become independent of mass (Herrmann, 1999). In general, the optimum catalyst concentration must be determined to avoid excess catalyst and ensure good adsorption of efficient photons (Saqib and Muneer, 2003). If catalyst loading is too much, there could be unfavourable light scattering and reduction of light penetration into the solution (Chun et al., 2000). The limit depends on the working conditions of the photoreactor. It was found that 1.3 mg  $\text{TiO}_2/\text{cm}^2$  was the limit for a fixed-bed, 2.5 mg  $\text{TiO}_2/\text{cm}^3$  for suspension and 2.5 g/L using a batch photoreactor (Herrmann, 1999). These limits correspond to the maximum amount of  $\text{TiO}_2$  when the whole surface is exposed and fully illuminated.

### Effect of catalyst type on the efficiency of photocatalysts of textile effluents

Surface morphology, particularly particle size and agglomerate size, greatly influences the performance of the photocatalyst (Dinga et al., 2005). The photomineralisation of organic compounds over  $\text{TiO}_2$  was found to be higher when the particle size of the catalyst was in the nano range (Maira et al., 2001). Since the reaction takes place in the adsorbed phase, the smaller the particle the higher the surface area for adsorption, hence the higher the degree of degradation.

Since reaction takes place only in the adsorbed phase of the semiconductor particle, it means that those substances that can adhere effectively to the surface of the photocatalyst are more susceptible to direct oxidation. The degradation of aromatic compounds depends on the substituent group. For instance nitrophenol degrades faster than phenol because it is a stronger adsorbate than phenol (Bhatkhande et al., 2004). Generally, compounds with electronegative atoms such as nitrobenzene and benzoic acid are good adsorbates in the dark compared to those with electron-donating groups (Palmisano et al., 2007).

The concentration of the substrate on the photocatalyst depends on the rate of its degradation. If the rate of degradation is lower than the rate of accumulation of the substrate, it results in the saturation of the surface of the photocatalyst, which diminishes photonic efficiency thus leading to catalyst deactivation (Arana et al., 2004).

### Effect of peroxide concentration on the efficiency of photocatalysts of effluents

Daneshvar et al. (2004) and other researchers investigated heterogeneous photocatalytic systems and found that hydrogen peroxide,  $\text{H}_2\text{O}_2$ , is an electron acceptor which is used to inhibit electron hole recombination by accepting the conduction band electron. The process increases the hydroxyl radical concentration and other oxidising species to accelerate the degradation efficiency of organic compounds (Ahmadi et al., 2014; Pekakis et al., 2006). Affam and Chaudhuri (2013) reported that the addition of  $\text{H}_2\text{O}_2$  in the process increases photoreaction performance in decomposing organic compounds in aqueous solutions with a high value of 100 ml/L concentration.

It is discussed that a lower concentration of  $\text{H}_2\text{O}_2$  will result in low photodecomposition of organic compounds due to direct photolysis of peroxide under UV which also generates hydroxyl radicals according to the available concentration of  $\text{H}_2\text{O}_2$  (Affam and Chaudhuri, 2013).

Excess  $\text{H}_2\text{O}_2$  concentration was reported to scavenge the hydroxyl radicals which should be used for organic compound photodecomposition purposes. Reaction between  $\text{H}_2\text{O}_2$  and hydroxyl radicals forms a weak oxidant which can scavenge useful formed hydroxide radicals (Affam and Chaudhuri, 2013).

### Conclusions on the effects of reaction conditions on photocatalysts of textile effluents

The factors which influence the performance of photocatalytic reactions in the treatment of textile effluents have been presented and discussed. The factors impacting on the photocatalytic performance are the optimisation of the photoreactor design and operation to produce the highest photo-efficiency. The parameters which have the greatest effect on photocatalytic performance are: catalyst load, initial dye concentration, light intensity, solution pH, initial substrate concentration, ionic components in the solution, solvent types, calcination temperature and time, oxidising agents/electron acceptors and catalyst application mode.

## **2.8 PRODUCTION OF NANOPHOTOCATALYSTS**

### **2.8.1 Introduction**

In this section of the literature review, different methods of synthesising  $\text{TiO}_2$  and doped  $\text{TiO}_2$  photocatalysts, including solvothermal, sol-gel, chemical vapour deposition (CVD), biosynthesis and continuous hydrothermal synthesis (CHS), are explored, with emphasis placed on CHS. The discussion includes methods on both a bench-top scale and a pilot-plant scale under laboratory conditions.

There are two approaches to producing nanoparticles. The top-down approach uses bulk materials which are reduced to smaller materials by physical methods such as milling. The bottom-up approach uses atoms, molecules or nanosized particles as building blocks for larger particles, and includes vapour phase deposition, plasma-assisted deposition, liquid phase and colloidal methods amongst others (Brydson and Hammond, 2005).

In 2009, Tsuzuki conducted a study on the trends in commercial scale up of inorganic nanoparticles. Taking zinc oxide as a case study, Tsuzuki related the properties of zinc oxide to its application and the advantages and disadvantages of particular methods for scale up. Of the 100 companies surveyed who produce nanoparticles for commercial applications, 9% used comminution methods, 1% used a solid phase method, 24% used liquid phase methods, 43% vapour phase methods and 5% used a combination of these methods.

The risk that minor changes in process conditions may be acceptable in the production of fine micro powders, could be detrimental for the large-scale production of nanoparticles.

### **2.8.2 Synthesis of $\text{TiO}_2$ nanoparticles using bench-scale laboratory conditions**

#### Review of methods for the synthesis of $\text{TiO}_2$ nanoparticles

There are several ways of synthesising  $\text{TiO}_2$  as a photocatalyst. Each method has its advantages and disadvantages. The choice as to which method to use depends on the desired end use of the nanomaterials. Some of the methods currently used are sol-gel, solvothermal, CHS, CVD, water in oil micro emulsion (W/O) and biosynthesis.

#### Sol-gel synthesis

This method of synthesis involves hydrolysis and condensation of an alkoxide-based precursor (metal oxide). The precursor is hydrolysed using water or dilute acid to form a dispersible solid known as a sol. A sol is a stable dispersion of colloidal particles or polymers in a solvent. The particles can be amorphous or crystalline. In gaseous phase, the particles form aerosols. A gel consists of a 3D continuous network which encloses a liquid; this network is built from the agglomeration of colloidal particles. A combination of these gives a sol-gel.

Sol-gel synthesis is used to prepare materials with a variety of shapes such as porous structures, thin films, dense powders and thin fibres. Several steps are involved when preparing a sol-gel such as hydrolysis and condensation of molecules, gelation, ageing and drying. The calcination of the dried gel produces the metal oxide.

### Hydrothermal or solvothermal synthesis

The term hydrothermal has geological origins and was first used by a British geologist, Sir Roderick Murchison (1792 to 1871) to describe the action of water at elevated temperature and pressure in bringing about changes in the earth's crust. Hydrothermal processing can be described as any heterogeneous reaction in the presence of aqueous solvents under high pressure and temperature conditions in order to dissolve and recrystallise materials which are relatively insoluble under normal conditions. The hydrothermal process is accomplished in the laboratory in stainless steel autoclave under pressure and temperature and often using near-supercritical or supercritical fluid conditions. Reaction temperature, time and solvent type can alter the properties of the nanoparticles (Andersson et al., 2002). The hydrothermal process has also been defined as any heterogeneous chemical reaction in the presence of a solvent (aqueous or non-aqueous) above room temperature and at a pressure greater than 1 atmosphere in a closed system (Byrappa et al., 2000).

The hydrothermal method is therefore ideal for the processing of very fine particles or substances with high purity, controlled stoichiometry, high crystallinity, controlled microstructure, narrow particle size distribution, high quality, high reactivity and controlled morphology (Einarsrud and Grande. 2012).

TiO<sub>2</sub> nanostructured particles (Xie et al., 2007), graphene (Choucair et al., 2008) and carbon (Kongsuebchart et al., 2006) have all been made by the solvothermal route, among other nanomaterials. The ability of the solvothermal method to precisely tailor TiO<sub>2</sub> nanostructures has the potential to maximise the efficiency of these nanomaterials for a wide range of applications in air pollution (Josset et al., 2007) self-sterilisation (Mitoraj et al., 2007), water purification (Yurdakal et al., 2007) and molecular hydrogen production for fuel cells.

Some of the various morphologies produced by hydrothermal synthesis are illustrated in Figure 2.5 (Einarsrud and Grande, 2012).

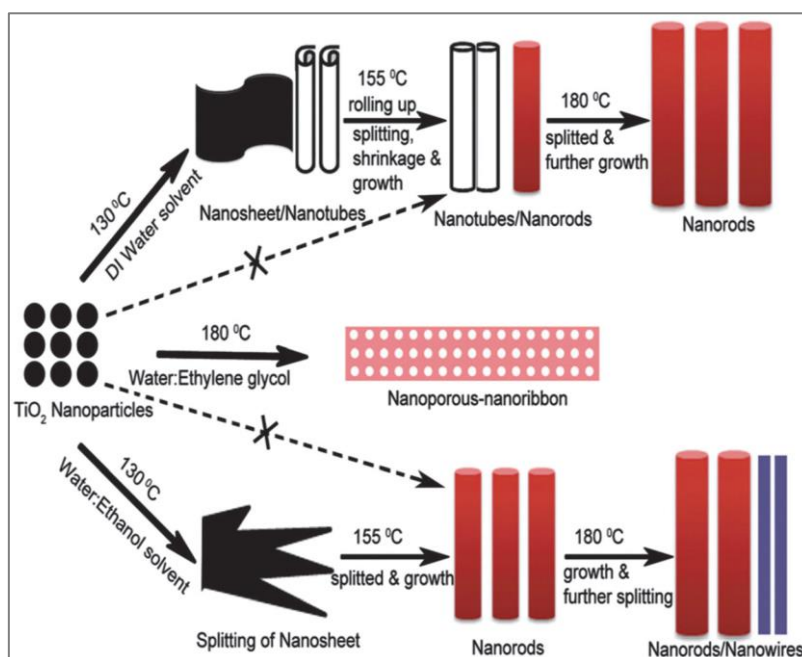


**Figure 2.5 Different morphologies produced via CHS (Einarsrud and Grande, 2012)**



The hydrothermal synthetic technique uses less energy, provides better nucleation control, has no or little pollution effect, allows for high dispersion, gives better shape control, meanwhile using lower temperatures in the presence of a solvent (Fan et al., 2012; Jiao et al., 2003; Sun et al., 2005; Wang et al., 2004; Byrappa and Wang 2007; Dai et al., 2014).

#### The water in oil (W/O) synthesis route

The W/O synthesis route involves inverted micellar aggregates which are made up of water droplets surrounded by a continuous non-polar phase. Water in oil micro emulsions have successfully been used for synthesis of inorganic nanoparticles. Nanoparticles such as Ag/Cu-TiO<sub>2</sub> have been prepared. Such materials have found use as photocatalysts under visible light for antimicrobial activities involving *E-Coli*, *Staphylococcus aureus*, yeast *Saccharomyces Cerevisiae* and pathogenic fungi such as those of the *Candida* family (Byrappa et al., 2000; Qian et al., 1993; Zielinska-Jurek et al. 2010, Sajjad et al., 2010).

Mingshan and co-workers (2011) demonstrated that spherical and quasi-cubic TiO<sub>2</sub>/Ag-based plasmonic photocatalysts can be synthesised by a one pot surfactant-assisted method with oil in water as the medium for synthesis. Their tests conducted on methyl orange (MO) showed stable photocatalytic performance during photodegradation, which was found to be morphology-dependent as illustrated in Figure 2.6 by Mingshan et al. (2011).

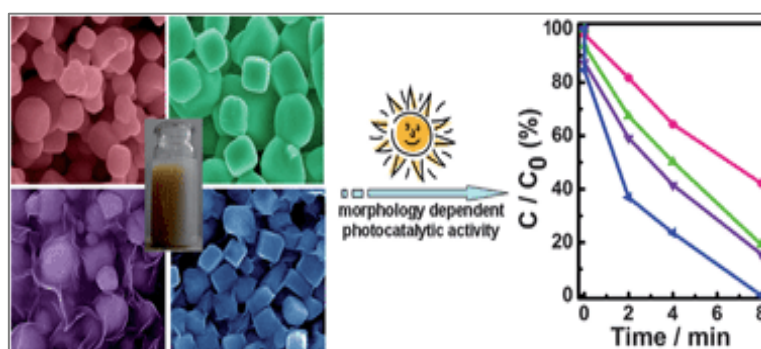


**Figure 2.6 Morphology-dependant photocatalytic activity (Mingshan et al., 2011)**

#### Chemical vapour deposition (CVD)

CVD is also another method of synthesising inorganic nanomaterials in powder form. Usually reactor temperatures are kept between 500 to 700°C to ensure that the metal is deposited on TiO<sub>2</sub> in the presence of a carrier gas. Giuanluca et al. (2008) have described CVD as an industrial chemical process that uses various deposition techniques to form thin films from different precursors onto a substrate, usually a semiconductor material.

In CVD, the substrate is exposed to a single or multicomponent volatile precursor (in gaseous phase) in an inert atmosphere at controlled temperature and pressure. The volatile precursor will either react or decompose onto the surface of the substrate creating a desired, deposited, thin-filmed material. The by-products are removed by flowing gas through the reactor.

This technique is used in the semiconductor industry to deposit thin films such as SiO<sub>2</sub>, silicon (polycrystalline, amorphous and exptaxial), silicon-germanium, silica nitride, titanium nitride, carbon fibres, filaments and nanotubes (Schropp et al., 2000; Jaeger, 2002; Smith, 1995; Dobkin and Zuraw, 2003; Qureshi et al., 2007; Perez et al., 2006; Zhu et al., 2007).

In preparing TiO<sub>2</sub> photocatalyst supported on activated carbon (AC) using CVD, the best route is to use metallo-organic chemical vapour deposition, MOCVD. Thus, the metallo- (organic/inorganic) precursors used

are usually titanium tetra-isopropoxide (TTIP), tetrabutyl titanate (TBOT), titanium tetrachloride and activated carbon support. The carrier gas usually used is N<sub>2</sub>, which is used to transport the vaporised precursor to the activated carbon support while maintaining an inert atmosphere at a specific pressure. The flow pressure is important to remove gases generated from the deposition reaction. Silica gel is used to ensure that the carrier gas is 99.9% dry. This is important because some precursor materials, like TTIP, are unstable once wet. The exhaust gases and excess precursor vapours are removed via a cold trap. The MOCVD helps to control titania crystal structure and growth on the support/substrate.

### Biosynthetic methods

Novel green chemistry methods of preparing TiO<sub>2</sub> nanoparticles have been reported. Scientists have been working on the development of simple, safe and eco-friendly methods of synthesis such as biosynthetic routes. Some of these methods include:

Jayaseelan et al. (2013) have developed a novel low-cost bacteria-mediated biosynthesis of titania nanoparticles using *Aeromonas hydrophila*. The nanoparticles produced as nanocrystals had a crystallite size of 40.5 nm and had significant antibacterial activity against a wide range of bacteria, while the morphology was smooth and spherical, though polydisperse. Hudlikar et al. (2012) have successfully developed a green synthesis of titania nanoparticles using 0.3% aqueous extracts of *Jatropha curcas* L. latex. The nanoparticles produced were however polydisperse with particles measuring 25 to 100 nm. The smaller of the particles were found to be spherical while the larger ones had uneven morphologies. Ordenes-Aenishanslins et al. (2014) have used an isolate of bacillus mycoides for the synthesis, and obtained polydisperse and spherical, anatase titania nanoparticles measuring 40 to 60 nm with an organic shell.

### Microwave-assisted synthesis

Microwave-assisted synthetic methods have been found to be easy to operate, efficient in terms of energy, more environmentally friendly and, above all, the use of microwaves reduces processing time, which usually arises due to the shortening of the nucleation step in reactions.

Microwaves have been used as a synthetic route for preparing electrochemically active TiO<sub>2</sub> particles in the work by Monti et al. (2013). Nanocrystalline anatase TiO<sub>2</sub> was synthesised using microwave irradiation of tetrabutyl orthotitanate solution in benzyl alcohol at a microwave irradiation of 200 to 300 W at 160 to 200 °C. After a short processing time of 1 to 3 minutes, the products were annealed at 500 °C to get rid of any residual organic compounds, resulting in nanocrystals with a crystallite size of 5 to 15 nm. The titania produced was not pure and had diverse polymorphs, even though it had good specific capacity values, and was used in electrochemical appliances such as in energy cells.

Bandas et al. (2011) also produced nanocrystalline anatase TiO<sub>2</sub> from TiCl<sub>4</sub> (98%) in 5% oxalic acid and ethanol irradiated with microwaves for 10 to 30 minutes at 1000 W at temperatures of 150 to 200 °C in a teflon autoclave. The process used in this case was a microwave-assisted hydrothermal synthesis. The crystallite size of the titania produced was around 10 nm.

### Synthesis of doped TiO<sub>2</sub> nanoparticles modified with nitrogen and carbon

Carbon and nitrogen separately or simultaneously doped to TiO<sub>2</sub> can be prepared through several methodologies including simple mixing, sol-gel, hydrothermal, solvothermal, hydrolysis, pyrolysis and oxidation processes, using several precursor materials (Inagaki et al., 2014; Presti et al., 2014; Daghrir et al., 2013; Leary and Westwood, 2011) as illustrated in Table 2.8. Combinations of different approaches such as sol-gel with hydrothermal (i.e. gel-hydrothermal, Wu et al., 2011), sol-gel with solvothermal (Wu et al., 2010) or even employing a non-hydrolytic sol-gel method by simply reacting titanium tetrachloride with benzyl alcohol at room temperature (Leong et al., 2014), among others, have also been attempted and shown to be successful. The synthesis techniques and types of precursors are summarised in Table 2.7.

**Table 2.7 Common TiO<sub>2</sub>, C-TiO<sub>2</sub>, N-TiO<sub>2</sub> and C-N-TiO<sub>2</sub> synthesis techniques and precursors**

Method	Common precursors		
	Titanium oxide	Carbon doping	Nitrogen doping
Simple mixing	*TiO <sub>2</sub> Titanium butoxide	Carbon nanomaterial Dodecylamine n-Hexane Tetraethylammonium hydroxide	Ammonia
Thermal oxidation	Ti metal	Titanium carbide	
Sol-gel	Titanium alkoxides, (R-O-) <sub>4</sub> Ti: Titanium butoxide Titanium ethoxide Titanium isopropoxide Titanium isobutoxide Titanium oxysulphate Titanium tetrachloride Melamine borate	Alcohols: methanol, ethanol, isopropanol, 1- and 2-butanol, tert-butanol. Cystine Glucose Titanium alkoxides*	Ammonia Cystine Ethylenediamine Triethylamine Nitric acid Urea
Hydrothermal	Titanium alkoxides Ammonium hexafluorotitanate	Glucose	Tetrabutylammonium hydroxide Urea
Solvothermal	*TiO <sub>2</sub> Titanium cyanide Titanium trichloride	Ethanol	Titanium cyanide*** Hexamethylenetetramine
Hydrolysis	Titanium alkoxides Titanium chloride		Ammonia Ammonium hydroxide Triethylamine Urea
Physical vapour deposition	Ti metal *TiO <sub>2</sub>	n-Hexane Ethanol	
Chemical vapour deposition	Titanium alkoxides Titanium (II) hydride	Titanium isopropoxide*	Atomic nitrogen flux Ammonia, Hydrazine, Ammonium chloride, Ammonium hydroxide Nitric acid Nitrogen gas
Electrophoretic deposition	*TiO <sub>2</sub>	Carbon nanomaterial	

\* In these approaches, TiO<sub>2</sub> is used as the starting material for doping, \*\*Titanium alkoxides are used as the metal-oxide precursor as well as the carbon source, \*\*\*Titanium cyanide is similarly used as the metal-oxide precursor as well as the nitrogen source.

Most of the synthetic approaches listed in Table 2.7 involve multiple steps and unstable and costly reagents. However, relatively simple procedures involving a mixture of TiO<sub>2</sub> precursors and doping agents followed by calcination in air have shown to result in the successful modification of TiO<sub>2</sub> photocatalyst (Joni et al., 2013; Dong et al., 2009; Gu et al., 2008). Recently, a simple procedure involving a mixture of TiO<sub>2</sub> and nitrogen sources such as urea following heat treatment at 800°C for 3 hours have been used and found to arguably introduce nitrogen atoms into the lattice of rutile nanoparticles (Joni et al., 2013). Nitrogen-doped TiO<sub>2</sub> has

also been also prepared by heat treatment of  $\text{TiO}_2$  at  $400^\circ\text{C}$  under atomic nitrogen flux as the nitrogen source (Tao et al., 2014). Gu et al. (2008) prepared micro-mesoporous C- $\text{TiO}_2$  using a low temperature procedure by simply dispersing  $\text{TiC}$  in a nitric acid and ethanol following heat treatment at  $60^\circ\text{C}$  and drying at  $120^\circ\text{C}$ .

#### Synthesis of doped $\text{TiO}_2$ nanoparticles using a heterojunction structure

Several strategies have been implemented to extend the band gap of  $\text{TiO}_2$  up to visible light range, i.e. substitution of different transition metal or anions to the Ti or oxygen sites. Combination of semiconductors, with matching band potential to create a heterojunction structure is of increasing interest as the heterojunction can be utilised to effectively separate the photogenerated electrons and holes. Beside the basic demand of the obvious matching band potential of the semiconductors, electron and hole conduction mobility in the electron and hole accepting semiconductors is important for the enhancement of photocatalytic activity (Huang et al., 2007). A number of studies have been conducted on combined semiconductors based on a  $\text{TiO}_2$  photocatalyst. Akaganeite ( $\beta\text{-FeOOH}$ ) is a semiconductor type of iron oxy hydroxide with a band gap of 2.12 eV (White, 1990), which is lower (2.6 eV) than that of previously reported  $\gamma\text{-FeOOH}$  (Rawal et al., 2009). Due to the relatively low band gap of  $\beta\text{-FeOOH}$  it can be excited under visible light irradiation.  $\beta\text{-FeOOH}$  has a large tunnel structure, where iron atoms are strongly bonded to the framework (Amine et al., 1999). Because of its tunnel type structure lithium can be intercalated and extracted freely in the tunnels ( $2 \times 2$ ) during discharge and charge processes, making it a potential material for battery electrodes (Shao et al., 2010). This implies that  $\beta\text{-FeOOH}$  possesses good electron conduction ability.

#### **2.8.3 Large-scale production of nanoparticles using CHS**

Large-scale production of nanoparticles is limited not only by technological challenges, but also regulatory challenges, and therefore both aspects are discussed here briefly. The methods that can potentially be used for large-scale production are listed and the advantages and disadvantages of each are discussed. A laboratory-scale batch process yields about 1g. Large-scale production in the laboratory is often regarded as anything between 10 to 100 g per batch (Tsuzuki, 2009). This is insufficient for commercial scale requirements.

Very few authors have reported the synthesis of titanium dioxide nanoparticles using a continuous flow reactor. Therefore, few data exist to compare with the findings in this study. Kawasaki et al. (2009) synthesised  $\text{TiO}_2$  particles in the range of 13 to 30 nanometres using  $\text{Ti}(\text{SO}_4)_2$  as a precursor, reporting high conversions of 99% for all experimental runs. They studied the effect of KOH concentration, temperature and residence time on the resulting average particle size and crystallinity. By altering the KOH concentration between 0.253 to 0.273 mol/L, they were able to control the average particle size between 13 nm to 30 nm. All particles were found to be anatase phase  $\text{TiO}_2$ , as determined through XRD, and an increase in KOH concentration was also found to promote an increase in crystallinity. The effect of temperature was studied at  $400^\circ\text{C}$ ,  $450^\circ\text{C}$  and  $500^\circ\text{C}$ , and it was found that temperature had little effect on average particle size (APS); however, crystallinity increased along with temperature. Increasing the reactor length from 1.5 m to 4.6 m resulted in no observable change in APS or crystallinity.

A study by Zhang et al. (2008) also reported the synthesis of nanosized  $\text{TiO}_2$  particles in CHS, using titanium (IV) bis (ammonium lactato) dihydroxide as a precursor. The particles were determined to be anatase phase  $\text{TiO}_2$  and very small, with an average particle size of 4.9 nm. The study did not focus on the effect of operating parameters, but rather on how the phase changes from anatase to rutile during heat treatment. As the heat treatment surpassed  $400^\circ\text{C}$ , some of the anatase changed to rutile. After roughly  $950^\circ\text{C}$ , all of the anatase had changed to take on the rutile phase. As the temperature of the heat treatment increased, the surface area of the particles reduced rapidly, decreasing the particles' photocatalytic ability. The optimal temperature for the synthesis of the best performing photocatalyst for the degradation of methyl blue was found to be  $300^\circ\text{C}$ , in their study. This was attributed to a good balance in crystallinity and high surface area.

## 2.9 IMMOBILISATION OF NANOPHOTOCATALYSTS

Separation of nanoparticles from solution has always posed a problem. The use of a centrifuge has been found to be the only way to effectively remove nanoparticles from solution. If the removal efficiency is less than 100%, it creates secondary pollution. For industrial-scale water treatment, this additional step for particle removal is not cost effective. Thus, immobilisation of the nanophotocatalysts on a support is desirable.

Generally, selecting a suitable method for photocatalyst preparation depends on the type of catalyst support/substrate system, the type of pollutant to be degraded and the degradation environment. This is due to the fact that the loading of titania catalyst, for example, onto a support material can have a profound effect on the photocatalytic properties of the  $\text{TiO}_2$ . The catalyst's active sites can be affected by several factors resulting in alteration of the chemical and physical structure of the catalyst due to temperature of preparing the supported titania as well as chemical bonds formed between the substrate and the titania particles. These can drastically change the  $\text{TiO}_2$  energy band gap. Energy band gap determines the effectiveness of the catalyst in producing hydroxyl radicals in an aqueous system. Catalyst surface area reduction due to particle bonding with the substrate material and the loss of titania particles in pore trappings within the substrate material where UV radiation cannot reach, are serious causes of concern when choosing any photocatalytic preparation method.

### 2.9.1 Types of catalyst supports

Some immobilisation methods for nanoparticles (NPs) are summarised in Table 2.8. The immobilisation substrates include electrospun fibres, textiles, glass slides, etc. The preparation of the metal and metal oxide NPs mostly includes application of the sol-gel process either to prepare NPs before deposition or during the immobilisation reaction step. The applications include photocatalysis, sensors and antibacterial surfaces.

Glass-based substrates for immobilisation have been investigated in a number of studies due to the transparency of the system even after immobilisation. Glass raschig rings/ $\text{Fe}_2\text{O}_3$  composite was developed by Bandara et al. (2007) for degradation of 4-Chlorophenol and orange II dye under simulated solar irradiation. Polyethylene grafted maleic anhydride (PEGMA) was used as a negative interfacial agent to coat the glass raschig rings with a thin film of  $\text{Fe}_2\text{O}_3$  nanoparticles. The composite material showed good photocatalytic properties under simulated solar irradiation. The authors proposed that the rugosity of the glass surface played an important role in sustaining the thin film on the raschig ring surface.

Phenolic derivatives were photodegraded under simulated solar irradiation by  $\text{TiO}_2$  coated glass raschig rings (Sampaio et al., 2013). The authors used a simple drop coating technique for depositing layers of  $\text{TiO}_2$  on glass raschig rings. The glass raschig rings were immersed in 5% W/V solution of ethanol and  $\text{TiO}_2$  nanoparticles. The suspension was sonicated, followed by calcination at  $450^\circ\text{C}$  for 2h. It was reported that photocatalytic efficiency is highly dependent on the type of  $\text{TiO}_2$  used, the number of layers applied on the raschig ring surface and the robustness of the catalyst film.

Besides the use of glass substrate for immobilisation, a new hybrid technology (ultrafiltration and photocatalysis combined) has been developed in recent years (Djafer et al., 2010; Athanasekou et al., 2012). An ultrafiltration membrane made with alumina and immobilised  $\text{TiO}_2$  surface was combined to operate separately in series, e.g. membrane filtration followed by photocatalytic degradation under UV irradiation. The authors reported good photocatalytic efficiency in the degradation of methyl orange. A different technique was developed where  $\text{TiO}_2$  photocatalytic layers via by CVD on both sides of tubular alumina membrane. The authors concluded that double side active  $\text{TiO}_2$  modified membranes showed high efficiency under UV irradiation when compared to common cross flow membrane.

**Table 2.8 The immobilisation of nanoparticles**

Reference	Type of NP	Supplier of NP /Synthesis of NP	Substrate	Method of immobilisation	Application
Im et al., 2008	TiO <sub>2</sub>	Anatase powder from Acros	Electrospun PAN	A 10% w/w PAN/DMF 10% TiO <sub>2</sub> solution was made and electrospun onto a rotating collector	Photocatalytic degradation of rhodamine B dye in a batch reactor with UV light.
Prahsarn et al., 2011	TiO <sub>2</sub>	Anatase from Aldrich	Electrospun PAN	5% w/w PAN/DMF solutions with different concentrations of TiO <sub>2</sub> (1, 2, and 3% wt). And the same solutions in which water was added (3 and 5% wt).	Photocatalytic degradation of methylene blue dye in a batch reactor with UV light.
Kim et al., 2008	TiO <sub>2</sub>	Aldrich Chemical Company	Electrospun PAN with graphene	A PAN-DMF solution was prepared and electrospun. Graphene was dissolved in DMF and sonicated (bath type). The PAN was then dissolved in this (graphene-DMF) solution and stirred until a homogenous solution formed and this solution was then spun into nanofibres. The PAN-DMF mats and the graphene-DMF mats were stabilised in air at 280°C. A sol solution was then made from titanium n-butoxide. Both stabilised mats were dipped into the sol solution, washed with ethanol and water, dried in air and carbonised.	Photocatalytic degradation of methylene blue dye in a batch reactor with UV light.
Pan et al., 2006	TiO <sub>2</sub> - SiO <sub>2</sub>	Titanium tetra-isopropoxide and tetraethylorthosilicate from Acros	Nonwoven textile	The precursor TTIP was hydrolysed in an acidic medium for 3 h then heated to 70°C for 24 h to create a transparent yellowish TiO <sub>2</sub> sol with 2% solids. A SiO <sub>2</sub> sol was prepared. TiO <sub>2</sub> sol and SiO <sub>2</sub> sol were mixed together at RT for 20 min. This mixture was then coated on the textile. The nonwoven was dipped into the sol mixture, then heated in an oven at 110°C for 1 h. The coated fibre was then heat treated by hot-pressing.	Photocatalytic degradation of 2-propanol (IPA) in a batch photoreactor with UV light.
Su et al., 2013	TiO <sub>2</sub>	Not specified	Electrospun PAN	PAN was dissolved in DMF and stirred until the solution was homogeneous, Tetrabutyl titanate [Ti(Obu) <sub>4</sub> ] was dropped slowly into the solution while stirring. This solution was then electrospun. The hydrothermal process: acetic acid was added to de-ionised water, while stirring a piece of [Ti(Obu) <sub>4</sub> /PAN] mat. These mixtures were left at 160°C for 12 h, cooled to room temperature and rinsed with de-ionised water and ethanol several times and dried at 60°C for 3 h in a vacuum oven to produce TiO <sub>2</sub> /PAN nanofibre mats.	Photocatalytic degradation of phenol in a batch photoreactor with UV light.
Xie et al., 2014	Ni	Not specified	Mesoporous silica	Ni precursor was delivered into SBA-15 by ethylene glycol (EG), then dried in a vacuum and paralysed under nitrogen. Removing the carbon templates by heating in air and <i>in situ</i> reduction process which formed highly dispersed Ni NPs.	Sintering and coking resistance.

Reference	Type of NP	Supplier of NP /Synthesis of NP	Substrate	Method of immobilisation	Application
Khataee et al., 2009	TiO <sub>2</sub>	Not specified	Glass plates	Heat attachment method: A suspension of TiO <sub>2</sub> in de-ionised water was prepared. The pH of the suspension was adjusted with the use of HNO <sub>3</sub> and was sonicated for 15 min. The suspension was poured onto the glass plates and was dried at RT for 12 h, then dried further for an hour at 100°C. The plate was then washed with NaOH. The plates were then washed with water.	Photocatalytic degradation of 3 azo dyes using a circulation photochemical reactor with a UV lamp
Kumar and Bansal, 2011	TiO <sub>2</sub>	P25	Film and glass slide	<p>Films: A TiO<sub>2</sub> suspension was prepared with TiO<sub>2</sub> powder in distilled water with stirring for 1h. Also, TiO<sub>2</sub> with activated carbon in distilled water with stirring for 1 h. Polyvinyl alcohol-formaldehyde binder was prepared by stirring in a 70°C water bath until it became a transparent polymer glue. This glue was then brushed onto a fibreglass slide, the TiO<sub>2</sub> suspensions are brushed on to bind the TiO<sub>2</sub> to create a film.</p> <p>Glass- A TiO<sub>2</sub> suspension was prepared with TiO<sub>2</sub> powder in distilled water with acrylic emulsion under vigorous stirring. Also, TiO<sub>2</sub> with activated carbon in distilled water with acrylic binder under vigorous stirring. This solution was then brushed onto glass slides to create a film on the slides. They were then left to dry at RT and recoated twice.</p>	Photocatalytic degradation of amaranth dye in a photocatalytic chamber with a UV lamp.

### 2.9.2 Electrospun catalyst supports using polyacrylonitrile, PAN

In this section, the electrospinning process is presented and discussed. Further, the stabilisation and carbonisation process and ideal conditions for electrospun mats are explored.

#### The electrospinning process

The process of electrospinning was first published in 1934. The early patents include: Formhals, A., US Patent, 1,975,504 (1934), Formhals, A., US Patent, 2,160,962 (1939) and Formhals, A., US Patent, 2,187, 306 (1940).

In the electrospinning process a high voltage is used to create an electrically charged jet of polymer solution or melt, which dries or solidifies on the electrode to leave a polymer fibre. One electrode is placed into the spinning solution/melt and the other is attached to a collector. An electric field is subjected to the end of the capillary tube or needle of a syringe pump, which contains the polymer dope held by its surface tension. This induces a charge on the surface of the liquid. Mutual charge repulsion causes a force directly opposite to the surface tension.

As the intensity of the electric field is increased, the hemispherical surface of the fluid at the tip of the capillary tube elongates to form a conical shape known as a Taylor cone. With increasing field strength, a critical value is attained when the repulsive electrostatic force overcomes the surface tension and a charged jet of fluid is ejected from the tip of the Taylor cone.

The discharged polymer solution jet undergoes a series of whipping instability processes wherein the solvent evaporates, leaving behind a charged polymer fibre, which is laid on a grounded collecting electrode. The instabilities result in small diameter fibres being produced. An example of an experimental set-up used for electrospinning is shown in Figure 2.7. The polymer solution or melt is contained in a glass tube, usually a pipette, or a syringe. A metering pump or gravity is used to control the feed rate. High voltage is applied to the spinning dope via metal wire immersed in the polymer solution in a pipette or a clamp on the syringe pump needle provides the driving force. DC high voltage source can typically generate up to 30 kV, and the set-up can be operated on either positive or negative polarity.

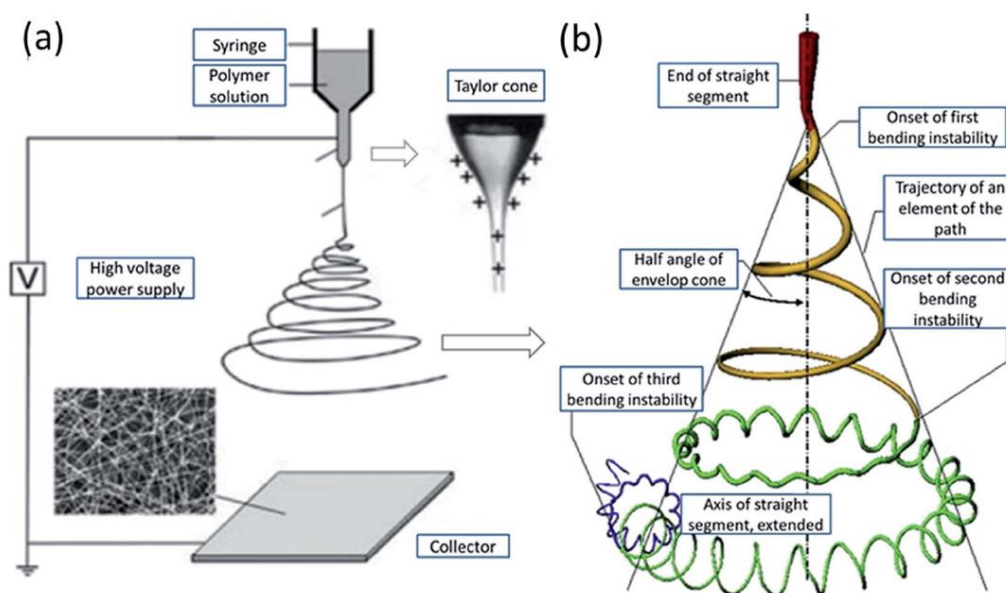


Figure 2.7 Schematic of the electrospinning process (Ke et al., 2014)



Parameters which affect the electrospinning process are: viscosity, surface tension, electric potential, distance between tip and collector, temperature, humidity and air velocity (Doshi & Reneker, 1995). (Chronakis, 2005) exclaims that the concentration, the flow rate of the polymer and the motion of the collector also have an effect on the process.

These fibres can range from a 2 nm to micron meters (Bhardwaj and Kundu, 2010; Nyamukamba, 2011; and Doshi and Reneker, 1995). These nanofibres have a high surface area. This is why they can be applied in many different fields of study, including nanocatalysis, tissue engineering, filtration, biomedical, pharmaceutical, optical electronics, environmental defence and security, electronics, etc. The advantage of this technique is that it is simple, it can be used with a wide variety of polymers, shape and size can be controlled during this process (Bhardwaj and Kundu, 2010; Niu and Lin, 2012), it has low weight and is cost effective (Chronakis, 2005).

In the electrospinning process, scientists thus far have utilised many experimental methods and many different precursors to produce TiO<sub>2</sub> nanoparticles, either inside the spinning dope or on the surface through a dipping process. Precursors for the synthesis of TiO<sub>2</sub> nanoparticles are titanium alkoxides and the synthesis conditions can play a major role in cluster formation and properties of the nanoparticles (Simonsen and Søgaaard, 2010). The most popular precursor used is titanium tetra-isopropoxide, TTIP, used with hydrolysis and condensation followed by calcination methods in the synthesis of nanoparticles in and on the fibres. In terms of a photocatalytic active fibre, Prahsarn (2011) and Im (2008) simply added the synthesised nanoparticles to a PAN solution to be electrospun and used for photocatalytic degradation. Teng et al. (2007) and Su (2013) mixed the precursors to the PAN solution, electrospun it into a mat and immersed the mats into solutions that would hydrolyse the precursor and produce nanoparticles while inside the electrospun mat. Dadvar (2011) dipped the PAN electrospun mat into a hydrolysed precursor solution calcinated and used for photocatalytic degradation.

#### Polyacrylonitrile and carbon fibre catalyst supports

The polymer used by McGann et al. (2012) was polyacrylonitrile (PAN) (Figure 2.8). The organic polymeric fibres need to be stabilised and carbonised so that the fibrous support itself is not degraded by the immobilised TiO<sub>2</sub> photocatalyst. Electrospun PAN nonwoven mat with sub-micron-sized fibres, is used as the backing polymer support and is applied in a trickle-bed reactor (TBR) in carbonised form. Carbonised PAN is used for the following reasons:

- The carbonised fibre is black which will assist in heating the fluid flowing through the TBR and thereby increase the rate of reaction.
- The fibre shrinks during carbonisation and thereby NPs which were imbedded in the fibre are exposed at the surface.
- The carbon mat cannot be degraded by the radical species generated during the photocatalysis.
- PAN is hydrophilic, whereas the carbon fibres are hydrophobic

Stabilisation by means of heat (240°C) allows the PAN structure to transform from a molecularly linear structure into a ladder structure. Further heating to about 1000°C transforms the ladder structure into a graphitic structure only containing carbons, making it one of the strongest known fibres (Rahaman et al., 2007).

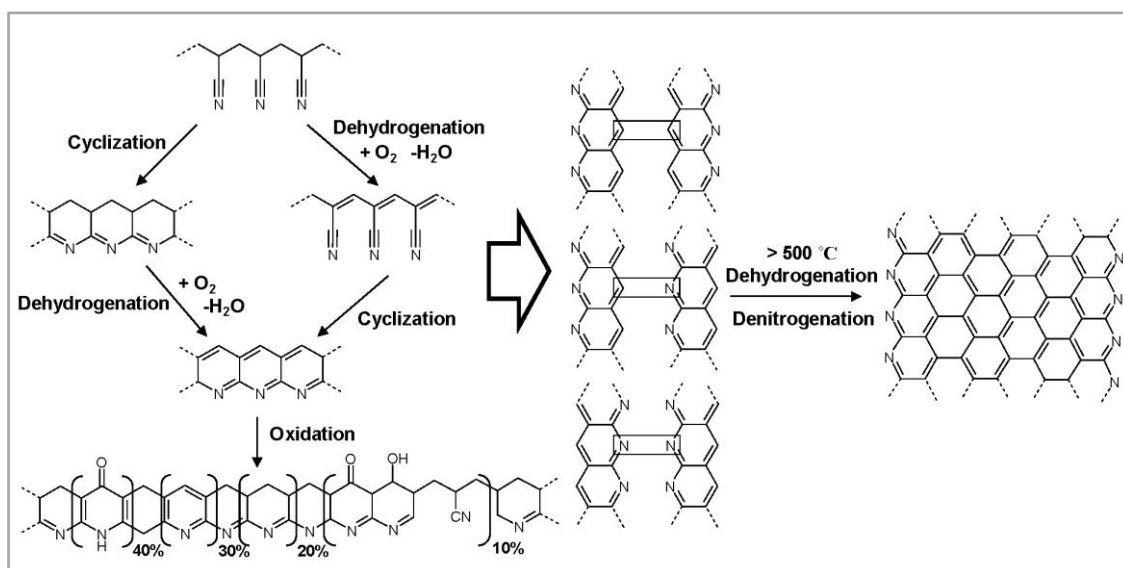


**Figure 2.8 Chemical reaction of the stabilisation and carbonisation of PAN (McGann et al., 2012)**

The stabilisation process usually takes place in an oxygen-rich atmosphere. Although it can be done in an inert atmosphere, it shows better stability when done in oxygen (Rahaman et al., 2007). Also the oxygen is an initiator for the formation of activated cyclisation. Cyclisation is the process by which the groups in the linear structure of the polymer react with the adjacent groups to form a stable ladder structure.

In the process of cyclisation, the triple bond between the carbon and the nitrogen is converted to a double bond with a carbon while also changing the linear structure to a ring structure. In the stabilisation process the structure of the fibre also undergoes dehydrogenation where hydrogen is lost within the structure and forms a second double bond which stabilises the structure further. Dehydrogenation can take place before or after cyclisation. The stabilisation process has a heating rate in oxygen.

When the fibre is carbonised, it shrinks causing the nanoparticles to be exposed on the surface of the fibres. This provides a large surface area for water and the contaminants to come in contact with the nanoparticles. The as-spun nanofibres, thermally treated at 800°C, shrink in diameter and lose approximately 25 to 30% of their weight (Faccini et al., 2015; Rahaman et al., 2007). The degree of shrinkage after stabilisation and carbonisation has been determined as 10% and 30% respectively (Jun et al., 2009)

Electrospun PAN fibres have a sub-micrometre diameter giving high surface area and better exposure on the surface (Prahsarn, 2011). PAN however is hydrophobic and this is a disadvantage when the nanoparticles need direct contact with water and the contaminant in the water for long periods of time without being damaged. The solution to this problem comes when a grade of PAN that is a precursor to carbon fibre is and can be carbonised with the nanoparticles within it. Zhou (2009) claims that after the PAN precursor is carbonised it has a high tensile strength and better mechanical properties, also the size of the fibre decreases as a higher temperature is used for carbonisation. This means that if a nanoparticle was present within the PAN fibre, it would be exposed on the surface after carbonisation; this was seen to be true when Teng et al. (2007) provided proof in scanning electron microscopy (SEM) images of crystalline structures on the surface of their spun and calcinated fibres.

The PAN fibre used for the production of carbon fibres is a copolymer that brings about structural changes in the chemical structure of the PAN fibre. The copolymer consists of acrylonitrile (93%), itaconic acid (1%) and methyl acrylate (6%). This copolymer PAN is the precursor to carbon fibre and, according to Rahaman et al. (2007), this precursor is most suitable for the production of carbon fibre because of its melting point and carbon yield. These specific attributes allow the polymer to change in certain conditions. Itaconic acid and

methacrylate allow the polymer to evolve under certain conditions instead of degrading before melting. These copolymers also strengthen the fibre further during evolution of the structure of the carbon fibres.

## 2.10 DESIGN OF LARGE-SCALE PHOTOCATALYTIC REACTORS

Solar-based reactors are receiving much attention in scientific literature. The materials used in these reactors need to be UV invisible and inert to the whole process, and the reactor needs to be designed to suit the application. In this section, large-scale solar reactors, based on fixed-bed reactors, are presented and discussed.

### 2.10.1 Photocatalyst reactors

Solar energy is a sustainable energy source and since the nanoparticles are active in daylight or can be modified to be active in daylight, solar energy can be used as a light source in photocatalytic reactors.

Fixed-bed reactors have been designed and used to hold the immobilised nanoparticles that can capture solar energy. These fixed-bed reactors can be packed with nanoparticle supports as shown in Figure 2.9 and Figure 2.10 or they can contain thin films, as seen in Figure 2.11, Figure 2.12 and Figure 2.13.

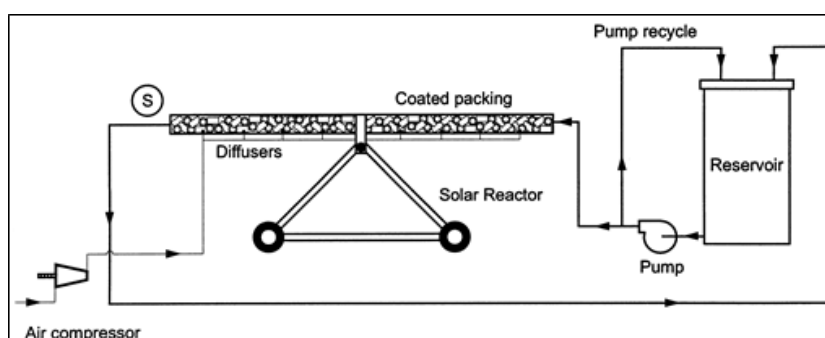


Figure 2.9 Packed bed photocatalyst reactor (Feitz et al., 2009)

The packed beds are used to increase the surface area exposed to water. In Figures 2.10 and 2.11 the reactors are energy intensive. The reactor in Figure 2.11 uses a lot of energy. It is not suitable for solar applications and requires an air feed to decolourise dyes.

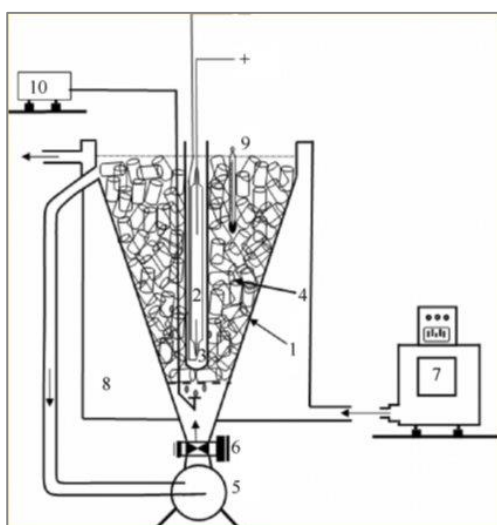


Figure 2.10 Packed bed photocatalytic reactor (Saïen et al., 2009)

Fixed-bed film reactor is more suited for solar applications, where the water is pumped from a reservoir up to the top of the bed. The water flows at a slow speed down the film while exposed to sunlight, and into the reservoir. The elevation angle in papers reviewed (Alberici et al., n.d.; Bahnemann, 2004; Feitz et al., 2000; Kernani et al., 2014; Kodom et al., 2013; Noorjahan et al., 2003; Saien et al., 2009; Verma et al., 2012; Zayani et al., 2009) is in a range of 10 to 25° for an optimised residence time for efficient operation. All scientific reviews show that organics can be reduced within 200 minutes, depending on the type of organic and the concentration.

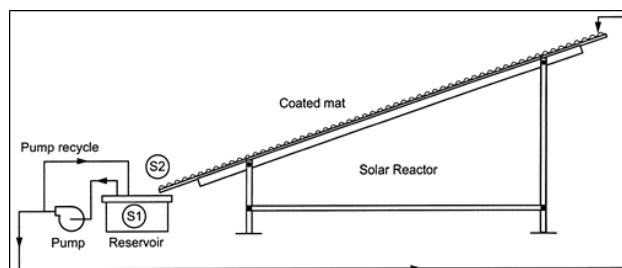


Figure 2.11 Thin film photocatalytic reactor (Feitz et al., 2000)

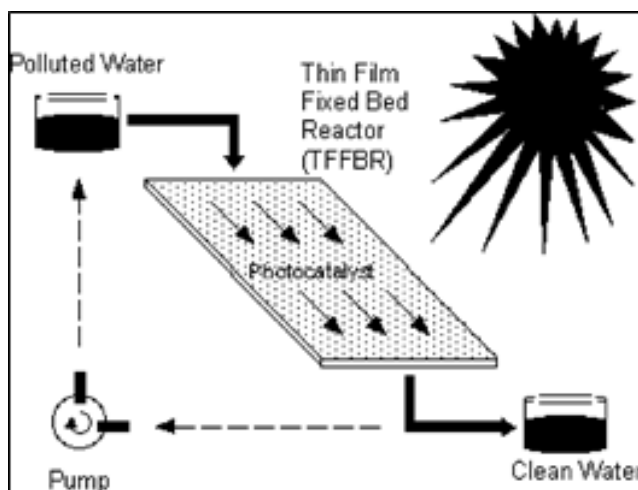


Figure 2.12 Thin film photocatalytic reactor (Bahnemann, 2004)

In some cases, the supported nanoparticles do not destroy the organics as fast or efficiently as a slurry would. In the case of large quantities of water to be treated, industrial pilot plants have been installed with fixed-bed film reactors in series, with the use of sunlight (Bahnemann, 2004).

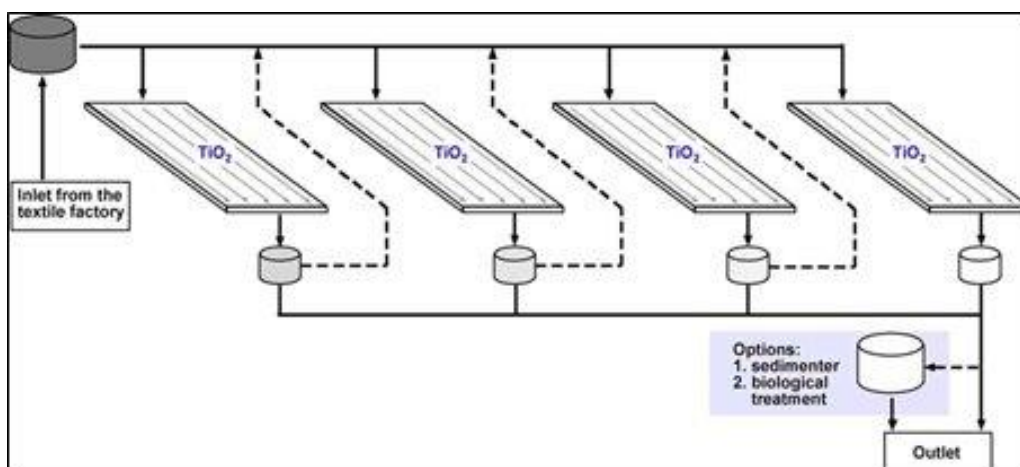


Figure 2.13 Pilot plant using sunlight as a light source (Bahnemann, 2004)

The flow rate in certain large TBR systems using P25 is provided in Table 2.9

**Table 2.9 TBR flow rates**

Author	Design	Dye	Flow ( $\text{m}^3\text{h}^{-1}\text{m}^{-2}$ )	Flow flux ( $\text{m}^3\text{hr}^{-1}\text{m}^{-2}$ )
Ghanem et al.	Thin film fixed-bed reactor 20° angle, 25 $\text{m}^2$	Azo dyes	3	0.032
Goswami et al.	Slurry tubular reactor, 15° angle 10 $\text{m}^2$	Contaminated ground water, (BTEX))	3	0.045
Feitz et al.	Coated mesh reactor, 20° angle, 3.25 $\text{m}^2$	Phenol	0.3	0.070
Feitz et al.	Packed bed reactor, 20° angle 2 $\text{m}^2$	Phenol	0.2	0.141

## 2.11 TOXICITY OF PHOTOCATALYSTS

The United States Environmental Protection Agency (EPA), is developing scientific methods to study and evaluate the unique properties of nanomaterials—how they behave during manufacturing, product use, and end of life disposal. To better protect human health and the environment, this research is used by the EPA's Chemical Safety and Pollution Prevention Office, and others, to inform policy and regulatory decisions about chemicals.

A European Union 7<sup>th</sup> Framework Programme (FP7) project, Engineered Nanoparticle Impact on Aquatic Environments: Structure, Activity and Toxicology (ENNSATOX), was run from 2009 to 2012 at a cost of €3,655,316 ([http://cordis.europa.eu/result/rcn/54945\\_en.html](http://cordis.europa.eu/result/rcn/54945_en.html)). The aim was to study and relate the structure and functionality of well characterised engineered nanoparticles, such as zinc oxide, titanium dioxide and silicon dioxide, to their biological activity in an aquatic environment, taking into account the impact of the nanoparticles on environmental systems from their initial release to uptake by organisms. The activity of the nanoparticles was studied in a series of biological models of increasing complexity from single cells to fish. A parallel study examined the behaviour of NPs in natural waters and how they modify the particles' chemical reactivity, physical form and biological activity.

These sets of particles are postulated to have different mechanisms for inducing toxicological responses (ZnO, as soluble zinc, titania in redox processes, and silica in membrane disruption). In relation to TiO<sub>2</sub>, aggregates were rapidly formed in biological solutions and no toxic effects were seen. In the case of ZnO and TiO<sub>2</sub> which are prone to aggregation, the interaction of the aggregates with cells was less than that of the disaggregated particles but is also related to the primary particle size.

Conventionally, TiO<sub>2</sub> NPs have been considered a low toxicity material. TiO<sub>2</sub> NPs possess different physicochemical properties compared to their fine particle, micron-sized analogues, which might alter their bioactivity. A full risk assessment for various routes of exposure to TiO<sub>2</sub> NPs requires further data. Apart from the National Institute for Occupational Safety and Health in the United States which has set a recommended exposure limit (REL), to date, no occupational or environmental exposure limits for TiO<sub>2</sub> NPs have been set by any other regulatory agency. Current understanding of their toxicity largely depends on a limited number of experimental animal or cell culture studies, where extrapolation to human exposure is required. Epidemiological studies thus far have not been able to detect an association between occupational exposure to TiO<sub>2</sub> particles and an increased risk for cancer. The physicochemical properties of TiO<sub>2</sub> NPs may strongly influence their bioavailability and toxicity. Most data imply that TiO<sub>2</sub> anatase NPs are cytotoxic or genotoxic. However, this conclusion was based on studies using TiO<sub>2</sub> anatase NPs only. Under conditions of occupational

exposure, inhalation of TiO<sub>2</sub> NPs is normally the principal route for entry into the human body (Shi et al., 2013). The focus of the risk assessment strategies is predominantly human risk based and Stone et al. (2010) caution that there is still a considerable lack of knowledge on uptake, biological fate, effects and modes of action of nanomaterials in species other than rodent and mammalian models. This is particularly the case for exposure and uptake routes other than the air (e.g. waterborne exposure, sediment exposures).

The three main research priorities that need to be addressed are:

- (i) The choice of NPs to use in biological experiments, and the tests (analysis of physicochemical properties, aggregation, sedimentation, etc.) needed to characterise them before, during and after these experiments;
- (ii) The need to examine the route of uptake of synthetic NPs by organisms in different environments (important for the behaviour of synthetic NPs in the food-chain);
- (iii) The choice of organisms and endpoints measured.

The South African government, recognising the potential undesirable health and environmental impacts of nanomaterials, is supporting a pilot health risk assessment of gold nanoparticles synthesised in South Africa, through its Department of Science and Technology (DST). This project is endorsed by the Organisation for Economic Cooperation and Development (OECD) and is led by the Toxicology and Biochemistry Section of the National Institute for Occupational Health (NIOH), under the guidance of Prof Mary Gulumian. As part of this project, occupational exposure during gold nanoparticle synthesis is being assessed. This is the first time that this will be done in South Africa and will lay the basis for exposure assessment for other engineered nanoparticles (ENPs) in the country. The risk assessment of engineered nanoparticles produced in South Africa has been given further impetus by the DST's recent initiative to establish a local ENP health and safety platform. In addition to contributing to addressing gaps in the health risk assessment of gold nanoparticles, the project will also contribute to increasing human capital in the country in this essential discipline.

Until very recently there has been a lack of support in South Africa for establishing the potential risks of ENMs and products to both humans and the environment (Musee, 2010; OECD, 2012). This phenomenon is, however, similar to what has been observed in other countries during their initial phase of implementing nanotechnology strategies and programmes. In 2010, the DST launched an initiative towards establishing a research platform on aspects related to health, safety and environmental risks of nanotechnology. A national steering committee, consisting of representatives from the National Institute for Occupational Health, the Council for Scientific and Industrial research (CSIR), the University of Johannesburg (UJ), and North West University (NWU), were tasked with examining the ethics and risks associated with nanotechnology. Rather than come up with an independent framework, a decision was made (Musee, 2010; Gulumian, 2011) to develop a framework that will be aligned with the current initiatives in the United States, the European Union and member countries, Japan (NNI, 2011; SCCP, 2007; Thomas et al., 2006).

The long-term health risks of nanoparticles remain poorly understood, which is a serious concern, given their prevalence in the environment from increased industrial and domestic use. The extent to which such compounds contribute to cellular toxicity is unclear, and although it is known that induction of oxidative stress pathways is associated with this process, the proteins and the metabolic pathways involved with nanoparticle-mediated oxidative stress and toxicity are largely unknown. To investigate this problem further, the effect of TiO<sub>2</sub> on the human keratinocyte cell line was examined. The data show that although TiO<sub>2</sub> does not affect cell cycle phase distribution, nor cell death, these nanoparticles have a considerable and rapid effect on mitochondrial function. Metabolic analysis was performed to identify 268 metabolites of the specific pathways involved and 85 biochemical metabolites were found to be significantly altered, many of which are known to be associated with the cellular stress response. Importantly, the uptake of nanoparticles into cultured cells was restricted to phagosomes; TiO<sub>2</sub> nanoparticles did not enter into the nucleus or any other cytoplasmic organelle. No other morphological changes were detected after 24 hours exposure, consistent with a specific role of mitochondria in this response.

# **CHAPTER 3: STREAM SEGREGATION SCOPING ASSESSMENT FOR A PROPOSED WASTEWATER TREATMENT PROCESS AT FALKE EUROSOCKS**

---

## **3.1 INTRODUCTION**

Falke Eurosocks is an international clothing and lifestyle brand and leg wear market leader. Headquartered in Germany, this textile group produces men's, ladies', and children's knitted socks, ladies' fully fashioned stockings, tights and bodies, menswear and other textile products, which are exported to more than 30 countries. The company has 16 factories worldwide, achieved an annual turnover in 2008 of €195.5 million, and employs over 2 600 people worldwide. The textile company, located in Bellville South, Cape Town, South Africa, currently discharges a single combined effluent stream to the Bellville municipal wastewater treatment works located in Sacks Circle via a discharge sump located on the Falke premises.

Previous research on industrial effluent treatment focused on the development of a unique operations strategy employing laboratory-scale membrane bioreactors for the treatment of wastewaters of industrial origin (WRC 1371/1/07; PCT/IB2008/05033; SA National patent 2009/00398). The process design facilitated a continuous development and acclimation strategy for generating consortia of micro-organisms capable of degrading specific industrial wastewaters. Subsequently, the technology was piloted at Falke and reported in WRC-TT556/12. The current work relates to a new WRC Project (K5/1003376) and refers to previous work outlined in WRC-TT556/12 related to the requirement for a revised stream segregation audit at Falke due to the incorporation of Western Province Yarn Dyers (WPYD), a merger that occurred subsequent to the work published in WRC Report TT556/12.

Historically, Falke's processing plant in Bellville consumed an average of 1 920 kL/month of potable water and discharged 95% (1 820 kL/month) of this as effluent to the municipal sewer. (The municipal effluent discharge tariff is based on a percentage as opposed to direct volumetric measurement). With the recent incorporation of WPYD into the Falke premises, the water consumption patterns have changed with yarn dyeing attributed to 95% of the processing, and direct sock dyeing making up the remaining 5%. Depending on consumer requirements which drive production schedules, in the last financial year effluent discharge volumes have varied between 950 kL/month and 1 800 kL/month. Municipal effluent discharge costs have increased by 84% between 2008 and 2014 (from R5.65/kL to R10.39/kL) and potable water costs have increased by 95% (from R6.95/kL to R13.51/kL).

This study includes a stream segregation scoping assessment for a proposed wastewater treatment process at Falke Eurosocks' factory in Bellville, South Africa.

The objectives of this work were:

- To conduct a review of the Falke factory dye house layout and water consumption as a result of the incorporation of WPYD;
- To qualify the piping and instrumentation layout in order to identify key stream take-off points in terms of a stream segregation audit.

## **3.2 DESCRIPTION OF CURRENT WASTEWATER DISCHARGE INFRASTRUCTURE AT FALKE**

The current wastewater discharge infrastructure at Falke's processing plant in Bellville is limited to an effluent settling tank which feeds into an overflow sump. Wastewater is then discharged from the overflow sump to the

municipal sewage system. Figure 3.1 is a process flow diagram (PFD), representing Falke's existing wastewater discharge process and infrastructure.

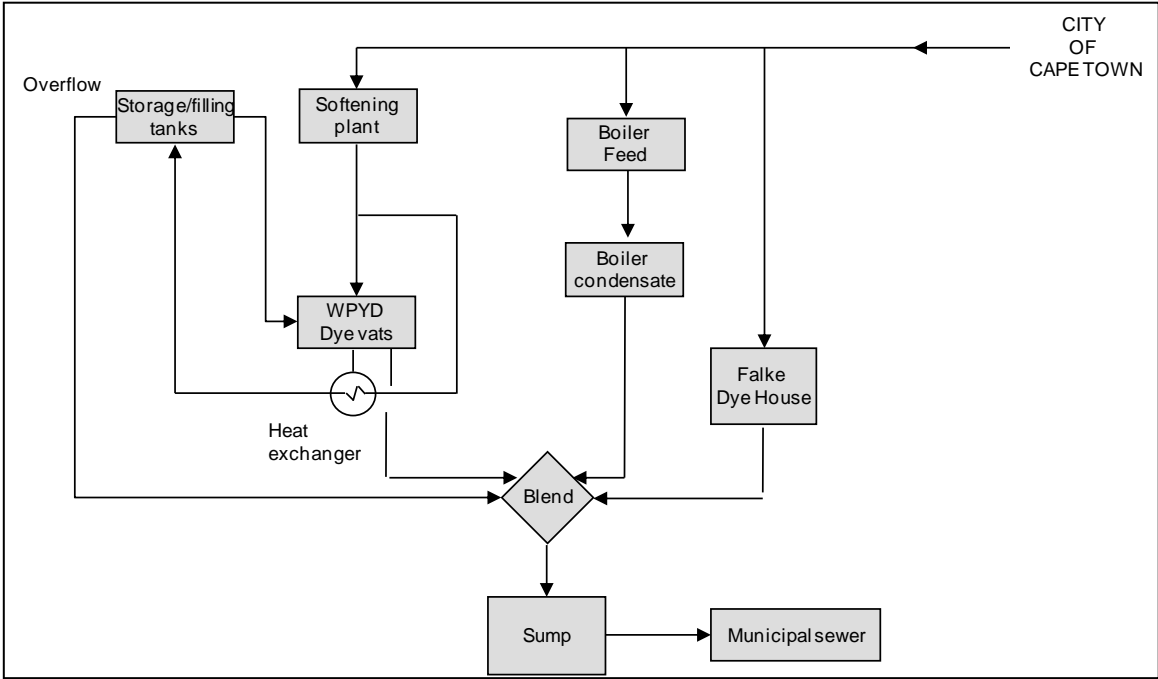


Figure 3.1 Process flow diagram of Falke's existing discharge infrastructure

As indicated in Figure 3.1, all effluent produced at Falke is channelled to the primary settling tank. To date, the water discharged to the municipal system is not within national discharge standards and not of sufficient quality for reuse.

A plant layout diagram which illustrates the relationship between the existing head works and the factory layout before the incorporation of WPYD is shown in Figure 3.2, with the current layout indicated in Figure 3.3. (Photos indicating the WPYD and Falke dye houses as well as the water softening plant located in the alley behind the dye house infrastructure are included in Annexure 1).

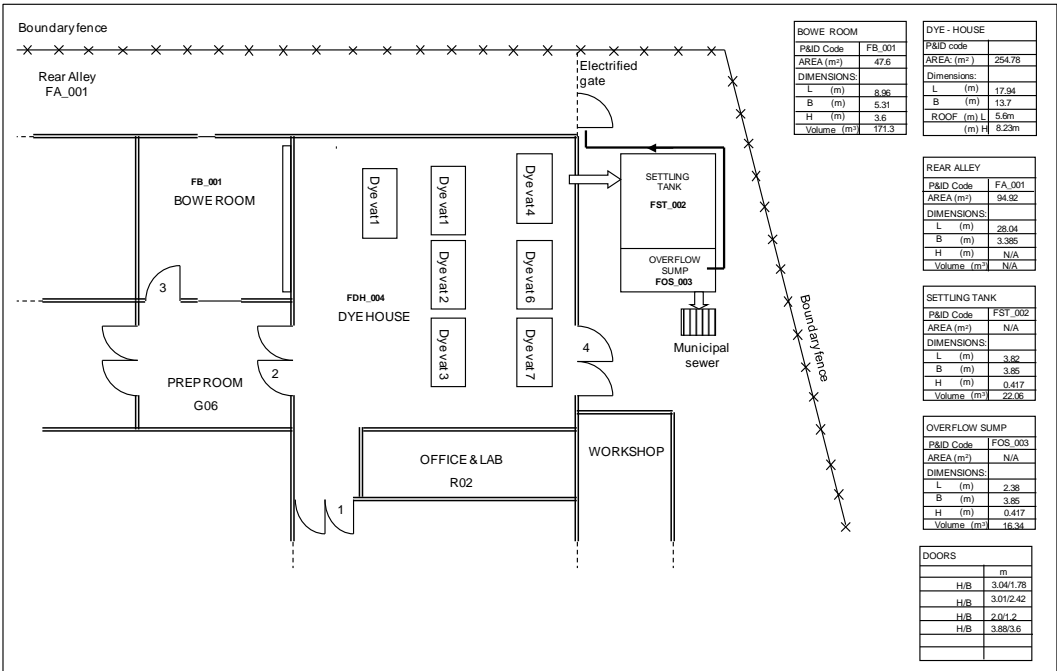


Figure 3.2 Schematic diagram of the factory layout at Falke before the incorporation of WPYD



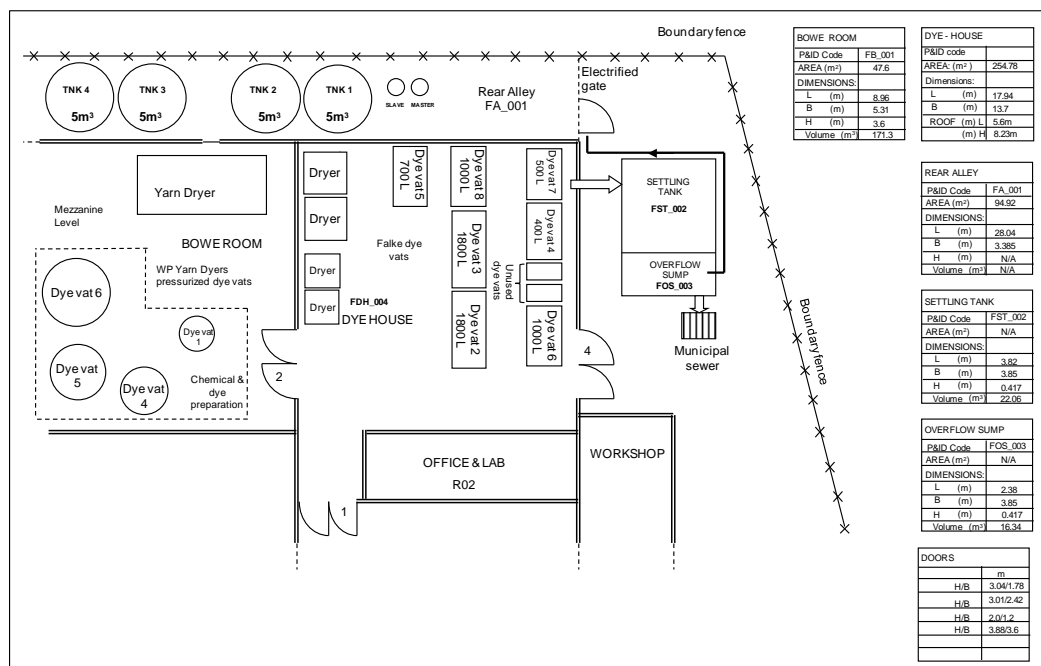


Figure 3.3 Schematic diagram of the current factory layout at Falke after the incorporation of WPYD

### 3.3 STREAM SEGREGATION EVALUATION

#### 3.3.1 Process design and strategy

The proposed wastewater treatment and water recycling process is based on a comprehensive stream segregation audit where the main process effluent streams are segregated based on composition and effluent strength as opposed to an end-of-pipe strategy where all effluent streams are mixed. The proposed treatment process is based on a two-phase strategy which will lead to lower capital expenditure (CAPEX) investment requirements and the ability to recycle a larger volume of effluent once treated.

In Phase 1 of the strategy, the high-volume dye-free effluent streams, identified as part of the stream segregation analysis, are treated using UF (ultrafiltration) to remove particulates and suspended solids. The filtered product stream is then treated using granular activated carbon (GAC) to remove any residual colour and then reused as process water.

In Phase 2 of the strategy, the main dye-containing effluent streams (dye-containing drops), identified as part of the stream segregation analysis described in Figure 7, are treated using UF and NF (nanofiltration) to remove and concentrate the dye fraction of the segregated stream. The concentrated dye fraction (NF retentate) is then treated using nanoparticles and then dewatered for solid waste removal. The NF dye-free permeate is then desalinated using reverse osmosis to remove the high salt content which is then evaporated for reuse in specific dye house processes.

#### 3.3.2 Piping and Instrumentation diagram

Preliminary site layout drawings in Figure 3.4 indicate the associated piping and instrumentation diagrams (P&IDs) for the water softening plant and the WPYD yarn dyeing process. The Falke dye house is currently a gravity-based effluent discharge process where dye drops are discharged into channels located in the flooring of the dye house.

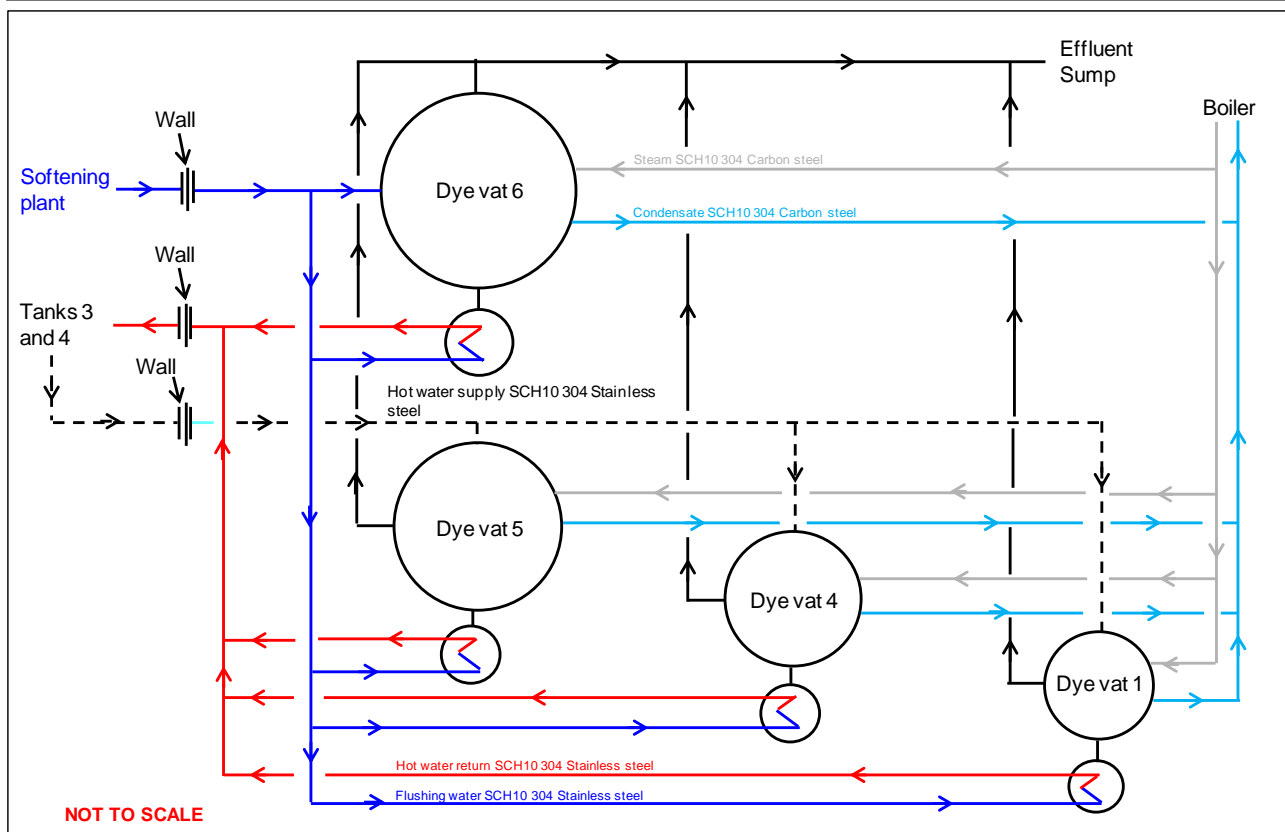
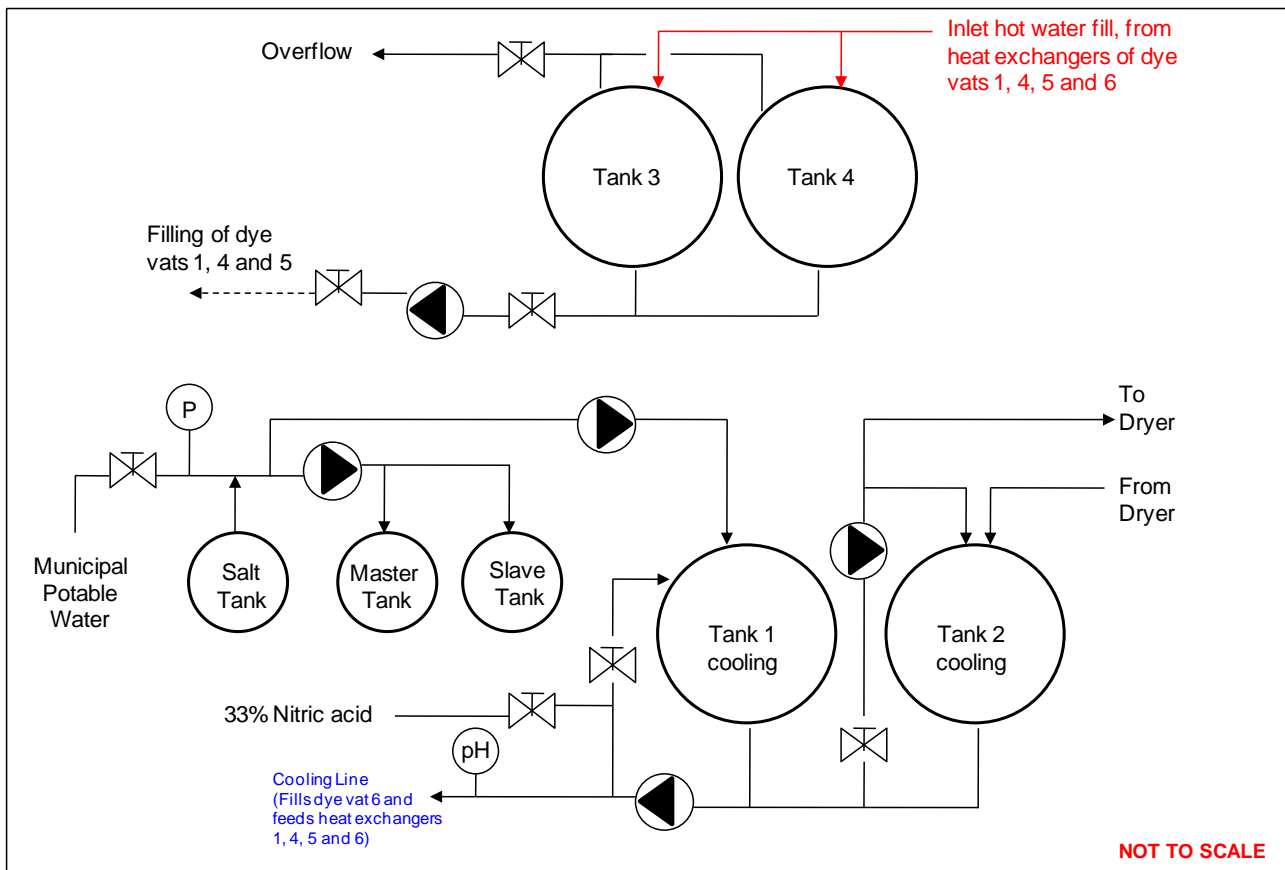
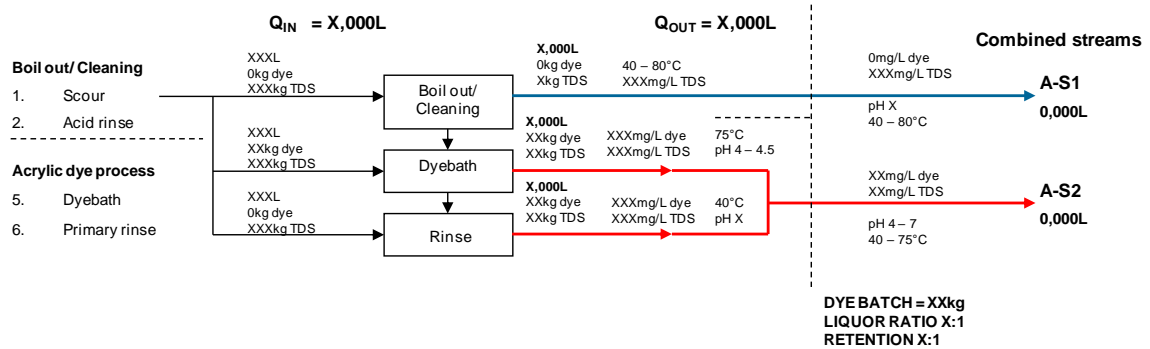


**Figure 3.4 P&ID schematics indicating relationships between dye process streams, heat exchanger infrastructure and the water softening plant**

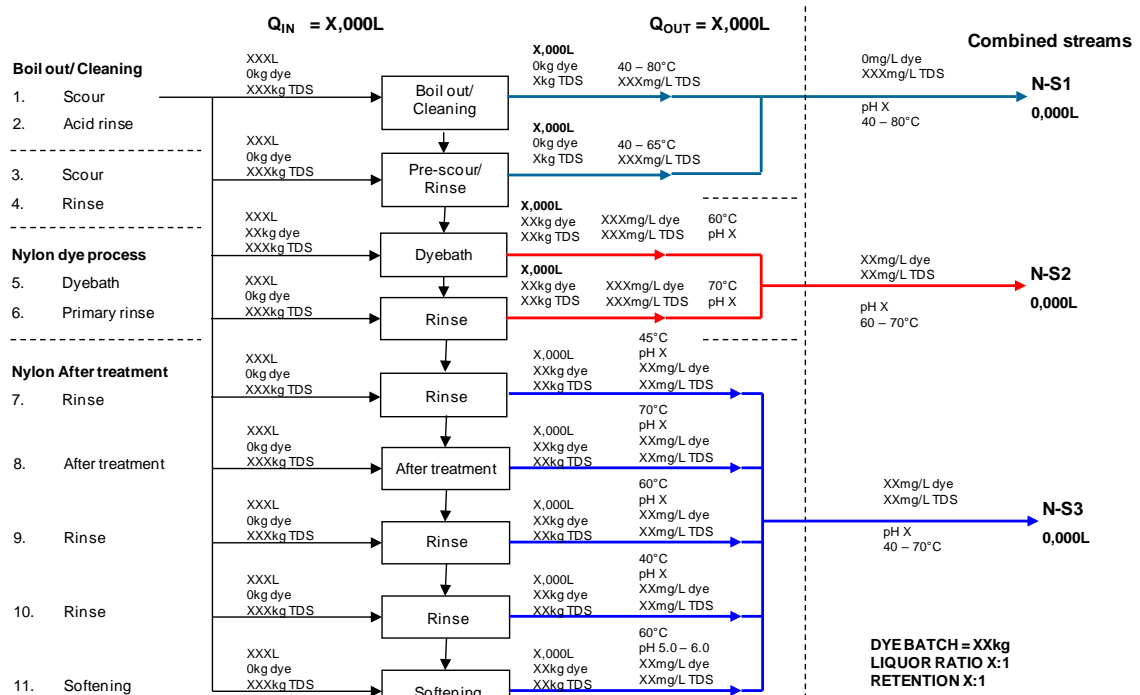
In order to facilitate the stream segregation, 3-way valves will be integrated into the piping infrastructure to separate the streams using a programmable timed event log that needs to be incorporated into the existing

dye vat PLC-based control. Figure 3.5 indicates the stream segregation audit for the various dye processes used for acrylics, nylon, polyester, and cotton.

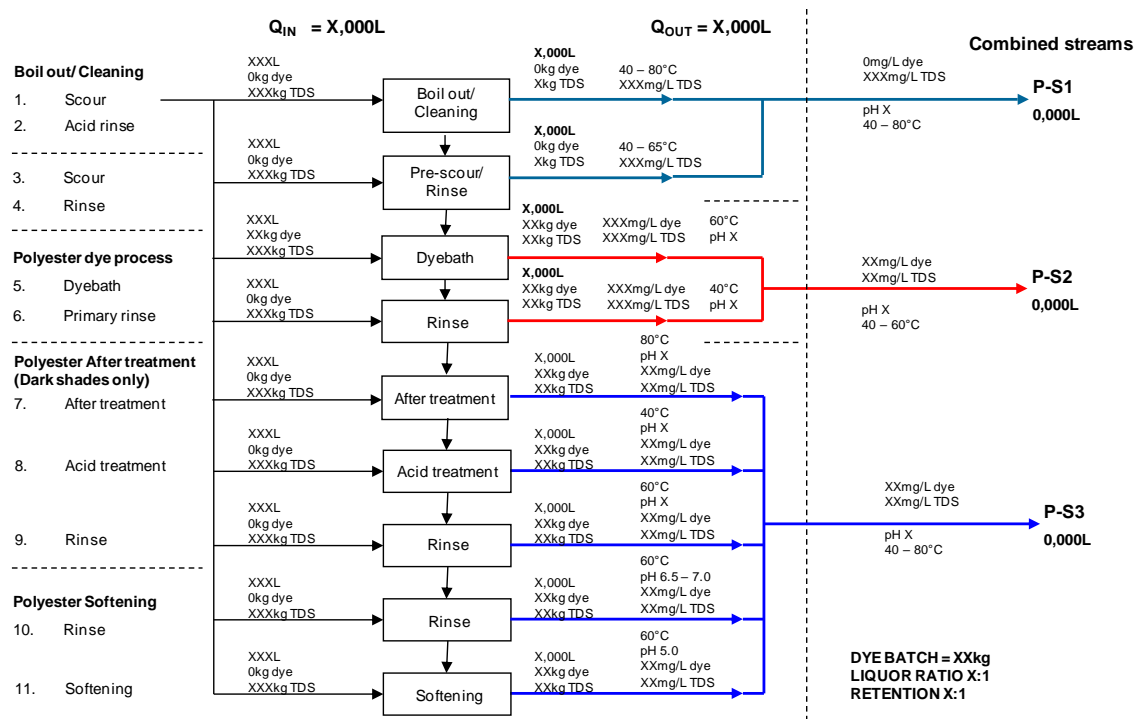
#### FALKE ACRYLIC DYE BATCH PROCESS (BASIC DYE CLASS)



#### FALKE NYLON DYE BATCH PROCESS (ACID/METAL COMPLEX DYE CLASS)



**FALKE POLYESTER DYE BATCH PROCESS  
(DISPERSED DYE CLASS)**



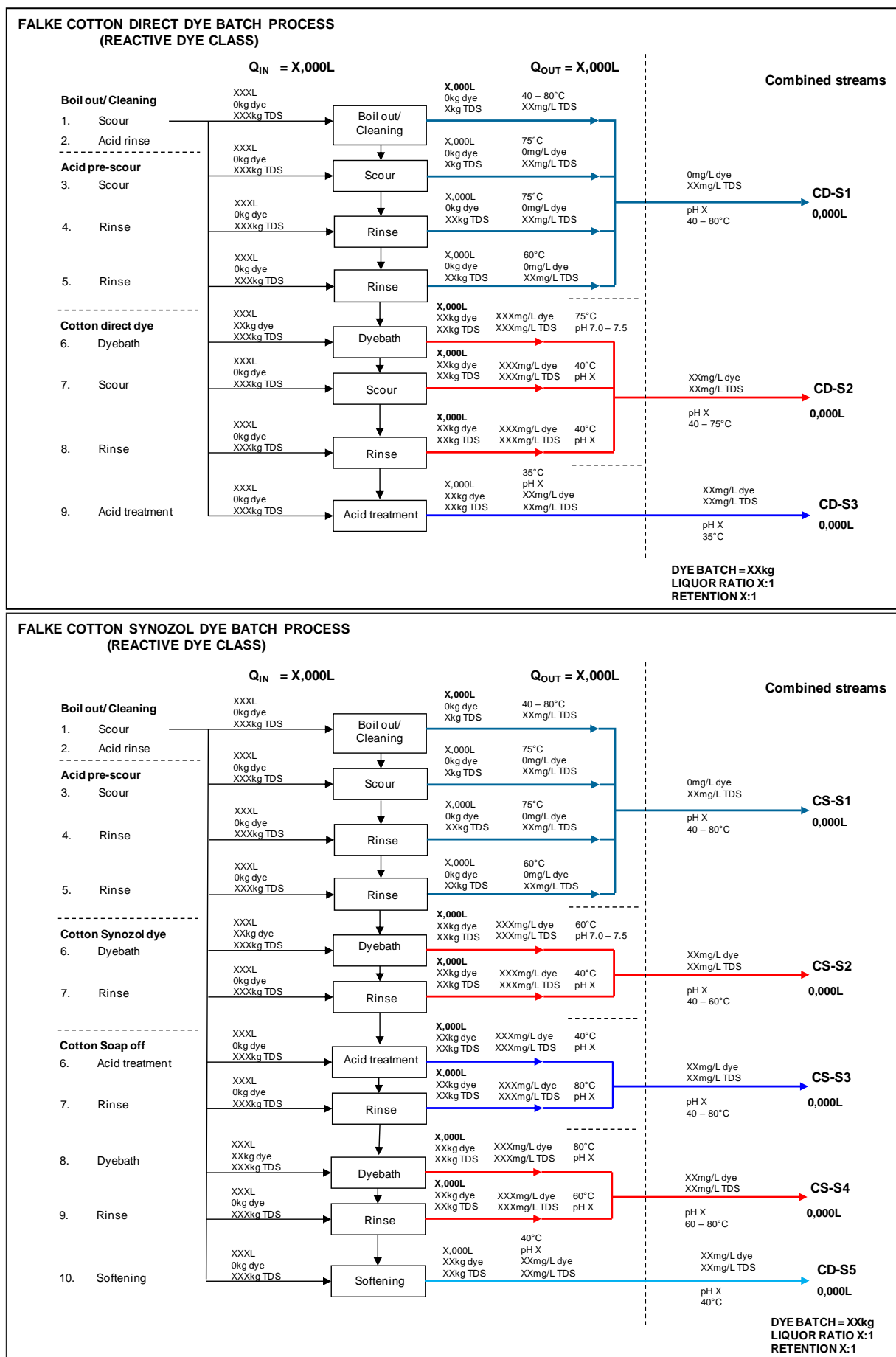


Figure 3.5 Stream segregation audit for acrylics, nylon, polyester, and cotton

Each of the typical polyester and cotton dyeing processes have been segregated according to the recipe-dependant specific number of drops per batch, and segregated into either high-dye (red arrows) or low-dye (light blue) exhaust streams. Initial prewash and preparatory streams are indicated in dark blue.

### 3.4 THE DYES AND DYEING EFFLUENTS FROM FALKE

This section discusses the types of dyestuffs used at Falke Eurosocks which were sampled for WRC K5/2386, and the purpose of the additional additives used in the dyeing processes at Falke Eurosocks.

#### Dyestuffs and additives

Figure 3.6 shows the dyes described in Table 3.1. This is a small reference selection of the more than 50 dye recipes in the sampled Falke dye bath effluents. The aim of presenting this graphic is to illustrate the wide range of dyes used in the textile dyeing process.



**Figure 3.6 Photograph of examples of Falke powder dyes**

Table 3.1 provides details of the randomly selected dyestuffs in the photograph in Figure 3.6. Note that this is just an illustrative limited selection of the more than 50 dyestuff types in the samples supplied to the Technology Station in Clothing and Textiles (TSCT) by Falke Eurosocks. Selective additives from Falke are listed in Table 3.2.

**Table 3.1 Selected dyestuffs from Falke**

No	Trade name	Batch no	Dye type	Fibre type
1	Synozol Yellow HF-4GL 150%	9421	Reactive	Cotton
2	Synocid Brill Flavine E-8GN	9434	Acid	Nylon
3	Bemacron Yellow	9488	Basic	Acrylic
4	Astrazon Golden Yellow GL-E 200%	9837	Basic	Acrylic
5	Synozol Yellow K-3RS	9421	Reactive	Cotton
6	Astrazon Red FBL 200%	9437	Basic	Acrylic
7	Synozol Turq Blue HFG 133%	9421	Acid	Nylon
8	Synoset Black	9497	Metal complex	Nylon

**Table 3.2 Selected additives from Falke**

Trade name	Additive type	Trade name	Additive type
Hydrosulphite	Scouring	Rucofil / AWG	Softening
Sodium acetate	Buffer (dye processing)	Katamin Uni	Softening
Abiologomer	Finishing	Tissocycl RCN	Scouring
Rapidoprint XRN	Washing	Astragal PAN	Retardent
Securon 28	Scouring sequestering agent	Optavon 4UD	Washing
Cetafex ENN	Scouring anti-foam	Stabfix F	Finishing after-treatment
Belfassen Wax	Softening		

A typical dye recipe for acid black consists of the following:

#### Dyeing chemicals

- 1 600 litres Water
- 83.83 kg Nylon yarn on spools
- 5029.8 g Acid black also known as Synoset® black
- 960 g Acetic acid

#### Scouring agents after dyeing

- 1600 g Serbid OL
- 838.3 g Sarabid C12
- 800 g Cefatex ENN
- 1600 g Sodium acetate

#### Dyeing method

Serabid OL® is added to the dye bath water and is kept for 30 minutes at 65°C. Cefatex ENN®, Sarabid C12® and sodium acetate are added to the water and mixed well. The pH is checked before the dye is added to the water and the pH adjusted to between 7 and 8. The dye is then added to the water and mixed well. The stacked yarn spools are then lowered into the dye reactor. The pH is checked and then adjusted to a pH of between 4 and 5.5, using acetic acid. After the dyeing stage, which typically takes 12 hours, the next stage is softening.

#### Softening chemicals/agents

- 838.3 g Stabifix®
- 1600 g Acetic acid
- 838.3 g Katamin®

#### Softening method

The softening bath water is pH stabilised by adding 800 g of acetic acid. Stabifix is dissolved in hot water and added to the bath. The rest of the components are then added to the bath. The yarn is then loaded into the dyeing reactor.

#### Analyses of Falke sump samples

Wastewater quality is usually characterised by global parameters like biological oxygen demand (BOD), chemical oxygen demand (COD), total organic carbon (TOC), total suspended solids (TSS), nitrogen, phosphorus and other contents (Eaton et al., 2005; EPA methods, 1996). The qualitative and quantitative determination of dyes from dyeing effluents is generally carried out using spectroscopic and chromatographic techniques such as inductively coupled plasma optical emission spectroscopy (ICP-OES), ultraviolet and visible spectroscopy (UV-VIS), liquid chromatography coupled to mass spectrometry (LC-MS), high performance liquid chromatography (HPLC), gas chromatography (GC), and ion chromatography (IC), among others. Figure 3.7 shows examples of Falke dye bath drop samples used for dyeing cotton.



**Figure 3.7 Photograph of Falke cotton and polyester dye bath drop samples**

All the wastewater parameters were characterised following the Standard Methods for the Examination of Water and Wastewater (Eaton et al., 2005) except when specified. ICP-OES was used for the determination of heavy metals. IC was used for the determination of selected anions. LC-MS was employed to analyse the textile dye effluents using congo red, reactive black, safranin, methylene blue, methylene violet, xylene orange, eosin yellow, brilliant green, methyl orange, acid black and disperse black as the standard dyes.

Table 3.3 summarises the results of dyeing effluents analysis using methods prescribed for sampling, preservation, testing and analysis of chemicals (Eaton et al., 2005; EPA methods, 1996). The BOD experiments were conducted immediately after sample reception without further preparation. The absence of seeding might have had a higher impact on the BOD due to the presence of halogen ions, as shown by the IC results, which are known to inhibit microorganism growth during incubation. The pH of the samples were either acidic or basic.

### **3.5 CONCLUSIONS**

A stream segregation audit was conducted at Falke to evaluate future water savings through possible stream segregation and treatment options.

A description of the current discharge infrastructure is provided and P&ID diagrams of the relationship between the dye process streams, heat exchanger infrastructure and water softening plant.

The physicochemical parameters for 13 effluents were determined. Only nitrates, cadmium and manganese levels were within the regulatory limits.



**Table 3.3 Physicochemical parameters of industrial dyeing effluents**

Parameters		Samples												
		9392	9434	9462	9464	9436	9437	9419	9439	9423	9435	9421	9448	9451
Sample ID		P1	N1	NM1	NM5	NM2	A1	NM3	P2	P4	C3	C2	P3	C1
pH		4.437	4.494	4.717	4.733	4.827	4.423	4.806	4.472	4.488	4.722	10.416	4.626	11.719
Conductivity (mS)		0.689	1.069	0.942	0.982	2.11	5.83	1.393	1.051	0.941	2.65	91.7	1.846	120.0
Total dissolved solids (TDS) (g/L <sup>-1</sup> )		1.58	1.38	3.68	1.46	2.06	5.25	1.62	3.32	2.50	2.79	73,24	5.45	113,43
Chemical oxygen demand (COD) (mg/L <sup>-1</sup> )		3080	2310	2780	1590	2040	3160	1780	6140	4500	2580	1970	9420	2920
Biological oxygen demand, 5-d, 20 °C, (BOD <sub>5</sub> , 20 °C) (mg/L <sup>-1</sup> )		289	258	270	221	262	267	213	271	226	198	77	129	65
Anions  (mg/L <sup>-1</sup> )	Bromides	52.03	36.65	40.41	45.09	56.07	62.51	55.32	53.03	55.86	61.80	4.44	51.43	-
	Fluorides	-	-	-	-	35,43	44,55	29,72	-	-	-	50,79	-	59,11
	Chlorides	16.59	-	-	-	-	-	-	-	0.056	-	-	-	-
	Nitrites	-	1.18	-	129.7	728.5	-	263.4	0.0879	-	833.2	-	247.9	-
	Nitrates	1.336	-	1.313	1.189	1.866	-	0.262	1.392	1.172	0.528	-	0.329	-
	Sulphates	0.674	0.876	1.155	17.45	-	-	0.819	1.744	1.865	-	52.49	1.66	16.67
Cations  (mg/L <sup>-1</sup> )	Aluminium	0.412	0.737	0.517	0.537	0.472	0.405	0.582	0.567	0.414	0.585	0.434	0.323	0.335
	Cadmium	0.0040	0.0027	0.0027	0.0040	0.0033	0.004	-	0.0013	0.0027	0.0020	0.0013	0.0007	0.003
	Cobalt	-	-	0.112	-	0.0007	0.004	1.181	0.584	-	0.203	0.120	0.031	0.027
	Chromium	0.0593	0.0453	0.095	0.501	0.436	0.168	0.500	0.320	0.0547	0.345	0.193	0.169	0.046
	Copper	0.233	0.239	0.224	0.223	0.227	0.196	0.130	0.164	0.213	0.201	4.44	2.28	0.101
	Iron	0.284	0.447	0.535	0.300	0.343	0.235	0.378	0.630	0.380	0.336	0.214	0.542	0.142
	Manganese	0.0360	0.103	0.191	0.168	0.155	0.184	0.128	0.099	0.0553	0.126	0.0627	0.0087	0.004
	Lead	-	-	0.0147	-	0.0020	0.003	-	-	-	0.009	0.0080	0.0033	-
	Titanium	0.0107	0.0133	0.0107	0.008	0.0153	0.013	0.014	0.019	0.0133	0.0160	0.0167	0.0180	0.019
	Zinc	0.917	0.919	1.189	0.895	0.943	1.901	1.221	0.641	0.789	0.794	0.919	0.533	0.403

## CHAPTER 4: CATALYST DEVELOPMENT AND EVALUATION IN A SLURRY REACTOR

---

In this work, several experimental procedures for the production of nanophotocatalysts are presented based on sol-gel techniques using titanium alkoxides as precursor materials. This chapter describes the synthesis strategies for controlled synthesis of  $\text{TiO}_2$  nanoparticles using batch sol-gel methods and continuous hydrothermal synthesis as well as the synthesis of a heterojunction  $\beta\text{-FeOOH}/\text{TiO}_2$ . Nanoparticles have an advantage over micron-sized particles in catalytic reactions due to the higher surface area, narrowing of the band gap due to another element creating a mixed metal oxide (MMO) and/or the narrowing of the band gap as the size of the nanoparticle approaches the Bohr radius. The methods presented here focus on the effect of process conditions on particle shape, crystalline phase and doping with an iron-based heterojunction to reduce the band gap of the  $\text{TiO}_2$ . This report includes a comparison of the results on a model dye methyl orange, methylene blue and two industrial Falke sump and NF concentrate samples, using  $\text{TiO}_2$  and  $\beta\text{-FeOOH}-\text{TiO}_2$  catalysts in a slurry reactor.

### 4.1 PREPARATION OF $\text{TiO}_2$ NPS CONSISTING OF VARIOUS POLYMORPHS USING SOL-GEL/HYDROTHERMAL SYNTHESIS

The fundamentals of  $\text{TiO}_2$  synthesis parameters which require greater understanding for optimum nanoparticle size are the type of Ti precursors, peptizing agent (acid), reagent concentrations and hydrothermal treatment duration and temperature. Chen et al. (2011) synthesised pure rutile  $\text{TiO}_2$  nanorod particles using the standard sol-gel method followed by hydrothermal treatment. Titanium (IV) n-butoxide was used as the Ti precursor and added drop wise under magnetic stirring for the formation of the sol in the presence of hydrochloric acid. It was found that at 3 M HCl concentration pure nanorod rutile nanoparticles were obtained. A set hydrothermal temperature with variations in hydrothermal treatment duration, from 1 to 24 hours was studied. It was concluded that for shorter hydrothermal treatment durations, smaller nanorods were synthesised and that particle size increased with increasing synthesis duration. A major limitation of this method was the duration of 72 hours sol-gel formation time (Chen et al., 2011).

The effects of alkoxide type (ethoxide, propoxide, isopropoxide, and butoxide), temperature, and use of alcohol (ethanol, propanol, isopropanol, and butanol) on the formation of stable  $\text{TiO}_2$  nanoparticle synthesis were investigated by Vorkapic and Matsoukas (1998). Experiments were performed by synthesising a sol in either purified water or a water alcohol mixture in a warm bath in temperatures varying between  $0^\circ\text{C}$  and  $90^\circ\text{C}$ . Titanium alkoxides were added drop wise into the mixture under magnetic stirring until a specific molar ratio of  $[\text{H}_2\text{O}]:[\text{Ti}]$  was reached in the presence of nitric acid. The results showed that titanium ethoxide formed the largest diameter nanoparticles, while titanium isopropoxide synthesised the smallest nanoparticles. Nanoparticle size increased with increasing concentrations of alcohol. A limitation of this work by Vorkapic and Matsoukas (1998) was that amorphous  $\text{TiO}_2$  nanoparticles were formed and only one acid was studied.

Wu and co-workers (2002) studied the use of variations of acids, their concentrations, varying in reaction temperatures and duration at the hydrothermal stage of the synthesis for sol-gel synthesis of pure rutile and anatase  $\text{TiO}_2$  nanoparticles. They also studied the effect of adding NaCl salt to gel before on particle size during hydrothermal treated. Titanium (IV) n-butoxide as the Ti precursor was used and added drop wise under magnetic stirring for the formation of the sol. The acids used were hydrochloric acid, nitric acid, sulphuric acid and carboxylic acid. Acid concentrations varied between 0.5 and 1.5%. It was found that using hydrochloric acid at 1.5 molar pure rutile  $\text{TiO}_2$  nanorods were formed, and using nitric acid, that and mixture of rutile and anatase nanoparticles formed. Pure anatase nanoparticles were synthesised for both sulphuric and carboxylic acid peptization agents of 1.5 molar. The titanium precursor concentration was varied between 0.25 and 0.5 molar and 0.25 molar was found to be optimum for the formation of rutile nanoparticles. The hydrothermal treatment temperatures used were 100, 140 and  $220^\circ\text{C}$  and the reaction durations were 5, 10, 20 and 72 hours. This work provided an in depth understanding of the effects of temperature and phase transformation,

but only for the hydrothermal treatment stage of the synthesis. No effort was made to decrease the sol-gel synthesis time to decrease the overall synthesis duration (Wu et al., 2002).

Hsu and Nacu (2003) studied the effect of HCl concentration (at 0.15 M and 0.77 M) on formation of  $\text{TiO}_2$  nanoparticles. No hydrothermal treatment was used in this study. It was found that  $\text{TiO}_2$  particle size decreased with increasing HCl concentration, decreasing the standard size deviation of particle size distribution. Hydrothermal treatment is important as it provides synthesised material with the needed kinetics for easy of transformation in morphology, with an added benefit of controlling particle size (Wu et al., 2002; Merrsews and Israel, 1976; Zhang and Banfield, 2005). As stated earlier, So et al. (1997) explain how stable sols that are hydrothermally treated at low temperatures will behave, and how unstable sols when hydrothermally treated form rod-like particles (So et al., 1997).

The experimental procedure for this work was derived from the studies by Chen et al. (2011), Wu et al. (2002) and Hsu and Nacu (2003). The use of HCl for the synthesis of  $\text{TiO}_2$  nanoparticles has been reported in a number of studies (Wu et al., 2011; Chen et al., 2011; Reyes-Coronado et al., 2008; Hsu and Nacu, 2003; Wu et al., 2002).  $\text{TiO}_2$  (110 and 001) plane growth can be suppressed and promoted with the use of the Cl-ion of HCl (Reyes-Coronado et al., 2008; Hosono et al., 2004). Increased concentration of HCl acid was selected to promote smaller standard particle size distribution for synthesis at shortened synthesis duration. The use of titanium isopropoxide as the titanium precursor in this work was based on the results by Vorkapic and Matsoukas (1998) as well as its cost effectiveness to evaluate if the acid concentration could be used to control the polymorph structure of the resulting  $\text{TiO}_2$ . Furthermore, understanding the impacts on crystal size and size distribution is needed for morphology control.

#### 4.1.1 Experimental method for sol-gel synthesis and hydrothermal treatment

All experiments were repeated two or three times to ensure reproducibility.

##### Synthesis of the sol

For synthesising the sol, 11 ml of titanium (IV) isopropoxide ( $\text{Ti}(\text{O-Iso})_4$ , ACROS), as Ti precursor, was added, at a rate of 1 ml per second, with a peristaltic pump (Watson Marlow. 505S) into a set volume of 50 ml of hydrochloric acid (HCl, C.J.LABS) as homogenous catalyst, under magnetic stirring (SCILOGEX. MS7-H550-Pro), until a clear solution or sol was formed. The HCl acid concentration was varied between 3, 4 and 5 molar for sol synthesis.

##### Synthesis of the gel

After forming the sol, it is vital to commence with the second stage otherwise the sol will undergo hydrolysis with the ambient moisture in the air. The pH of the solution was not altered after the sol was formed. The  $\text{TiO}_2$  gel is achieved by hydrolysis, followed by simultaneous polycondensation. Previous work showed that the smallest nanoparticles obtained for a Ti ion to water ratio was 0.25:1 M (Chen et al., 2011). Thus 150 ml of purified water (Lasec, Purewater300) was added using a peristaltic pump under constant stirring, over a variety of gel formation times of 12, 24, 48 and 72 hours. When an opaque white gel is visible within the glass beaker, the gel has been formed (Figure 4.1).



**Figure 4.1 Amorphous  $\text{TiO}_2$  gel before hydrothermal treatment**

### Hydrothermal treatment procedure

Gel formation was followed by hydrothermal treatment for 1 hour at 220°C to promote crystallization of amorphous gel. The 250 ml glass beaker was emptied into a one litre Teflon liner which was inserted into the hydrothermal reactor (Figure 4.2). The temperature controller (GEFRAN 800P AND 600 controllers) was set to increase the temperature of the gel mixture by 2°C per minute, until a reaction temperature of 220°C was reached. An oscillation band of  $\pm 2^\circ\text{C}$  was set to avoid runaway temperatures. The reaction temperature was recorded using a data logger (Testo 176T2 logger).



**Figure 4.2 Hydrothermal reactor used for the conversion of amorphous  $\text{TiO}_2$  nanoparticles to crystalline  $\text{TiO}_2$  nanoparticles**

After the set time of hydrothermal treatment, the supernatant liquid was decanted and the residual solids washed several times with water and ethanol and then dried in an oven at 150°C. In addition, the effect of hydrothermal treatment time on the growth of particles produced at shorter sol-gel formation times was also investigated for times of 2, 4, 6, 8, 10, 12 and 20 hours.

### Particle characterisation

High resolution transmission electron microscopy (HRTEM) was conducted at the University of the Western Cape's Electron Microscopy Unit to determine the particle size, size distribution and shape. A Tecnai G2 F20 X-Twin Mat200 kV Field Emission HRTEM (operated at 200 kV) was utilised. The  $\text{TiO}_2$  sample was dispersed in 10 ml of ethanol, sonicated for 20 minutes and pipetted onto the copper-coated carbon grid. X-ray diffraction was used to study the crystal structure of the  $\text{TiO}_2$  synthesised and tests were conducted at the University of Cape Town's Department of Geological Sciences. A small amount (less than 1 g) of each sample was prepared by fine grinding with a mortar and pestle into a powder. The powdered sample was placed in a sample holder and loaded into an XRD for analysis. The instrument used was a Philips PW 1390 XRD, which uses a copper K- $\alpha$  x-ray tube with x-ray wavelength of 1.542 Å, accelerating voltage of 40 kV and a current of 25 mA. Bragg  $2\theta$  angles between  $3^\circ$  and  $70^\circ$  were used for analysis. A continuous scan step size of  $0.025^\circ$  was applied with a scan step time of 0.5 seconds. Qualitative analyses were conducted using X'pert Highscore software.

## **4.1.2 Results and discussion of $\text{TiO}_2$ nanoparticles using a sol-gel/hydrothermal**

### **4.1.2.1 Particle shape and size**

Figure 4.3 shows the change in particle shape with change in gel formation time. Transformation and stability of phase has been found to be dependent on particle size in the ranges of 11-35 nm (Zhang and Banfield, 2000). Shapes identified in order of decreasing gel formation time are nanorods at 72 and 48 hours and 24 hours large were rod-like, smaller mixed shaped particles and thereafter a mixture of elliptic and spherical particles formed. It is evident that only gel formation time affects particle shape. Similar results were seen for

work performed by So et al. (1997), using titanium isopropoxide, isopropanol and nitric acid to alter the  $\text{H}_2\text{O}$ /titanium isopropoxide ratio with varying hydrothermal times.

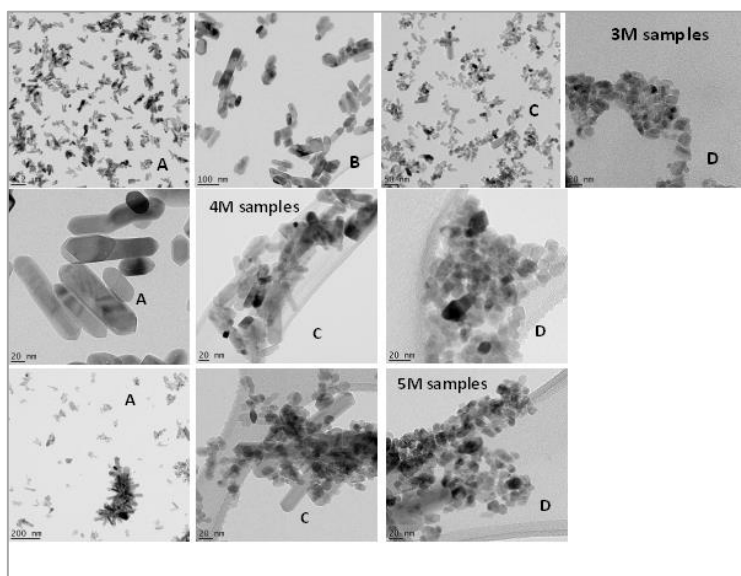


**Figure 4.3 Evolution of  $\text{TiO}_2$  nanoparticle shape for a 3, 4 and 5 M HCl concentration and gel formation time of 72 (A), 48 (B), 24 (C), and 12 (D) hours**

Figure 4.4 presents the effects of HCl concentration and gel formation time on particle size. The length and/or diameter were measured for 200 particles produced under each set of process conditions. The effect that HCl has on particle size is best seen for 72 hours' gel formation time where the size decreases by 29% for 4 M. 66% for 5 M change in particle size compared to 3 M. The change in particle size from 72 hours to 12 hours was more pronounced for 3 M and 4 M HCl acid concentrations compared to 5 M HCl. The average particle size for 12 hours' gel formation time was  $\approx 15$  nm for all samples. The maximum particle size for 3, 4 and 5 M was approximately  $80 \pm 8$  nm,  $60 \pm 8$ , and  $30 \pm 5$  nm respectively. Acid concentration also proved useful in particle size control at higher gel formation times.

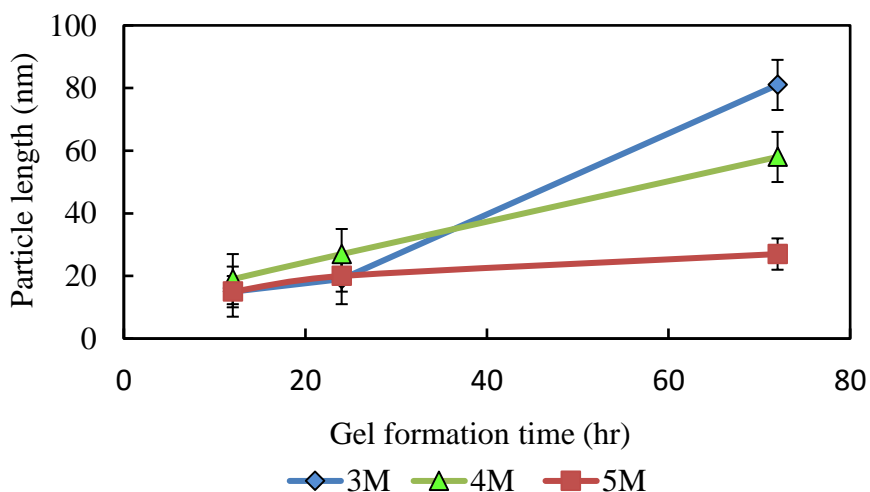


**Figure 4.4 Effect of gel formation time and concentration of HCl acid on particle size**

#### 4.1.2.2 Effect of acid concentration and gel formation time phase of TiO<sub>2</sub> nanoparticles

According to Wu et al. (2002), where several homogenous acids were used to synthesise TiO<sub>2</sub>, it was found that synthesis in a HCl medium forms pure rutile nanoparticles. However, the formation of pure rutile was dependent on a concentration of HCl greater than 1.5 M at a constant gel formation time of 72 hours. Figure 4.5 presents the transformation of TiO<sub>2</sub> nanoparticles for gel formation times ranging from 72 to 12 hours in the presence of 3, 4 and 5 M HCl. Pure rutile was formed at 72 and 48 hours. Additional peaks to that of rutile were observed in the XRD pattern at 25°, 37°, 48° (2 Theta) for 24 and 12 hours, indicating the presence of brookite and anatase polymorphs. Increasing the HCl concentration to 4 M and 5 M did not suppress the formation of other TiO<sub>2</sub> phases.

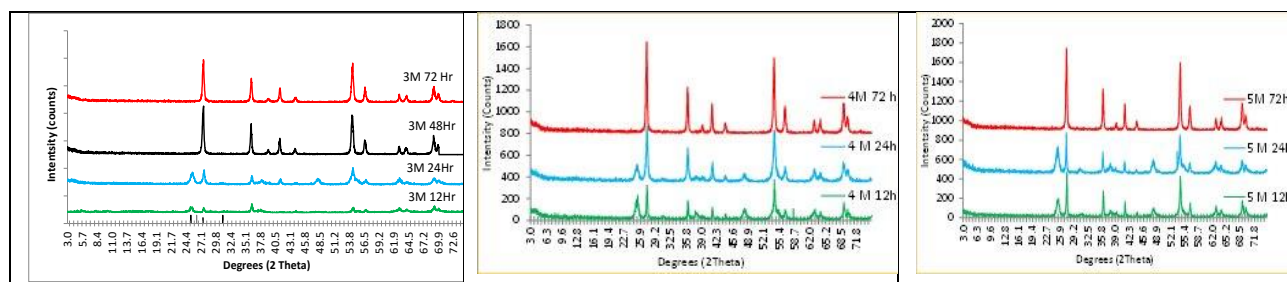


**Figure 4.5 XRD patterns of TiO<sub>2</sub> nanoparticles for various gel formation times for 3, 4 and 5 M HCl**

The intensity of the peaks was analysed for each HCl concentration at different gel formation times, to quantify the percentage of each phase formed in the sample. Figure 4.6 presents the quantity of rutile formed for 72 to 12 hours' gel formation time for three HCl concentrations used. At 72 hours, only pure rutile was formed, regardless of the HCl concentration. This agrees with the findings of Wu et al. (2002) that pure rutile will be formed at a HCl concentration greater than 1.5 M, (though they only tested up to 2 M HCl), and Chen et al. (2011) who extended the HCl range to 3 M. The trend for rutile formation for 3 and 4 molar HCl is very similar. The percentage of rutile obtained at 24 hours was 90% and 82% respectively for 3 M and 4 M HCl. A further reduction in gel formation time to 12 hours led to a significant drop in the percentage rutile to 28% and 42% for 3 M and 4 M respectively. A contrast was observed for 5 M HCl. At 24 hours, the percentage of rutile obtained was only 52%, a significant drop from that produced at 72 hours, but remained approximately constant towards 12 hours.

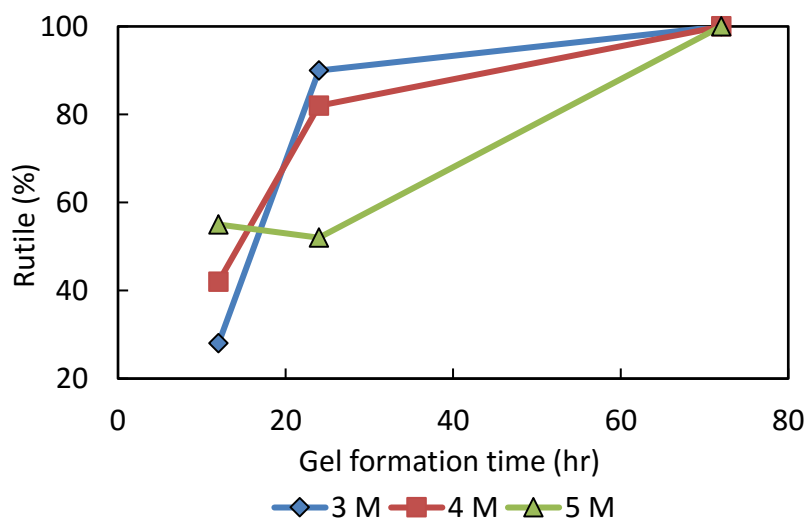


**Figure 4.6 Percentage rutile formed for increasing HCl concentration and gel formation time**

Figure 4.7 presents the evolution of  $\text{TiO}_2$  polymorphs formed with increasing HCl concentration for gel formation times of 24 and 12 hours. It is evident that brookite and rutile were dominant, with anatase percentages of up to 15%. Li et al. (2007) suggested that brookite was an intermediate phase of anatase and rutile depending on the energy available. Brookite, when hydrothermally synthesised, can deform from rutile when too little energy is supplied or solution pH is too high, and deform from anatase where too much energy is supplied or solution pH is too low (Li et al., 2007). However, situations were described where brookite is not only an intermediate phase, but become more dominant. as in this study. Pottier et al. (2001), found that high  $\text{Cl}^-$  ion concentration and high acidity of solution will favour brookite formation to that of anatase which is favoured by sulphate ions and lower acidity.

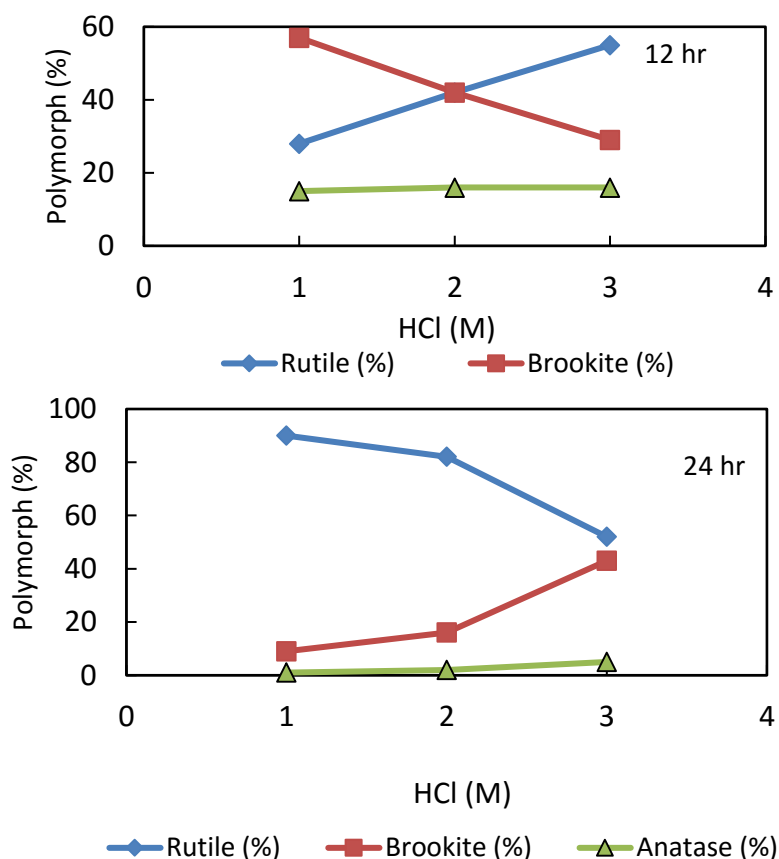


**Figure 4.7 Phase transformation of  $\text{TiO}_2$  for with HCl concentration at gel formation times of 24 and 12 hours**

In this work, at 12 hours for 3 M HCl, a brookite-rich sample was obtained which transformed into a rutile-rich sample at 24 hours. This is supported by Hu et al. (2003) who reported that large volumes of brookite provide more nucleation sites which provide a higher reaction rate and assist in anatase and brookite transformation to rutile. Increasing the HCl concentration to 4 M resulted in the same transformation mechanism but with a 5% reduction in the final percentage of rutile obtained. However, a significant reduction of 30% rutile is seen at 5 M HCl. Reye-Coronado et al. (2008) proposed that, in contrast to anatase formation that is dominated by surface energy effects, rutile and brookite formation is driven by continuous dissolution and precipitation which is favoured by highly acidic conditions. This may well be the reason for the significant reduction in rutile and increase in brookite in this work at 5M HCl, and this mechanism warrants further investigation. Using acid concentration as a means for polymorph manipulation is only effective at gel formation times less than 72 hours. With an increase in HCl concentration at 24 hours' gel formation time a reduction in initially rutile-rich sample is seen; furthermore, virtually equal proportions of rutile and brookite are observed for 5M HCl. At 12 hours' gel formation time, rutile growth is dependent on acid concentration; however, with increased gel formation time a reduction in dependency of acid concentration is observed. It provides a mechanism to prepare either brookite-rich, rutile-rich or equal proportions of rutile and brookite. However, anatase growth is



independent of the acid concentration for 24 and 12 hours' gel formation time, with a maximum yield of 5% and 15% respectively. This work suggests that a much greater HCl concentration than 5 M will be needed to suppress anatase growth and formation, compared to the 1.5 M suggested by Chen et al. (2011).

#### 4.1.3 Photocatalytic properties of batch-produced TiO<sub>2</sub> multi-polymorph powders

This section evaluates the effect of synthesised TiO<sub>2</sub> NPs on the photodegradation of methylene blue (MB). Initially the effects of MB degradation by UV light without P25 and P25 without UV light were evaluated. The effects of phase, size and shape of pure rutile (synthesised at 3M 72 hours), pure anatase (commercially available from Sigma), P25 and synthesised TiO<sub>2</sub> (synthesised for 3M, 4M and 5M at 24 hour and 12 hour gel formation time) were evaluated thereafter.

Figure 4.8 presents the degradation of methylene blue in the presence of various catalysts with UV light irradiation for 120 minutes. Pure rutile, anatase and P25 were used as standards for comparison with synthesised mixed-phase TiO<sub>2</sub>.

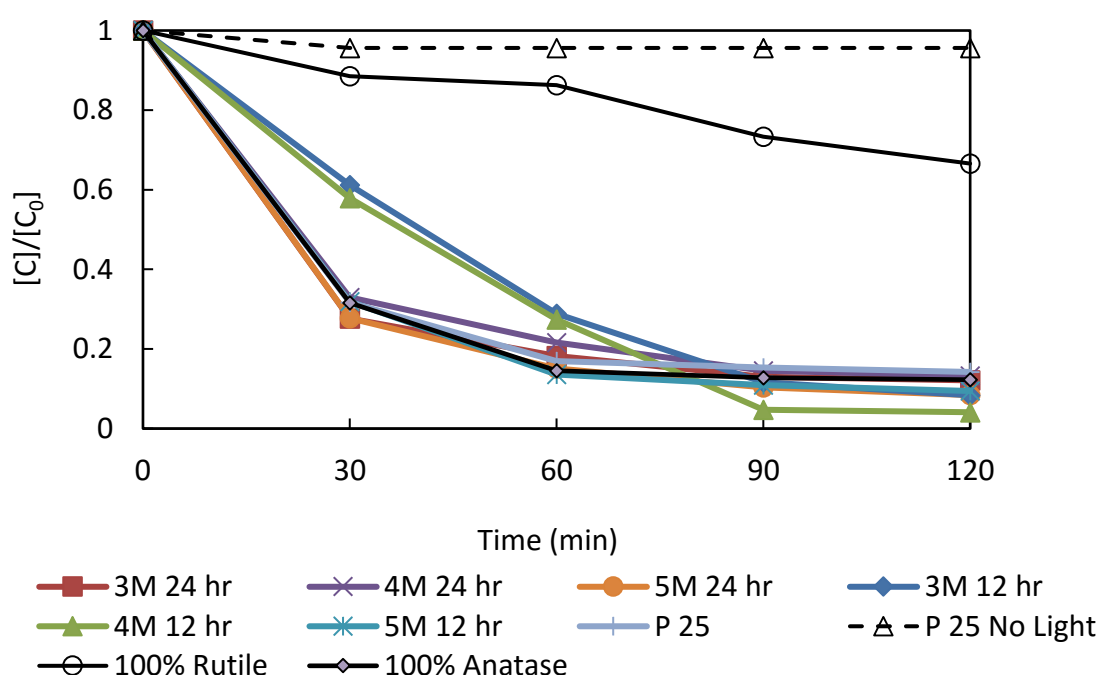


**Figure 4.8 Degradation of methylene blue in the presence of various catalysts**

The effect of UV radiation only showed 13% degradation of MB, with a reaction rate of 0.053 min<sup>-1</sup>. Thomas and Burgess (2007) found that degradation of organic dyes in the presence of UV light was possible; however, this will take a longer time than when in the presence of a photocatalyst. P25, in the absence of UV light, was shown to degrade 5% of MB within 30 minutes and remain constant until 120 minutes, with a reaction rate of 0.0182 min<sup>-1</sup>. This work is in agreement with the findings of Su et al. (2006) who showed that photocatalysts can absorb a percentage of dye on a particle surface. Furthermore, if a catalyst is present, it is observed that phase and percentage of phase is vital for improved photocatalytic efficiency. The effect of pure rutile, pure anatase and P25 in the presence of UV light on the degradation reaction was then evaluated for 120 minutes. A 35% change in MB concentration is observed when irradiating in the presence of pure rutile, with a reaction rate of 0.139 min<sup>-1</sup>. According to Liao and Liao (2007), the pure rutile phase is known to be the least photocatalytically active of the three polymorphs. An 88% change in MB concentration is observed when irradiating in the presence of pure anatase, with a reaction rate of 0.365 min<sup>-1</sup>. According to literature (Kim et al., 2005; Liao and Liao, 2007; Scanlon et al., 2013), the anatase phase is known to be the most photocatalytically active of the three phases. This can be accounted for by the surface chemistry, in that



anatase has a high concentration of OH<sup>-</sup> ions at the surface of the nanoparticle, which are released as a hydroxide radical on UV light irradiation, as found by Bischoff and Anderson (1995). According to literature (Andersson et al., 2002; Cozzoli et al., 2003; Su et al., 2006; Dong et al., 2010), anatase is more photocatalytically active than rutile. Multi-polymorph TiO<sub>2</sub> has received great attention as it was found to be more efficient than single-polymorph TiO<sub>2</sub>. for different reaction conditions (Andersson et al., 2002; Lachheb et al., 2002; Testino et al. 2007; Di Paola et al., 2008; Gupta and Tripathi 2011; Gupta and Tripathi 2012; Krivec et al., 2013; Scanlon et al., 2013). An 86% change in MB concentration is observed when irradiating in the presence of P25 (20% rutile and 80% anatase, according to MSDS of Degussa Company), with a reaction rate of 0.357 min<sup>-1</sup>. Similar results are observed for pure anatase and P25; this contradicts findings by Testino et al. (2007). Where different phase mixtures were compared with P25. However, P25 is observed to be more photocatalytically efficient than pure rutile and similar results were found by Testino et al. (2007) and Di Paola et al. (2008). Phase percentage and size of synthesised TiO<sub>2</sub> are presented in Table 4.1.

**Table 4.1 Catalyst size, phase and photocatalytic activity**

TiO <sub>2</sub> sample	Average particle length (nm)	Average particle diameter (nm)	Phase percentage (%)			Reaction rate constant k <sub>a</sub> (min <sup>-1</sup> )	Initial pH
			Rutile	Anatase	Brookite		
3M 72 Hours	81±8	29±5	100	-	-	0.139	3.61
3M 48 Hours	60±9	20±6	100	-	-	-	-
3M 24 Hours	19±4	11±3	90	1	9	0.366	3.25
3M 12 Hours	15±4	10±3	28	12	60	0.382	3.68
4M 72 Hours	58±8	27±5	100	-	-	-	-
4M 24 Hours	27±5	14±3	82	2	16	0.361	3.38
4M 12 Hours	19±4	10±3	42	16	42	0.399	3.42
5M 72 Hours	27±5	15±3	100	-	-	-	-
5M 24 Hours	20±4	12±3	52	5	43	0.382	3.38
5M 12 Hours	15±4	12±3	55	16	29	0.386	3.55
P 25	21		20	80	-	0.357	4.38
Pure anatase	<25		-	100	-	0.366	6.39

It is noted that the addition of anatase does not equate to a remarkable increase in photocatalytic reactivity. For example, the sample with 1% anatase and 9% brookite improved photocatalytic activity by 55%. The sample with 16% anatase and 29% brookite improved photocatalyst activity by 58%. This work agrees with the findings of Kandiel et al. (2013), where it was found that brookite was more photocatalytically efficient than anatase for degradation of methanol. An increase in photocatalytic activity efficiency is observed when using a mixed-phase photocatalyst, with an increasing brookite percentage and decreased average particle size. In the presence of catalysts synthesised for 12 hour gel formation time at varying HCl concentrations and irradiated for 120 minutes, changes in MB concentration and reaction rates were 92%, 96%, 91% and 0.3818, 0.3995, 0.3859 min<sup>-1</sup> for TiO<sub>2</sub> synthesised at 3 M, 4 M and 5 M HCl respectively. This can be accounted for by the increase of brookite phase by 51%, 26% and 14% for 3 M, 4 M and 5 M respectively. This work is in agreement with the findings by Jang et al. (2001), Li et al. (2007) and Testino et al. (2007), where the particle size and phase percentage of the TiO<sub>2</sub> nanoparticles will affect the rate of decomposition of bacteria and industrial textile dye respectively. For varying mixed-phase percentages of rutile and brookite, it is observed that increasing the brookite phase percentage by 9% will dramatically increase the photocatalytic efficiency of rutile. Rutile-rich mixed-phase TiO<sub>2</sub> was found to be more photocatalytic active than P25, pure anatase phase and pure rutile. This can be accounted for greater band gaps available by the three phase of TiO<sub>2</sub> for electrons to readily create radicals, as found by Testino et al. (2007) and Yan et al. (2007) and further explained by Li et al. (2007) and Gupta and Tripathi (2011). This work is in agreement with that of Testino et al. (2007) and Di Paola et al. (2008), where brookite was found to have high photocatalytic efficiency; however, rutile and brookite mixed-phase photocatalysts were more efficient with decreased rutile phase percentage (for

photocatalysts consisting of all three phases). This can be due to the synergy of the three band gaps being available to be excited by UV light, as found by Gupta and Tripathi (2011) and Testino et al. (2007). Methylene blue was photodegraded in the presence of three (rutile-rich) catalysts, synthesised using a 24 hour gel formation time and varying HCl concentrations. Changes in MB concentration and reaction rates were 88%, 87%, 92% and 0.3662, 0.3614, 0.3816 min<sup>-1</sup> for TiO<sub>2</sub> synthesised at 3 M, 4 M and 5 M respectively. The change in photocatalytic reaction rate can be accounted for by the decrease in rutile percentage from 3 M to 5 M (from 90% to 55%) and particle size for 3M and 5M. 18 nm to 20 nm). Similar trends for photocatalytic efficiency were found by Yang et al. (2005) as changes in phase percentage of anatase-rich particles with varying particle size were observed. Yan et al. (2007) found TiO<sub>2</sub> of mixed phased with varying phase percentages to have greater photocatalytic activity than pure phase. This was true for synthesised and physically prepared mixed phase of varying phase percentages.

## 4.2 CONTINUOUS HYDROTHERMAL SYNTHESIS (CHS) OF TiO<sub>2</sub> NANOPARTICLES

Very few authors have reported the synthesis of titanium dioxide nanoparticles using a continuous flow reactor. Therefore, little data exist to compare with the findings in this study. Kawasaki et al. (2009) synthesised TiO<sub>2</sub> particles in the range of 13-30 nanometres using Ti(SO<sub>4</sub>)<sub>2</sub> as a precursor, reporting high conversions of 99% for all experimental runs. They studied the effect of KOH concentration, temperature and residence time on the resulting average particle size and crystallinity. By altering the KOH concentration between 0.253 and 0.273 mol/L, they were able to control the average particle size between 13-30nm. All particles were found to be anatase phase TiO<sub>2</sub> as determined through XRD, and an increase in KOH concentration was also found to promote an increase in crystallinity. The effect of temperature was studied at 400, 450 and 500°C and it was found that temperature had little effect on the APS. However, crystallinity increased along with temperature. Increasing the reactor length from 1.5 to 4.6 metres resulted in no observable change in APS or crystallinity. Another study by Zhang et al. (2008) reported the synthesis of nanosized TiO<sub>2</sub> particles in CHS, using titanium(IV) bis(ammonium lactato) dihydroxide as a precursor. The particles were determined to be anatase phase TiO<sub>2</sub> and very small, with an average particle size of 4.9 nm. The study did not focus on the effect of operating parameters. but rather on how the phase changes from anatase to rutile during heat treatment. As shown in Figure 2.1, as the heat treatment surpasses 400°C, some of the anatase changes to rutile. After roughly 950°C, all of the anatase had changed to take on the rutile phase. As the temperature of the heat treatment increased, the surface area of the particles reduced rapidly, decreasing the particles' photocatalytic ability. The TiO<sub>2</sub> produced at 300°C was found to be the most efficient in their study for the degradation of methylene blue and this was attributed to a good balance in crystallinity and high surface area.

The objectives of the current study were to identify the process parameters that affect TiO<sub>2</sub> particle characteristics to produce sub-10 nm particles.

### 4.2.1 CHS pilot plant and experimental methods

The CHS pilot plant was designed to operate under a wide range of conditions in order to manipulate process conditions such as temperature, pressure and flow rate. By selectively controlling certain variables, it was possible to control parameters such as the reactor residence time and the mixing conditions in the reactor.

#### Overview of CHS pilot plant

A flow diagram of the pilot plant is depicted in Figure 4.9 and the 3D design and an actual picture of the pilot plant is shown in Figure 4.10. It consists of two Isco Teledyne 260D high pressure syringe pumps (water pumps) set up in a dual system for the constant delivery of supercritical water of up to 80 ml/min. A Milton Roy metallic diaphragm dosing pump was used for pumping the precursor solution, which was capable of pumping corrosive fluids at up to 96.6 ml/min. Two plate heaters in series were used for heating the water feed, followed by a mixing tee. a reactor/crystalliser, a pipe in pipe cooling column and a back-pressure regulator supplied by Tescom, leading to a sample collection vessel. All tubing was supplied by Swagelok, where 3.175 mm O.D (1/8") stainless steel 316 was used up to the mixing tee (except for the 6.35 mm OD tubing used in the plate heaters); afterwards, 6.35 mm OD (1/4") stainless steel 316 tubing was used up to the collection vessel.

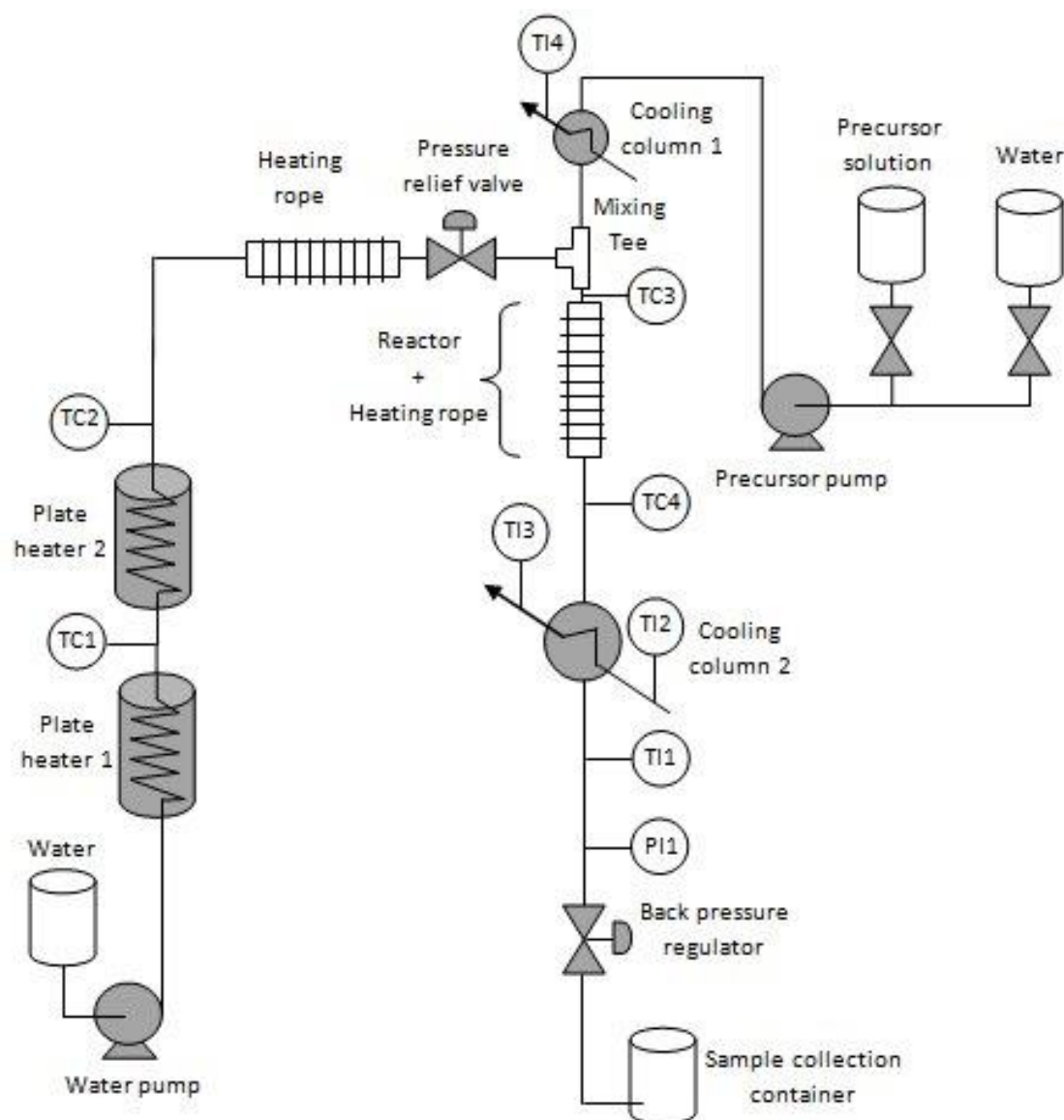


**Figure 4.9 Process flow design of the CHS pilot plant used in this study**

For process control, four temperature feedback controllers and five temperature indicators, along with eight thermocouples (five in-line and three clamp type), were supplied by Unitemp, RSA, for temperature monitoring and control. A pressure gauge (Model: PGI-63B-PG200-LAOX) was supplied by Swagelok to monitor the pressure in the system. For safety purposes, a check valve was placed after each pump to prevent reverse flow, and a pressure release valve (set to fail at 320 atm) was installed in case of a pressure build-up due to failure of the back-pressure regulator.

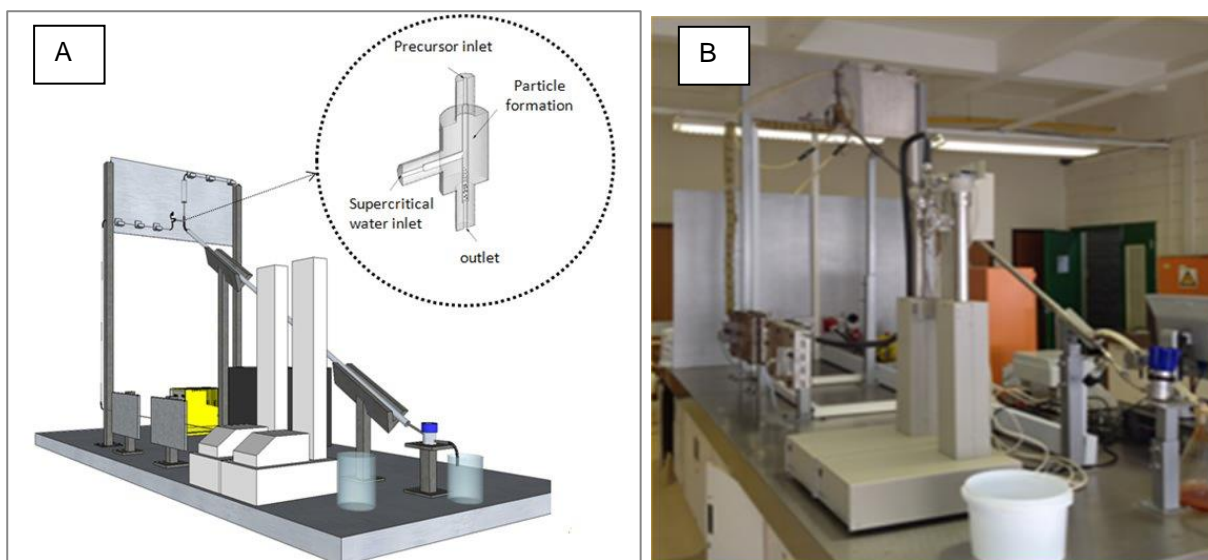


**Figure 4.10 (A) 3D design of CHS pilot plant (B) CHS plant in lab at Cape Peninsula University of Technology**

### Chemicals used

The following chemicals were used in this research:

- Titanium isopropoxide ( $C_{12}H_{28}O_4Ti$ ) (>98%) was supplied by Sigma-Aldrich.
- De-ionised water was used, which was de-ionised in the Lab using a Lasec Purite® deioniser.
- Laboratory-grade 99% ethanol was used, as supplied by CJ Labs.
- A 7 Molar nitric acid was used, as supplied by Sigma-Aldrich.

### CHS procedure

Each precursor consisted of 120 ml of solution, with 99% ethanol being used as the base solvent. Depending on the experimental conditions, a set volume of 7 M nitric acid was sometimes added, followed by a constant addition of 4 ml (0.0135 moles) of titanium isopropoxide. The desired volume of ethanol was added in a continuously stirred beaker using a pipette, followed by the addition of nitric acid if necessary. The 4 ml of titanium isopropoxide were then added drop wise to form a sol. Once the CHS plant was running at a steady state and at the desired parameters for the experimental run, the precursor line was flushed with 99% ethanol to avoid premature crystallization. Once flushed, the precursor solution was pumped through the system and reacted in a 3:2 ratio of water to precursor solution. A precise volume of 250 ml of product solution was collected at the end of the process and stored until separation. The particles were separated through centrifugation at 5000 rpm for five minutes. The separated particles were then dispersed in de-ionised water and dried in an oven at 60°C for 24 hours. The yield of each experimental run was determined by weighing each empty petri dish and full dish of particles after drying, using an electric balance accurate to two decimal places.

### Box-Behnken factorial design for CHS optimisation

A 3-level Box-Behnken factorial design was used to statistically analyse the interactions between operating parameters using Stat Ease Design Expert V 7.0.0 software. It has been identified by Mujtaba et al. (2014) as an effective method for exploration of quadratic response surfaces for the construction of second order polynomial models, aiding in process optimisation. The selected parameters included reaction temperature, pressure and flow rate and the measured responses were effect on the average particle size, particle size distribution and product yield as shown in Table 4.2.

**Table 4.2 Variables in Box-Behnken design**

Formulation variables	Levels used		
	Low	medium	high
Temperature (°C)	250 (-1)	290 (0)	330 (+1)
Pressure (MPa)	20 (-1)	25 (0)	30 (+1)
Nitric acid addition (ml)	0 (-1)	7.5 (0)	15 (+1)

### Particle characterisation

High resolution transmission electron microscopy or HRTEM was performed at the University of Cape Town to determine grain size, size distribution, morphology and the composition of TiO<sub>2</sub>. The TiO<sub>2</sub> particles were dispersed in methanol and then sonicated for 20 minutes prior to being placed onto a copper-coated carbon grid. Once dried, the samples were placed inside the TEM and the surface morphology of the nanoscale crystals was studied using a Tecnai TF20 thermoionic TEM, equipped with a LaB6 filament and a Gatan GIF energy filter. The images were captured at 200 keV in bright field mode. Using Image J version 1.47 software, 50 individual crystals were counted in order to determine the APS and particle size distribution (PSD). The effects of operating parameters on the resulting APS were analysed, as the process parameters were varied in the factorial trial.

The APS and standard deviation were calculated using the data collected from counting 50 individual crystals. The APS and standard deviation were then used to calculate the coefficient of variance which is a more accurate representation of the particle size distribution, as explained by Jain and Sandhu (2009). The coefficient of variance has been defined as the percentage expression of standard deviation, and provided a quantitative method for analysing the PSD. The coefficient of variance can be calculated as follows:

$$CV = \frac{\text{standard deviation}}{\text{average particle size}} \times 100 \quad (4.1)$$

The effect of process parameters on the resulting PSD was therefore analysed by evaluating the coefficient of variation under different process conditions.

X-ray diffraction was used to study the crystal structure of the TiO<sub>2</sub> synthesised. Tests were conducted at UCT Geological Science department using a Philips PW 1390 XRD with a Copper K-α X-ray tube with an X-ray wavelength of 1.542 Å, accelerating voltage of 40 kV and current of 25 mA and Bragg 2θ angles between 3° and 70°. A continuous scan step size of 0.025° was applied with a scan step time of 0.5 seconds. A small amount (less than 1 g) of each sample was prepared by being finely ground into a powder using a mortar and pestle. The powdered sample was placed in a sample holder and loaded into the XRD for analysis. With the use of X'pert Highscore software, qualitative analyses of these particles were possible. Quantitative analysis was conducted on the data provided for Run 1 to Run 15. The phases were identified using Bruker Topas 4.1 software and the relative phase amounts (weight%) were estimated using the Rietveld method.

### **4.2.2 Results and discussion of continuous hydrothermal synthesis (CHS) of TiO<sub>2</sub>**

The operating parameters and the resulting responses of the factorial trial are provided in Table 4.3. Unfortunately, the sample for run 9 got lost when they conducted the TEM analyses. Due to the fact that the factorial trial is run in specific sequence this individual run could not be repeated at random. However, the analysis of the results was not affected by these missing data points.

**Table 4.3 Factorial trial sample matrix–Operating parameters and their respective particle characteristics**

Run	Temp. (°C)	Pressure (MPa)	Nitric acid (ml)	Particle Size (nm)	Coefficient of variance (%)	Product yield (%)	Anatase (%)	Brookite (%)	Rutile (%)
1	290	20	15	4.2±0.8	19.4	100	62.9	28.1	9.0
2	290	25	7.5	5.2±0.9	17.1	96.3	65.7	27.4	6.9
3	330	20	7.5	5.5±1.2	21.6	92.1	68.3	25.9	5.8
4	330	30	7.5	5.2±1.0	19.1	86.2	68.3	24.7	7.0
5	250	25	15	5.1±0.9	16.8	87.5	63.5	29.5	7.0
6	250	30	7.5	2.3±0.4	19.1	100	65.4	26.6	8.0
7	290	25	7.5	5.9±1.3	21.9	99.9	67.3	25.3	7.5
8	330	25	15	6.2±0.9	15.1	100	67.5	24.7	7.8
9	290	30	0	*	*	81.0	68.1	25.7	6.2
10	290	20	0	6.4±1.2	19.2	55.1	66.0	27.3	6.7
11	330	25	0	7.4±1.2	16.5	86.3	68.6	25.2	6.2
12	250	20	7.5	4.0±0.7	17.8	100	62.7	29.4	7.8
13	250	25	0	5.7±0.9	15.9	16.0	65.9	28.9	5.2
14	290	25	7.5	4.6±1.1	23.2	100	64.1	27.2	8.7
15	290	30	15	4.5±0.9	21	83.4	65.8	25.7	8.6

\* - missing data points

#### 4.2.2.1 Effect of operating parameters on average particle size

The APS was found to vary between 2.3 nm and 7.4 nm as the process parameters were altered. Correlation factors were determined for each parameter, identifying their significance on the APS. As shown in Table 4.4, temperature was found to majorly increase APS, with acid addition significantly decreasing APS, and pressure promoting a lesser decrease in APS. The effect of operating parameters on APS is also illustrated in the 3D plots in Figure 4.11.

**Table 4.4 Correlation factors of operating parameters on particle size**

Operating parameter	Correlation factor on APS
Temperature	0.572
Pressure	-0.251
Nitric acid addition	-0.398

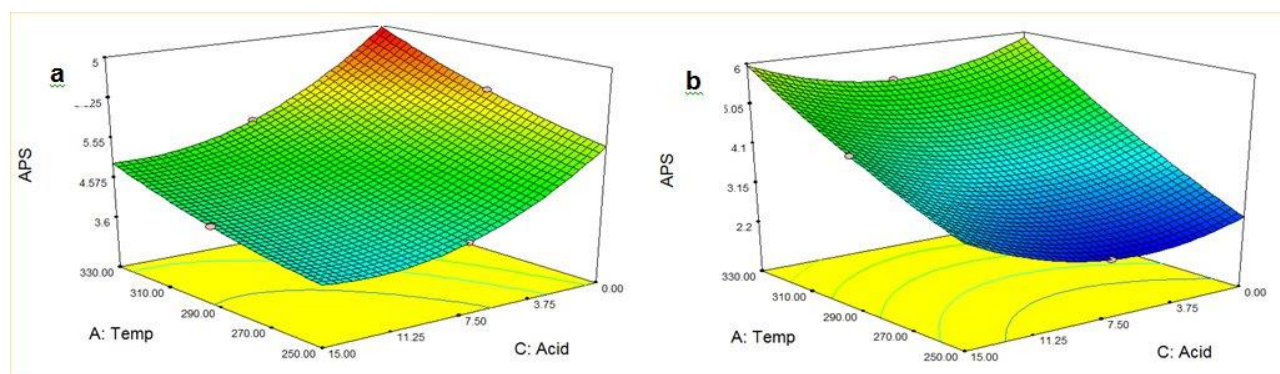


**Figure 4.11 3D quadratic plot of temperature versus acid addition on the effect of APS at (a) low pressure (20 MPa) and (b) high pressure (30 MPa)**



#### 4.2.2.2 Effect of temperature on APS

Temperature was found to have the largest effect on APS, with a correlation factor of 0.572 as shown in Table 4.4. As the temperature was increased from 250°C to 330°C at a constant 30 MPa and 7.5 ml acid addition, the APS was found to increase from 2.3 nm to 5.2 nm, as depicted in Figure 4.12.

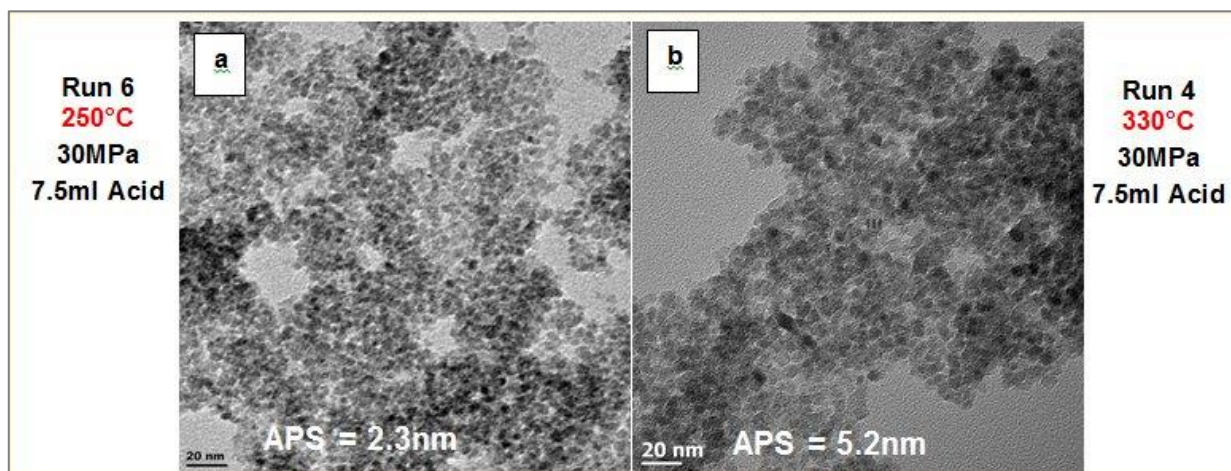


**Figure 4.12 TEM images showing the effect of temperature on APS**

#### 4.2.2.3 Effect of pressure on APS

Pressure was found to have a small decreasing effect on APS, with a correlation factor of -0.251. When comparing Run 3 and 4, at a constant 330°C and 7.5 mL acid addition, the APS remained unchanged as the pressure increased from 20 MPa to 30 MPa, as shown in Figure 4.12.

#### 4.2.2.4 Effect of nitric acid addition on APS

The addition of nitric acid was also found to have a decreasing effect on APS. A correlation factor of -0.398 revealed that it had a stronger decreasing effect than pressure. When comparing Run 5 and 13, at a constant 250°C and 25 MPa, the APS was found to decrease from 5.7 nm to 5.1 nm as the nitric acid addition was increased from 0 to 15 mL.

#### 4.2.2.5 Effect of operating parameters on the particle size distribution (PSD)

The PSD was found to vary between 15.1% and 23.2% as the process parameters were altered. Correlation factors were determined for each parameter, identifying their significance on the PSD. As shown in Table 4.5, temperature and nitric acid addition were found to have a minor increasing effect on PSD, with pressure having negligible effect. The effect of operating parameters on PSD is also illustrated in the 3D plots in Figure 4.13 a and b.

**Table 4.5 Correlation factor of operating parameters on particle size distribution**

Operating parameter	Correlation factor on PSD
Temperature	0.108
Pressure	0.002
Nitric acid addition	0.080

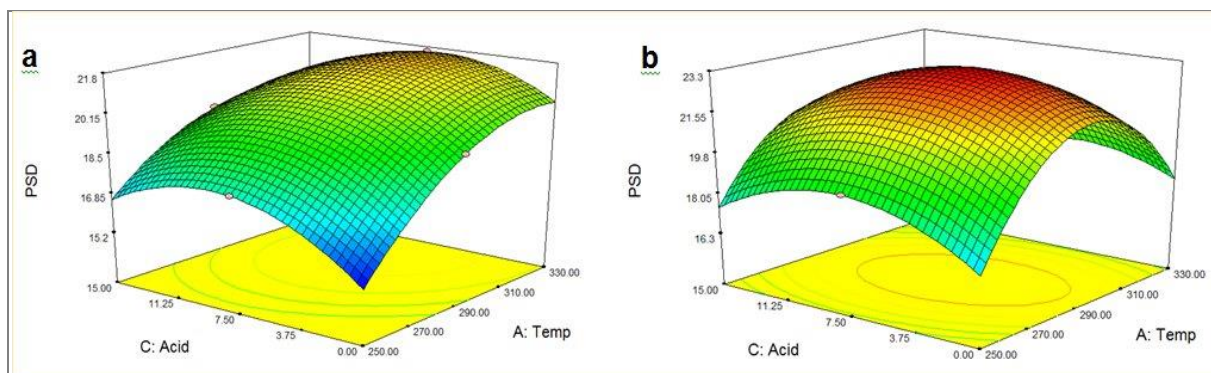


**Figure 4.13 A 3D quadratic plot of temperature versus acid addition on the effect of PSD at (a) low pressure (20 MPa) and (b) high pressure (30 MPa)**

#### 4.2.2.6 Effect of operating parameters on the product yield

The product yield (PY) was found to vary between 16% and 100% as the process parameters were altered. Correlation factors were determined for each parameter, identifying their significance on the PY. As shown in Table 4.6, the addition of acid was found to have a major influence on increasing the PY, while temperature had a slight, but still significant, increasing effect. The pressure was shown to have negligible effect. The effect of operating parameters on PY is also illustrated in the 3D plots in Figure 4.14 a and b.

**Table 4.6 Correlation factor of operating parameters on product yield**

Operating parameter	Correlation factor on PY
Temperature	0.225
Pressure	0.030
Nitric acid addition	0.550

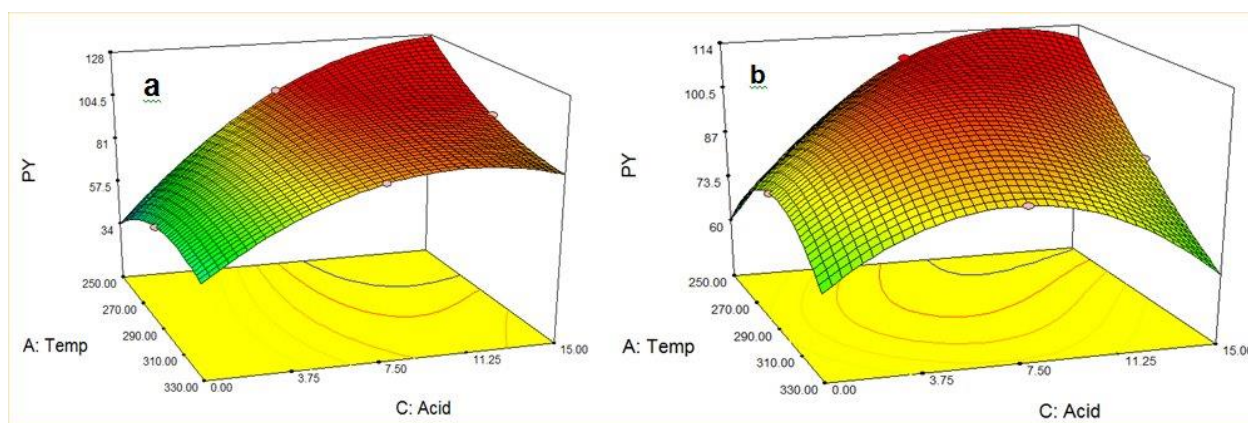


**Figure 4.14 A 3D quadratic plot of temperature versus acid addition on the effect of PY at (a) low pressure (20 MPa) and (b) high pressure (30 MPa)**

#### 4.2.2.7 Effect of temperature on PY

Temperature was found to have a minor increasing effect on PY, with a correlation factor of 0.225, as shown in Table 4.6. As the temperature was increased from 250°C to 330°C at a constant 25 MPa and 15 ml acid addition, the PY was found to increase from 87.5% to 100%, as depicted in Figure 4.14.



#### 4.2.2.8 Effect of pressure on PY

Pressure was found to have negligible effect on PY, with a 0.030 correlation factor. No specific trend was observed, and the PY was found to either increase or decrease as the pressure increased. Run 12 and Run 6 showed a PY of 100% as the pressure increased at a constant 250°C and 7.5 ml nitric acid addition. On the other hand, the PY was found to decrease from 92.1% to 86.2% as the pressure increased at a constant 330°C and 7.5 ml nitric acid addition, as identified when comparing Run 3 and Run 4.

#### 4.2.2.9 Effect of nitric acid addition on PY

The addition of acid was found to have the largest effect on PY, with a 0.550 correlation factor. When comparing Run 10 and Run 1, the PY was found to almost double as nitric acid was introduced to the system. The PY was found to increase from 55.1% to 100.0% as the acid was increased from 0 to 15 ml. at a constant 290°C and 20 MPa.

#### 4.2.2.10 Effect of process parameter on crystal structure

Quantitative analysis of the XRD results showed that the crystal structure and phase percentage of TiO<sub>2</sub> polymorphs were independent of the process conditions for all the trial runs, as shown in Figure 4.15, with an average of 66±2% anatase, 27±2% brookite and 7±1% rutile.

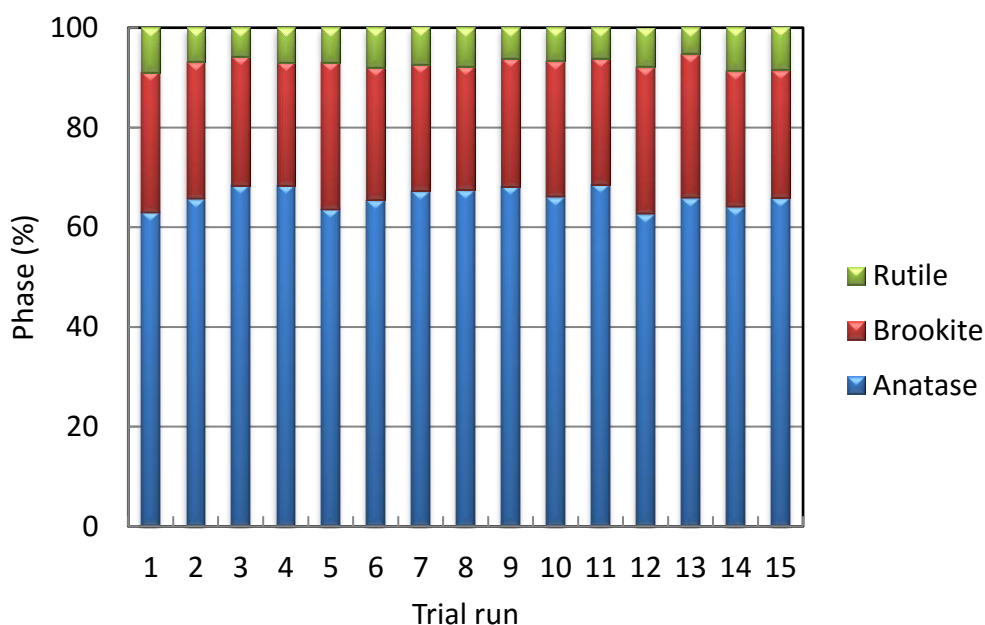


Figure 4.15 Quantitative analysis of XRD results

#### 4.2.3 Conclusion from factorial trial

The summary of correlation factors (Table 4.7) showed that temperature has a major increasing effect on the APS, with a minor influence on PSD and PY, while pressure seemed to have a negligible effect on the entire system, apart from a minor reducing effect on PSD. The addition of nitric acid is the most influential on the system. as it not only has a strong reducing effect on the APS, which increases the area and potentially photocatalytic effect, but also majorly increases the PY. Therefore, adding acid can possibly make the CHS process commercially viable by producing small particles with a narrow size distribution at a high yield. It is incredible that under the wide range of conditions the polymorph percentage of the produce TiO<sub>2</sub> powder remained consisted. This makes CHS a very robust system for the continuous production of high qualityTiO<sub>2</sub> powders of less than 10 nm in size for use in photocatalysis.

**Table 4.7 Summary of correlation factors**

Operating parameter	Correlation factor on APS	Correlation factor on PSD	Correlation factor on PY
Temperature	0.572	0.108	0.225
Pressure	-0.251	0.002	0.030
Nitric acid addition	-0.398	0.080	0.550

### 4.3 SYNTHESIS OF ULTRA-SMALL $\beta$ -FeOOH/TiO<sub>2</sub> HETEROJUNCTION NP

Several strategies have been implemented to extend the band gap of TiO<sub>2</sub> up to visible light range, i.e. substitution of different transition metal or anions to the Ti or oxygen sites. Combination of semiconductors, with matching band potential, to create a heterojunction structure is of increasing interest as the heterojunction can be utilised to effectively separate the photogenerated electrons and holes. Beside the basic demand of the obvious matching band potential of the semiconductors, electron and hole conduction mobility in the electron and hole accepting semiconductors is important for the enhancement of photocatalytic activity (Huang et al., 2007). A number of studies have been conducted on combined semiconductors based on TiO<sub>2</sub> photocatalyst. Akaganeite ( $\beta$ -FeOOH) is a semiconductor type of iron oxy hydroxide with a band gap of 2.12 eV (White, 1990), which is lower (2.6 eV) than that of previously reported  $\gamma$ -FeOOH (Rawal et al., 2009). Due to the relatively low band gap of  $\beta$ -FeOOH it can be excited under visible light irradiation.  $\beta$ -FeOOH has a large tunnel structure, where iron atoms are strongly bonded to the framework (Amine et al., 1999). Because of its tunnel-type structure lithium can be intercalated and extracted freely in the tunnels (2 X 2) during discharge and charge processes, making it a potential material for battery electrodes (Shao et al., 2005). This implies that  $\beta$ -FeOOH possesses good electron conduction ability. This work reports on the photocatalytic activity of the prepared  $\beta$ -FeOOH/TiO<sub>2</sub> heterojunction structure for the degradation of model dye methyl orange. Actual textile effluent was also used to evaluate the photocatalytic performance of the material. The real textile effluent was obtained from Falke.

#### 4.3.1 Experimental methods for synthesis of $\beta$ -FeOOH/TiO<sub>2</sub> heterojunction NP

##### Preparation of $\beta$ -FeOOH nanoparticles

$\beta$ -FeOOH nanorods were synthesised using a hydrothermal method (Chowdhury et al., 2014). For a typical synthesis 120 ml of de-ionised water was mixed with 280 mL of absolute ethanol. The pH of the solution was raised to 10 by drop wise addition of NH<sub>4</sub>OH. FeCl<sub>3</sub>.6H<sub>2</sub>O (1.62 g) was added to the solution and stirred to dissolve. The final pH of the solution was kept at 2 in all cases. The solution was placed in a Teflon-lined reactor and heated at 100°C for 2 hours. The reactor was allowed to cool naturally after completion of the reaction. The next steps were decantation of the supernatant liquid, centrifugation, washing of the solids with ethanol several times to remove residual chloride ions, and storage in a desiccator.

##### Preparation of $\beta$ -FeOOH/TiO<sub>2</sub> heterojunction structures

A chemically bonded interface between TiO<sub>2</sub> (pure anatase) particles, with an average diameter of about 100 nm, and  $\beta$ -FeOOH was formed via an organic linker. The method of preparation of  $\beta$ -FeOOH/TiO<sub>2</sub> heterojunction structure was adopted from a previous study (Rawal et al., 2009). Maleic acid was used as an organic linker (Kim et al., 2009) in this study. Three different mol% loadings of  $\beta$ -FeOOH (2, 5 and 10%) on TiO<sub>2</sub> were prepared in this study. For a typical synthesis of 5 mol %  $\beta$ -FeOOH and 95 mol % TiO<sub>2</sub>, (labelled as 5%  $\beta$ -FeOOH/TiO<sub>2</sub>) 0.059 g of  $\beta$ -FeOOH was suspended in 30 mL of ethanol. An amount of 10 mL of 0.1 M maleic acid solution was added to the mixture. In a separate beaker, 1 g of TiO<sub>2</sub> was dispersed in 30 mL ethanol. The two mixtures were stirred for 5 hours separately. After 5 hours, the TiO<sub>2</sub> mixture was added to the  $\beta$ -FeOOH mixture and stirred for 16 hours. The mixture was centrifuged, washed several times and dried

overnight in air at 60°C. The dried powder was annealed at 200°C for 4 hours in an oven under air to evaporate the organic components. Finally, the annealed samples were treated under 9 W UV light for 4 hours to remove any residual organic on the surface of the catalyst.

### Characterisation

The crystal structures of the synthesised products were determined using a Phillips PW 3830/40 Generator with Cu-K $\alpha$  radiation ( $\lambda = 1.506 \text{ \AA}$ ). The surface morphology of the synthesised crystals was studied using a Tecnai TF20 thermionic TEM, equipped with a LaB6 filament and a Gatan GIF energy filter. Images were captured at 200 keV in bright field mode. Selected area electron diffraction (SAED) patterns were obtained using the smallest area aperture available. Infrared spectra were collected with a Perkin Elmer 1000 series FTIR spectrometer in the range of 4000 to 200  $\text{cm}^{-1}$  in a KBr matrix. UV-VIS diffuse reflectance spectra were collected using a Perkin Elmer lambda 35 spectrophotometer. Photoluminescence was measured using a Perkin Elmer 2565 Luminescence Spectrometer.

## **4.3.2 Results and discussion of the preparation of $\beta\text{-FeOOH/TiO}_2$**

### *4.3.2.1 Structural analysis*

Figure 4.16 (a) shows the X-ray diffraction spectroscopy (XRD) patterns of the pure  $\beta\text{-FeOOH}$  (JCPDS. No. 42-1315),  $\text{TiO}_2$  (JCPDS. No. 71-1166) and three different  $\beta\text{-FeOOH/TiO}_2$  heterojunction structures. However, no  $\beta\text{-FeOOH}$  diffraction peaks were observed in the XRD patterns of the 2, 5 and 10%  $\beta\text{-FeOOH/TiO}_2$  heterojunction structure. X-ray diffraction data are not sensitive to distribution of Ti and Fe in oxides since they are surrounded by the same number of electrons. Hence, it is difficult to distinguish between Ti and Fe in XRD since X-rays are scattered by electron density. Figure 4.16 (b) presents a TEM image of the pure  $\beta\text{-FeOOH}$  nanorods. It can be seen from the TEM image that the  $\beta\text{-FeOOH}$  has a very narrow size distribution. Interestingly no rod-shaped particles were found in the TEM grid Figure 4.16 (c) of the as-prepared  $\beta\text{-FeOOH/TiO}_2$  composite.

It can be seen that a tight contact between smaller and large particles has been formed. The d-spacing of the particles was measured from the HRTEM image in Figure 4.16 (d) and were found to be 1.49 nm and 1.89 nm for smaller and larger particles respectively. The d-spacing value of the smaller particles corresponds to the (701) plane of the pure  $\beta\text{-FeOOH}$  particles (JCPDS. No. 42-1315). And the d-spacing value of the bigger particles matches the diffraction plane (200) of  $\text{TiO}_2$  particles. Hence, it was postulated that rod-like  $\beta\text{-FeOOH}$  transformed into pseudo-spherical shape particles, marked with a white dotted circle in Figure 4.16 (c), coupled with  $\text{TiO}_2$  particles, in the heterojunction structure. It is well known that  $\beta\text{-FeOOH}$  transforms into  $\alpha\text{-Fe}_2\text{O}_3$  at elevated temperature. However, high temperature XRD patterns, shown in Figure 4.16 (e), of the pure  $\beta\text{-FeOOH}$  obtained in this study reveal that synthesised pure  $\beta\text{-FeOOH}$  is stable up to 300°C, without any phase transformation to  $\alpha\text{-Fe}_2\text{O}_3$ . With increasing temperature from 100°C to 200 and 300°C, most of the  $\beta\text{-FeOOH}$  peaks observed at 100°C diminish; however, a new peak corresponding to (701) plane of  $\beta\text{-FeOOH}$  appears (JCPDS. No. 42-1315). The new peak can be attributed to the structural changes in the  $\beta\text{-FeOOH}$  material that occurred during the annealing period at 200°C. Moreover, at an elevated temperature of 300°C the pristine  $\beta\text{-FeOOH}$  nanorods don't collapse, as was shown by TEM image (data not shown). This clearly suggests that no phase transformation of  $\beta\text{-FeOOH}$  took place during the heat treatment of the heterojunction structure at 200°C. The transformation of rod-shape to spherical particles can be explained by the fact that during heat treatment (200°C) a certain fraction of ultra-small  $\beta\text{-FeOOH}$  diffused into  $\text{TiO}_2$  at the chemically bonded interface. In fact, the ionic radius of  $\text{Fe}^{3+}$  is similar to that of  $\text{Ti}^{4+}$  and the substitution of iron in the  $\text{TiO}_2$  matrix is a favourable process.

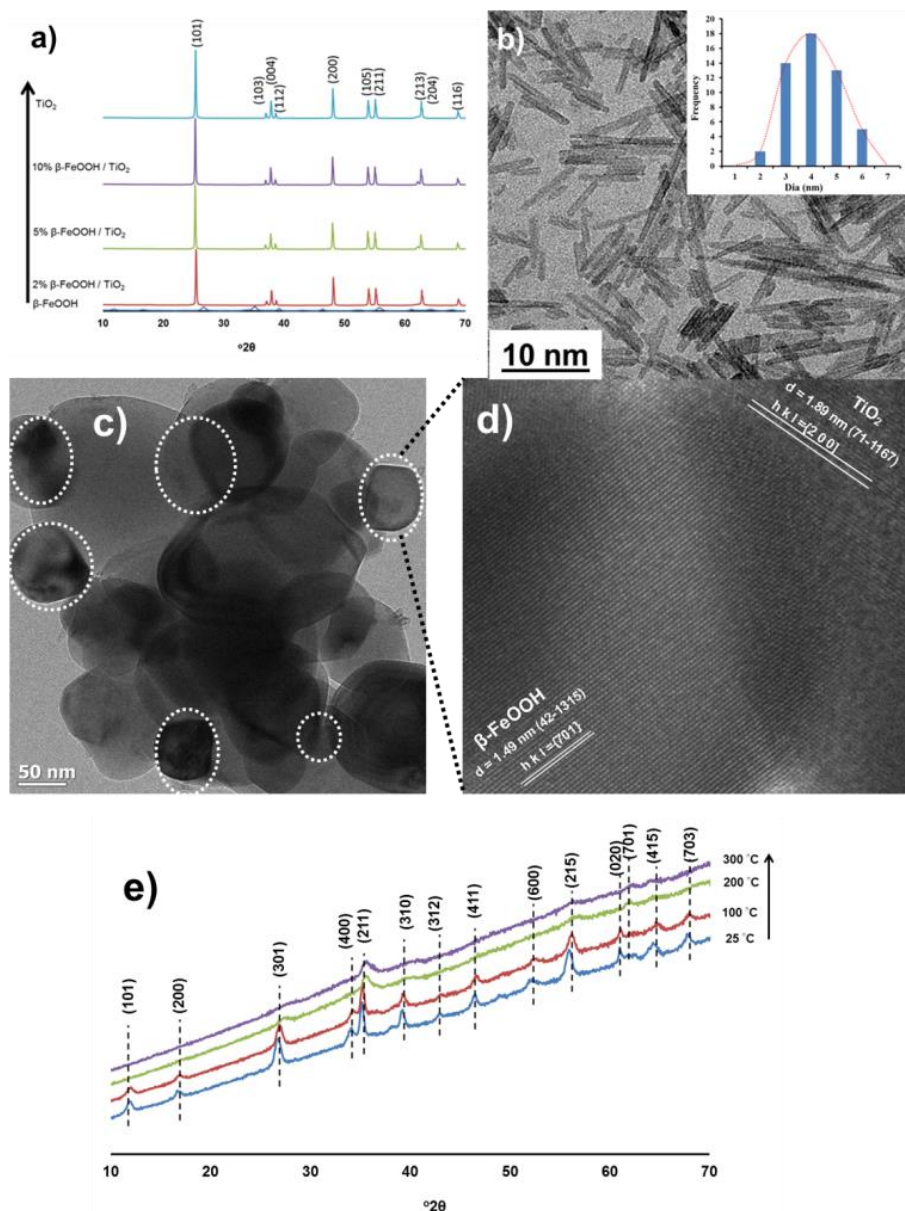


**Figure 4.16** a) XRD patterns of the different materials b) TEM image of 5%  $\beta$ -FeOOH rod-like particle (inset shows PSD) c) Heterojunction structure of  $\beta$ -FeOOH/TiO<sub>2</sub> d) HRTEM image of  $\beta$ -FeOOH/TiO<sub>2</sub> heterojunction and e) High temperature XRD of the  $\beta$ -FeOOH particles

#### Evaluation of the photocatalytic performance of $\beta$ -FeOOH/TiO<sub>2</sub>

Photocatalytic degradation of methyl orange (MO) was carried out in an aqueous solution at about 63 °C due to heat generated by a 300 W halogen tungsten lamp. An aliquot of 0.02 g of catalyst was added in a 100 mL of 80 ppm MO solution. Three millilitres (3 mL) of 30% H<sub>2</sub>O<sub>2</sub> was added to the solution and sonicated for 15 minutes. The solution was kept in the dark under magnetic stirring for an hour to reach absorption equilibrium. A halogen tungsten lamp was used to simulate sunlight. After the solution had reached equilibrium, a 300 W halogen tungsten lamp was immersed in the solution and irradiated. Cooling water was circulated around the reaction vessel to keep the temperature constant. Two millilitres of the sample were withdrawn at regular intervals and centrifuged immediately for 5 minutes to separate the suspended solids. The absorbance of the supernatant, MO, at 464 nm was analysed by UV-VIS spectroscopy.

Controlled experiments were conducted on the photodegradation kinetics of an 80 ppm MO solution to evaluate the role of H<sub>2</sub>O<sub>2</sub> only, under halogen tungsten lamp irradiation, for the degradation of MO in the absence of the catalyst, as shown in Figure 4.17. Approximately 40% degradation of MO occurred under identical conditions in the absence of the catalyst for both 3 mL and 5 mL of H<sub>2</sub>O<sub>2</sub> addition and therefore 3 mL H<sub>2</sub>O<sub>2</sub> was selected for the evaluation of the catalyst's performance.

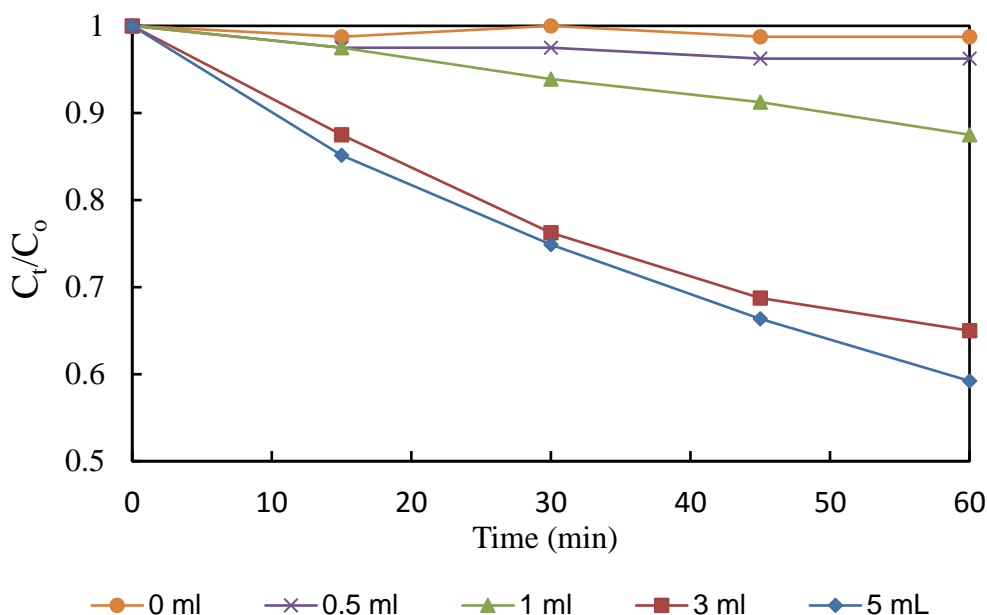


**Figure 4.17 Role of H<sub>2</sub>O<sub>2</sub> concentration on MO degradation in the absence of catalysts**

Photodegradation kinetics of an 80 ppm MO solution in the presence of 3 mL 30% H<sub>2</sub>O<sub>2</sub> and 0.01 g/L  $\beta$ -FeOOH/TiO<sub>2</sub> (2, 5 and 10%) catalyst under a 300 W halogen tungsten lamp is presented in Figure 4.18. It is remarkable to note that the addition of  $\beta$ -FeOOH in a heterojunction improved the photocatalytic performance of pristine anatase by 45 to 60%. An increase in the efficiency of the catalyst was evident from 2%  $\beta$ -FeOOH/TiO<sub>2</sub> to 5%  $\beta$ -FeOOH/TiO<sub>2</sub>. However, a further increase in  $\beta$ -FeOOH content (10%) reduced the photocatalytic activity of the heterojunction structure. Two plausible explanations can be provided for this phenomenon. 1) non-interacting materials at the heterointerface of  $\beta$ -FeOOH/TiO<sub>2</sub> with increasing  $\beta$ -FeOOH content and 2) an increase in recombination sites. It is well known that for photogenerated electrons to achieve spatial inter semiconductor transfer, a tightly bonded interface is essential at the heterointerface of the combined semiconductors. The colour of the MO solution changed from dark to colourless in 60 minutes using 5%  $\beta$ -FeOOH/TiO<sub>2</sub> composite material as shown in Error! Reference source not found. (inset). A degradation efficiency of 97% was achieved within 60 minutes. It can be seen that MO does not degrade under photolysis in the absence of the catalyst and H<sub>2</sub>O<sub>2</sub>. When the MO solution was kept in the dark, only 10% MO was degraded or absorbed. Pristine TiO<sub>2</sub> (anatase) and  $\beta$ -FeOOH only degrade 39% and 18% of MO within 60 minutes under identical conditions. Commercially available P25 was also used to degrade MO under identical conditions. Only about 40% MO degradation was achieved using P25 as a photocatalyst, which is similar to the performance of anatase. Thus, it can be said that the prepared  $\beta$ -FeOOH/TiO<sub>2</sub> heterojunction structure has good photocatalytic activity under simulated solar irradiation. The 5%  $\beta$ -FeOOH/TiO<sub>2</sub> composite material was used for all other experiments.

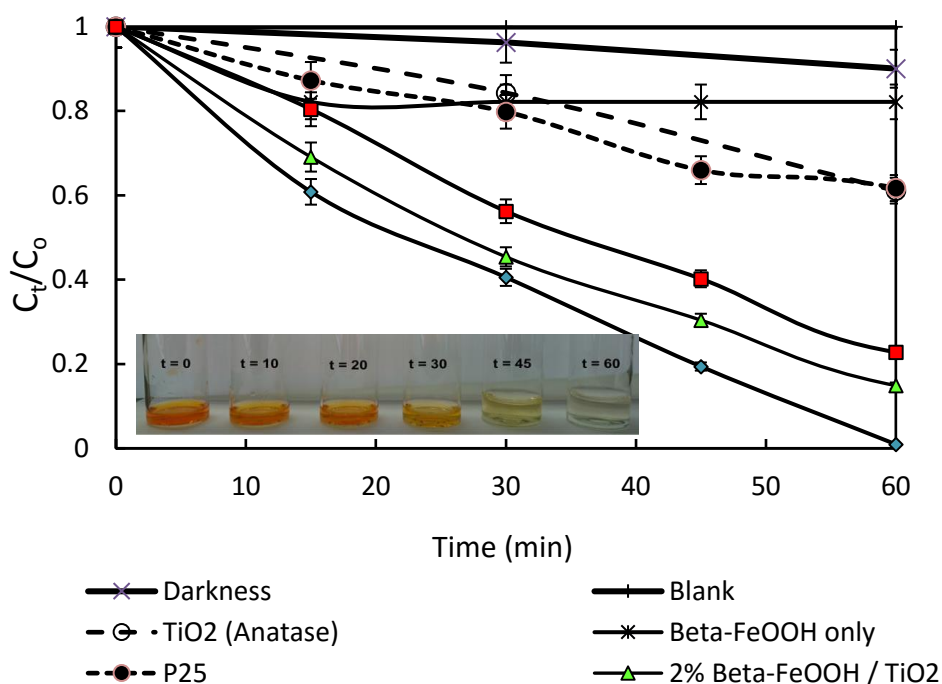


**Figure 4.18 MO degradation using various catalysts**

#### 4.3.3 Comparison of catalyst performance of ultra-small $\beta$ -FeOOH/TiO<sub>2</sub> heterojunction

A comparison of commercial anatase TiO<sub>2</sub> and the TiO<sub>2</sub> produced locally in the CHS pilot plant was conducted. The optimum conditions obtained during preparation of the catalyst, as reported earlier in this chapter, of a catalyst concentration of 800 mg/L, H<sub>2</sub>O<sub>2</sub> addition of 50 ml/L and a pH of 4.4 was used without further optimisation. The catalysts were further evaluated to determine the reproducibility of results. Figure 4.19 shows the repeatability of  $\beta$ -FeOOH/TiO<sub>2</sub> anatase test results. Run 1 and Run 2 were conducted by one operator preparing two identical solutions of MO and running an experiment in the morning and afternoon. Run 3 and Run 4 were conducted by another operator, using a different reactor of the same volume and a similar spec lamp, also using solutions prepared separately. The standard deviation of  $C_t/C_o$  was 0.02 and the uncertainty of the reaction rate constant of  $0.043 \pm 0.002 \text{ min}^{-1}$  was obtained with total degradation of approximately 97% for 60 minutes.

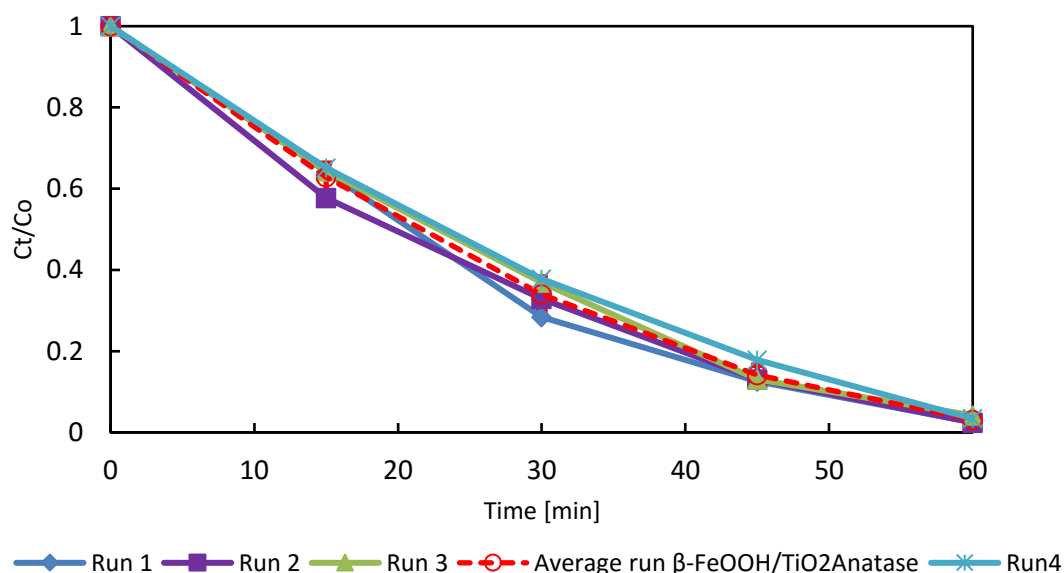


**Figure 4.19 Repeatability tests of MO degradation using  $\beta$ -FeOOH/TiO<sub>2</sub> anatase**

Similar tests were conducted using  $\beta$ -FeOOH/TiO<sub>2</sub>CHS with the TiO<sub>2</sub> produced in the CHS system in comparison to the performance of the commercially available anatase. The standard deviation of  $C_t/C_0$  was 0.02. The rate constant of  $0.061 \pm 0.003 \text{ min}^{-1}$  was determined for the  $\beta$ -FeOOH/TiO<sub>2</sub>CHS compared to  $0.043 \pm 0.002 \text{ min}^{-1}$  for  $\beta$ -FeOOH/TiO<sub>2</sub>Anatase. Although the final concentration was the same, this concentration was already reached after 45 minutes with the CHS-produced TiO<sub>2</sub> compared to 60 minutes for the anatase heterojunction NP. The CHS TiO<sub>2</sub> consisted of all 3 polymorphs, namely 63% anatase, 29% brookite and 8% rutile, previously shown to improve photocatalytic properties compared to single polymorphs systems.

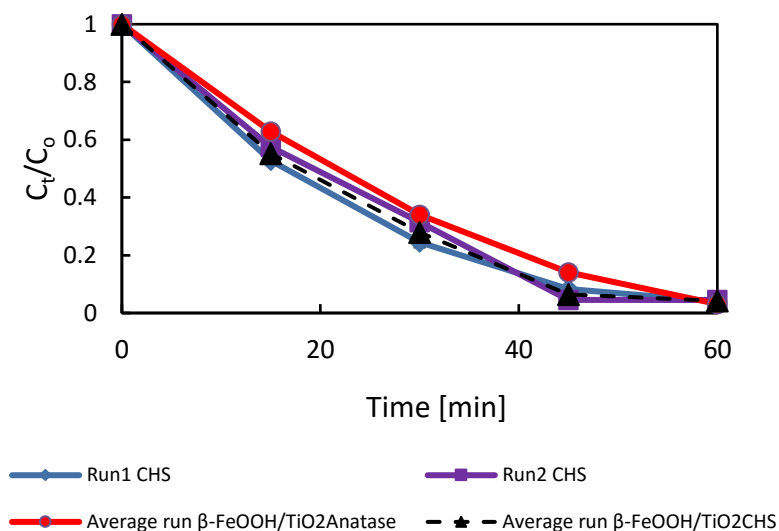


**Figure 4.20 Comparison of MO degradation using  $\beta$ -FeOOH/TiO<sub>2</sub>Anatase and  $\beta$ -FeOOH/TiO<sub>2</sub>CHS**

#### 4.4 CONCLUSIONS

Several strategies for the development of TiO<sub>2</sub> photocatalyst powders were evaluated to enhance the capacity for local manufacturing. The synthesis time for the sol-gel method for batch hydrothermal synthesis was successfully decreased from 72 hours to 18 hours to produce a superior multi-polymorph TiO<sub>2</sub> powder with better performance under UV irradiation compared to that reported in literature. The addition of brookite to rutile significantly improved the photocatalytic performance of the powder. The percentage of anatase was

constant (~15%) over all the process conditions. It was shown that acid concentration can be used as a means to control polymorph composition at shorter gel formation times.

A continuous hydrothermal synthesis pilot plant was used to conduct a factorial trial to establish robust process conditions for the manufacturing of an anatase-rich  $\text{TiO}_2$  nanopowder with particle size less than 10 nm. The polymorph combination was consistent at approximately 65% anatase, 25% brookite and 10% rutile over a wide range of process conditions. The acid played a major role in increasing product yield, among other effects. The particle size under all conditions was less than 10 nm. Furthermore, pure anatase was produced using the CHS test rig with similar, if not better, performance than commercially available anatase.

A heterojunction  $\beta\text{-FeOOH}/\text{TiO}_2^{\text{Anatase}}$  was produced which showed improved photocatalytic properties over anatase and P25 (anatase and rutile mixture). The CHS  $\text{TiO}_2$  was also combined in a heterojunction with  $\beta\text{-FeOOH}$  and showed similar to improved photocatalytic performance. These results are very encouraging, showing the possibilities for locally manufactured photocatalysts to be used in the treatment of textile effluents.



## CHAPTER 5: CATALYST IMMOBILISATION AND EVALUATION IN A TRICKLE-BED REACTOR

---

Immobilisation of nanophotocatalysts plays a major role in the cost and environmental impact of the utilisation of TiO<sub>2</sub> and modified TiO<sub>2</sub> as BMOs in an industrial-scale application of this proposed technology. The use of a slurry reactor requires that the suspended nanophotocatalytic TiO<sub>2</sub>-based catalysts be removed, typically by centrifugation, which is time-consuming and costly. The objectives of this work were to:

1. Immobilise TiO<sub>2</sub> nanoparticles in and on PAN fibre using electrospinning;
2. Evaluate the efficiency of each immobilised-TiO<sub>2</sub> scaffold to degrade
  - model dyes in trickle-bed reactors (TBRs)
  - sump effluent from Falke
  - nanofiltrate brine from the UF/NF pilot plant at Falke.

### 5.1 PREPARATION OF IMMOBILISED NANO-TiO<sub>2</sub> PARTICLES

#### 5.1.1 Experimental method for electrospinning PAN, stabilisation and carbonisation

##### Materials used for electrospinning

PAN from BluestarFibres (UK and now China) where the monomer ratio is AN: MA: IA = 96:6:1 in the copolymer. The molecular weight (MW) of the UK fibre is about 120 000 Daltons. Chinese fibre was supplied with information that it has a higher molecular weight. It was determined that for an equivalent of the viscosity of the 8% (wt/wt) UK fibre, that the concentration of the Chinese fibre should be 6.7% (wt/wt) and is further named 8% PAN. Dimethyl-sulphoxide (DMSO) or dimethyl formamide (DMF) from B and M Scientific was used as a solvent for the spinning dope. Aluminium foil was used as the grounded stationary electrode. A nonwoven material manufactured by Freudenberg was used as a backing material, so that the electrospun scaffold can be removed easily. This material was used to cover the aluminium electrode so that the electrospun scaffold will spin onto the nonwoven material and not the aluminium.

##### Preparation of the electrospinning dope

A weighed sample of 8 g of the PAN micron-sized commercial fibre was added to 96 g of DMSO or DMF. The solution was stirred at 50°C for 2 hours, until a clear straw-coloured solution was obtained. The solution was then cooled to room temperature in a desiccator.

##### Electrospinning equipment

The high voltage supply was obtained from Gamma HV, USA. The positive DC supply can be adjusted from 10 to 30 kV. The positive electrode was either immersed inside a dope with a copper wire in a long-nosed Pasteur pipette for gravity feed, or attached to the metal, blunt-nosed needle of a syringe in a metering syringe pump.

##### Electrospinning parameters

Spinning was carried out in a fume-hood with an atmosphere maintained at 30°C and a relative humidity of 65%. The spinning distance between the charged solution and the collector was maintained at 20 cm. The spinning voltage was set at 20 kV. These conditions had been optimised for this grade of polymer by Greyling (2010). The gravity feed system from the pipette was paced at a 30° angle to the horizontal. When the horizontal syringe pump was used, the flow rate was set at 2 ml per hour.

The mats were all dried in an oven at 100°C for 24 hours, to evaporate any excess solvent, and then stored in an evaporator until further characterisation using SEM or usage in the TBR.

#### PAN stabilisation and carbonisation in a furnace

The spun mats were sectioned into 3 cm by 30 cm samples and the edges wrapped over wire nets with dimensions of 2.8 cm by 28 cm.

The furnace at the TSCT used for stabilisation was supplied by Kiln Contractors. It was not possible to totally seal this furnace for carbonisation heating in an inert atmosphere and thus a quartz tube furnace at the University of the Western Cape (UWC), supplied by Labotec, was utilised. Figure 5.1 shows the furnace equipment at the TSCT at Cape Peninsula University of Technology.



**Figure 5.1 Programmable furnace used for the thermal treatment of electrospun PAN mats (stabilisation and carbonisation)**

The heating rate for stabilisation was set at 2°C per minute up to about 250°C, in an air atmosphere. The isothermal dwell time was set at 240°C to 280°C for 2 hours. It was then treated in an inert atmosphere, with heating rates at 2°C per minute up to about 600°C to 900°C.

#### **5.1.2 Experimental method for electrospinning with TiO<sub>2</sub> and TiO<sub>2</sub> precursors**

The following methods of immobilisation have been applied to prepare mats for application in the TBR:

- Immobilisation of commercial P25® inside electrospun fibres
- Immobilisation of titanium precursors inside electrospun fibres
- Immobilisation of titanium precursors outside electrospun fibres through dip-coating
- Stabilisation and carbonisation of Ti containing PAN electrospun fibres.

#### TiO<sub>2</sub> nanoparticles inside the electrospun fibres

The spinning dope for an 8% PAN in DMSO dope was prepared as described previously. The P25 nanoparticles were added to the prepared dope as 1, 3 and 6% (wt/wt). The solution was sonicated two times for 15 minutes using a sonication probe. The solution was spun immediately and constantly re-sonicated to prevent re-agglomeration of the NPs, before being injected into the pipette of syringe. Anatase TiO<sub>2</sub> from Sigma-Aldrich was also included in the same spinning dope at 3% (wt/wt).

### Ti precursors inside the electrospun fibres

Spinning solutions were prepared as in 5.1.2.1. Titanium sol-gel precursors were added to the solutions in a concentration ratio such that the number of moles of Ti in the precursor to number of moles of acrylonitrile was 0.1:1, 0.5:1 or 2.5:1. The titanium precursors used in this study included:

- (a) Titanium tetrachloride (TTC)  $\text{TiCl}_4$  obtained from Sigma-Aldrich

According to Okolongo (2013), 94 g of DMSO was weighed and separated into two parts. One part was mixed with 6 g of PAN to make a PAN solution. This solution was stirred for 2 hours, while 8.5 ml DMSO was used to make the precursor solution. This solution was made by adding acetic acid to the DMSO while stirring vigorously; the  $\text{TiCl}_4$  was then added to the DMSO/acetic acid solution to make a precursor solution. The precursor solution was added to the PAN solution and stirred vigorously for 15 minutes. This was then electrospun into a scaffold.

- (b) Titanium iso-butoxide (TBT)  $\text{C}_{16}\text{H}_{36}\text{O}_4\text{Ti}$  obtained from B and M Scientific

According to Teng et al. (2007), 6 g of PAN was added to 75 ml DMSO and dissolved with a sonicator. An aliquot of 18 ml of TBT was added to 12 ml acetic acid. This solution was added to the dissolved PAN solution. This mixture was sonicated until the mixture was homogenous (90 minutes). The solution was electrospun and stabilised at 250°C for an hour. These fibres were dipped in  $\text{H}_3\text{PO}_4$  or water for 2 hours and dried. These fibres were calcinated in an inert atmosphere using nitrogen at 600°C for 2 hours.

- (c) Titanium tetra-iso-propoxide (TTIP)  $\text{Ti}\{\text{OCH}(\text{CH}_3)_2\}_4$  obtained from KIMIX

A TTIP/ethanol mixture with a weight ratio of 1:1. According to Mehrpouya (2012), TTIP was weighed out to 4.5 g. ethanol to 4.5 g and mixed together. This mixture was added to a 6% PAN/DMSO solution very slowly and stirred vigorously. This solution was electrospun into a nonwoven fibre scaffold, stabilised and carbonised.

### Immobilisation of titanium precursors outside fibres through dip-coating

- (a) TTIP sol-gel on PAN

The sol was prepared according to Segota (2011) where the molar ratios of TTIP: acetyl acetone: Ethanol:  $\text{H}_2\text{O}$ : acetic acid were 1:1.3:40:0.9:12.5. The TTIP (10.022 g) was dissolved in Ethanol (64.97 g) with stirring. The acetyl acetone (4.589 g), acetic acid (1.9056 g) and distilled water (7.0955 g) were added and the solution was stirred for 2 hours and sonicated for 30 minutes. The electrospun, stabilised mats were dipped into the above-mentioned sol-gel and removed at a rate of 10mm/min, dried in an oven for 60 min at 100°C and calcinated in nitrogen at 800°C. Carbon tissue was also dipped into the TTIP sol, dried and stabilised.

- (b) TBT sol-gel on PAN

A sol-gel was prepared according to Wang (2013) by separating with ethanol into equal parts. One part was mixed with acetone, the other mixed with water. The ethanol/acetone solution was mixed with TBT and acetyl acetone and mixed for 30 min. The ethanol/water solution was added and the solution was mixed for 2 h and aged for 72 h.

Electrospun, stabilised PAN fibres were dipped into this precursor for 1 minute and dip-coated by a homemade dip coater. The fibres were coated with a withdrawal speed of X m/s. These coated fibres were dried at 100°C and calcinated in nitrogen at 800°C.

### (c) $\text{TiCl}_4$ sol-gel on PAN

Titanium tetrachloride was used to prepare a Titanium ethoxide  $[\text{Ti}(\text{OEt})_4]$  precursor. A solution of 2.24 M was prepared by adding 37.54 ml Ethanol to 12.35 ml  $\text{TiCl}_4$ . This is an exothermic reaction and has to be conducted in an ice bath with vigorous stirring (Nyamukamba, 2011). The solution has a yellow colour. An ethanol/water (50/50) solution was then added to the  $\text{Ti}(\text{OEt})_4$  for hydrolysis to occur. This was also prepared in an ice bath with vigorous stirring (colourless solution). This solution is then heated and stirred for 2 hours. The carbon fibre tissue was then dipped into the solution, stabilised and carbonised. Electrospun PAN mats and a commercial carbon fibre were dipped into TTIP solutions at a slow rate to form  $\text{TiO}_2$  particles immobilised on the outside of fibres after hydrolysatation and heating for calcination.

#### Characterisation of the immobilised $\text{TiO}_2$ in and on PAN

The electrospun fibres with the titanium-based additives were analysed by SEM at the University of Cape Town Electron Microscopy Unit. Energy dispersive X-ray analyses (EDX) and elemental mapping were conducted on the same SEM microscope.

## 5.2 CHARACTERISATION OF PAN ELECTROSPUN FIBRES AND MATS

This section presents the results and discussion of the characterisation of developed nanoparticles as powders and immobilised on electrospun scaffolds.

### 5.2.1 PAN electrospun fibres – the role of electrospinning (ES) parameters on fibre formation

Micrographs of ES nonwoven mats produced using an 8% PAN solution in a DMSO solvent are shown in Figure 5.2, and micrographs of ES nonwoven mats produced using a 12% PAN solution in a DMF solvent are shown in Figure 5.3. The PAN solvents, DMSO and DMF, were shown to be interchangeable. The average fibre diameter for the 8% PAN as-spun mat was 213.2 nm; after stabilisation at  $240^\circ\text{C}$ , the average fibre diameter was 141.6 nm. For the 12% PAN, as spun, average fibre diameter was 1000.6 nm, and for the stabilised fibres, 810 nm. The shrinkage is expected during the stabilisation process. The surfaces of the fibres was smooth and the mats were bead-free. The 8% PAN with the lower concentration and thus thinner fibres was selected for further experiments.

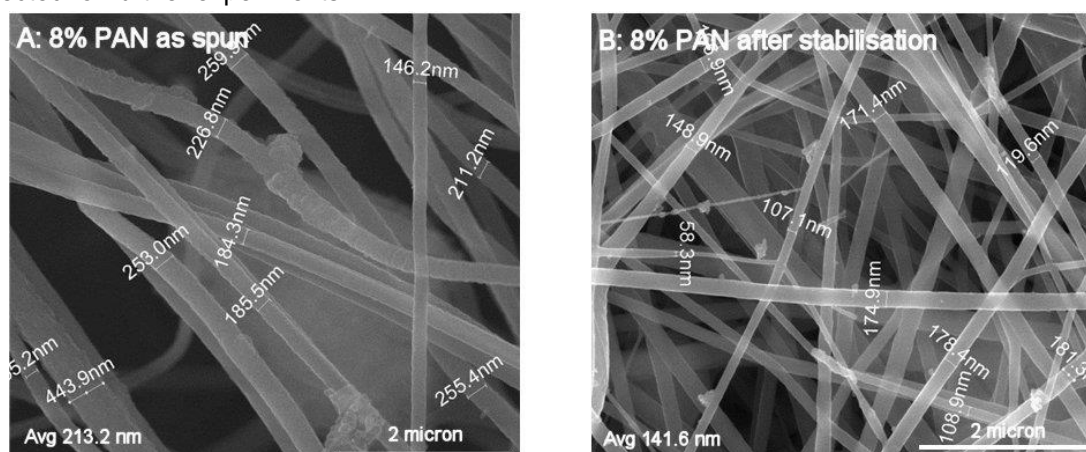


**Figure 5.2 Micrographs of 8% PAN/DMSO, as spun and after stabilisation**

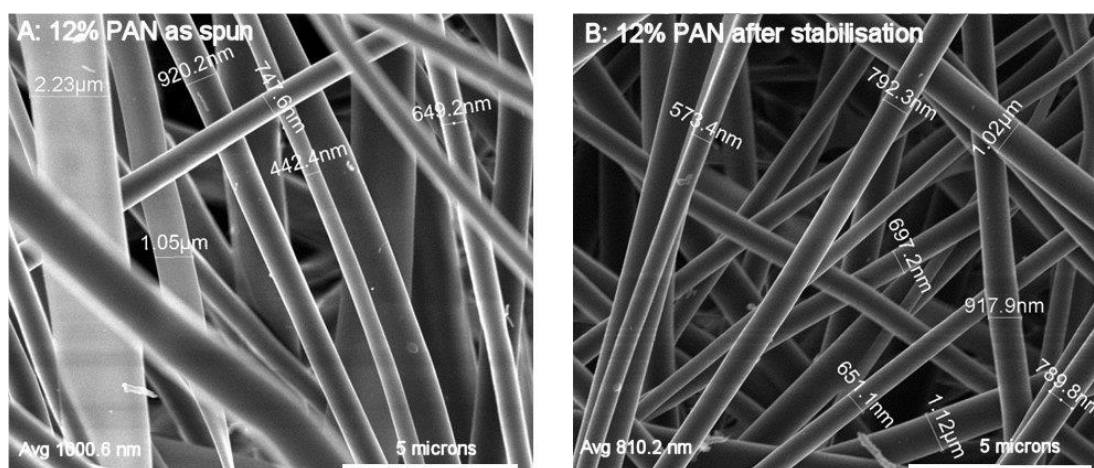
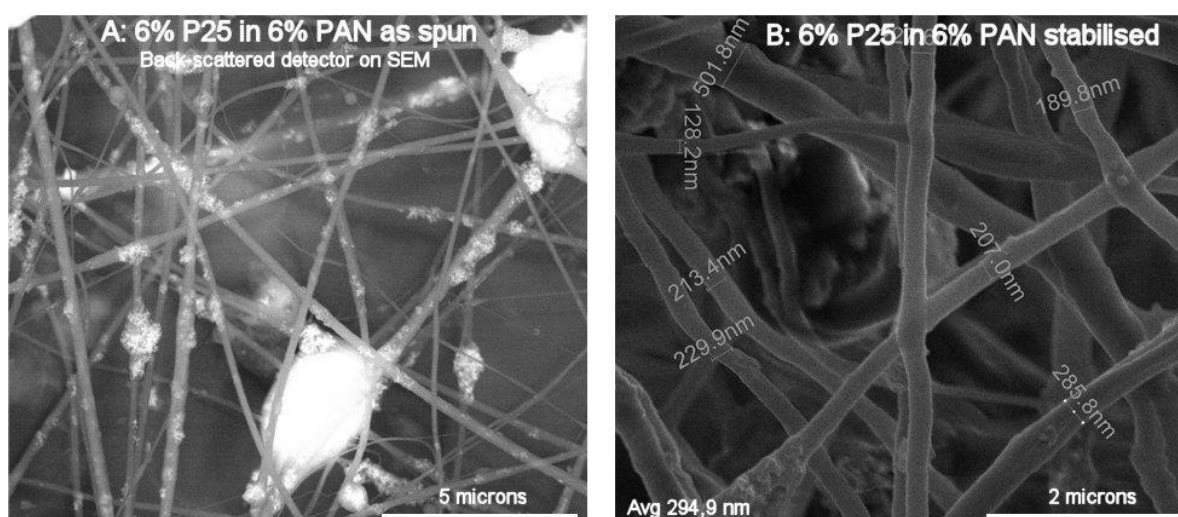


**Figure 5.3 Micrographs of 12% PAN/DMF, as spun and after stabilisation**

### 5.2.2 Immobilisation of nanophotocatalyst particles in and on PAN fibres

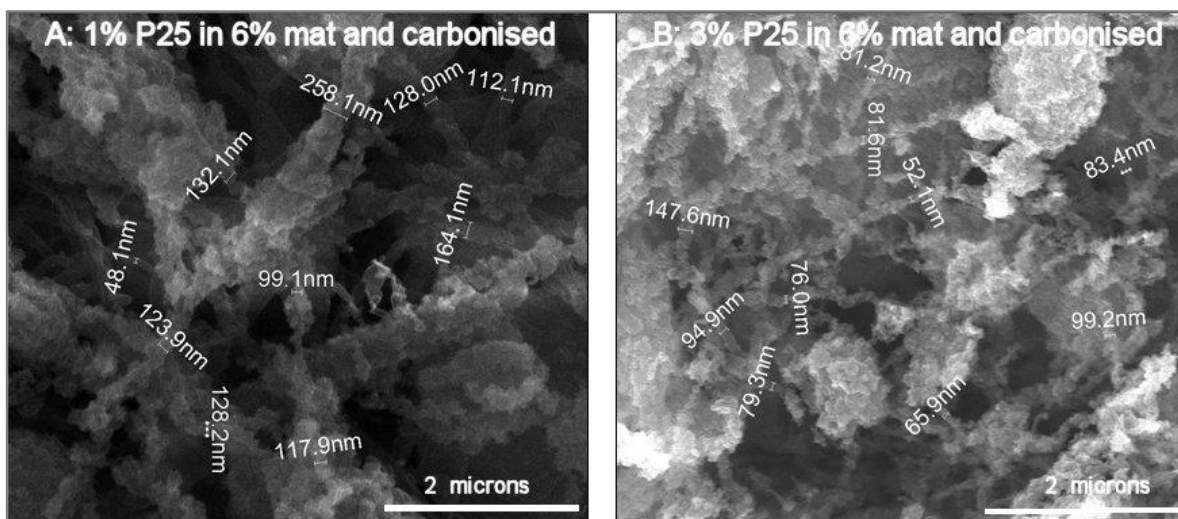
Micrographs for fibres spun with P25 dispersed in the spinning dope with 6% P25 are provided in Figure 5.4, as spun and after stabilisation. Figure 5.4 A was recorded using a back-scattered detector which shows the titanium-rich domains. The clusters of the P25 are noted as being in the micrometre range indicating agglomeration of the nanoparticles. This spinning dope had not been sonicated.

Figure 5.4 B shows the stabilised mat of the 6% P25 in 6% PAN fibres spun after sonication. It is noted that the surface of the P25 containing fibres is rougher than the surface of the fibres spun under the same conditions without titanium-based additives. Accordingly, the average fibre diameter, with the nanoparticle additives, is higher, with the average diameter for a 6% P25 in 6% PAN at 294.9 nm versus the plain 6% P25 in 6% PAN fibres with an average diameter of about 100 nm (not shown). Figure 5.5 clearly shows that the homogeneously distributed nano-TiO<sub>2</sub> of P25 are distributed exposed on the surface of the carbonised fibres.



**Figure 5.4 Micrographs of 6% P25 in 6% PAN/DMF, as spun and after stabilisation**





**Figure 5.5 Micrographs of 1% and 3% P25 in 6% PAN/DMF, after carbonisation**

### 5.2.3 Results and discussion for ES PAN mats with $\text{TiO}_2$ precursors in the spinning dope

#### TTIP, titanium based precursor in the electrospinning dope

Micrographs of the as spun and stabilised fibres from titanium tetra-isopropoxide (TTIP) mixed into the ES 6% PAN dope are presented in Figure 5.6. The average fibre diameters are 774.3 nm and 546 nm respectively for the as spun and stabilised fibres. The EDX elemental mapping presented in Figure 5.7 shows a homogeneous distribution of titanium from the TTIP within the stabilised PAN/TTIP fibres. The titanium present is still in the precursor phase but the process of  $\text{TiO}_2$  production within the fibre has already started. The Ti species are not yet exposed on the surface.

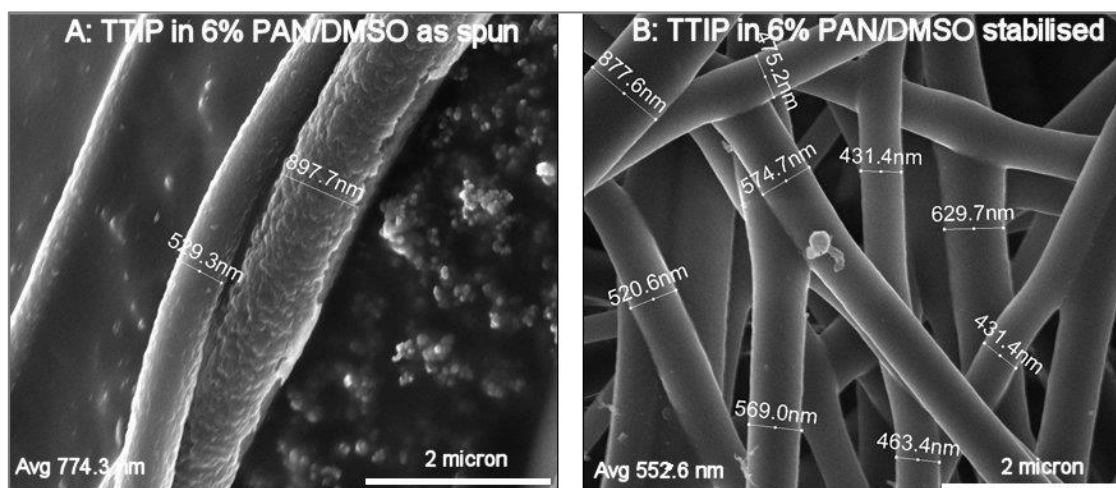


**Figure 5.6 TTIP in 6% PAN/DMSO as spun and stabilised**

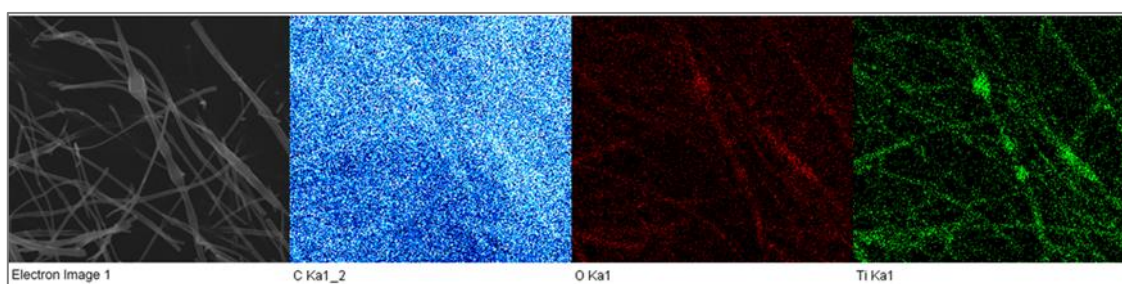


**Figure 5.7 EDS elemental mapping for titanium in TTIP in 6% PAN/DMSO as spun and stabilised**

#### TiCl<sub>4</sub> precursor in the electrospinning dope

Micrographs of the stabilised and carbonised ES fibres of titanium tetrachloride mixed into the ES 6% PAN dope are presented in Figure 5.8. It can be noted in in Figure 4.27 B that where the fibres intercept one can see the fibres below, indicating that the organic fibre has been transformed into an inorganic carbon structure. The average fibre diameter after carbonisation was 138 nm.

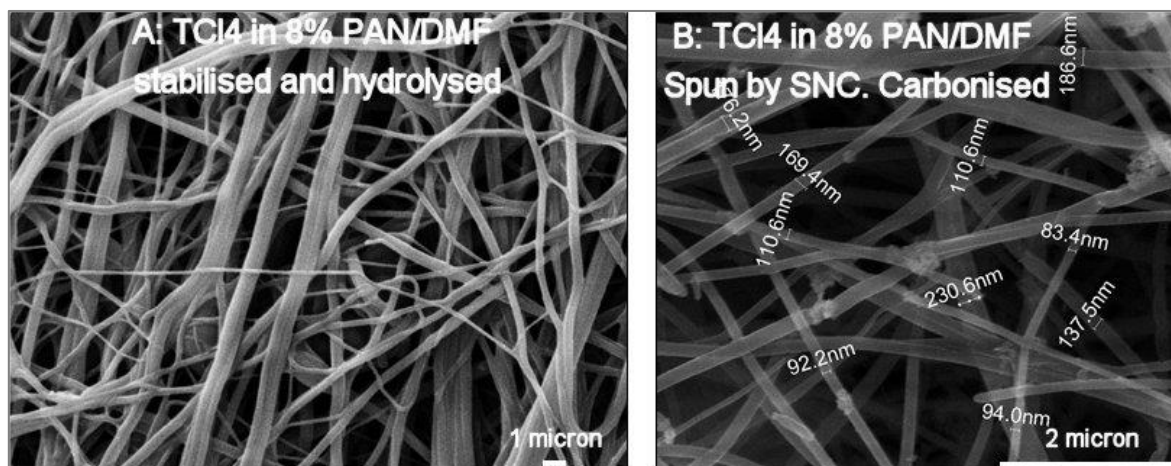


**Figure 5.8 Micrographs of TiCl<sub>4</sub> in 8% PAN/DMF**

The fine, homogeneous diameter fibres were spun by the Stellenbosch Nanofibre Company on a large-scale, electrospinning set-up, for producing mats of up to 2 metres' width, using a patented multi-spinneret system with a spinning dope supplied by the TSCT.

In early method development, the fibres containing TiCl<sub>4</sub> without hydrolysis were found to melt during the stabilisation process as the precursor interrupted the ladder formation of the PAN molecules and thereby lowered the melting temperature. Hydrolysis of the TiCl<sub>4</sub> was conducted by dipping the mat into water (thus forming the TiO<sub>2</sub> particles within the fibre) before stabilisation. The fibre diameter decreases after stabilisation, which allows more nanoparticles to be exposed on the surface of the fibre.

#### **5.2.4 Results and discussion for carbon and PAN mats dipped into TiO<sub>2</sub> precursor solutions**

Figure 5.9 shows the fibres dipped into a solution of TTIP and then stabilised. In Figure 5.9 A. the mat dipped was a commercial carbon tissue mat with micron-sized diameter fibres. This mat was soaked in the TTIP solution and the loading is shown to have been too high as the TiO<sub>2</sub> film coating after stabilisation is thick and had breached between fibres and had not contracted sufficiently to form individual TiO<sub>2</sub> particles.

In Figure 5.9 B an ES 8% PAN/DMF mat was dipped at a very slow rate in a modified TTIP solution. Some fibres are still breached, but in general there was a thin coating over all fibres which provided the growth of TiO<sub>2</sub> nanoparticles on the surface after carbonisation.

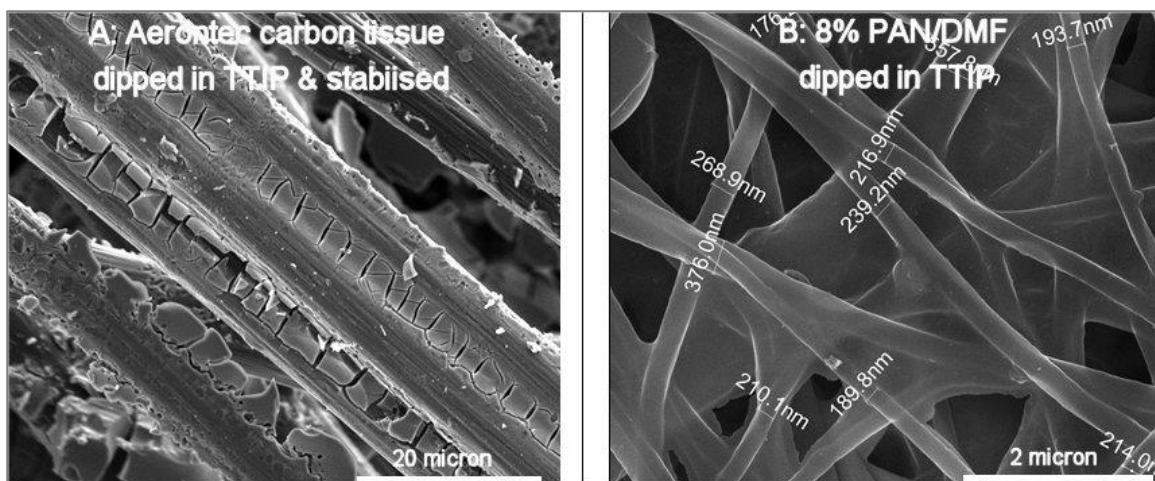


**Figure 5.9 Micrographs of carbon fibre mat and ES PAN dipped in TTIP**

The reason for the film forming between the fibres is because the scaffolds have been removed from the sol-gel too quickly and not at a constant rate and, because the scaffold has a rough surface, the sol-gel will sit in the open spaces. The image in Figure 5.9 B shows an 8% PAN/DMSO mat after being stabilised. It was dipped as slowly as possible (manually) in TTIP and then washed with ethanol. Washing the scaffold with ethanol allows a thin film of precursor to form over the fibres. The fibres still connect to each other with the precursor which is undesired, but if a dip-coating machine is used with a slow speed (1 mm/s), a desired thin film can be attained.

### 5.2.5 Stabilisation and carbonisation of fibres

Polyacrylonitrile undergoes shrinkage during stabilisation and carbonisation. According to a PAN carbon fibre precursor manufacturer, BlueStar Fibres, the about 13 micron precursor shrinks by about 20% during stabilisation and an additional 4% during carbonisation, in the factory process. The degree of shrinkage is controlled by adjusting the tension of the fibres in the furnace. The micron-sized PAN fibres were carbonised at the TSCT, on wire meshes and in a frame, and strong, black-coloured fibres were produced.

Figure 5.10 shows the as-prepared mats before and after stabilisation. The samples are described as a) 6% PAN/DMSO. b) PAN containing  $\text{TiCl}_4$ . c) PAN containing P25 nanoparticles. d) PAN dipped into TTIP precursor and e) carbon tissue dipped in TTIP precursor, and are shown before and after stabilisation.

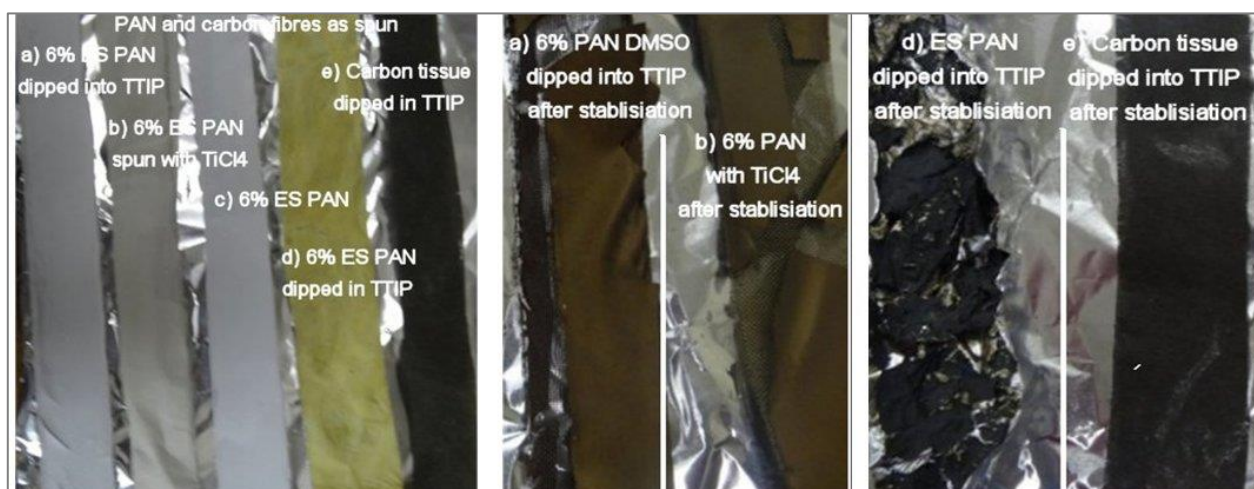


**Figure 5.10 PAN and PAN composites before and after stabilisation**



The first noted deviation from the micron-sized fibre carbonisation was that the ES mats changed in colour from cream to brown, and not black. The scaffolds tended to break/crack.

The effect of varying stabilisation temperatures is shown in Figure 5.11. It was ascertained that the lower temperature of 240°C provided the lowest shrinkage, of less than 20%. These results were obtained by allowing free shrinkage of the mat on a wire mesh inside a loose frame.

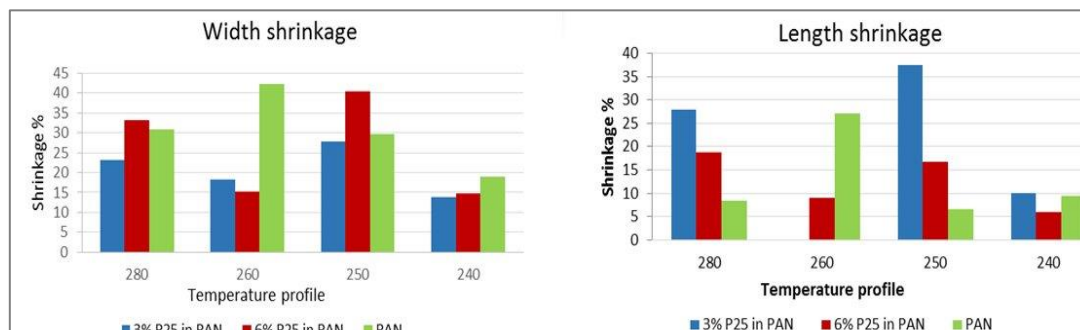


**Figure 5.11 Degree of shrinkage of ES PAN mats during stabilisation and carbonisation**

The degree of shrinkage was found to be dependent on the type of additive in the ES fibres. In addition, the thickness of the mat affected the structural integrity of the stabilised and carbonised scaffolds. The type and concentration of additives such as P25 and titanium precursors affects the required optimum conditions for the stabilisation and carbonisation of ES PAN scaffolds. The optimum conditions for the stabilisation of the ES PAN with and without additives was determined to be a temperature of 240°C with a dwell time of 2 hours on a mesh in a loose frame (to prevent curling). The optimum conditions for the carbonisation of the stabilised fibres was determined to be 700°C in a quartz tube furnace, under nitrogen at a heating rate of 2°C per minute from 240°C. Higher carbonisation temperatures resulted in brittle and cracked mats.

### 5.3 EXPERIMENTAL METHOD OF CATALYST EFFICIENCY IN A TRICKLE-BED REACTOR (TBR)

This section provides the results of evaluation of the various electrospun mats as a photocatalyst in a trickle-bed reactor (fixed-bed reactor) using simulated daylight and UV lamps, (A, B and C) lamp under controlled laboratory conditions. The test solutions included model dyes, methyl orange, Sinaset® acid black and Everzol® navy blue, industrial samples from Falke, dyebath drops, sump samples and NF concentrate samples of acid black and reactive navy blue dyes.

#### 5.3.1 Description of the TBR and light sources used in the TBR experiments

##### The laboratory-scale TBR

The TBR used in this study is shown in Figure 5.12. The effluent to be degraded by the immobilised nanoparticles is placed in a reservoir and pumped from the reservoir to the bed where it is trickled over the scaffolds containing nanoparticles. The surface area of the lab-scale TBR pilot plant is  $31.1 \text{ cm}^2 = 0.0031 \text{ m}^2$ . The flow rate on the peristaltic pump feed to the TBR was set at 1 L/h in order to be equivalent to the average flow flux of TBRs reported in literature of  $0.07 \text{ m}^3 \cdot \text{hr}^{-1} \cdot \text{m}^{-2}$  as shown in Table 5.1

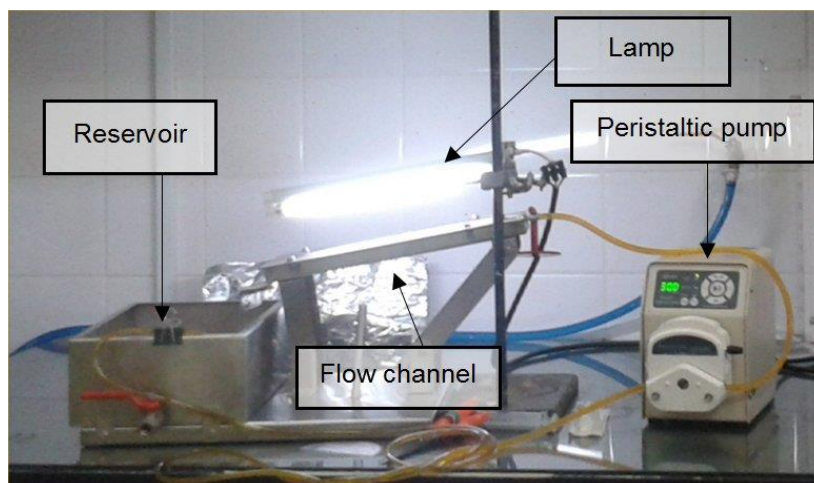


Figure 5.12 The laboratory-scale trickle-bed reactor

Table 5.1 Trick bed reactor parameters from literature

Author	Design	Dye	Flow ( $\text{m}^3 \cdot \text{h}^{-1} \cdot \text{m}^{-2}$ )	Flow flux ( $\text{m}^3 \cdot \text{h}^{-1} \cdot \text{m}^{-2}$ )
Ghanem et al., 2012	Thin-film, fixed-bed reactor $20^\circ$ angle, $25 \text{ m}^2$	Azo dyes	$3 \text{ m}^3 \cdot \text{h}^{-1}$	$0.032 \text{ m}^3 \cdot \text{h}^{-1} \cdot \text{m}^{-2}$
Goswami et al., 2000	Slurry tubular reactor, $15^\circ$ angle $10 \text{ m}^2$	Contaminated ground water. (BTEX))	$3 \text{ m}^3 \cdot \text{h}^{-1}$	$0.045 \text{ m}^3 \cdot \text{h}^{-1} \cdot \text{m}^{-2}$
Feitz et al., 2009	Coated mesh reactor, $20^\circ$ angle, $3.25 \text{ m}^2$	Phenol	$5 \text{ L} \cdot \text{min}^{-1} = 0.3 \text{ m}^3 \cdot \text{h}^{-1}$	$0.07 \text{ m}^3 \cdot \text{h}^{-1} \cdot \text{m}^{-2}$
Feitz et al., 2009	Packed bed reactor, $20^\circ$ angle $2 \text{ m}^2$	Phenol	$3 \text{ L} \cdot \text{min}^{-1} = 0.18 \text{ m}^3 \cdot \text{h}^{-1}$	$0.141 \text{ m}^3 \cdot \text{h}^{-1} \cdot \text{m}^{-2}$

Raw, stabilised and carbonised scaffolds were placed into the trickle bed, and a channel in which the dye effluent could flow was created. This TBR bed was adjusted to have an angle of  $20^\circ$ . A “T” manifold, that is connected to a peristaltic pump, was placed at the top of the trickle bed and the daylight lamp or UVB/C was placed 1 cm from the scaffold. The peristaltic pump pumped the dye-filled water from the reservoir tank to the “T” manifold and the water flowed over the scaffold with a surface area of  $0.0032 \text{ m}^2$  at a rate of  $0.092 \text{ m}^3/\text{h}$ , whilst exposed to the lamps. Dye water was collected from the reservoir every hour and analysed for the decrease in dye/effluent concentration over time.

#### The characterisation of light sources

The average horizontal irradiation in the Western Cape, South Africa, is  $2200 \text{ kWh/m}^2$ . The height of the 9 W daylight lamp was set at 1 cm above the catalyst mat, to be equivalent to actual daylight irradiance. The spectral output of the lamps was measured and the results are provided in Figure 5.13. As expected, the daylight lamp had the highest output within the visible light spectrum between the wavelengths of 420 nm and 760 nm.

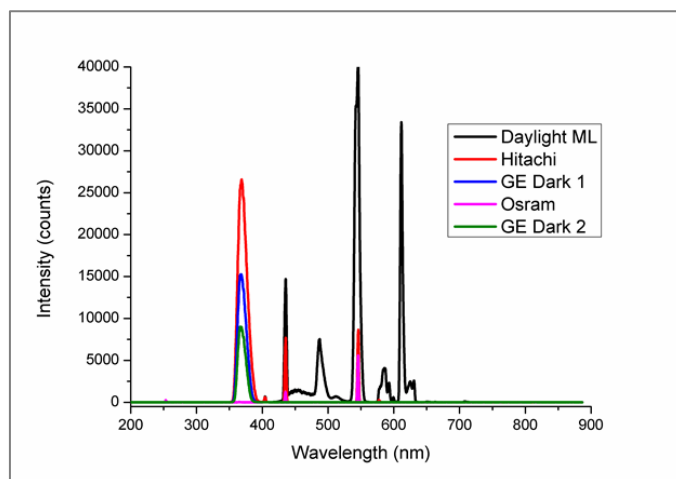


Figure 5.13 Spectral output of lamps used in the TBR experiments

Table 5.2 Lux and lumen values of lamps used in the TBR experiments at 1 cm from the lamp surface

	Chinese ML (daylight)	Osram (UVA)	Hitachi (UVB)	GE Dark 2 (UVB)	GE Dark 2 (UVB)	Outside in cloudy conditions
Lumens	0.056	0.0036	0.003	0.0001	0.0000	0.24
Lux	1480	110	80.1	3.36	1.90	6600

The luminescence of the Chinese ML daylight lamp at varying distances. At a distance from the lamp of 10 mm, the lux value of the lamp most closely represents the typical irradiance of sunlight in the Western Cape, South Africa. As can be seen, the outside conditions had a higher lux value than all the lamps measured at a distance of 80 mm. The Chinese lamp was used at a distance of 10 mm.

Table 5.3 Measurement of the daylight lamp intensity at different distances above the catalyst

Distance (mm)	Lux	Lumens	PAR
80	1 930	0.075	31
70	2 470	0.097	35
60	3 170	0.13	50
50	3 750	0.15	58
40	4 610	0.18	72
30	6 000	0.24	93
20	8 600	0.34	135
10	>10 000 (Off scale)	0.65	250

#### Mats with immobilised $\text{TiO}_2$ used in the TBR experiments

The degradation efficiencies of the following ES mats were used in the degradation studies.

- 3% P25 in 8% PAN/DMSO electrospun, as spun
- 6% P25 in 8% PAN/DMSO electrospun, as spun
- Hydrolysed TTIP in 8% PAN/DMSO electrospun, as spun
- Hydrolysed TTIP in 8% PAN/DMSO electrospun, stabilised
- $\text{TiCl}_4$  in 8% PAN/DMF from SNC
- 6% PAN/DMSO mats dipped in hydrolysed TTIP
- 6% PAN/DMSO mats dipped in hydrolysed TTIP, stabilised

- Carbon tissue dipped in hydrolysed TTIP
- Anatase TiO<sub>2</sub> in 8% PAN/DMF, as spun
- TiO<sub>2</sub> nanofibres electrospun from TBT, PVP calcined.

#### Experimental method for evaluating model dyes

The concentration used for degradation was 50 ppm for all model dyes used in the TBR. A stock solution of 500 ppm methyl orange, acid black and Eversol® navy blue was prepared from the powder dyes, for the calibration curves for each of the 3 model dyes, standards with 10, 20, 30, 40 and 50 ppm. These samples were analysed on a scanning UV/VIS spectrophotometer (Pharo 300 from Merck) at Community Water and Sanitation Services at Cape Peninsula University of Technology. For the dye degradation in the TBR the stock solution was diluted to provide 100 ml solutions of 50 ppm. The samples were analysed with the UV/VIS every 60 minutes by withdrawing a 3 ml aliquot. During analysis, the TBR was stopped. The analysed sample was then added back into the TBR feed and the volume was made up to 100 ml to compensate for evaporation.

#### Plant sampling points of real textile effluent

The real effluent tested (Figure 5.14) and the sampling points were as follows:

- Dye bath drop: This sample was taken directly from the stream flowing to the sump; dye bath sump line.
- Sump: This sample was taken from the first holding tank. This tank draws directly from the sump before any filtration occurs.
- NF brine: Taken from the concentrate line of the NF filter.
- NF permeates: Taken from the final filtration (has therefore undergone UF and NF).



**Figure 5.14 Falke Synoset® acid black and Everzol® navy blue samples**

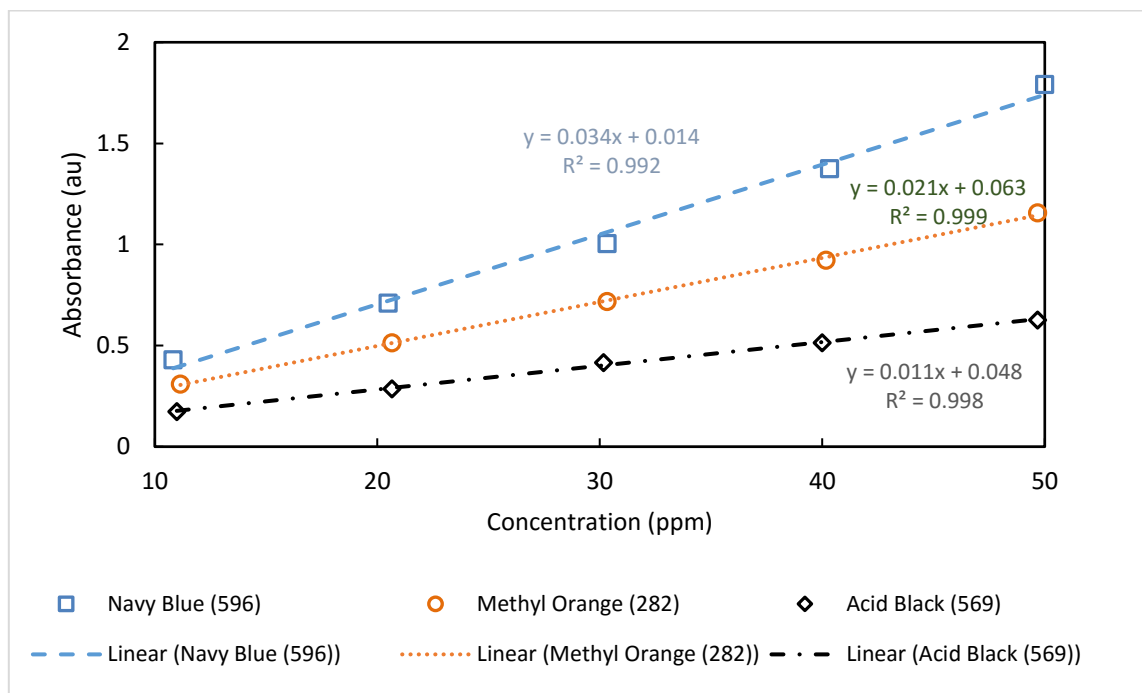
## **5.4 RESULTS AND DISCUSSION OF THE TREATMENT OF MODEL DYES IN THE TRICKLE-BED REACTOR**

In this section, the results of treatment of model dye stuffs are presented. Methyl orange (MO) was used as a model dye to enable benchmarking with results published in literature. The commercial acid black (AB) and navy blue (NB) dyes were prepared in the laboratory from dye powders obtained from Falke and thus differ from actual effluents as they do not contain any additives, such as buffers or scouring and finishing agents. The results were collected using both a colorimeter at a single wavelength and absorbance scans over a range of wavelengths using a UV/VIS spectrophotometer.

#### Calibration curves for MO, AB and NB

Figure 5.15 shows the UV/VIS results for the calibration of the standard laboratory-prepared dye solutions at 10, 20, 30, 40, and 50 ppm from powder dye samples of MO, AB and NB. All model dyes show a linear relationship between the dye concentration and absorbance on the UV/VIS spectrophotometer in accordance

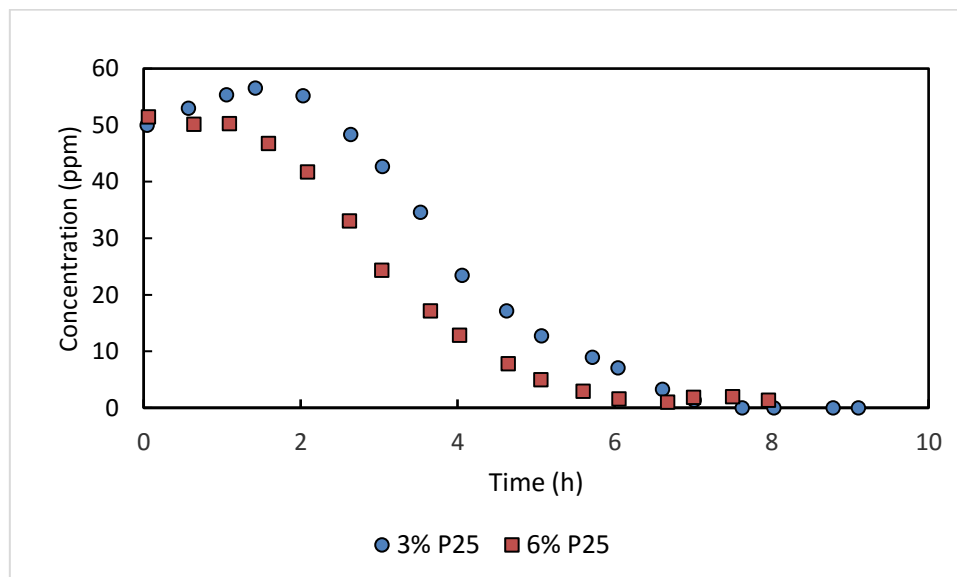
with the Beer-Lambert law, which states that absorbance is directly proportional to concentration. The correlation factors are all close to  $R^2 = 1$  and as such, show a good correlation. The data points provided above are for MO at 282 nm, for AB at 569 nm and the NB sample at 596 nm.



**Figure 5.15 Calibration curves for laboratory-prepared dye samples of MO, AB and NB**

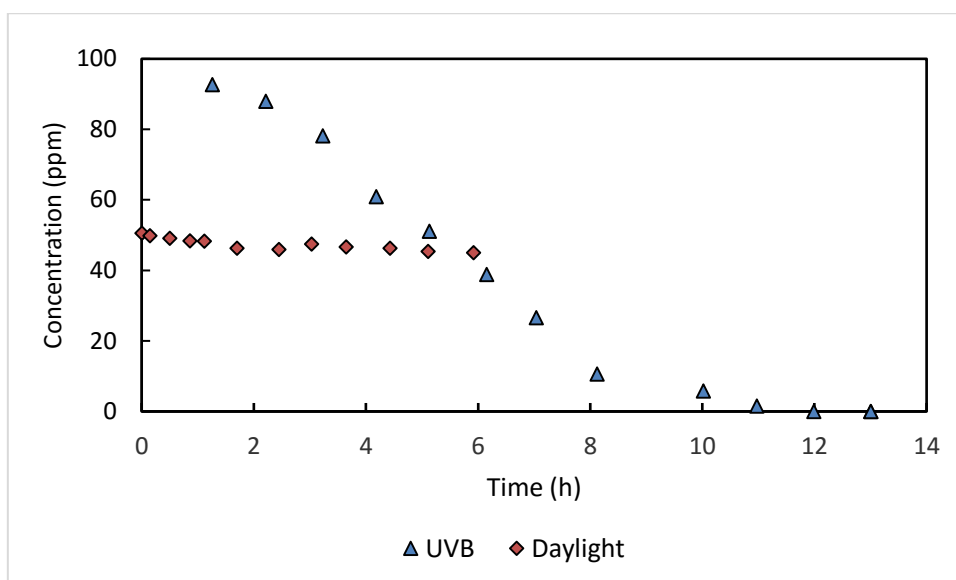
#### MO degradation in the TBR using different lamps on P25 TiO<sub>2</sub> mats

Figure 5.16 shows the rate of degradation under a UVC lamp in the TBR on mats with 3% and 6% P25 in an 8% PAN as-spun mat as measured using colorimetry over time for a 50 ppm MO solution.



**Figure 5.16 Reduction in colour of MO in the TBR with UVC lamp for P25/8% PAN mats**

Under UVC illumination, the 6% P25 mat shows, as expected, a higher rate of decolourisation than the 3% P25 mat. The colour of MO was shown to decrease to zero using the colorimeter after 6 hours on the 6% P25 mat, whereas the 3% mat took 8 hours to decolourise.



**Figure 5.17 Reduction in colour of MO in the TBR with UVB and daylight on 3% P25/8% PAN mat**

The effect of different lamps/illumination energy on the rate of decolourisation was evaluated using a UVB and a daylight lamp. In Figure 5.17, the decolourisation of MO on an as-spun 3% P25 in 8% PAN is presented after treatment under UVB and a daylight lamp. For total colour removal using the lower energy UVB lamp, the time required for treatment was 11 hours versus 8 hours with the UVC lamp. The rate of degradation with the daylight lamp was extremely significantly slower with only a 2% reduction in MO concentration after 6 hours.

#### MO degradation in the TBR using UVC lamp

Electrospun mats of 8% PAN with 3 wt% were prepared and the efficiency of decolourisation of MO was evaluated using UV-VIS spectroscopy as shown in Figure 5.18.

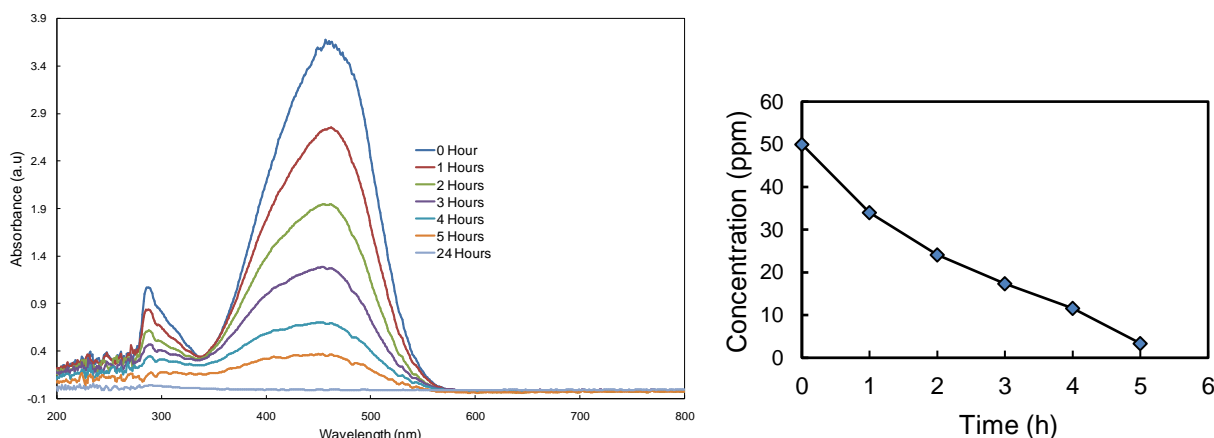


**Figure 5.18 Reduction in colour of MO in the TBR with UVC on 3% TiO<sub>2</sub> anatase 8% PAN mat**

The UV-VIS results measured at 282 nm show that the MO concentration was reduced to 10% after 5 hours and totally reduced by 24 hours, in comparison with the results in Figure 5.17 for the 3% P25, which reduced the MO concentration to 10% after 6.5 hours. This shows that anatase TiO<sub>2</sub> is a more efficient catalyst than the P25 TiO<sub>2</sub>.

### AB degradation in the TBR using a UVC lamp

Figure 5.19 shows the degradation of a 50 ppm Synoset® AB solution prepared from the dye powder after treatment in the laboratory-scale TBR, using a black UVC lamp, and sampled hourly from 1 to 9 hours. The photodegradation was performed on a catalyst mat with 3% P25.  $\text{TiO}_2$  immobilised on a mat as spun from an 8% PAN solution (as-spun, without stabilisation or carbonisation). The data was collected using a UV/VIS spectrophotometer. Figure 5.19 shows a scan across the spectrum from 200 to 800 nm versus the absorbance in arbitrary units. The UV/VIS data of the concentration versus sampling time at a wavelength of 569 nm is also provided.

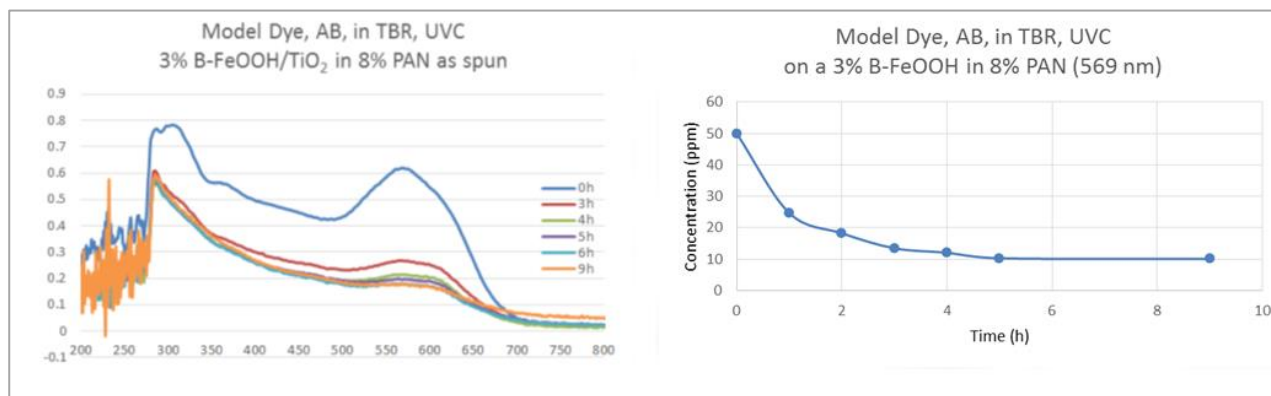


**Figure 5.19 Degradation of laboratory prepared 50 ppm AB in the TBR with UVC**

The results show the presence of two strong chromophores which absorb at about 300 nm in the UV spectrum and at 569 nm in the daylight spectrum are reduced by about 90% after 5 hours' treatment in the TBR using a UVC lamp and a mat of 3% P25 in an 8% PAN. Further treatment time to 9 hours did not increase the degree of degradation of the dyestuff. The presence of the peak at about 300 nm is due to organics in the effluent which have not degraded. The solution was visibly colourless after 6 hours but still contained organics which do not absorb in the visible light spectrum.

The degree of AB dye removal was 80% after 5 hours and did not decrease further after 9 hours' treatment.

## **5.5 DEGRADATION OF THE FALKE EFFLUENT FROM DIFFERENT SAMPLING POINTS**

### **5.5.1 Degradation of the Falke AB sump sample in the TBR**

The Falke AB sump effluent was treated in the TBR with a UVC lamp using a catalyst mat with 3% P25 in 8% PAN. The UV-VIS spectra, from 200 to 800 nm, are shown in Figure 5.20, sampled hourly for 9 hours.



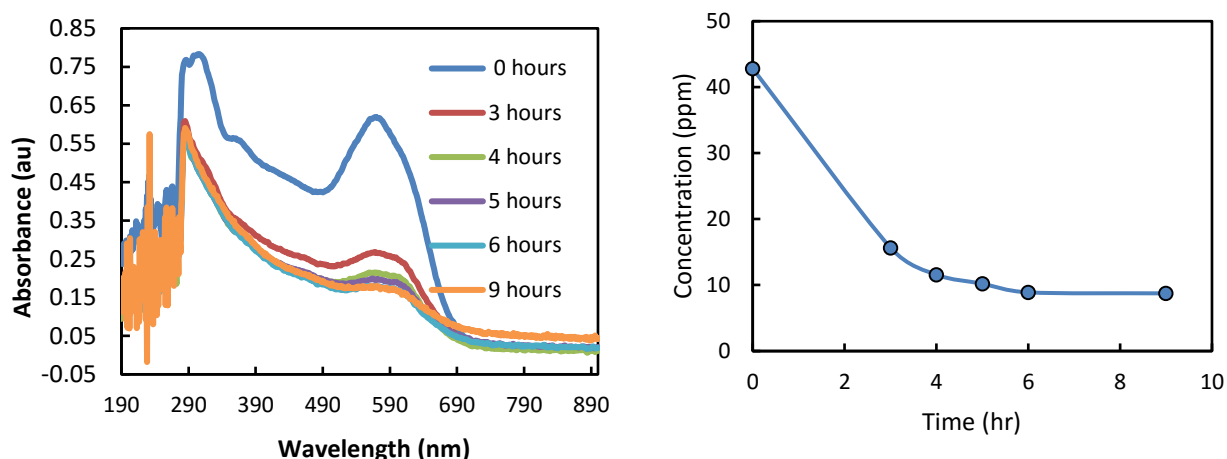


**Figure 5.20 UV/VIS spectra for the degradation of AB sump with UVC on 3% P25/8% PAN**

The spectra show that after 9 hours' treatment under UVC, the colour of AB was reduced by about 60%.

#### Treatment of the Falke NB sump sample in the TBR

The Falke NB sump effluent was treated in the TBR with a UVC lamp using a catalyst mat with 3% P25 in 8% PAN. The UV-VIS spectra, from 200 to 800 nm, are shown in Figure 5.21 sampled each hour for 9 hours. The spectra show that after 3 hours' treatment under UVC, the colour of NB was reduced by less than 10%.

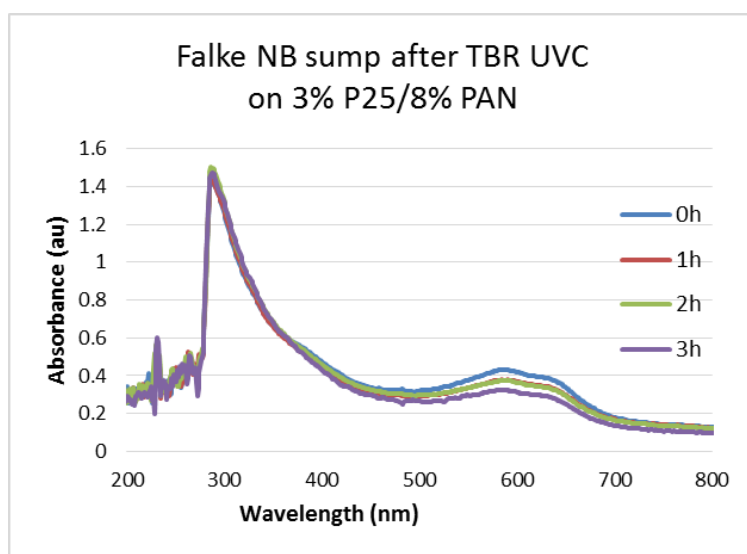


**Figure 5.21 UV/VIS spectra for the degradation of NB sump with UVC on 3% P25/8% PAN**

#### **5.5.2 Degradation of NF brine after treatment in the TBR**

The Falke NB NF brine was treated in the TBR with a UVC lamp using a catalyst mat with 3% P25 in 8% PAN. The UV-VIS spectra, from 200 to 800 nm, are shown in Figure 5.22 sampled each hour for 5 hours.



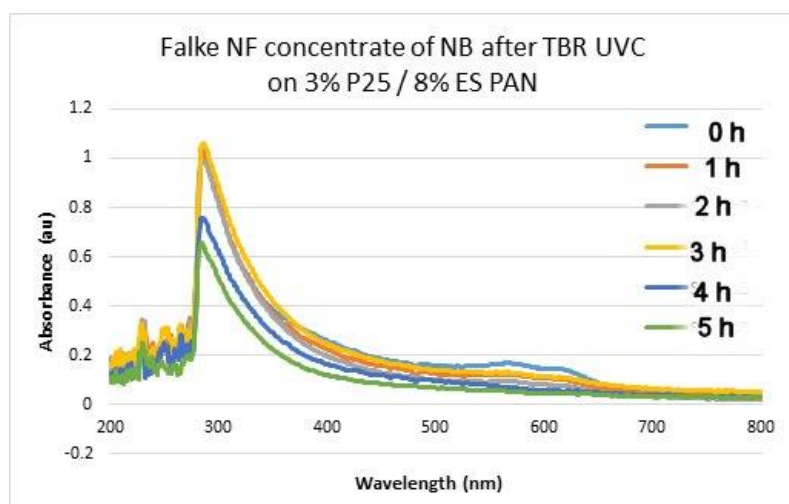


**Figure 5.22 UV/VIS spectra for the degradation of NB sump in the TBR with UVC and a catalyst mat of 3% P25/8%PAN stabilised over time till 5 hours' treatment**

The same Falke NF concentrate was treated in the TBR on a 3%  $\beta$ -FeOOH/TiO<sub>2</sub> mat and results are shown in Figure 5.23.

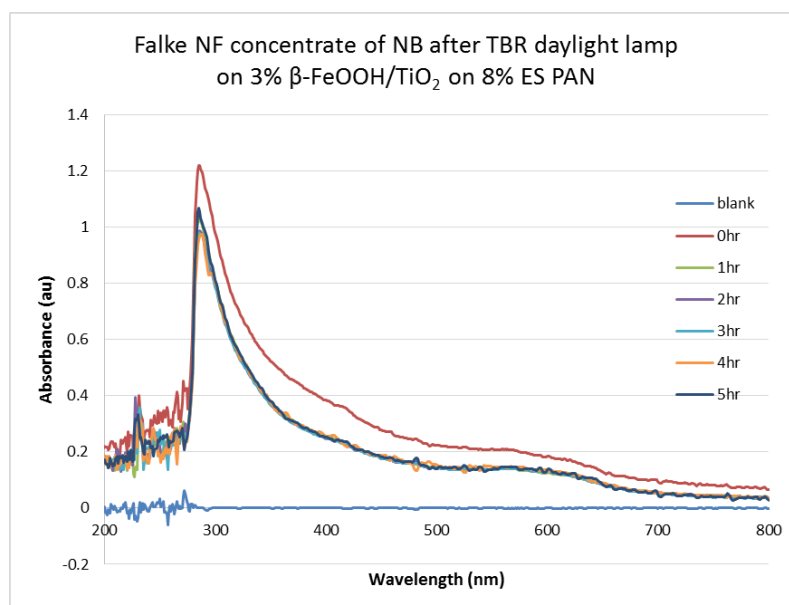


**Figure 5.23 Degradation of NB sump in the TBR with daylight mat of 3%  $\beta$ -FeOOH/TiO<sub>2</sub>/8%PAN**

## 5.6 CONCLUSIONS

Several methods of immobilising TiO<sub>2</sub> inside and outside of electrospun PAN fibres were evaluated using commercial P25 titanium precursors as well as methods to carbonise these mats to be used in a TBR. It was found that the type of spun fibre characteristics was independent of the solvent used and that both DMSO and DMF resulted in useable fibres. The fibre diameter increased with polyacrylonitrile concentration.

Fibres containing TiO<sub>2</sub> on the surface were produced using both TiO<sub>2</sub> precursor solutions or TiO<sub>2</sub> powders. Hydrolysis played an important role in the effective stabilisation of TiCl<sub>4</sub> spun fibres. The optimum temperature

for stabilisation was found to be 240°C as it provided the lowest shrinkage, but the degree of shrinkage was dependent on the type of additive in the electrospun fibre. The optimum carbonisation temperature to prevent brittle and cracked mats was found to be 700°C under nitrogen, compared to 800°C to 1000°C as found in literature.

Both model dye solutions as well as real effluent were degraded in the TBR using electrospun fibre mats with immobilised TiO<sub>2</sub>.

The efficiencies of different lamp were evaluated and were found to be, from best to worst, the UVC, UVB and daylight lamps. To accelerate the evaluation studies, only the UVC lamp was used for comparing the performance of the various types of ES mats.

Degradation studies under UVC irradiation with TiO<sub>2</sub> on 8% PAN mats were found to be most efficient. Degradation increased with the amount of TiO<sub>2</sub> in the ES PAN mat. Anatase containing ES PAN mats appeared to be more efficient than those with P25 and 3% β-FeOOH/Anatase heterojunction-structured photocatalysts. However, this needs to be verified and quantified.

Both AB and NB effluents from the Falke sump could be degraded by up to 60% in the TBR with 3% P25 8% PAN ES mats, in 9 hours.

In summary, techniques to immobilise TiO<sub>2</sub> on electrospun fibres were developed. It was shown that these mats are able to degrade model dye solutions, real effluent from the Falke sump and light colour brines from the nanofilter under UV and daylight.

The industrial potential for the utilisation of the TiO<sub>2</sub> immobilisation techniques developed in this work is great since there is a nanofibre spinning company in Cape Town (Stellenbosch Nanofibre Company) that is able to produce mats of up to 2-metres wide. These larger mats could be incorporated in a multistage thin-film, fixed-bed photocatalytic reactor for upscaling of the process using artificial and/or natural sunlight.

# CHAPTER 6: CATALYST IMMOBILISATION USING CHELATING LINKERS AND EVALUATION IN A COMMERCIAL PHOTOCATALYTIC REACTOR

---

This work reports the synthesis and characterisation of TiO<sub>2</sub> nanoparticles novelly supported on functionalised electrospun polyacrylonitrile nanofibres.

## 6.1 INTRODUCTION

The use of TiO<sub>2</sub> nanoparticles (TNPs) to degrade organic pollutants has been widely reported in open literature. Such enormous interest in TNPs is owed to their small band gap. Low surface energy and chemical inertness (Leary and Westwood. 2011). The photocatalytic activity of TiO<sub>2</sub> is usually enhanced by a number of methods including metal particle loading, metallic and non-metallic doping, use of co-catalysts, dye sensitisation, and surface functionalisation with organic materials (Inagaki et al., 2014; Daghrir et al., 2013; Dolat et al., 2012; and Ni et al., 2007). However, their large-scale application is accompanied with some short-comings, mainly the removal of spent nanocatalyst from treated effluents (Qu et al., 2013). Hence chemical immobilisation of TNPs onto the surface of nanofibrous supports is highly attractive. This is because nanofibres are characteristic of high surface area per unit mass (in comparison to commercial powders) thereby providing excellent separation ability through settling or filtration (Leary and Westwood. 2011). Thus, by chemically binding TNPs onto the surface of PAN nanofibres (PNFs). The leaching of the spent nanocatalyst would be minimised.

Generally, nanofibres are prepared by a number of methods, viz. self-assembly, phase separation, drawing and electrospinning. Electrospinning is credited for its overall applicability to making nanofibres on a large scale, which is attributed to its simplicity and reproducibility (Fang et al., 2008). Hence, this technique is widely reported for the preparation of PNFs which are thermally stable, chemically modifiable and inert against most organic solvents. In recent years, chemical reactions involving the nitrile (C≡N) groups on the surface of electrospun PNFs, with chelating agents such as ethylenediaminetetraacetic acid (Chaúque et al., 2016, diethylenetriamine (Hong et al., 2015; Kampalanonwat and Supaphol, 2014; Deng et al., 2003) and amidoxime (Anirudhan and Ramachandran, 2008) have been reported. PNFs can be subjected to heat treatment under specific experimental conditions to undergo dehydrogenation and cyclisation reactions (Wang et al., 2012). This process allows the formation of a ladder-like structure of carbon fibres with enhanced robustness, inertness and thermal stability (Nataraj et al., 2012). These properties make PNFs an interesting material to serve as a support for TNPs.

It has also been discovered that carboxylic groups can attach to the surface of TNPs through either physical (such as electrostatic attraction and hydrogen bonding) or chemical interactions (such as ester linkage, bridging and chelation) (Qu et al., 2010; Lin et al., 2008). However, the hydrolysis of the ester linkage in aqueous solution limits its application in non-hydrolytic media. On the other hand, the bridging and chelation of the TNPs with the modifying molecule finds suitability for application in the aqueous environment.

A simple physical incorporation of TNPs on nanofibres was recently reported to be achievable by electrospinning a mixture of readily available TNPs or TiO<sub>2</sub> precursor solution and PAN in N,N-dimethylformamide (DMF) or dimethylsulphoxide (DMSO) solvent (Jo and Kang, 2013; Nguyen and Deng, 2012; Wang et al., 2012). Nguyen and Deng (2012) fabricated TiO<sub>2</sub>/PNF with photocatalytic activity in the visible light range by simply electrospinning a mixture of titanium isopropoxide, PAN, acetone and DMSO. In the same year, Wang et al. (2012) also prepared CdS-OH/PAN composite nanofibres by electrospinning a mixture of the CdS-OH nanoparticles' suspension with PAN using DMF as solvent. In the following year, the separate combinations of electrospinning with hydrothermal and electrospray techniques were respectively used to impregnate TNPs on the surface of PAN and polylactic acid nanofibres (Gupta et al., 2013; Su et al., 2013). Similarly, a combination of the solvothermal and electrospinning techniques was also used to introduce bismuth oxychloride (BiOCl) nanosheets onto electrospun PNFs (Chou et al., 2012). The adsorption of TNPs onto the surface of oxidised PAN following heat treatment (T °C ≈ 300) was also suggested by Luo et al.

(2012). However, during the application of physically attached TNPs on the surface of nanofibres (especially in aqueous media), desorption of the TNPs (by elution) may occur due to the weak force of adhesion. Hence, chemical incorporation of TNPs on the surface of nanofibres is highly desirable.

The incorporation of chelating agents on the surface of TNPs is often achieved by either *in situ* or post-modification methodology. The former consists in introducing the modifying agents during the crystallisation of TNPs. This method was implemented by Qu et al. (2010), when carboxylic acids were chemically attached to TNPs using an autoclave reactor at 100°C. On the other hand, the post-modification approach is carried out by simply mixing the TNPs with the modifying agents at room temperature or by ligand exchange. This method was applied by Nakayama and Hayashi (2008) when chemically binding carboxylic and amine groups to the surface of TNPs. In this work, colloidal solutions of TiO<sub>2</sub> were mixed with carboxylic acids and amines at room temperature. However, the post-modification approach usually results in a weak and unstable binding of the modifying agents onto TNPs which may lead to desorption during application (Qu et al., 2010).

Currently, to the best of our knowledge, there is no available research that reports the chemical attachment of TNPs onto the surface of nanofibres using chelating agents as crosslinkers. Hence, this study reports on the chemical immobilisation of TNPs onto the surface of PNFs pre-modified with EDTA-EDA chelating agents. The incorporation of the nanoparticles on the nanofibres was intended to simultaneously explore the combined advantages of composite materials, such as the unique catalytic, optical and magnetic properties of TNPs, along with the excellent thermal stability, chemical inertness and high mechanical strength of PNFs for potential application in the photodegradation of dyes (Inagaki et al., 2014; Leary and Westwood, 2011).

## 6.2 MATERIALS AND METHODS

### 6.2.1 Reagents

Analytical grade reagents such as ethylenediamine (EDA), ethylenediaminetetraacetic acid (EDTA), triethylamine, pyridine, acetic anhydride, diethyl ether, 45% titanium (III) sulphate solution in dilute H<sub>2</sub>SO<sub>4</sub>, methylene blue (MB), methyl orange (MO), NaOH and HCl were sourced from Sigma-Aldrich (Gauteng, South Africa). All reagents were used as received. The PAN fibres, composed of 93% acrylonitrile (AN), 6% methyl acrylate (MA) and 1% itaconic acid (IA) were obtained from BlueStar Fibres Company Limited (United Kingdom).

### 6.2.2 Preparation and modification of PAN nanofibres

PNFs were fabricated using the electrospinning technique and modified with EDTA following the same experimental conditions described in our previous work (Chaúque et al., 2016). Briefly, 12.5% (w/v) PAN-DMF solution was electrospun at a voltage of 15 kV, at a 0.6 mL h<sup>-1</sup> flow rate and 17.5 cm spinneret-collector distance, giving an electric field strength of 0.857 kV cm<sup>-1</sup>.

Ethylenediaminetetraacetic acid dianhydride (EDTAD) was prepared using a procedure from open literature (Geigy, 1969) as follows: 10 g of EDTA was added to a mixture of 16 and 14 mL of pyridine and acetic anhydride respectively, before heating at 7°C for 24 h under N<sub>2</sub> atmosphere. The formed crystals were collected by filtration and washed with dry diethyl ether before oven-drying to constant weight at 50°C.

Thereafter, the electrospun PNFs were modified as follows: ca. 0.2 g of the fibres was refluxed with EDA in a water bath at 95°C for 2 h duration. The obtained aminated PAN nanofibres (EDA-PNFs) were washed with de-ionised water and oven-dried to constant weight. Then EDTA was impregnated on the surface of the EDA-PNFs using 2 g of EDTAD in 40 mL tetrahydrofuran in the presence of an aprotic base (7 mL of triethylamine) in a ring-opening reaction at room temperature under N<sub>2</sub> gas. After the reaction was completed, the pH of the nanomaterial was neutralised using 2 M HCl solution before the material was copiously rinsed with de-ionised water and oven-dried. Finally, the modified (EDTA-EDA-PNFs) nanofibres were stored in a desiccator prior to characterisation.

### 6.2.3 Preparation of composite nanofibres

Into a beaker containing 200 mL de-ionised water of pH 1.75 (the pH was adjusted using 0.1 M solutions of HCl and NaOH), 5 mL of 45% titanium (III) sulphate solution in dilute H<sub>2</sub>SO<sub>4</sub> was added. This was followed by a few drops of H<sub>2</sub>O<sub>2</sub> added until the solution became light blue, under vigorous stirring, indicating an oxidation reaction of Ti(III) to Ti(IV). The solution was continuously stirred in air for 3 h for the oxidation reaction to reach completion which was evinced by the solution becoming colourless. Small pieces of EDTA-EDA-PNFs (approximately 40x40 cm<sup>2</sup>) were immersed and the solution and allowed to incubate in a water bath at 40°C for 24 h. Finally, the as-formed composite nanofibres (TiO<sub>2</sub>-EDTA-EDA-PNFs) were copiously washed with de-ionised water and oven-dried prior to heat treatment at gradient temperature (up to 240°C) in a tube furnace under N<sub>2</sub> gas for 4 h.

### 6.2.4 Photocatalytic test

The photocatalytic activity of TiO<sub>2</sub>-EDTA-EDA-PAN composite nanofibres was determined against MB and MO. A UV light source of 365 nm was exposed in a cylindrical glass photoreactor at a distance of 15 cm. The catalytic test was performed by putting a piece of catalyst (ca. 0.10 g) into 100 mL of 10 and 30 mgL<sup>-1</sup> synthetic water solution of MB and MO respectively. Prior to irradiation, the solution was magnetically stirred in the dark for 30 min to establish an adsorption-desorption equilibrium between the TiO<sub>2</sub>-EDTA-EDA-PAN catalyst and the MB or MO solution. The concentration of MB and MO was determined using the spectrophotometer method.

### 6.2.5 Characterisation techniques

Physical characterisation of test samples was first carried out by assessing the surface area and porosity of pristine and modified PNFs. This was achieved with the aid of a Brunauer–Emmett–Teller (BET) surface area analyser (ASAP 2020. Micromeritics Instruments, USA), using N<sub>2</sub> adsorption and desorption isotherms. Then SEM micrographs were collected using scanning electron microscopy (TESCAN, Performance in Nanospace, Model – Vega 3LMH. no. VG 97 31276ZA) under the following experimental conditions: 50/60 Hz, 230 V and 1300 VA; Vega TC3 software. The Quorum Q 300T ES sputtering apparatus was used to coat the nanofibres with a thin layer of carbon prior to the collection of SEM images. The imageJ™ software was employed to estimate the average diameter of nanofibres with 45 individual segments measurement. By coupling the SEM analyser with energy dispersive X-ray spectroscopy (SEM/EDS), elemental analysis by surface mapping was enabled.

The main chemical characterisation was carried out with a Fourier transform infrared (FT-IR) spectrometer (PerkinElmer Spectrum 100), popularly used to identify the functional groups on solid surfaces. Here, small pieces of PNFs, EDA-PNFs, EDTA-EDA-PNFs or TiO<sub>2</sub>-EDTA-EDA-PNFs were mixed with KBr at a mass ratio of ca. 1:100. Each mixture was pulverised with a mortar and pestle and pressed into a disk to make a pellet prior to the FT-IR analysis in the 4000-450 cm<sup>-1</sup> range.

The core-level C 1s, N 1s, O 1s, Ti 2p spectra were measured using AXIS SUPRA X-ray photoelectron spectroscopy (XPS) equipment. All measurements were taken under the same experimental conditions, as follows: working pressure of 1.8x10<sup>-8</sup> torr, 15 mA emission current, resolution 80, dwell time 100 and sweeps 2. The charge neutraliser mode was applied due to the non-conducting nature of the samples.

Finally, X-ray diffraction (XRD) (Philips, X'Pert PRO MPD mineral powder diffraction) analysis was carried out to investigate the crystallinity of the composite nanofibres. The instrument uses an X-ray source of Cu $\alpha$  radiation beam with an excitation wavelength of 0.15406 nm for the analysis.

## 6.3 RESULTS AND DISCUSSION

### 6.3.1 Surface morphology of the nanofibres

The BET results showed a significant reduction in both the surface area (from 10.58 to 9.88 m<sup>2</sup>g<sup>-1</sup>) and the average pore diameter (from 14.40 to 11.40 nm) following the transformation of pristine PNFs to EDTA-EDA-PNFs. These observations corroborate a recent report on an analogous study by Makaremi et al. (2015). Such depletion in the specific surface area and pore size is attributed to the chelating agents coating the external surface and inner pore walls of the nanofibres. In furtherance, the incorporation of TNPs on the surface of EDTA-EDA-PNFs resulted in a substantial increase in the surface area to 16.84 m<sup>2</sup>g<sup>-1</sup> but a slight reduction of the pore diameter to 8.26 nm. This observation was expected based on the fact that the incorporation of TNPs on the nanofibres increases the total surface area while reducing the space between the nanofibres due to the coating of the external surface.

The surface morphology of nanofibres was further investigated using SEM-EDS couple. Figure 6.1 (a) and (b) show SEM micrographs of PAN and EDTA-EDA-PAN nanofibres, where an average diameter of 289 ± 31 and 288 ± 68 nm. was observed, respectively. From these results, chemical modification of PAN was found to induce mere increase in the average diameter of the nanofibres. This observation agrees with research reported by Zhao et al. (2015), where they partially converted the surface nitrile groups into amidoxime groups for subsequent remediation of trace metal pollution. Although the incorporation of EDA and EDTA on the PNFs changed the distribution of the nanofibres, as proximity increased, the nanofibrous structure of the pure PNFs was not altered (Saeed et al., 2008). In addition, Figure 6.1 (c) and (d) show SEM micrographs and EDS mapping of TiO<sub>2</sub>-EDTA-EDA-PNFs composite, respectively. From these figures, it was observed that the TNPs were attached to the surface of nanofibres. This suggests the preferential attachment of Ti<sup>4+</sup> and posterior self-growth of TNPs on the surface of nanofibres rich with carboxylic and amine groups (derived from EDTA-EDA chelating agents) chemically tethered onto the PNFs. These findings demonstrate that substantial modifications were induced to the structural properties of pristine PNFs when treated with EDTA-EDA complexing agents and Ti<sup>4+</sup> solutions.

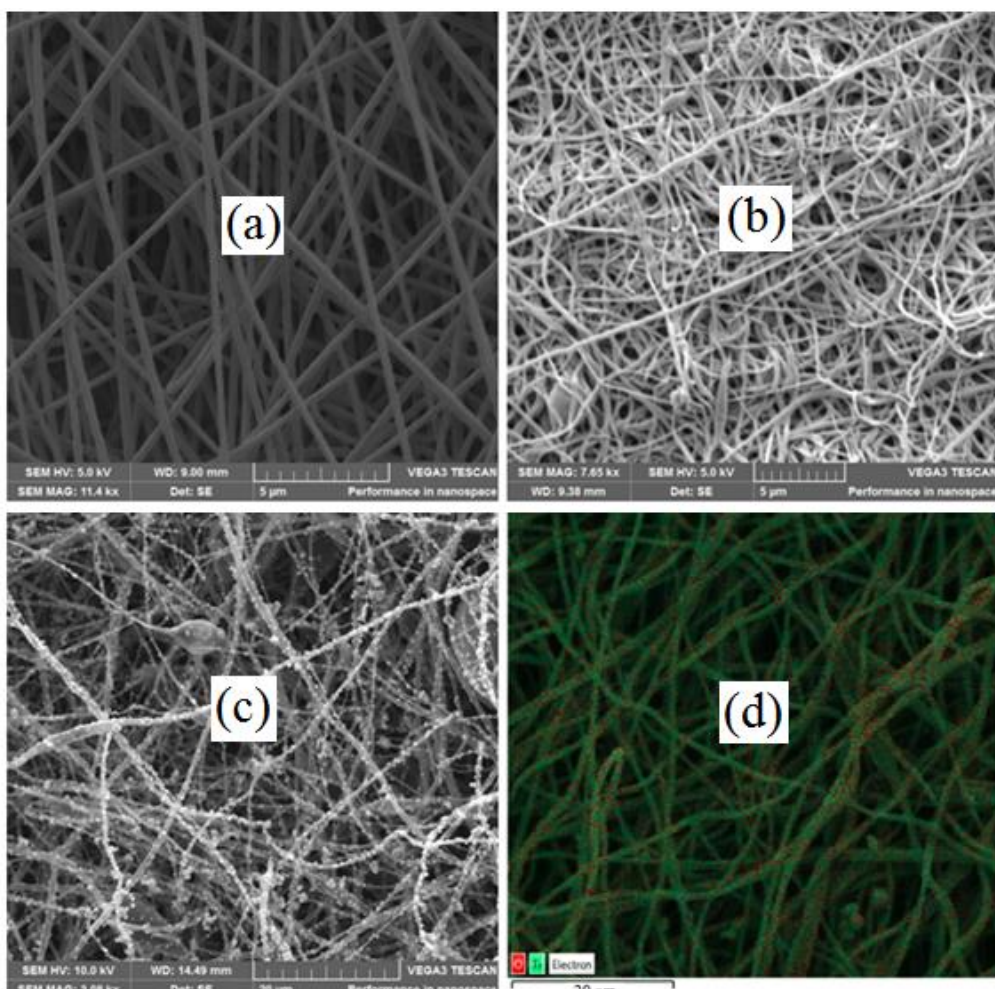


**Figure 6.1 SEM micrographs of (a) pristine PNFs (b) EDTA-EDA-PNFs. (c) TiO<sub>2</sub>-EDTA-EDA-PNFs (d) EDS mapping for Ti and O on TiO<sub>2</sub>-EDTA-EDA-PNFs stabilised at 240 °C for 4 h**

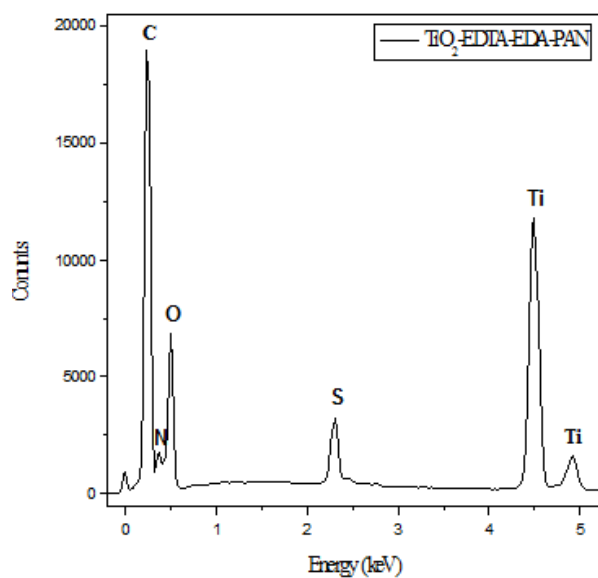


**Figure 6.2 EDS spectra of TiO<sub>2</sub>-EDTA-EDA-PNFs composite.**

### 6.3.2 Surface chemistry of the nanofibres

FT-IR spectroscopy is an analytical technique generally applied for the qualitative determination of functional groups in a wide range of samples. The characteristic tendency of each functional group to absorb IR energy at specific wavelengths is used in their identification. However, closely related functional groups do overlap if occurring simultaneously in the analytical sample. For example, assigning distinctly different peaks to functional groups such as C=C, N=N, and C=N is challenging when two or all of the groups are present in a test sample, given that they all absorb IR radiation at ca.  $1600\text{ cm}^{-1}$  (Fatiadi, 1967). From the IR spectrograms obtained for both pristine and modified electrospun nanofibres, illustrated in Figure 6.3, the absorption frequencies (in  $\text{cm}^{-1}$ ) for the electrospun PNFs are assigned as follows: 3437 (OH stretching). 2939 and 2872 (CH stretching in CH,  $\text{CH}_2$ , and  $\text{CH}_3$  groups), 2243 ( $\text{C}\equiv\text{N}$  stretching), 1734 ( $\text{C}=\text{O}$  stretching), 1454 (CH blending),  $1384\text{ cm}^{-1}$  (symmetric blending of  $\text{CH}_3$  in  $\text{CCH}_3$ ),  $1072\text{ cm}^{-1}$  (C–O stretching in acetate ester).

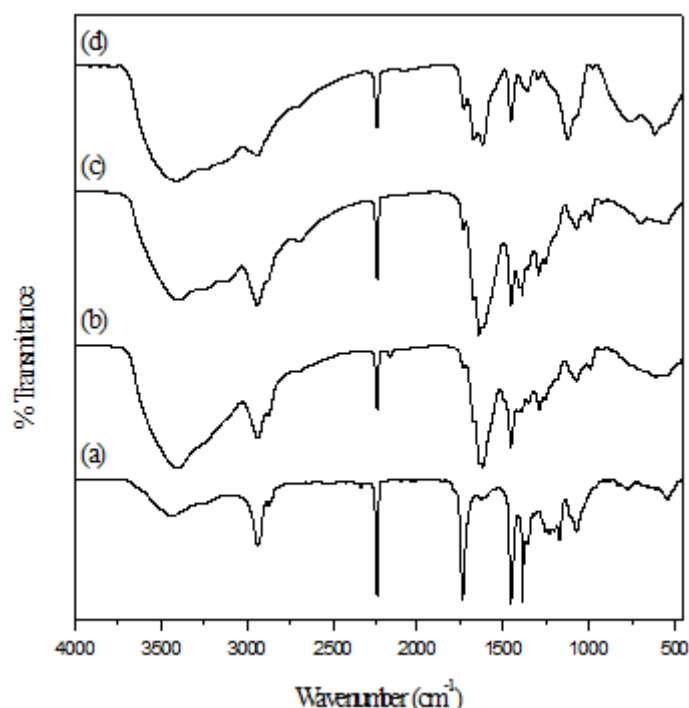


**Figure 6.3 FT-IR spectra of (a) PNFs (b) EDA-PNFs (c) EDTA-EDA-PNFs and (d)  $\text{TiO}_2$ -EDA-EDA-PNFs**

Upon reacting PAN with EDA, significant changes in the spectrum of EDA-PNFs were observed and are described as follows: the weak and broad peak at  $3437\text{ cm}^{-1}$  for the OH stretching in PNFs was transformed to a strong and broad band with maximum frequency at  $3389\text{ cm}^{-1}$  for the EDA-PNFs. This band is derived from the combined intensities of OH and NH stretching and vibration bands on the surface of EDA-PNFs, as similarly pointed out by Deng and Bai (2003), where chemical binding of diethylenetriamine with PNFs was reported. The significant reduction in intensity of the peak at  $2243\text{ cm}^{-1}$  for EDA-PNFs indicates partial conversion of the surface nitrile groups (derived from ethylenediamine attachment) during the formation of the amidine groups ( $\text{N}=\text{C}=\text{N}$ ) which absorb at wavenumber  $1639\text{ cm}^{-1}$  (Zhao et al., 2015; Kampalanonwat and Supaphol, 2010; Anirudhan and Ramachandran, 2008). In addition, the reduction in intensity of the peaks at  $1731\text{ cm}^{-1}$  ( $\text{C}=\text{O}$  stretching),  $1454\text{ cm}^{-1}$  (CH blending),  $1384\text{ cm}^{-1}$  (symmetric blending of  $\text{CH}_3$  in  $\text{CCH}_3$ ) and  $1072\text{ cm}^{-1}$  (C–O stretching) suggests the hydrolysis of the esters of itaconic and methacrylic acid monomers (Deng et al., 2003). These reductions were accompanied by the appearance of new peaks at  $1674$  and  $1612\text{ cm}^{-1}$ , assigned to the stretching vibrations of  $\text{C}=\text{O}$  groups in amides and primary amines ( $\text{NH}_2$ ), respectively. These findings suggest that both amide and amine groups were introduced onto the surface of the EDA-PNFs. After the incorporation of EDTA on the nanofibres (through ring-opening reaction of EDA-PNFs with EDTAD), additional new peaks were observed. The broad band with absorption peak at  $3389\text{ cm}^{-1}$ , characteristic of the EDA-PNFs was substituted by three distinctive peaks at  $3110$ ,  $3250$  and  $3395\text{ cm}^{-1}$  of O–H stretching vibrations in carboxylic acids and N–H stretching vibrations in amines and amides, respectively. In addition, the peaks at



1674 and 1612  $\text{cm}^{-1}$ , respectively associated with the stretching vibrations of C=O in carboxylic and N–H in primary amines, were enhanced on the surface of EDTA-EDA-PNFs.

After the chelation of  $\text{Ti}^{4+}$  ions with surface carboxylic and amine groups of the EDTA-EDA-PNFs (following self-growth of TNPs during the incubation process), additional changes were observed in the FT-IR spectra of the modified PNFs. The peaks at 1670 and 1618  $\text{cm}^{-1}$  associated with the stretching vibrations of C=O in carboxylic and N–H in primary amines, respectively, were significantly reduced on the  $\text{TiO}_2$ -EDTA-EDA-PNFs composite. This observation expectedly evinced the involvement of carboxylic and amine groups in the attachment of the TNPs onto the modified PNFs. Based on these results from the FT-IR analysis. The hypothetical chemical reactions proposed for the modification of the surface of PNFs are illustrated in Figure 6.4

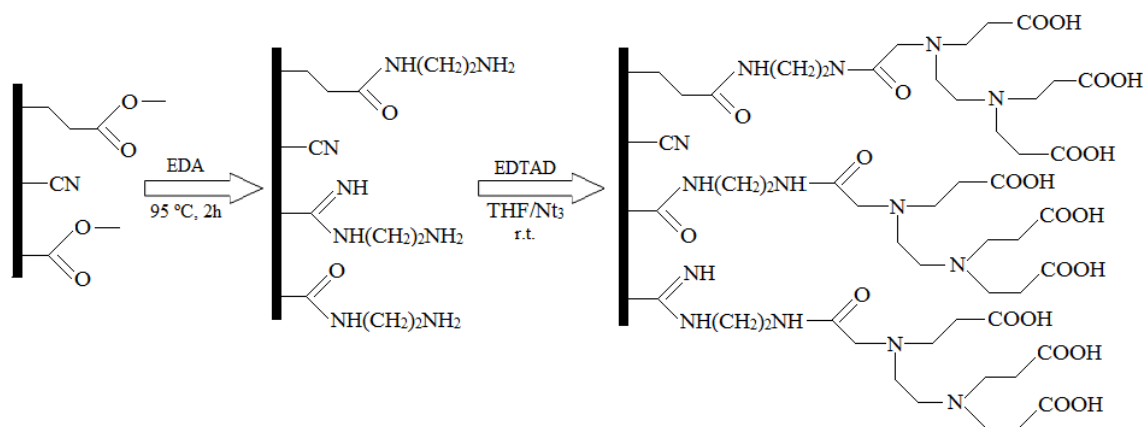


**Figure 6.4 Proposed chemical reaction pathways for the modification of PNFs by EDTA-EDA chelating agent**

The surface chemistry of pristine and modified EDTA-EDA-PNFs subjected to *in situ* incorporation of TNPs were further investigated using the XPS technique. This analytical tool has been applied to assessing the interaction between metals and functional groups on adsorbents' surfaces (Deng et al., 2003). This is particularly achieved by monitoring the alteration in the normal distribution of electrons around the core-level (indicated by the binding energy) of the surface functionalities due to the presence of metal atoms/ions. Thus, electron-donating ligands reduce the binding energy of the core-level electrons while the electron-withdrawing ligands behave otherwise (Deng et al., 2003). The XPS wide range spectra for the EDTA-EDA-PNFs and  $\text{TiO}_2$ -EDTA-EDA-PNF composites are given in Figure 6.5. From these results, it can be seen that the EDTA-EDA-PNF composites exhibit lucid C 1s, O 1s and N 1s peaks. However, the survey spectrum of  $\text{TiO}_2$ -EDTA-EDA-PNF composites shows an additional peak for Ti 2p spin-splitting orbital which indicates the incorporation of  $\text{TiO}_2$  on nanofibres.

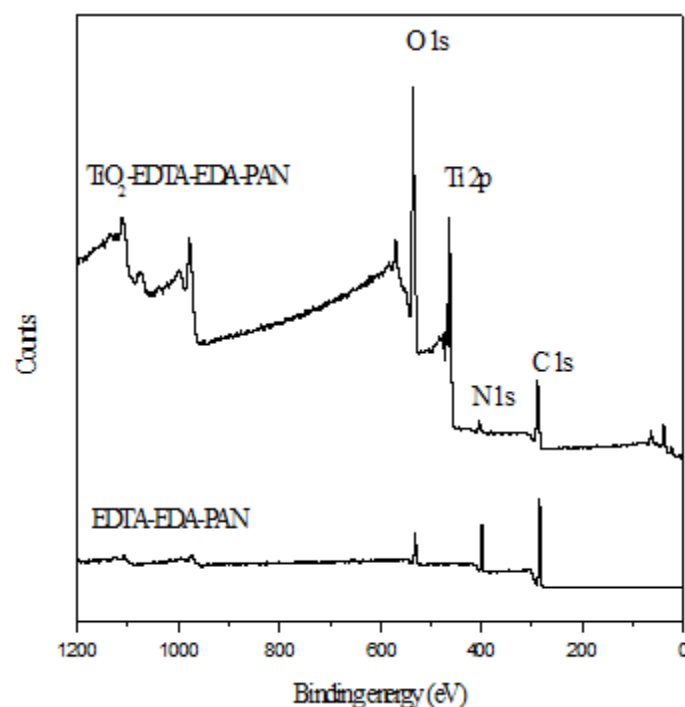


**Figure 6.5 XPS spectra of EDTA-EDA-PNFs and  $\text{TiO}_2$ -EDTA-EDA-PNF composites**

The spin-orbital splitting photoelectrons of  $\text{Ti } 2p^{3/2}$  and  $\text{Ti } 2p^{1/2}$  for  $\text{TiO}_2$ -EDTA-EDA-PNF composites are found at binding energies of 458.85 and 464.75 eV, respectively, as shown in Figure 6.6. The separation between these peaks of 5.90 eV demonstrates that part of Ti is in the form of TNPs. This finding corroborates a report by Erdem et al. (2001), where the Ti 2p doublet peak separation of 5.92 eV was observed for the TNPs used in the polymer encapsulation.

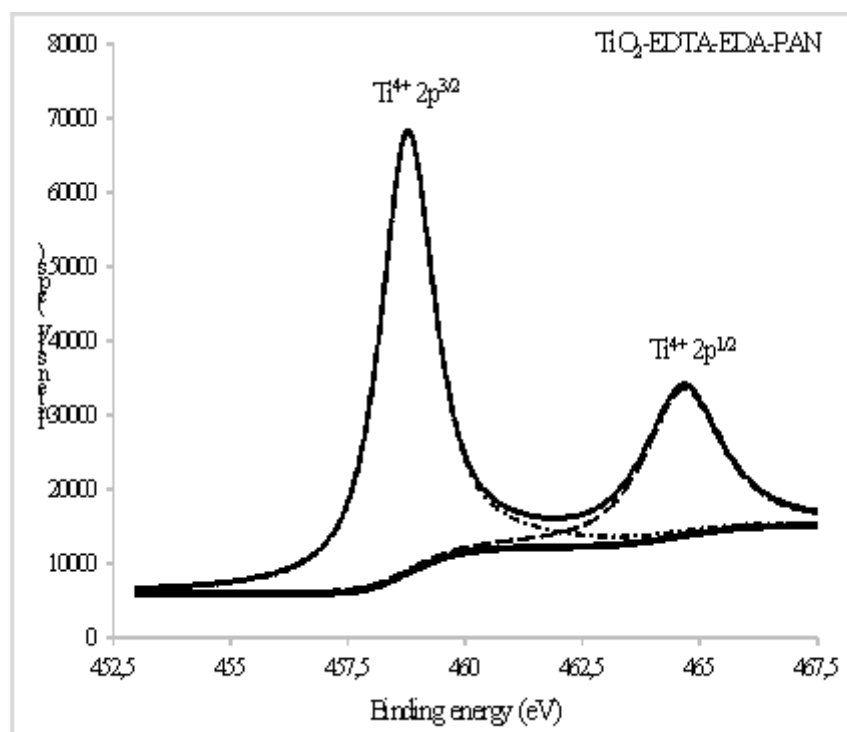


**Figure 6.6 XPS spectra for the Ti 2p states of  $\text{TiO}_2$ -EDTA-EDA-PNF composite**

The deconvolution of O 1s peak of  $\text{TiO}_2$ -EDTA-EDA-PNF composite resulted in four peaks at 530.3, 531.35, 532.2 and 534.2 eV assigned to bulk oxide ( $\text{O}^{2-}$ ), carbonyl, hydroxyl and carboxylic groups, respectively. The binding energies of oxygen species are in line with those available in open literature (Erdem et al., 2001;

McCafferty and Wightman, 1998). The separation of the binding energies for hydroxyl (-OH) and oxide ( $O^{2-}$ ) species is usually within 1.1–1.5 eV but the chemisorption of water molecules can shift it up to 3 eV (McCafferty and Wightman, 1998). Hence, the observed peak separation for the aforementioned oxygen species of 1.9 eV evinced the presence of residual water molecules strongly bound to the fabricated nanofibres. In furtherance, the 71.45 eV difference in the binding energy for the O 1s ( $O^{2-}$ ) and Ti 2p<sup>3/2</sup> is also in line with the reported values for TNPs (Erdem et al., 2001). This observation corroborates the findings about the resolution of the Ti 2p peak described previously and both infer that the TNPs were successfully synthesised and impregnated on the surface of the modified PNFs. The ratio of titanium to oxygen in the TiO<sub>2</sub>-EDTA-EDA-PNFs was determined by integrating the Ti 2p and O 1s peak areas which were corrected by their respective Scofield photo-ionisation cross sections of the core-level photoelectrons, as previously described by Erdem et al. (2001). The titanium to oxygen ratio (Ti:O) of 0.46:1 is not in accordance with the TiO<sub>2</sub> stoichiometry. However, we opine that the excess O atoms on the surface of the nanofibres were derived from the combined contributions of the unbound carbonyl and carboxyl groups from EDTA-EDA chelating agents on the modified PNFs (Figure 6.7).

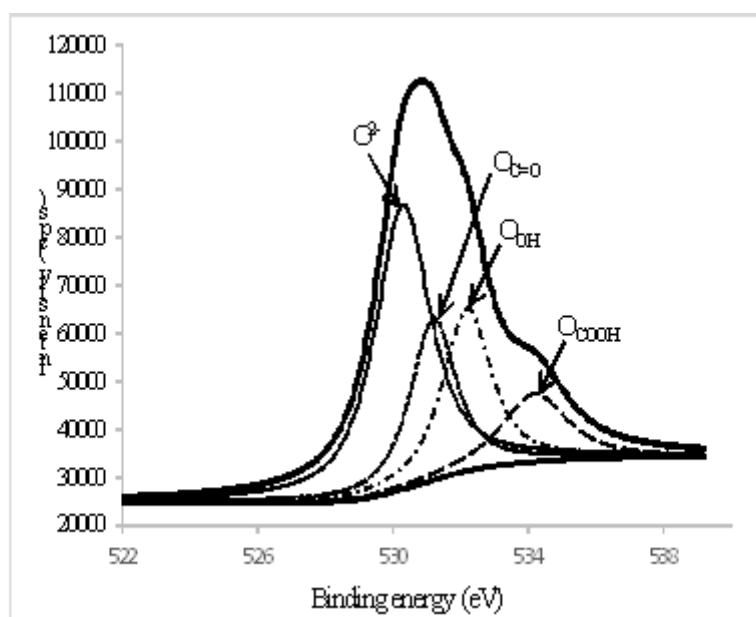


**Figure 6.7 XPS spectra for the O 1s states of TiO<sub>2</sub>-EDTA-EDA-PNFs**

The high-resolution C 1s spectra of the EDTA-EDA-PNFs, in Figure 6.8 (a), show three composing peaks at 284.6, 286.1 and 287.3, assigned to C–C, carbonyl and carboxyl groups, respectively. After the *in situ* incorporation of TiO<sub>2</sub> on the EDTA-EDA-PNFs, considerable changes are observed in the high resolution C 1s peak of the eventual TiO<sub>2</sub>-EDTA-EDA-PNF composites, as shown in Figure 6.8 (b). The peaks at 286.3, 287.6 and 289.6 are assigned to carbonyl, carboxyl and hydroxyl groups respectively. Particular interest is given to the depletion of carboxyl groups (Figure 6.10) and the prominence hydroxyl groups on the surface of the composite nanofibres. The reduction of surface carboxylic groups from 42.97% to 7.3% indicates that the carboxylic groups are directly involved in the attachment of TNPs to the surface of nanofibres via one or more physicochemical interactions such as: (i) electrostatic attraction, (ii) H-bonding, (iii) monodentate (ester-like) linkage, (iv) bidentate bridging, and (v) bidentate chelating (Qu et al., 2010). Also, the appearance of hydroxyl groups indicates the presence of non-calcined TNPs on the nanofibres. This observation is in agreement with that reported by Erdem et al. (2001), where the formation of a layer of -OH covering the outermost surface of TNPs, or an oxide film, was confirmed.

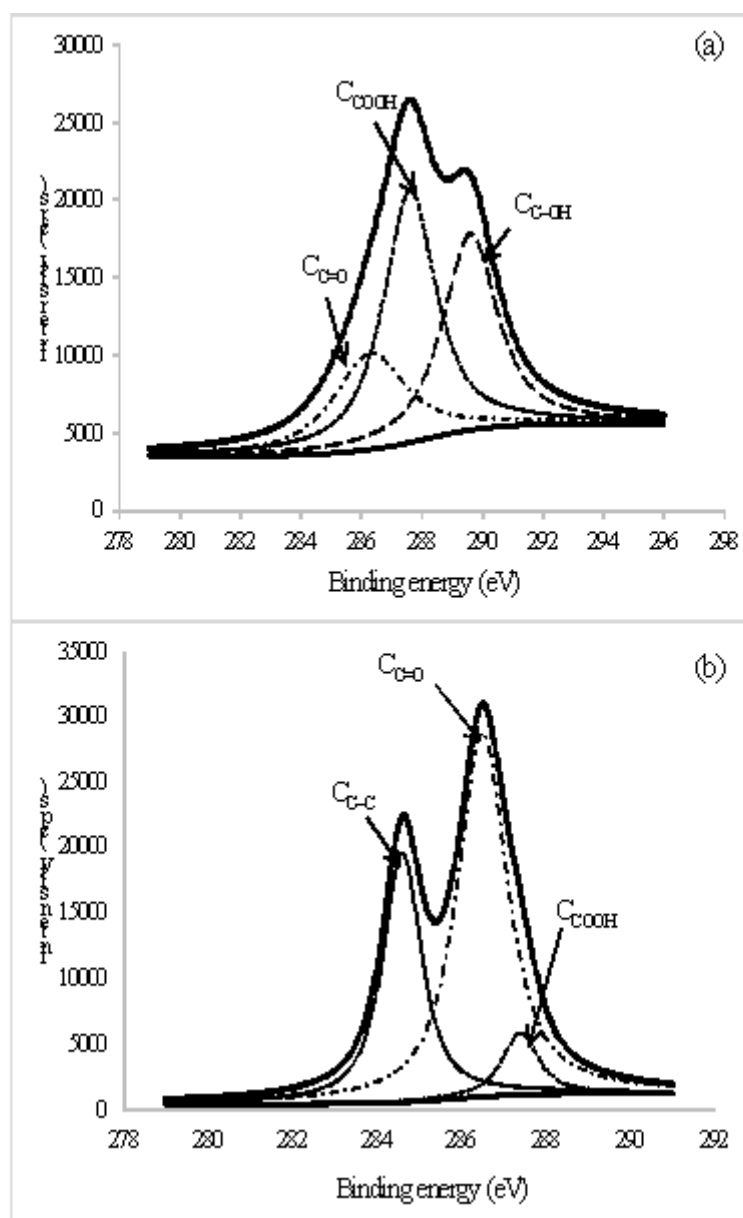


**Figure 6.8 XPS C 1s spectra of (a) EDTA-EDA-PNFs and (b) TiO<sub>2</sub>-EDTA-EDA-PNFs.**

The high resolution N 1s peak for the EDTA-EDA-PNFs, in Figure 6.8(a), shows two peaks at 400 and 401.6 eV, which are assigned to amines ( $\text{-NH}_2$  and  $\text{-NH-}$ ) and  $\pi^*$  orbital delocalised over the amide ( $\text{O=C-NH}$ ) groups respectively (Barazouk and Daneault, 2012; Liu et al., 2006). However, the N 1s curve-resolved for the TiO<sub>2</sub>-EDTA-EDA-PAN composite nanofibres shows considerable changes. The peaks at 400, 401.6 and 405.4 are assigned to amines ( $\text{-NH}_2$  and  $\text{-NH-}$ ),  $\pi^*$  orbital delocalized over the amide ( $\text{O=C-NH}$ ) groups and C–N groups, respectively. However, similarly to the trend given by the carboxyl groups, the surface amine also reduced more than two times from 68.66 to 29.73%. This observation is a good indication that amine groups are also involved in the attachment of TNPs onto the surface of the modified PNFs. Analogous observations were pointed out by Deng et al. (2003), where the lone pair of electrons possessed by the amine N forms a shared bond with lead and copper ions. On the other hand, the increased percentage of the carbonyl and amide groups (Figure 6.10) on the surface of the TiO<sub>2</sub>-EDTA-EDA-PNF composites indicates less involvement of these functional groups in the bond formation with the TNPs' surfaces.

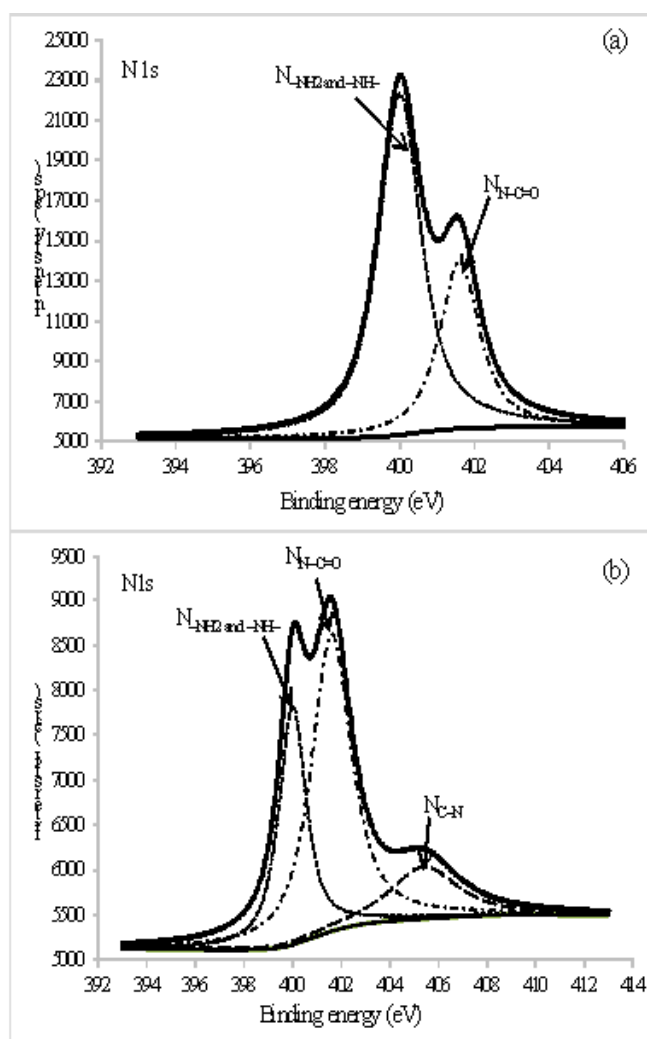


Figure 6.9 XPS spectra for the N 1s states of (a) EDTA-EDA-PNFs and (b) TiO<sub>2</sub>-EDTA-EDA-PNFs

Figure 6.10 Comparison of the surface composition of EDTA-EDA-PNFs and TiO<sub>2</sub>- EDTA-EDA-PNF composites given by C 1s and N 1s peaks

	EDTA-EDA-PNFs			TiO <sub>2</sub> -EDTA-EDA-PNFs		
	BE (eV)	Peak area	% conc.	BE (eV)	Peak area	% conc.
<b>C 1s</b>	—	—	—	284.6	30 796	32.3
	286.3	26 118	22.67	286.1	57 560	60.4
	287.6	49 529	42.97	287.3	6 9701	7.3
	289.6	39 609	34.37	—	—	—
<b>N 1s</b>	400.0	33 978	68.66	400.0	5 245	29.73
	401.6	15 510	31.34	401.6	9 568	54.24
				405.4	2 828	16.03

The morphology of TNPs on the surface of modified PAN nanofibres was further investigated using XRD. The XRD patterns of the EDTA-EDA-PNFs and the heat-treated TiO<sub>2</sub>-EDTA-EDA-PNF composites are given in Figure 6.11. The broad peak with maximum height at 23.63° indicates that the EDTA-EDA-PNFs are in the amorphous phase. Conversely, the XRD peaks of the heat-treated TiO<sub>2</sub>-EDTA-EDA-PNF composites are assigned to TiO<sub>2</sub> (JCPDS Card No. 01-075-2546). Furthermore, the spectrum of TiO<sub>2</sub>-EDTA-EDA-PNF composites, presented in Figure 6.11 (b) shows characteristic peaks at 25.39°, 38.07°, 47.79°, 54.38° and 62.79°, corresponding to the 101, 112, 200, 211, and 204 crystal planes of TiO<sub>2</sub> anatase, respectively (Su et al., 2013; Gupta et al., 2013).

The Scherrer equation, given as equation 1:

$$D = K\lambda/\beta\cos\theta \quad (6.1)$$

where  $K = 0.9$ ,  $\lambda$  is the X-ray wavelength (0.154 nm),  $\beta$  is the full width at half maximum and  $\theta$  is the Bragg's diffraction angle, was used to determine the  $\text{TiO}_2$  particle size (Gupta et al., 2013). The crystallites sizes were found to be 9.37 nm.

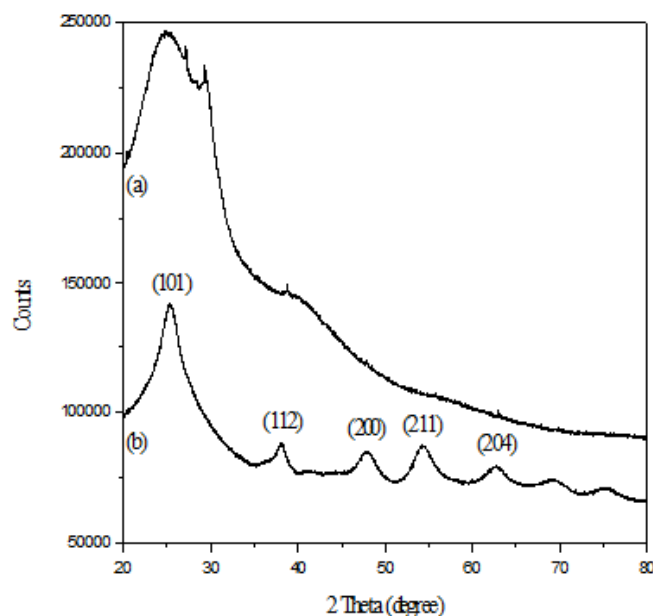


**Figure 6.11 XRD spectra of (a) EDTA-EDA-PNF and (b)  $\text{TiO}_2$ -EDTA-EDA-PNF composites.**

Results shown in Figure 6.11 reveal that the crystallisation of TNPs did not reach completion at the gradient temperature reaching 240°C for 4 h duration. This observation was evinced by the broad characteristic peaks for the TNPs suggesting the presence of a mixture of amorphous and crystallite structures. Higher calcination temperatures were avoided due to the decomposition of EDTA-EDA chelating agents on the nanofibres as demonstrated in our previous study (Cháuque et al., 2016).

### 6.3.3 Photodegradation of dyes

Degradation of MB and MO using  $\text{TiO}_2$ -EDTA-EDA-PAN composite nanofibres under UV radiation was compared to degradation of MB and MO when using commercial  $\text{TiO}_2$  P25 (Figure 6.12). From the results it can be observed that the fabricated composite fibres have higher photocatalytic activity against MO (Figure 6.12 (a)) and the same performance against MB (Figure 6.12 (b)) compared to commercial  $\text{TiO}_2$  P25. Furthermore, the modified nanofibres possessed higher affinity to the dyes compared to the commercial  $\text{TiO}_2$  P25. This observation derives from the fact that when the adsorption-desorption equilibrium was established, and prior to UV irradiation, almost all dye had been extracted to the surface of the nanofibres.

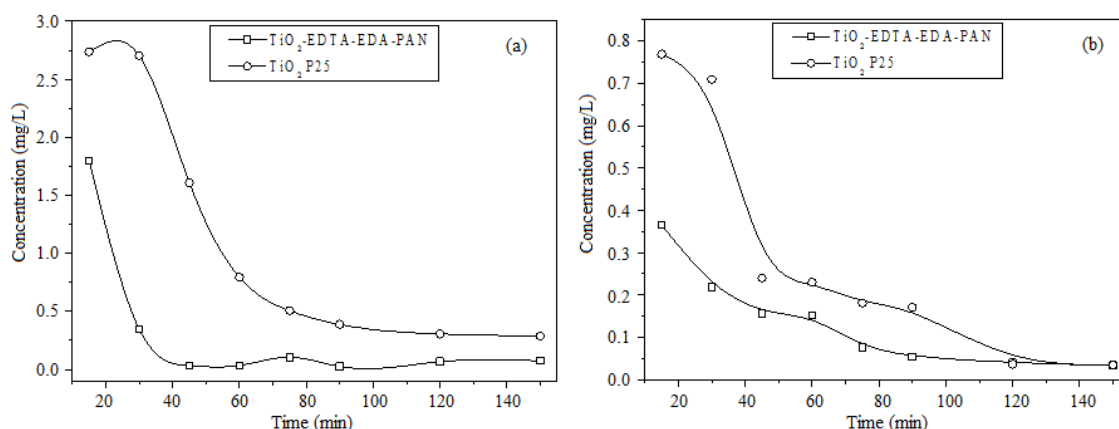


**Figure 6.12 Photocatalytic degradation of MO (a) and MB (b) using  $\text{TiO}_2\text{-EDTA-EDA-PAN}$  and commercial  $\text{TiO}_2\text{ P25}$  (mass of catalyst 0.10 g, volume of solution 100 mL, and an initial concentration of  $30\text{ mgL}^{-1}$  MO and  $10\text{ mgL}^{-1}$  MB).**

## 6.4 CONCLUSIONS

The TNPs were successfully bound to the surface of PNFs using the EDTA-EDA chelating agents. It was observed from the SEM micrographs that TNPs self-assembled at preferential areas on the surface of PNFs and most probably the ones rich in carboxylic and amine functional groups. This observation was further confirmed by the XPS analysis as evidenced by the reduced percentage of surface amine and carboxylic groups after the incorporation of the TNPs on the EDTA-EDA-PNFs. The XRD spectroscopic analyses confirmed the crystallite phase of the synthesised  $\text{TiO}_2$  to be anatase. In summary, the successfully fabricated, novel  $\text{TiO}_2\text{-EDTA-EDA-PNF}$  composites exhibit higher photocatalytic activity compared to commercial  $\text{TiO}_2\text{ P25}$  against MB and MO under UV irradiation. Therefore, fabricated novel  $\text{TiO}_2\text{-EDTA-EDA-PNF}$  composites evince the required nanophotocatalytic properties for the degradation of dyes in an aqueous environment.

## CHAPTER 7: SURFACE MODIFICATION OF PAN NANOFIBRES USING CHELATING LINKERS FOR THE REMOVAL OF DYES

---

This work reports the preparation of polyacrylonitrile nanofibres modified with EDTA for adsorption of methylene blue (MB), methyl orange (MO) and reactive red (RR).

### 7.1 INTRODUCTION

Through the years, as socioeconomic development has relied on industrialisation, environmental pollution was inevitable. Industrial effluents usually contain toxic and hazardous substances. As a result, stringent regulations have been introduced worldwide for ecological restoration. Among the synthetic pollutants released to the aquatic environment, dyes and dyestuffs are of high concern due to their persistence and recalcitrance. Currently, over 280 000 tons of textile dyes are released from industrial effluents per annum (Jin et al., 2007). Among the synthetic dyes, azo dyes find widespread use due to their ability to covalently bond cellulosic materials. These colourants possess broad colour range, brightness, high wet fastness with shade profiles, low energy consumption and ease of application (Solis et al., 2012; Ghoreishi and Haghighi, 2003). During textile processing, large amounts of water (80–100 m<sup>3</sup>/ton of finished textile) are employed. However, inefficient dyeing process usually results in coloured wastewater being released to aquatic systems as their final sinks. These effluents are characterised by strong colouration, high organic matter content (115–175 kg of COD/ton of finished textile), metals, salinity, a broad pH range (pH 3–11), pigments and recalcitrant substances (Savin and Butnaru, 2008). The devastating adverse effect exerted on the ecosystem of receiving water bodies is currently the subject of scientific scrutiny (Nguyen and Juang, 2013; Riu et al., 1997). Hence the viability of dye effluent reuse represents an ecological and socioeconomic challenge for the textile industry.

The treatment of dye wastewater involves physicochemical and biological processes. The use of micro-organisms (i.e. bacteria, protozoa and fungi) is eco-friendly and economically viable but technically challenging (Keskin et al., 2012). This is because biological treatment of dye wastewater demands a lot of space while having restricted design flexibility. The process is also affected by the presence of toxic substances and dark colouration (Brown, 1986). On the other hand, physicochemical treatment of dye wastewater uses processes such as flocculation, coagulation, membrane filtration, ozonolysis, Fenton's reactions, H<sub>2</sub>O<sub>2</sub> under UV radiation, and adsorption (Szpyrkowicz et al., 2001; Kusic et al., 2013). Some of these methods are effective though not economically limiting.

The adsorption of dyes is usually related to the use of activated carbon, organic waste, among others (Root and Minke, 2000). The surface chemistry of adsorbents is widely reported to play a pivotal role in the sorption of dyes and dyestuffs. This is owed to the complex physicochemical nature of dyes which can be grouped as acidic, basic, reactive, direct, disperse, sulphur and metallic dyes (Cooper, 1993; Graham et al., 2001; Al-Degs et al., 2000). The use of powdery adsorbents is advantageous due to a high surface area per unit mass. However, these materials raise challenges concerning the removal of the spent powdery adsorbents which may result in secondary pollution. Hence the use of nanofibres may present an effective alternative for the remediation of organic pollutants from wastewater. This is because nanofibres possess a high surface area per mass ratio compared to commercial powders (Leary and Westwood, 2011). Furthermore, the surface chemistry of nanofibres can also be tuned without necessarily destroying their nanofibrous structure. This is particularly important for the sorption of target pollutants with specific physicochemical properties. Therefore, the use of nanofibres as adsorbents can be advantageous due to the combined high surface area per unit mass, surface chemistry and easy separation of spent nanofibres from treated effluents. In addition, their surface can be modified with suitable functional groups depending on the chemistry of the precursor polymer. The incorporation of chelating agents such as ethylenediaminetetraacetic acid (EDTA) and ethylenediamine (EDA) on the surface of PAN nanofibres can add value in targeting ionic dyes by simply manipulating the pH of the media. Therefore, this study is focused in the modification of the surface chemistry of PAN nanofibres with EDTA-EDA chelating agents for the sorption of MB, MO and RR from synthetic water samples.



## 7.2 MATERIALS AND METHODS

### 7.2.1 Reagents

The EDTA, pyridine, diethyl ether, acetic anhydride, EDA, triethylamine, MB, MO (85%), RB, sodium hydroxide and hydrochloric acid were sourced from Sigma-Aldrich (Gauteng, South Africa). All chemicals, except MB, MO and RB, were of analytical grade. All chemicals were used as received without further purification. The polyacrylonitrile fibres, composed of 93% acrylonitrile (AN), 6% methyl acrylate (MA) and 1% itaconic acid (IA), were sourced from Bluestar Fibres Company Limited (United Kingdom). The dye effluents were sampled from the effluent treatment and water recovery process at Falke Eurosocks, Belville, South Africa.

### 7.2.2 Functionalisation reactions of PAN nanofibres

The surface modification reactions of PAN nanofibres followed the preparation of PAN nanofibres and ethylenediaminetetraacetic acid dianhydride (EDTAD) as precursor materials, as described in our previous work (Chaúque et al., 2016). PAN nanofibres were prepared by electrospinning 12.5% (w/v) PAN solutions in dimethyl formamide (DMF) at 0.6 mL h<sup>-1</sup> flow rate under 15 kV voltage and 17.5 cm distance between the spinneret–aluminium foil collector. The EDTAD was prepared following a procedure given by Geigy (1969). Briefly, 10 g of EDTA was added to a mixture of 16 mL and 14 mL of pyridine and acetic anhydride respectively, which was then heated at 70°C for 24 h under nitrogen atmosphere. The formed crystals were collected by filtration and washed with dry diethyl ether before oven-drying to constant weight at 50°C.

Then the electrospun PAN nanofibres were modified as follows: ca. 0.2 g of the fibres was refluxed with EDA in a water bath at 95°C for 2 h duration. The aminated nanofibres (EDA-PAN nanofibres) were washed with de-ionised water and oven-dried at 60°C to constant weight. Then EDTA was impregnated on the surface of the EDA-PAN nanofibres using EDTAD in tetrahydrofuran in the presence of an aprotic base (triethylamine) in a ring-opening reaction. After the reaction had reached completion, the nanomaterial was neutralised using 2 M HCl solution before being copiously rinsed with de-ionised water and oven-dried at 50°C. Finally, the modified nanofibres (EDTA-EDA-PAN) were stored in a desiccator prior to further use.

### 7.2.3 Instrumentation

The surface area and porosity of the nanofibres was examined using a surface area analyser (ASAP 2020. Micromeritics Instruments, USA). SEM micrographs (TESCAN, Performance in Nanospace. Model – Vega 3LMH. no. VG 97 31276ZA; Vega TC3 software, USA) of pristine and modified PAN nanofibres were collected under the following analytical conditions: 50/60 Hz, 230 V, and 1300 VA. The EMScope SC-500 sputtering apparatus was used to coat nanofibres with a thin layer of gold prior to the surface imaging. ImageJ™ software was used to estimate the average diameter of the nanofibres, with 45 individual segment measurements. The thermal stability of the nanofibres was evaluated using the SDT Q600 V20.9 Build 20 (Simultaneous TGA/DSC, Module DSC-TGA Standard, Belgium). The operating temperature was ramped from 25 to 900°C (at a heating rate of 10°C min<sup>-1</sup>) under nitrogen atmosphere, passed at a 10 mL min<sup>-1</sup> flow rate. The functional groups on the surface of the nanofibres were accessed using the FT-IR spectrometer (PerkinElmer Spectrum 100. USA). Samples of nanofibres mixed with KBr were pelletised prior to analysis in the 4000-450 cm<sup>-1</sup> range. Total organic carbon (TOC) was determined using a fusion UV/Persulphate TOC Analyser (TELEDYNE TEKMAR. USA). The concentration of dyes was estimated using the UV-Vis spectrophotometer (Agilent Technologies, Cary 60 UV-Vis, USA).

### 7.2.4 Adsorption experiments

The adsorption of MB, MO and RR onto EDTA-EDA-PAN nanofibres was carried out batch wise. The adsorption capacities were estimated by introducing 25 mL of dye solution into 40 mL glass bottles containing 0.05 g of nanofibres. The stock dye solutions were prepared from their powders dissolved in Millipore water (type I). The pH of the dye solutions was adjusted using 0.1 M NaOH or HCl solutions. The mixture of dyes and nanofibres was shaken at room temperature at 75 rpm using a bench shaker. After predefined time intervals, the nanofibres were withdrawn from the solution, rinsed with de-ionised water and oven-dried at 50°C

before being stored in a desiccator. The supernatant solution was centrifuged at 4000 rpm and the dye content determined using a UV-Vis spectrometer. Synthetic aqueous dye samples prepared without the addition of nanofibres served as controls. The amount of dyes sorbed onto EDTA-EDA-PAN nanofibres was calculated by the equation given as follows:

$$q_e = \frac{(C_0 - C_e)V}{m} \quad (7.1)$$

where,  $q_e$  is the amount of dye extracted ( $\text{mg g}^{-1}$ ),  $C_0$  and  $C_e$  are the initial and the respective equilibrium dye concentration ( $\text{mg L}^{-1}$ ),  $V$  is the solution volume (L) and  $m$  the amount of EDTA-EDA-PAN nanofibres employed (g).

The effect of pH, initial concentration and contact time for the adsorption of dyes onto EDTA-EDA-PAN nanofibres was also evaluated. This was achieved by varying the initial pH from 3 to 12, and concentration of the adsorbing dye solution from 5 to 300  $\text{mg L}^{-1}$  for up to 30 h.

### 7.2.5 Reusability of EDTA-EDA-PAN nanofibres

Experiments for the sorption and desorption cycles of dyes on EDTA-EDA-PAN nanofibres were carried out to examine the reutilisation of the modified nanofibres. The desorption of dyes from dye-laden EDTA-EDA-PAN nanofibres was performed by washing them with NaOH solution followed by de-ionised water. The sorption/desorption cycles were repeated for five cycles. The desorption ratio (D%) of the dyes was estimated using equation 2 given by Samadi et al. (2015):

$$D\% = \frac{C_d V_d}{(C_0 - C_e)V} \times 100 \quad (7.2)$$

where  $V$  is the volume of the sorption solution (L),  $C_d$  is the concentration of the dye in the desorption solution ( $\text{mg L}^{-1}$ ) and  $V_d$  is the volume of the desorption solution (L).

## 7.3 RESULTS AND DISCUSSION

### 7.3.1 Textural analysis

The BET results showed depletion in both surface area and average pore diameter after modification of the fibres, as a significant reduction from 10.5853 to 9.8820  $\text{m}^2\text{g}^{-1}$  and from 14.40 to 11.40 nm was recorded for PAN and EDTA-EDA-PAN, respectively. These observations corroborate a recent report on a similar study[11]. Such depletion in specific surface area and pore size is attributed to the coating of the impregnants on the external surface and inner pore walls of the nanofibres. However, since the kinetic diameter of Cr(VI) and Cd(II) are 0.206 and 0.218 nm respectively. and the diameter of a water molecule (at room temperature) is 9.58 nm, the mesopores of the fabricated nanofibres are sufficiently capacious as well as narrow to scavenge the targets onto the pore walls as the aqueous medium percolates through.

### 7.3.2 Surface imaging

Changes to the surface of the nanofibres via chemical modification were further investigated using SEM, where alterations in the surface morphology could be monitored. Figure 7.1 shows SEM micrographs of PAN, EDA-PAN and EDTA-EDA-PAN nanofibres, with average diameter of  $289 \pm 31$ ,  $294 \pm 55$  and  $288 \pm 68$  nm, respectively. From these results, chemical modification of PAN was found to induce mere increase in the average diameter of nanofibres. This observation is in line with that reported by Zhao and co-workers (2015) where they partially converted the surface nitrile groups into amidoxime groups for subsequent remediation of trace metal pollution. Although the incorporation of EDA and EDTA on the surface of PAN changed the distribution of the nanofibres, as proximity was increased (accompanied by reduced softness), the nanofibrous structure of the pure PAN nanofibres was not altered.

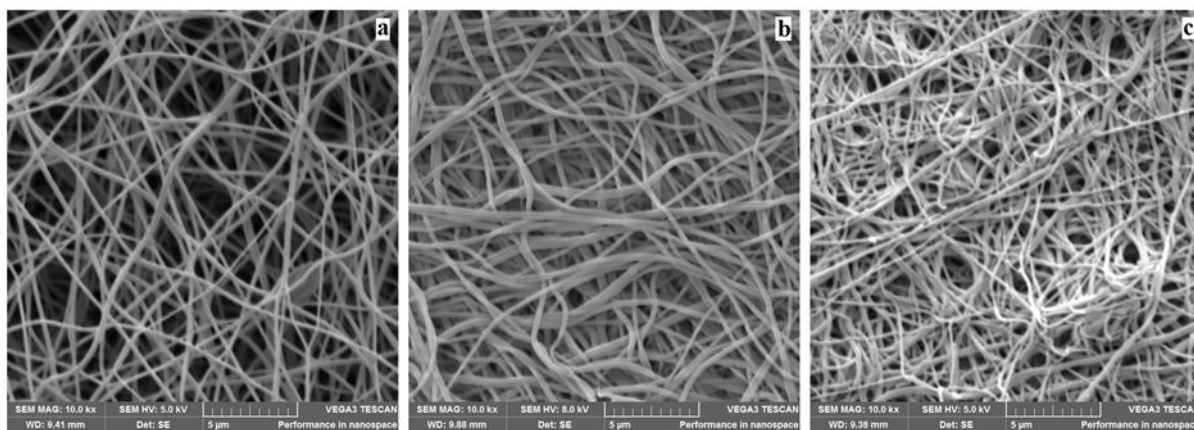


**Figure 7.1 SE micrographs of the (a) electrospun PAN (b) EDA-PAN and (c) EDTA-EDA-PAN nanofibres at  $\times 10,000$  magnification**

From the results obtained from the surface (BET) analysis, porous and micrographic (SEM) investigations, we infer that no significant alterations were induced to the structural properties of the pristine PAN when treated with EDTA-EDA complexing agents. Therefore, we anticipate that any noticeable differences (improvement or depreciation) in the removal efficiencies of neat and modified nanofibres against the target metal ions can be attributed to changes in the fibres' surface chemistry.

### 7.3.3 Thermal properties

TGA thermograms of PAN, EDA-PAN and EDTA-EDA-PAN nanofibres are shown in Figure 7.2. One degradation step was observed for PAN from 280 to 450°C. This phase change could be assigned to the release of nitrogenous gases (i.e.  $\text{NH}_3$  and  $\text{HCN}$ ) due to dehydrogenation, cyclisation, aromatisation and cross-linking reactions of nitrile groups [31,32]. In the case of EDA-PAN, observed weight loss at ca. 117°C could be assigned to loss of moisture content and release of physically adsorbed EDA while weight loss in the range of 143-270°C evinced the thermal degradation of chemically bound EDA to the PAN surface. The chemical transformations of the nitrile groups occurred in the temperature range of 270 to 450°C. Similarly to EDA-PAN, the first weight loss exhibited by the EDTA-EDA-PAN nanofibres occurred in a broad range of 140-290°C as a result of simultaneous loss of moisture and degradation of EDA and EDTA. The chemical transformation of nitrile groups was initiated at around 300°C. In the temperature range 450-900°C, ca. 17% weight loss of the EDTA-EDA-PAN nanofibres was noticed; almost doubling that observed with EDA-PAN nanofibres (ca. 8%) at a similar temperature range. This indicates less thermal stability for EDTA-EDA-PAN and could be attributed to the degradation of both PAN and chemically bound EDTA at the temperature.

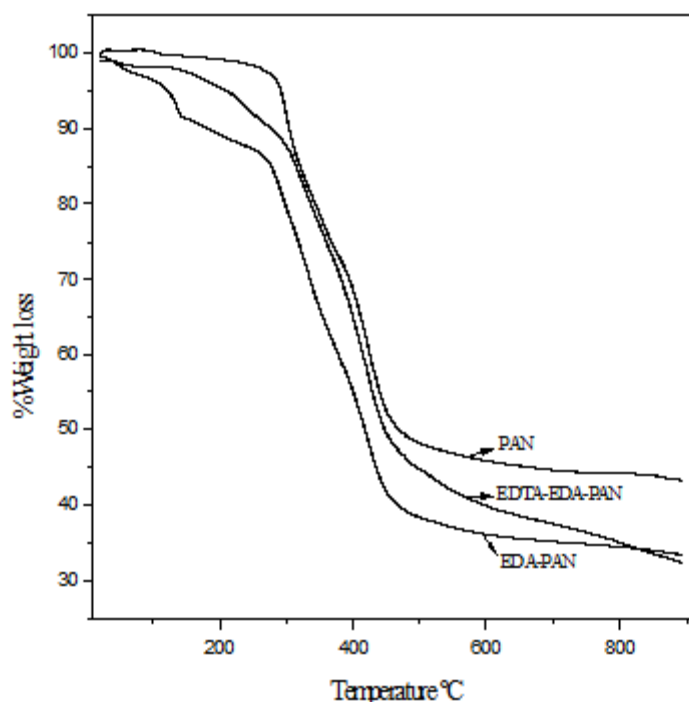


Figure 7.2 TGA patterns of PAN, EDA-PAN and EDTA-EDA-PAN nanofibres

#### 7.3.4 Surface chemistry

FT-IR spectroscopy is an analytical technique generally applied for the qualitative determination of functional groups in a wide range of samples [19]. The characteristic tendency of each functional group to absorb IR energy at a specific wavelength is used in their identification. However, closely related functional groups do overlap if occurring simultaneously in the same substance. For example, assigning different peaks to functional groups such as C=C, N=N, and C=N is challenging when two, or all, of the groups occur simultaneously in a test sample, considering they all absorb IR at ca.  $1600\text{ cm}^{-1}$  [33]. From the infrared spectrograms for the neat and modified electrospun nanofibres, illustrated in Figure 7.3, the absorption frequencies for the electrospun PAN nanofibres are assigned as follows:  $3437\text{ cm}^{-1}$  (OH stretching),  $2939$  and  $2872\text{ cm}^{-1}$  (CH stretching in CH,  $\text{CH}_2$ , and  $\text{CH}_3$  groups),  $2243\text{ cm}^{-1}$  (C≡N stretching),  $1734\text{ cm}^{-1}$  (C=O stretching),  $1454\text{ cm}^{-1}$  (CH bending),  $1384\text{ cm}^{-1}$  (symmetric bending of  $\text{CH}_3$  in  $\text{CCH}_3$ ),  $1072\text{ cm}^{-1}$  (C–O stretching in acetate ester).

Upon reacting PAN with EDA, significant changes in the spectrum of EDA-PAN were observed and are described as follows: the weak and broad peak at  $3437\text{ cm}^{-1}$  for the OH stretching in PAN nanofibres was transformed to a strong and broad band with maximum frequency at  $3389\text{ cm}^{-1}$  for the EDA-PAN nanofibres. This band is derived from the combined intensities of OH and NH stretching and vibration bands on the surface of EDA-PAN nanofibres, as similarly pointed out by Deng and Bai, where chemical binding of diethylenetriamine with PAN fibres was reported. The significant reduction in intensity of the peak at  $2243\text{ cm}^{-1}$  for EDA-PAN nanofibres indicates partial conversion of the surface nitrile groups with ethylenediamine during the formation of the amidine groups (N–C=N) which absorb at wavenumber  $1639\text{ cm}^{-1}$  [13.29.34]. In addition, the reductions in intensities of the peaks at  $1731\text{ cm}^{-1}$  (C=O stretching),  $1454\text{ cm}^{-1}$  (CH bending),  $1384\text{ cm}^{-1}$  (symmetric bending of  $\text{CH}_3$  in  $\text{CCH}_3$ ) and  $1072\text{ cm}^{-1}$  (C–O stretching) suggest hydrolysis of the esters of itaconic and methacrylic acid monomers. These reductions were accompanied by the appearance of new peaks at  $1674$  and  $1612\text{ cm}^{-1}$ , assigned for the stretching vibrations of C=O groups in amides and primary amines ( $\text{NH}_2$ ), respectively. These findings suggest that both amide and amine groups were introduced onto the surface of the EDA-PAN nanofibres. After the incorporation of EDTA on the surface of the nanofibres (through a ring-opening reaction between EDA-PAN nanofibres with EDTAD), additional new peaks were observed. The broad band with absorption peak at  $3389\text{ cm}^{-1}$  characteristic of the EDA-PAN nanofibres was substituted by three distinctive peaks at  $3110$ ,  $3250$  and  $3395\text{ cm}^{-1}$  of the O–H stretching vibrations in carboxylic acids and N–H stretching vibrations in amines and amides, respectively. In addition, the peaks at

1674 and 1612  $\text{cm}^{-1}$  associated with the stretching vibrations of C=O in carboxylic and N–H in primary amines. Respectively, were enhanced on the surface of EDTA-EDA-PAN nanofibres.

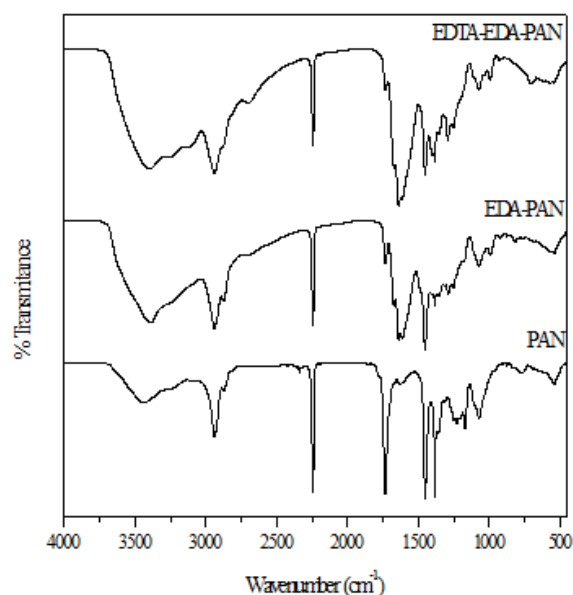


**Figure 7.3 FT-IR spectra of the as-prepared and modified electrospun PAN nanofibres**

From the FT-IR data analysis, the proposed chemical reactions for the modification of the surface of PAN nanofibres are illustrated in Figure 7.4.

### 7.3.5 Electrostatic properties of nanofibres

The  $\xi$  potentials of the PAN and EDTA-EDA-PAN nanofibres at various pH values are shown in Figure 7.4. For pristine PAN nanofibres,  $\xi$  potentials are positive at pH values below 1.3. After modification with EDTA using EDA as the cross-linker, various carboxylic and amine groups were introduced on its surface. As a result, the pH at zero point of charge ( $\text{pH}_{\text{zpc}}$ ) shifted from 1.3 for PAN to 7.6 for EDTA-EDA-PAN nanofibres. A plausible reason for this effect is protonation of the surface of the nanofibres. A similar finding was previously reported by Deng and Bai [19] when introducing OH and NH groups to the surface of PAN fibres.

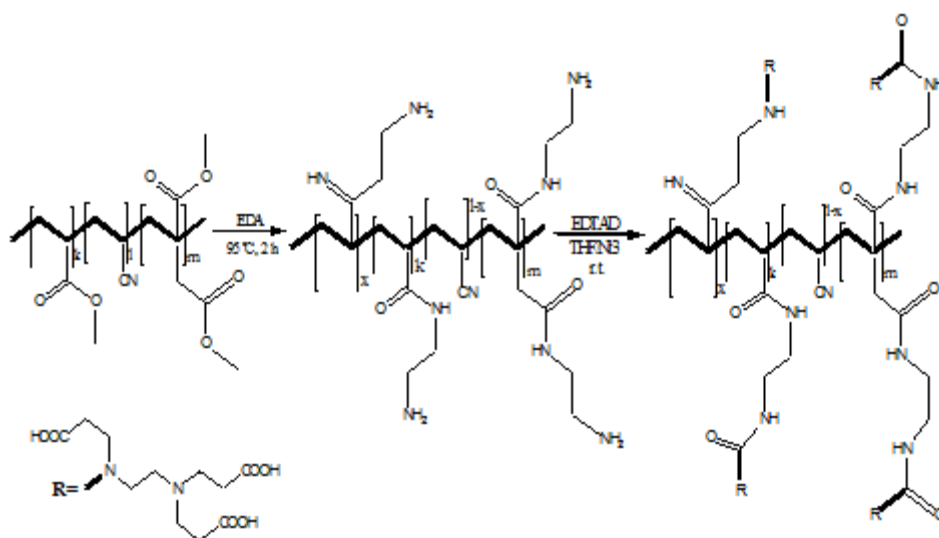


**Figure 7.4 Chemical reactions for the modification of PAN nanofibres (where EDA is ethylenediamine, EDTAD is ethylenediaminetetraacetic acid dianhydride (EDTAD), THF is tetrahydrofuran, Nt3 is triethyleneamine). The monomers *l*, *k* and *m* correspond to 93, 6 and 1% respectively)**

### 7.3.6 Adsorption studies

#### Effect of pH

The pH of a solution is believed to affect the electrostatic properties of adsorbents. This is because the ionic state of functional groups on the surface of adsorbents changes according to the pH of the solution. Hence, the optimum adsorption of MB, MO and RR was investigated in the pH range 3-12 at 25°C as shown in Figure 7.5. The optimum pH of 4 and 12 were chosen for further adsorption experiments for anionic (MO and RR) and cationic (MB) dye molecules, respectively.

The observed maximum adsorption capacities for anionic dyes at acidic media and for cationic dyes at basic media can be explained by the surface properties of EDTA-EDA-PAN nanofibres. From Figure 7.5, it was observed that when the pH of the dye solution is lower than the  $pH_{zpc}$ , the surface of EDTA-EDA-PAN is positively charged, while at pH values higher than the  $pH_{zpc}$ , the adsorbent's surface is negatively charged. Therefore, the electrostatic repulsion forces between the positively charged surface of EDTA-EDA-PAN nanofibres and MB inhibits the adsorption capacities at this pH range. However, in the same acidic conditions, an opposite behaviour for the adsorption of MO and RR was observed. In this case, the electrostatic attraction forces between the positively charged surfaces of EDTA-EDA-PAN nanofibres and the negatively charged MO and RR molecules increased the contact between the pair. When solution pH values were higher than  $pH_{zpc}$ , we observed an increase in the adsorption capacities of MB due to the electrostatic attraction forces whilst a decrease for MO and RR was noticed as electrostatic repulsion force at the adsorption interphase was dominant.

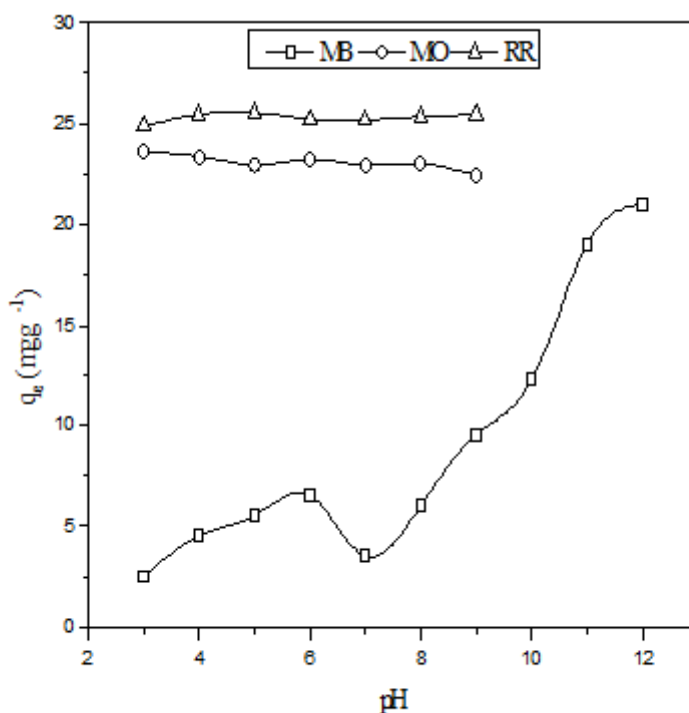


**Figure 7.5 Effect of pH on the adsorption of dyes on EDTA-EDA-PAN nanofibres using 0.05 g nanofibres in 25 mL 50  $mg\ L^{-1}$  dye solutions**

#### Effect of contact time

The time required for quantitative adsorption of MB, MO and RR was determined in order to optimise the utilisation period of the adsorbent. Adsorption experiments were conducted over a contact period reaching 30 h, as shown in Figure 7.6, using 0.05 g nanofibres in 25 mL 150  $mg\ L^{-1}$  dye solutions of MO, MB and RR. Results showed that 8 h was required for the sorption of dye molecules to reach equilibrium. Based on this, 12 h was taken as the optimum adsorption time in subsequent adsorption experiments.

### Effect of initial concentration

The effect of the initial concentration of MB, MO and RR on their adsorption was investigated using a concentration range of 10 to 300 mgL<sup>-1</sup>. We noticed that as the concentration increased, the available adsorption sites reduced, as the surface of the EDTA-EDA-PAN nanofibres became saturated, as depicted in Figure 7.7 using 0.05 g nanofibres in 25 mL 10 to 300 mgL<sup>-1</sup> dye solutions. Results show linear adsorption of dye molecules with increments in concentration up to 150 mgL<sup>-1</sup>. Beyond this point, a non-linear plot was observed. With this knowledge, real life application of the fabricated nanofibre mat could be optimised for each or both dye molecules, depending on their existing concentrations during wastewater purification.

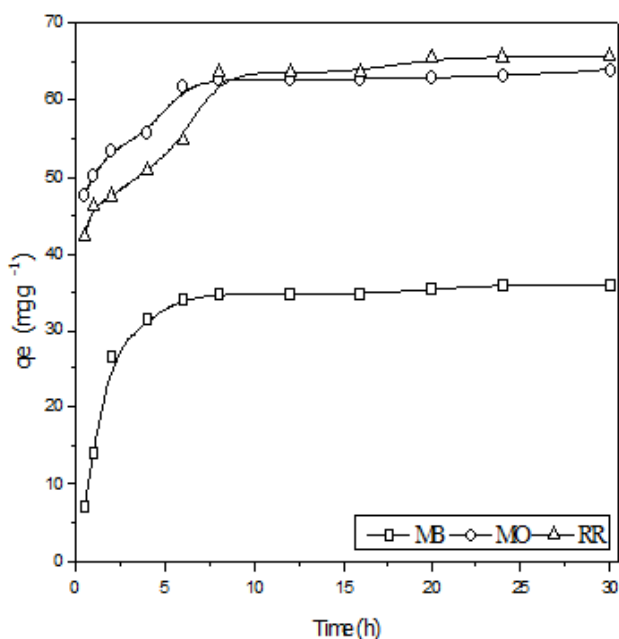


**Figure 7.6** Effect of contact time for the adsorption of dyes on EDTA-EDA-PAN nanofibres

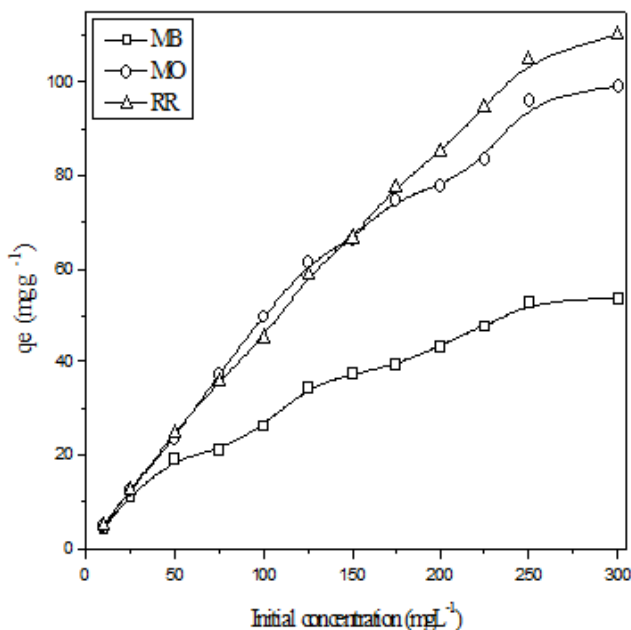


**Figure 7.7** Effect of initial concentration for the adsorption of dyes on EDTA-EDA-PAN nanofibres

### **7.3.7 Adsorption isotherms**

The fitting of experimental adsorption isotherm data into linearized plots of the Langmuir, Freundlich and Temkin models are depicted in Figure 7.8, Figure 7.9 and Figure 7.10, respectively, for dye solution concentrations of 150 mgL<sup>-1</sup>, adsorbent dose 2 gL<sup>-1</sup>, time 24 h, and pH 4 for MO and RR and pH 12 for MB. The extrapolated theoretical parameters for the selected models are given in Table 7.1.

The Langmuir model shows a substantial difference between the experimental value ( $q_e$ ) and  $q_m$  for MO compared to that of MB and RR. However, by virtue of their corresponding error function ( $R^2$ ), shown in Table 7.1, the Langmuir isotherm provided a better fit and extrapolations for MO and RR compared to MB which was well correlated with the Freundlich model. The Temkin model did not provide a reliable fit as compared to Langmuir and Freundlich. From this, we could infer that the collection of the adsorptive on the nanofibres followed the three strict rules of Langmuir and collected on a homogeneous surface of the nanofibres, chemically fabricated by the EDTA-EDA functionalisation; the exception was MB that was well described by the Freundlich model. By considering the values of the Freundlich constant  $n$  as follows: (i) when  $n = 1$ , the adsorption process is linear; (ii) when  $1 < n < 10$ , the adsorption process is favourable with higher values of  $n$  indicating stronger adsorbate-adsorbent interaction; and (iii) when  $0 < n < 1$ , this is an indication of a concave isotherm also known as a solvent-affinity type isotherm [5.43]. From Table 7.1, we observed that the adsorption of MO is favourable (i.e.  $1 < n < 10$ ) while the adsorption of MB and RR follows a concave isotherm as also evinced by the values of their  $R^2$ .

**Table 7.1 Isotherm parameters for MB, MO and RR molecule adsorption on the EDTA-EDA-PAN nanofibres**

		MB	MO	RR
Experimental adsorption capacity $q_e$ (mg g <sup>-1</sup> )		53.90	99.15	110.0
Isotherm models	Parameters			
Langmuir (L)	$q_m$ (mg g <sup>-1</sup> )	62.50	100.0	125.0
	$k_L$ (Lmg <sup>-1</sup> )	0.0275	0.2222	0.1290
	$R^2$	0.9067	0.9799	0.9611
	$R_L$	0.7843	0.3104	0.4367
Freundlich (F)	$k_F$	0.0306	27.03	0.0012
	$n$	0.4634	3.300	0.4458
	$R^2$	0.9384	0.6167	0.9427
Temkin (Te)	$b_T$	0.1080	0.0852	0.0645
	$A_T$	0.8938	26.88	7.697
	$R^2$	0.8052	0.8697	0.8925

The results obtained with the Temkin isotherm showed the adsorbent to have high values of  $A_T$  values (which indicate the binding strength at the adsorption interphase) for MO and RR and lower for MB. This implies that MO and RR interaction with the EDTA-EDA-PAN nanofibres was much stronger (toward chemisorption) than MB interaction.

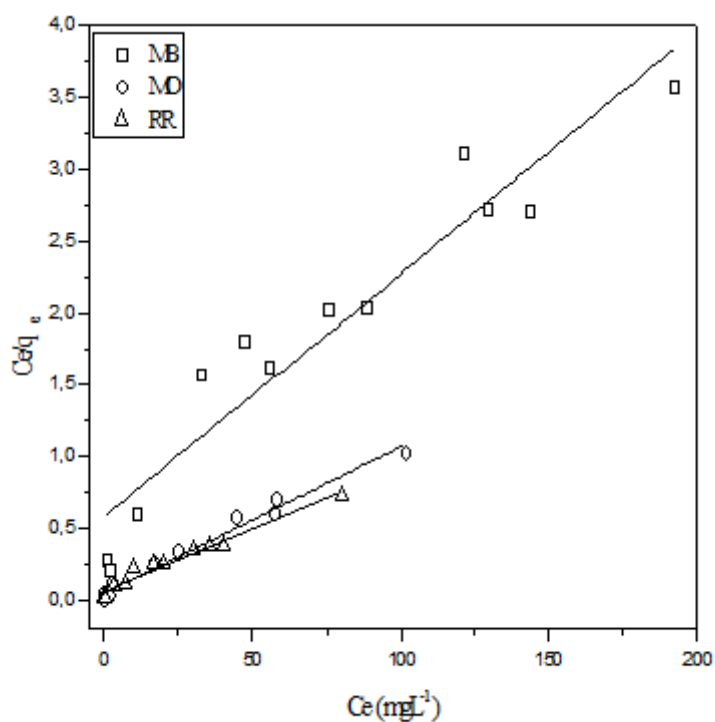


**Figure 7.8 Langmuir model for the adsorption of MB, MO and RR onto EDTA-EDA-PAN nanofibres**



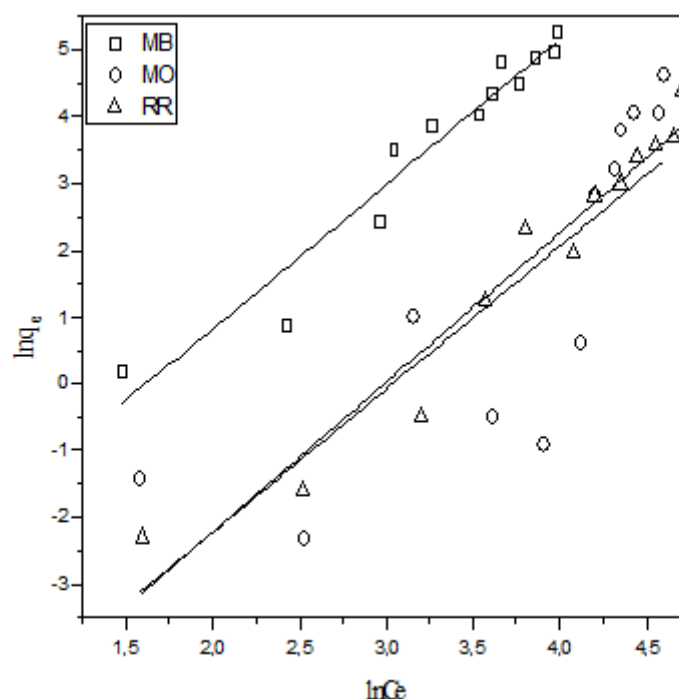


Figure 7.9 Freundlich model for the adsorption of MB, MO and RR onto EDTA-EDA-PAN nanofibres

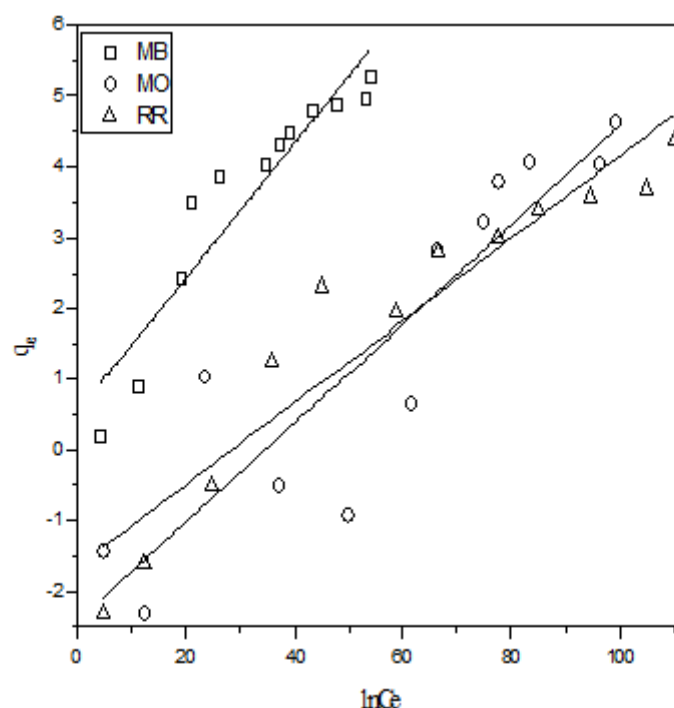


Figure 7.10 Temkin model for the adsorption of MB, MO and RR onto EDTA-EDA-PAN nanofibres

### 7.3.8 Adsorption kinetics

Adsorption kinetics data for MB, MO and RR collection onto the surface of EDTA-EDA-PAN nanofibres was acquired through the examination of data for the effect of contact time given in the session 3.4.2. For the pseudo- first and second order, the plots of  $\log(q_e - q_t)$  vs  $t$  (Figure 7.11) and  $t/q_t$  vs  $t$  (Figure 7.12) were used to obtain  $k_1$  and  $k_2$  values respectively. The extrapolated  $q_e$  for MB, MO and RR (dye solution concentrations  $150 \text{ mgL}^{-1}$ , adsorbent dose  $2 \text{ gL}^{-1}$ , time 24 h, pH 4 for MO and RR and pH 12 for MB) along with the rate constants ( $k_1$  and  $k_2$ ) are given in Table 7.2.

**Table 7.2 Parameters of the kinetic models for dye molecule adsorption on the EDTA-EDA-PAN nanofibres**

Kinetic models	Parameters	Dye molecules		
		MB	MO	RR
Pseudo-first-order	$q_{e \text{ exp.}}$ (mg g <sup>-1</sup> )	36.05	63.85	65.65
	$q_{e \text{ calc.}}$ (mg g <sup>-1</sup> )	13.20	10.01	28.17
	$k_1$ (min <sup>-1</sup> )	-0.0029	-0.0022	-0.0030
	$R^2$	0.7342	0.7561	0.9357
Pseudo-second-order	$q_{e \text{ exp.}}$ (mg g <sup>-1</sup> )	36.05	63.85	65.65
	$q_{e \text{ calc.}}$ (mg g <sup>-1</sup> )	38.17	63.94	67.57
	$k_2$ (min <sup>-1</sup> )	0.5057	3.530	1.449
	$R^2$	0.9936	0.9998	0.9980

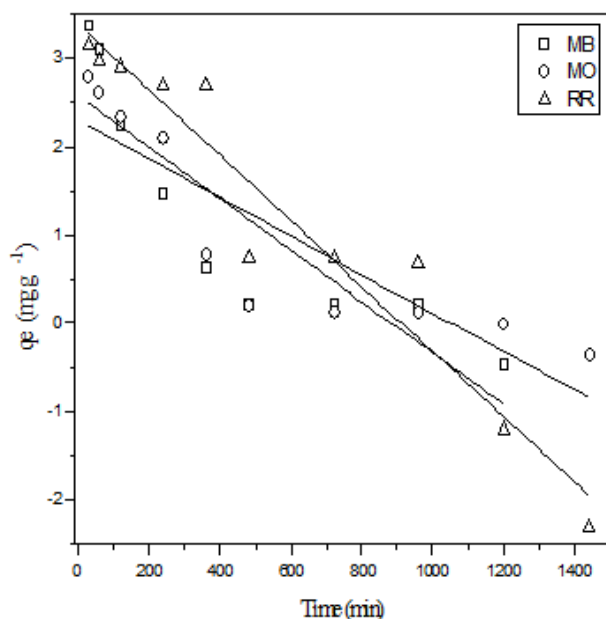


**Figure 7.11 Adsorption kinetic of MB, MO and RR onto the EDTA-EDA-PAN nanofibres using pseudo-first-order kinetic model**

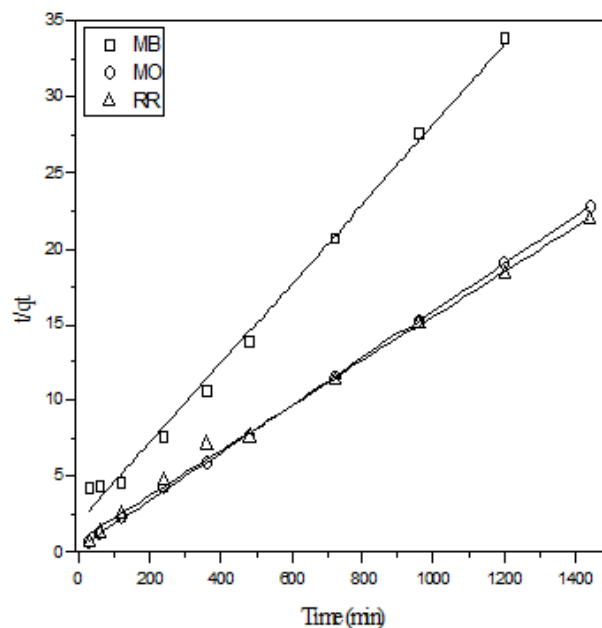


**Figure 7.12 Adsorption kinetic of MB, MO and RR onto the EDTA-EDA-PAN nanofibres using pseudo-second-order models, Pseudo-second-order kinetic model**

The pseudo-second-order kinetic model provided a better fit, as derived from the higher correlation factor ( $R^2$ ) and proximity of values for the calculated and experimental adsorption capacity.

## 7.4 CONCLUSIONS

PAN was electrospun and modified with EDTA-EDA chelating agents for the removal of dyes from aqueous synthetic water samples. Observations were made and inferences were drawn, as follows: (i) EDTA was successfully attached on the surface of PAN nanofibres using EDA as the cross-linker; (ii) the functionalised nanofibres effectively removed MB, MO and RR from synthetic water samples and from the kinetic study; around 8 h was necessary for the adsorption to reach equilibrium; (iii) the sorption of dye molecules follows a pseudo-second-order reaction which suggests that the rate of adsorption is a function of the sorbent's active sites as well as the concentration of the sorptives; (iv) the linear isotherm model showed a better fit of the experimental data to the Langmuir model for MO and RR while the Freundlich model was suitable for MB. This observation infers that MO and RR were collected on homogeneous surface and MB on heterogeneous surface, derived from functionalisation with EDTA-EDA chelating agents. Overall, the fabricated nanofibres have demonstrated potential application for the extraction of dyes from water effluents.

## CHAPTER 8: DESIGN, INSTALLATION AND EVALUATION OF A UF/NF PILOT PLANT AND PHOTOCATALYTIC TREATMENT OF NF BRINE

---

Atl-Hydro's proposed wastewater treatment and water recycle process is based on a comprehensive stream segregation audit where the main process effluent streams are segregated based on composition and effluent strength, as opposed to an end-of-pipe strategy where all effluent streams are mixed. The proposed treatment process is based on a two-phase strategy which will lead to lower CAPEX investment requirements and the ability to recycle a larger volume of effluent once treated.

In Phase 1, the high-volume, dye-free effluent streams, identified as part of the stream segregation analysis, are treated using UF (ultrafiltration) to remove particulates and suspended solids. The filtered product stream is treated using GAC (granular activated carbon) to remove any residual colour and then reused as process water.

In Phase 2, the main dye-containing effluent streams (dye-containing drops), identified as part of the stream segregation analysis previously described, are treated using UF and NF (nanofiltration) to remove and concentrate the dye fraction of the segregated stream. The concentrated dye fraction (NF retentate/brine) is treated using nanoparticles and then dewatered for solid waste removal. The NF dye-free permeate can then be desalinated using RO (reverse osmosis) to remove the high salt content which may then be evaporated for reuse in specific dye house processes.

### 8.1 DESIGN CONSIDERATIONS

Pre-treatment using UF is a critical design element for NF membrane filtration configurations. The DOW SP 2660 ultrafiltration modules are made from high-strength PVDF polymeric hollow fibre membranes that offer the following features:

- 30 nm nominal pore diameter for removal of bacteria, viruses and particulates including colloids
- Hydrophilic PVDF fibres for easy cleaning and wettability that help maintain long-term performance
- Outside-in flow configuration for high tolerance to feed solids and the use of air scour cleaning
- U-PVC housings eliminate the need for pressure vessels and are resistant to UV light.

The outside-in flow configuration is tolerant of wide-ranging feed water qualities and allows air scour cleaning. The dead-end flow offers higher recovery and energy savings. The pressurised, vertical shell-and-tube design eliminates the need for separate pressure vessels and allows easy removal of air from cleaning and integrity testing steps.

The hollow fibre membranes are 1.3 mm outside diameter and 0.7 mm inside diameter and are made from PVDF polymer. The fibres are strong because of the combination of the PVDF polymer, an asymmetric dense spongy layer, and skins formed on each side of the fibre. The PVDF membranes offer high chemical resistance and are tolerant to temperatures of 40°C. The hydrophilicity of the PVDF fibres is increased by using a proprietary treatment during manufacturing, lowering the propensity for hydrophobic compound fouling.

The 30-nm nominal pore size combines high filtration performance and high flux. The smaller pore size provides stable long-term filtration performance compared to microfiltration.

### 8.2 PIPING AND INSTRUMENTATION DIAGRAM

The integrated UF and NF pilot plant skid facilitates both Phase 1 and Phase 2 operation simultaneously depending on the volumetric NF retentate yield requirements. Figure 8.1 is the UF/NF piping and instrumentation diagram (P&ID) for the pilot plant skid, indicating integrated UF and NF operating loops.

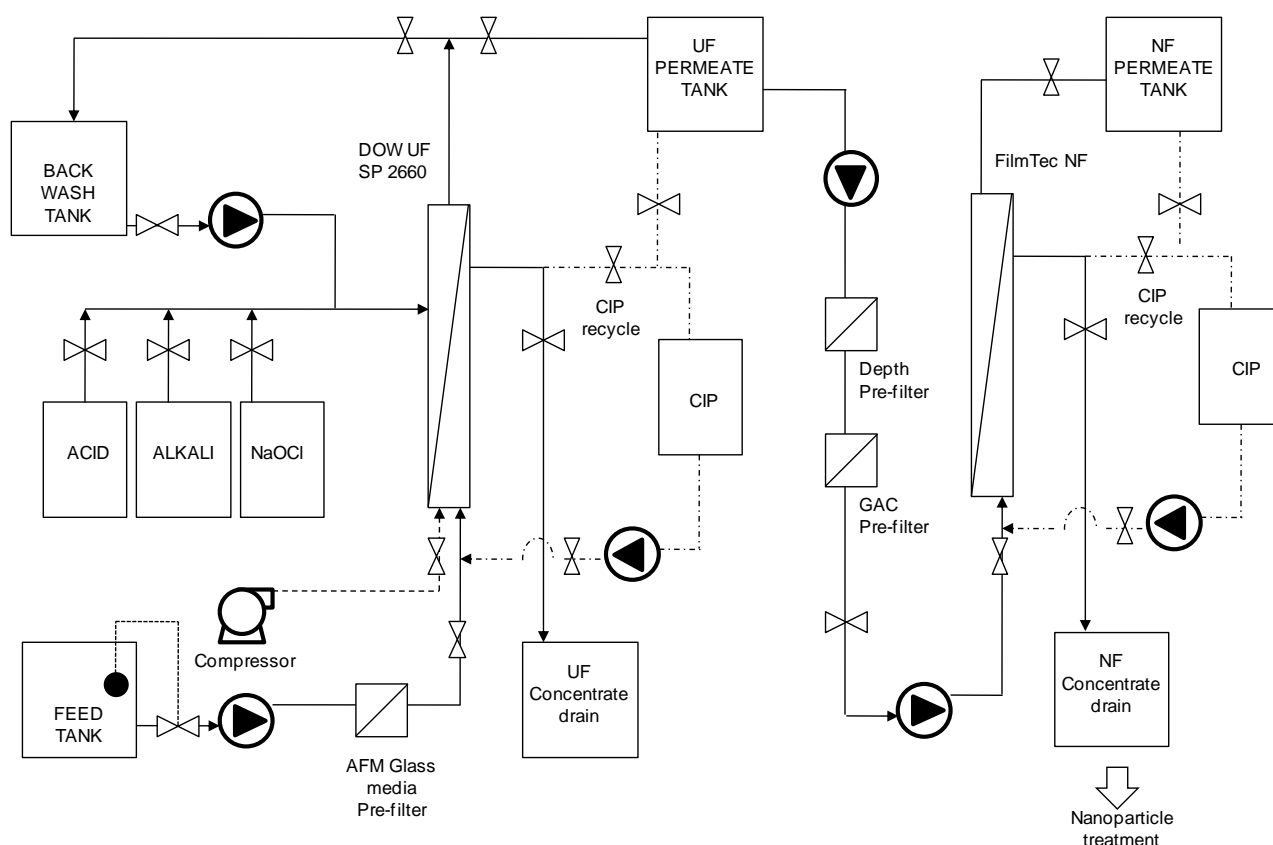


**Figure 8.1 Process flow diagram of UF/NF pilot plant**

The NF dye-retention stage requires UF as well as downstream depth and GAC pre-filtration to ensure longevity and lowered potential for fouling of the NF membranes. The NF concentrate product stream is then used as the feed stream for the nanoparticle dye oxidation.

### 8.3 PILOT PLANT LAYOUT

The process flow diagram for the UF/NF pilot plant is given in Figure 8.2. A single skid was selected to lower costs and to ensure automated UF pre-treatment prior to NF filtration; a requirement for producing the NF concentrate which is the focus of this study. The combined UF/NF process design is as follows:

1. Pre-filtration through AFM glass media – layered bed
2. Automated ultrafiltration with backwash and air injection (No CEB but manual clean in place (CIP)) – Dow SP 2660 module
3. 400 L/h nanofiltration system with sediment and carbon pre-filtration and CIP connections

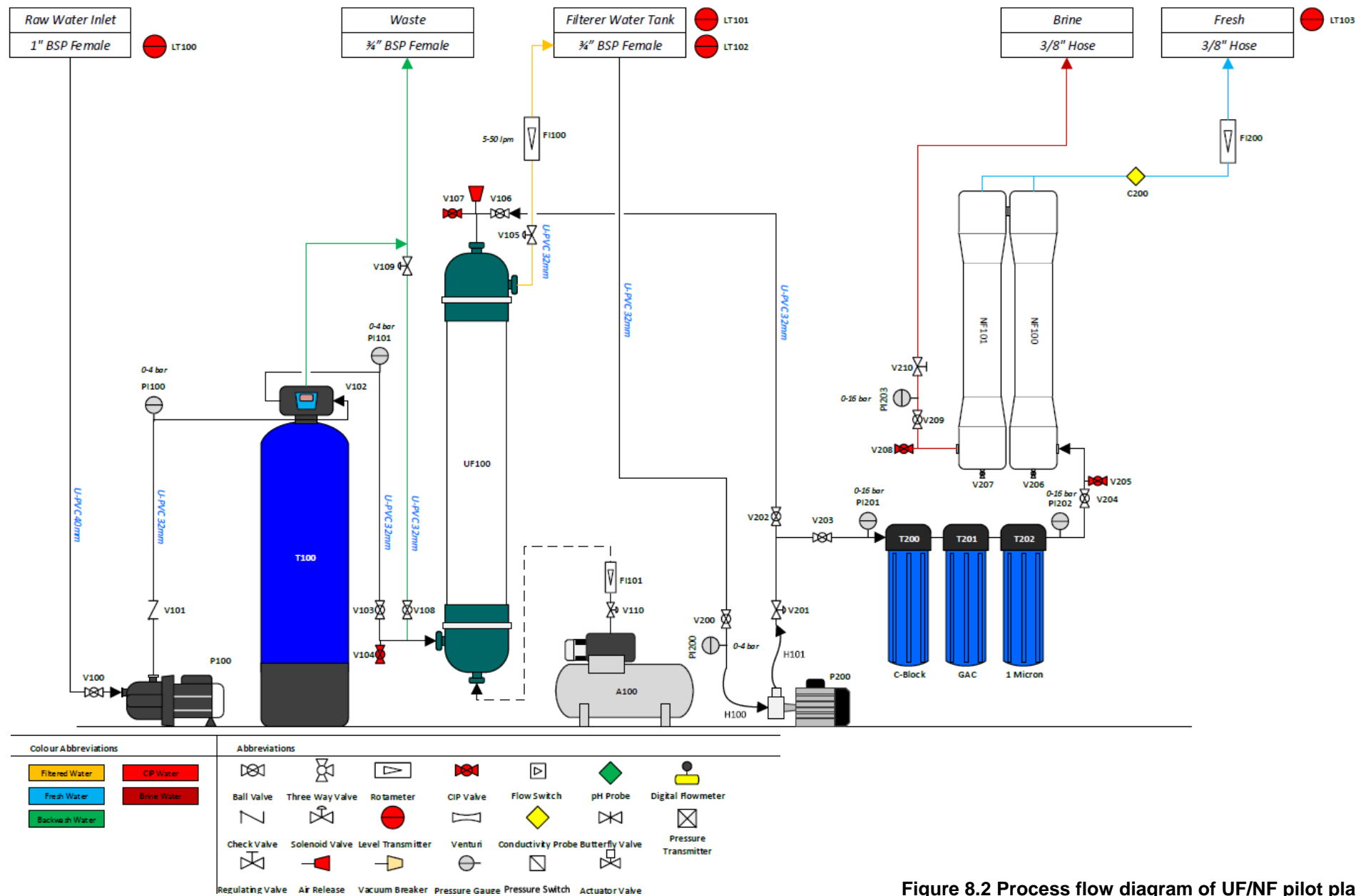


Figure 8.2 Process flow diagram of UF/NF pilot plant

The detailed parts of the pilot plant are as follows:

- Feed booster pump and motor
- 1054 FRP pressure vessel with Runxin automatic backwash head
- AFM glass media
- Dow SP 2660 ultrafiltration module
- Pressure gauges
- Solenoid valves
- Electrical control panel
- Air compressor and air regulating assembly
- Rotamer flowmeter
- Floatswitch on filtered water tank
- CIP cleaning system and connections
- Feed pump for nanofiltration
- Big Blue Filters – 5-micron Carbon block – GAC – Sediment Filter 1 micron
- Powder-coated steel frame
- x Filmtec NF90-4040 membranes
- x FRP 300 psi side port pressure vessels
- Stainless steel victualic couplings
- Electrical control panel and conductivity meter
- Pressure gauges
- Float switch for auto stop/start
- PVC pipework and fittings
- Flowmeters on the permeate, brine and recycle.

The pilot plant, as set up at Falke, is shown in Figure 8.3.



**Figure 8.3 UF/NF pilot plant set up at Falke**

## **8.4 COMMISSIONING AND OPERATION**

The commissioning and operation of the UF/NF pilot rig is per the manufacturer's guidelines and is governed by strict pre-treatment and operating guidelines. Table 8.1 is a summary of the various operating modes that will be followed during initial commissioning and operation (source: DOW UF operating manual and recommendations; Ver.3.2011):

**Table 8.1 Specification for the ATL-HYDRO UF/NF rig at Falke**

Model NF90-4040-2			Membrane NF90-4040		
<b>Feed TDS</b>	300 ppm	<b>Raw Flow</b>	1 m <sup>3</sup> /hr	<b>Flow stage 1</b>	1 m <sup>3</sup> /hr
<b>Expected TDS</b>	20 ppm	<b>Feed pressure</b>	4.7 bar	<b>Recovery</b>	40%
<b>Permeate flow</b>	7 lpm	<b>Conc. flow</b>	10 lpm	<b>Recirc flow</b>	n/a

Normal operation refers to the routine operating sequence of the DOW Ultrafiltration module and includes the operating and backwash steps. At initial start up, the modules are flushed using a “forward flush” to remove any residual chemicals or trapped air from the module. The flush occurs on the outside of the fibres and does not filter the feed water to make filtrate. After the forward flush is discontinued, the modules can be placed in the operating mode. An operating cycle ranges from 20 to 60 minutes. While operating, 100% of the feed water is converted to filtrate. As contaminants are removed during the operating step the transmembrane pressure will rise. At the end of the pre-set operating cycle time, a backwash sequence is triggered.

The backwash mode occurs automatically and may include an air scour, but always includes draining. backwash through the top drain, backwash through the bottom drain, and a forward flush. The air scour step, when included, is used to loosen particulates deposited on the outside of the membrane surface. Air is introduced on the outside of the fibres and displaced feed flow/concentrate is allowed to discharge through the top of the module for disposal. After 20 to 30 seconds of air scour, the module is drained by gravity to remove dislodged particulates. If the air flush is not included, the backwash sequence starts with simply draining the module by gravity to remove the concentrated feed water before starting any backwashing.

After draining, the *first backwash* step is performed. Filtrate flow is reversed from the inside of the fibre to the outside and backwash flow is removed from the module housing through the top drain on the module. A top draining backwash is performed first to remove contaminants in the area of greatest concentration. The *second backwash* step is performed to remove contaminants through the bottom of the module housing. Filtrate flow is reversed from the inside of the fibre to the outside and backwash flow is removed from the module housing through the bottom drain on the module for efficient removal of heavier materials. The two steps of backwash can be repeated numerous times depending on the degree of fouling. After backwash is complete, a *forward flush* is performed to remove any remaining contaminants and remove any air trapped on the outside of the fibres. After a backwash, the modules are returned to the *operating* mode.

A CIP operation includes a backwash and chemical recycle to clean the fibres. CIP is an on-demand operation. The frequency of a CIP depends on the feed water quality, and can range from one to three months. Prior to a CIP, the routine backwash steps, including air scour, draining, backwash through the top drain, and backwash through the bottom drain, are performed. The backwash steps are repeated three to eight times to remove contaminants or foulants not requiring chemical removal. After completing the backwash steps, the module is drained by gravity to remove excess water and prevent dilution of the CIP chemicals. CIP chemicals are recycled on the outside of the module for 30 minutes through the chemical cleaning tank. A small chemical filtrate stream will also be collected and recycled to the chemical cleaning tank. Note that the CIP solution can be heated up to 40°C to improve its effectiveness at removing contaminants from the membrane. A soak follows the initial recycle step, for 60 minutes or longer, depending on the degree of fouling that has occurred. After the soak step, CIP chemicals are again recycled on the outside of the module for 30 minutes. When the recycle is completed, an air scour is performed and then the module is drained to remove concentrated chemicals. The two steps of backwash and a forward flush are performed to remove any remaining contaminants on the outside of the fibres. After a CIP and at the start of the operating step, filtrate may be used to remove residual chemicals held in the fibre or module. The CIP steps described above are for a single alkali or acid chemical solution. If an acid and alkali cleaning are required, the CIP steps would be repeated for each chemical solution.

## 8.5 MASS BALANCE ANALYSIS

The principle of stream segregation in lowering CAPEX costs associated with industrial effluent treatment is based on a systematised  $\text{water}_{\text{in}} - \text{water}_{\text{out}}$  stream analysis in terms of defining the various stages of production with respect to flow rates, volumes and associated pollutant load. This analysis was applied to Falke's cotton reactive dye production sequences for Bell Blue, Black and Olive product lines. At each phase of the pre-treatment, dyeing, and post-treatment stages for each dyeing 'recipe' sequence, specifically looking only at 'reactive' dyeing, independently measurable quantities of system (1) inputs minus outputs and (2) water loss/gain were assessed within the boundary conditions of the dye house (excluding other  $\text{water}_{\text{in}} - \text{water}_{\text{out}}$  contributions from auxiliary process such as steam, domestic and cooling requirements within the factory) – effectively.  $\Delta S = Q_i - Q_o$ .

A detailed mass balance at each stage of specific dyeing recipe procedures was not within the scope of this project; however, a crude volumetric and mass input analysis was conducted for Bell Blue, Black and Olive dyeing procedures using two dye vat types (700 L and 3 500 L volumes).

For the Olive and Bell Blue reactive dyeing sequences, initial liquor ratios were approximately 16.5:1. with fabric/thread water retentions approaching 50%, requiring refill ratios of 8.25:1. (Thus for a 700 L dye vat, a refill volume of approximately 350 L was required for each stage). For the Black dye sequence using a 3500 L dye vat. and batch sizes of approximately 40 kg, initial liquor ratios were significantly higher at 87:1. Figure 8.6 indicates the volumetric and mass input analysis for Bell Blue, Black and Olive.

### 8.5.1 Dye drop mass balance analysis after pre-treatment, UF and NF treatment

Stream segregation analysis indicated that the primary dye-containing fractions for Olive and Bell Blue dyeing procedures comprised the 3<sup>rd</sup> and 4<sup>th</sup> drain events (containing primary dye fractions from Phase 1 and 2 dye drop sequences). These 'drop' fractions comprised 25% of the total  $\text{water}_{\text{in}} - \text{water}_{\text{out}}$  (within the dye house boundary conditions). For cotton reactive Black dyeing, the primary dye-containing fraction comprised only 17% of the total  $\text{water}_{\text{in}} - \text{water}_{\text{out}}$ . Consequently, sump dilution factors ranged between 0.14 and 0.39 depending on the sequence of drops from the other production vats operating concurrently. The ideal scenario for implementing stream segregation is to have 3-way directional valves on the dyeing vats linked to SCADA control in the dye house facilitating the concentrated dye drops to be redirected to separate sumps. Unfortunately, due to project budget constraints this was not possible – instead, manual stream segregation was implemented; consequently, a certain volume of pre- and post-dye drop streams were intermittently mixed with the dye drops leading to a high degree of variability with respect to sump dilution ratios which impacted on any accurate mass balance analysis (Figure 8.5).



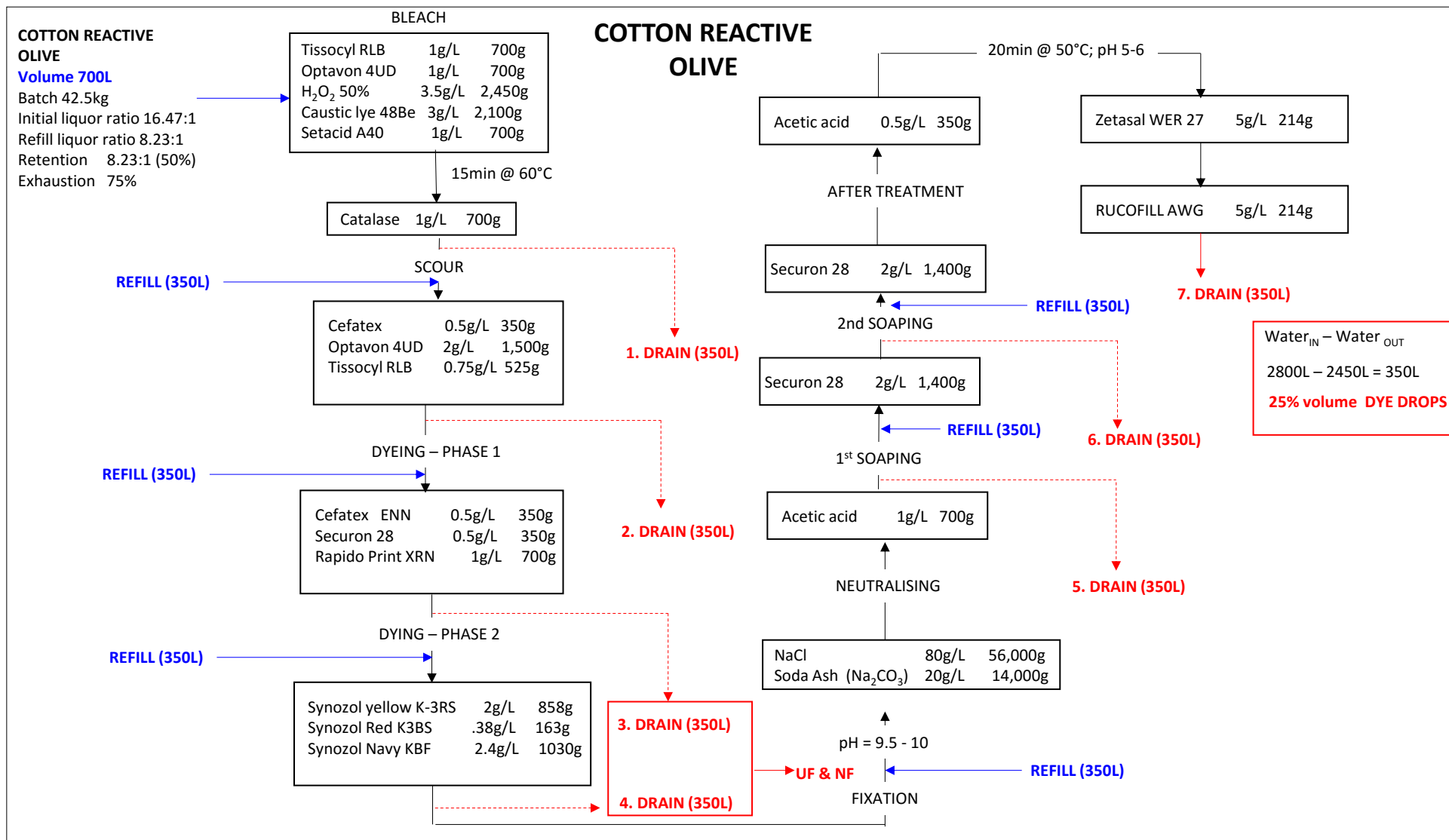


Figure 8.4 Volumetric and mass input analysis for Olive dye sequences.

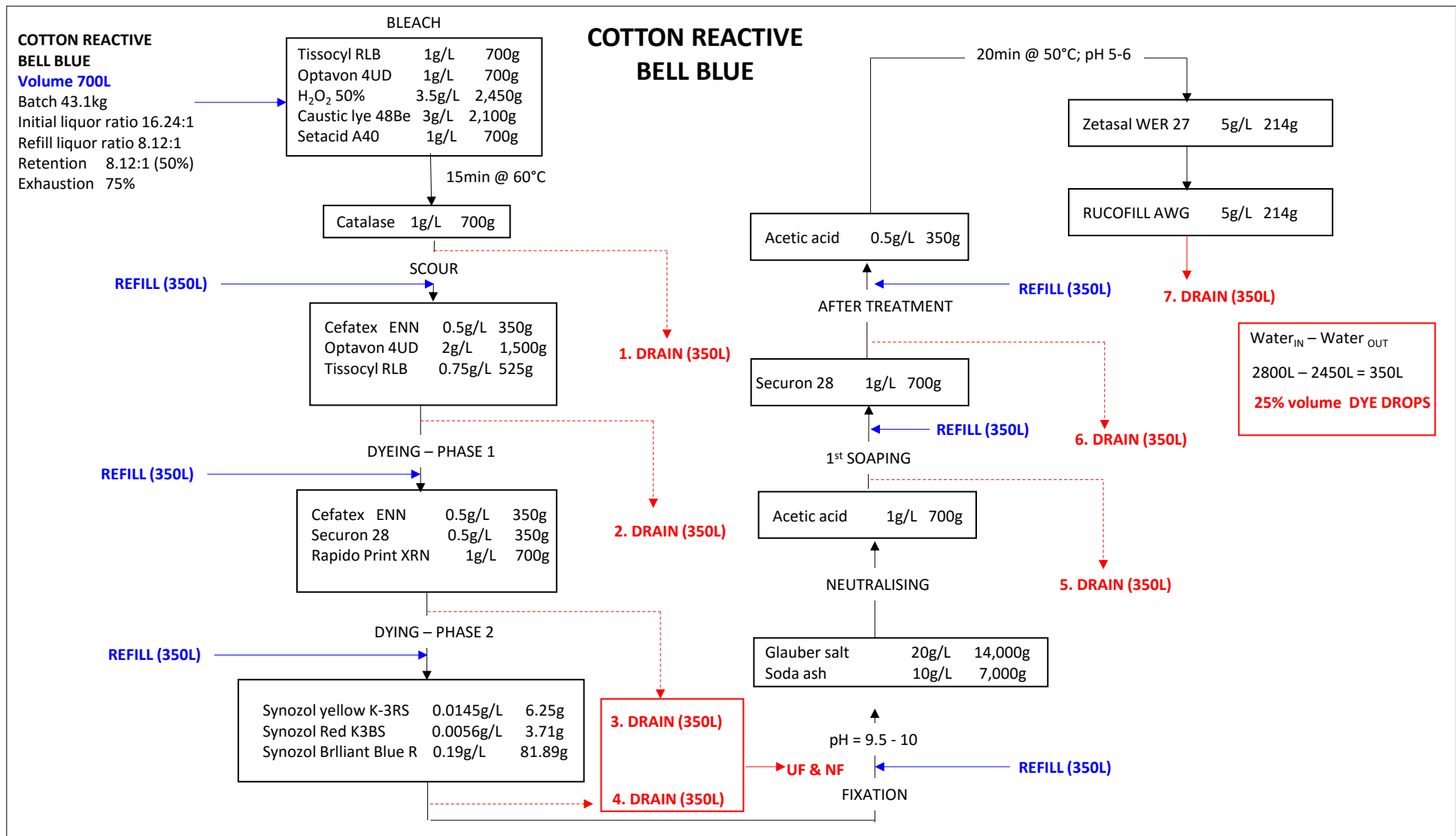


Figure 8.5 Volumetric and mass input analysis for Bell Blue dye sequences.

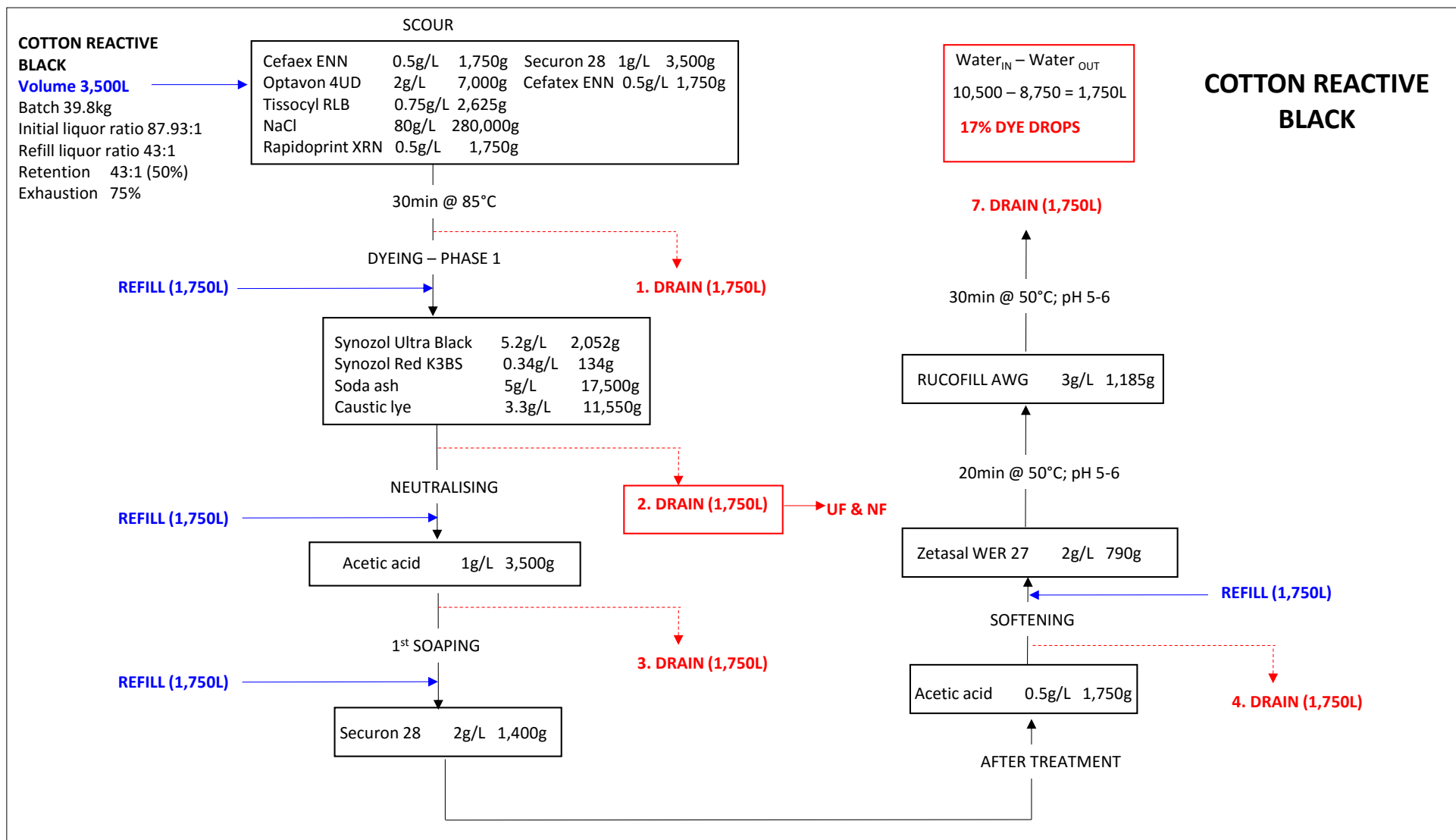


Figure 8.6 Volumetric and mass input analysis for Black cotton reactive dye sequences.

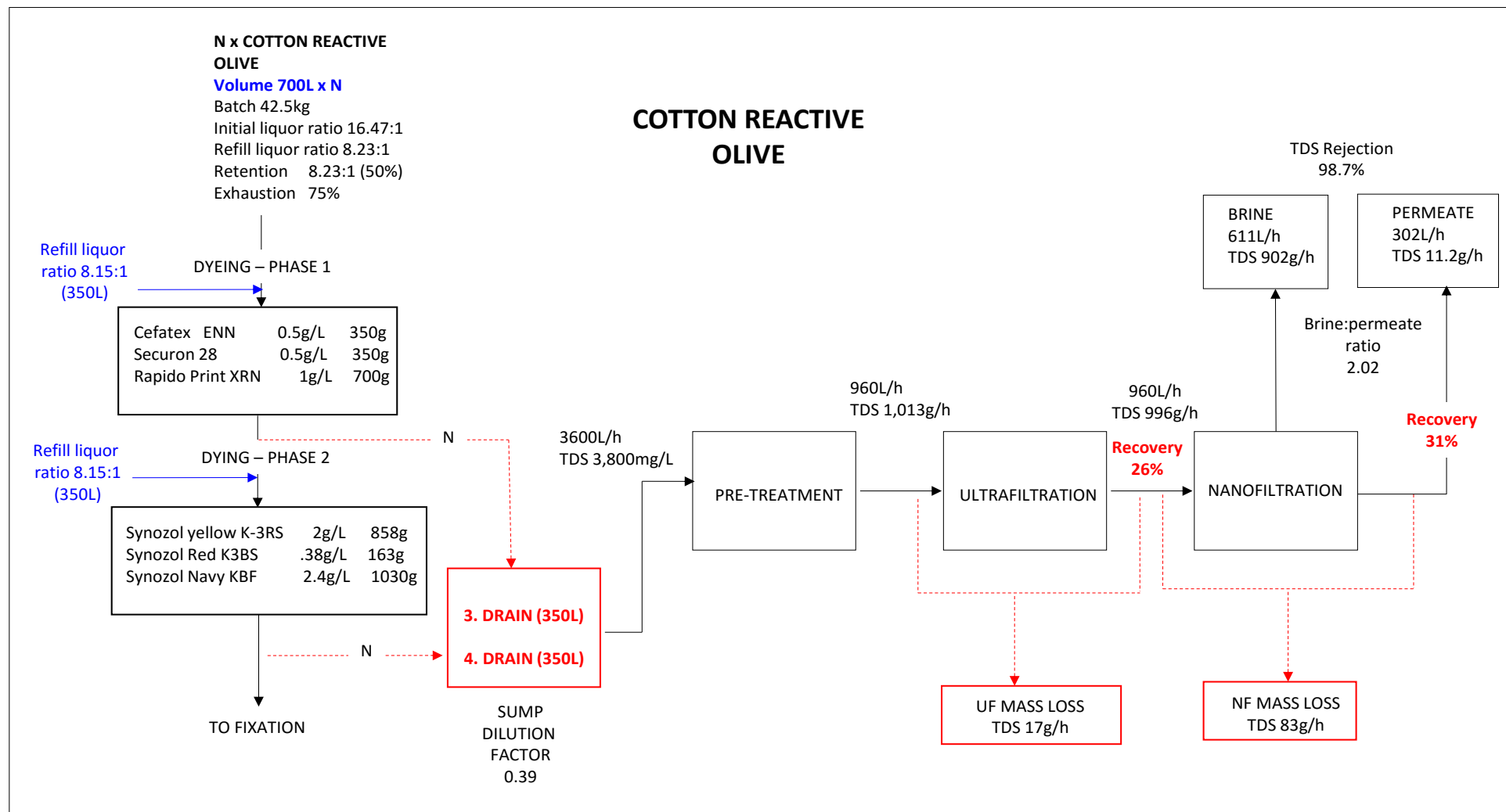
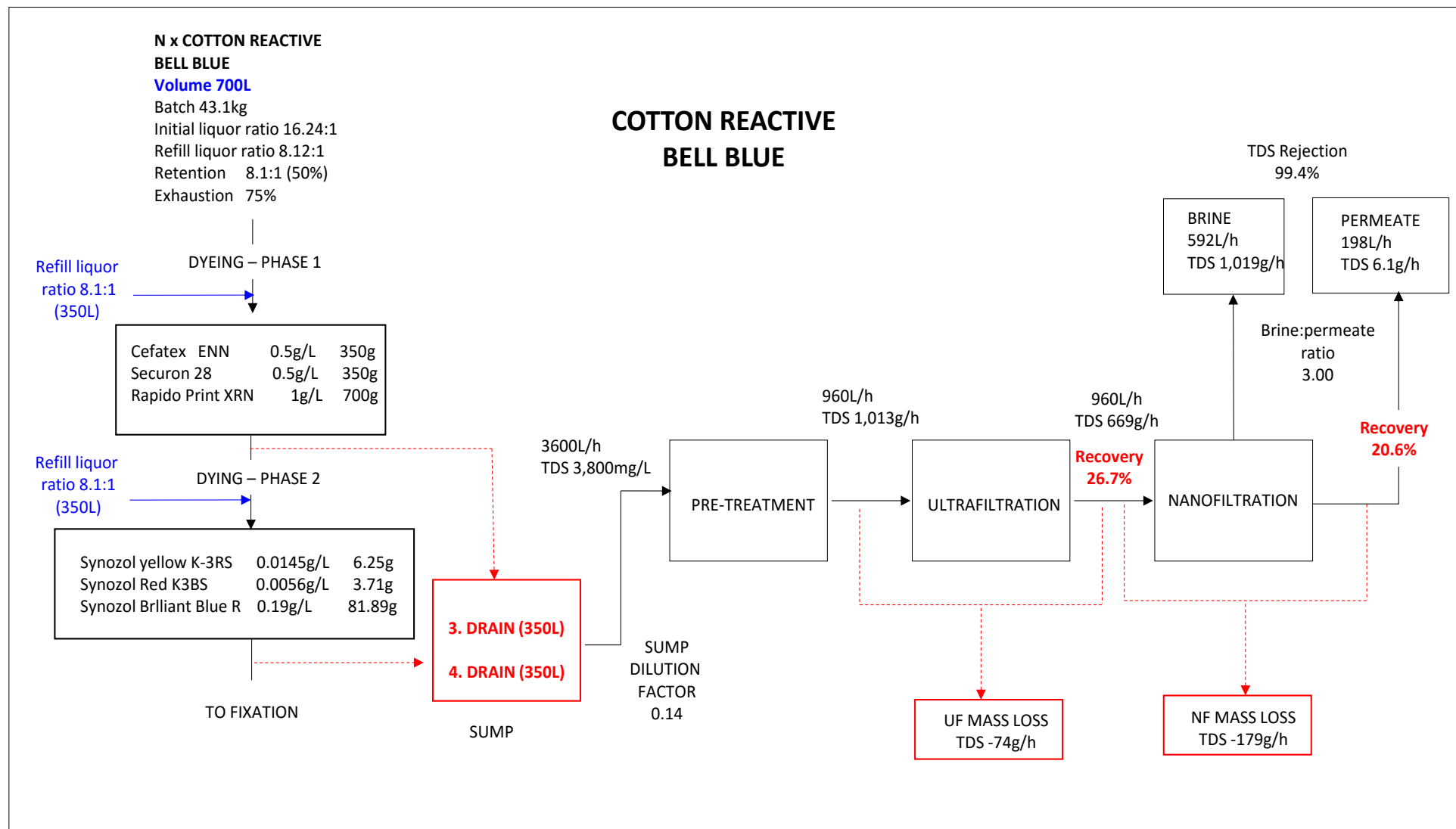


Figure 8.7 Cotton reactive Olive UF and NF mass balances.



**Figure 8.8 Cotton reactive Bell Blue UF and NF mass balances.**

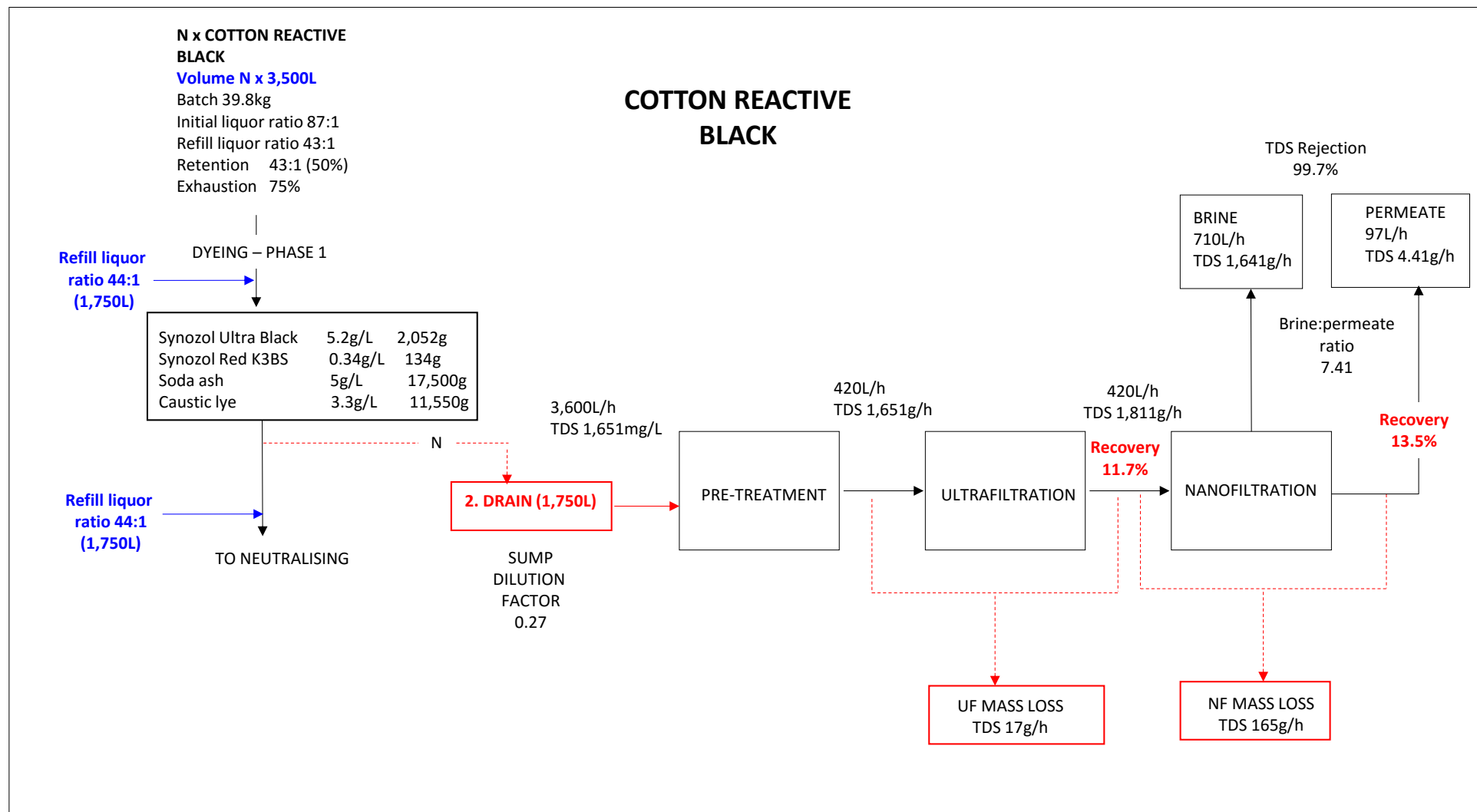
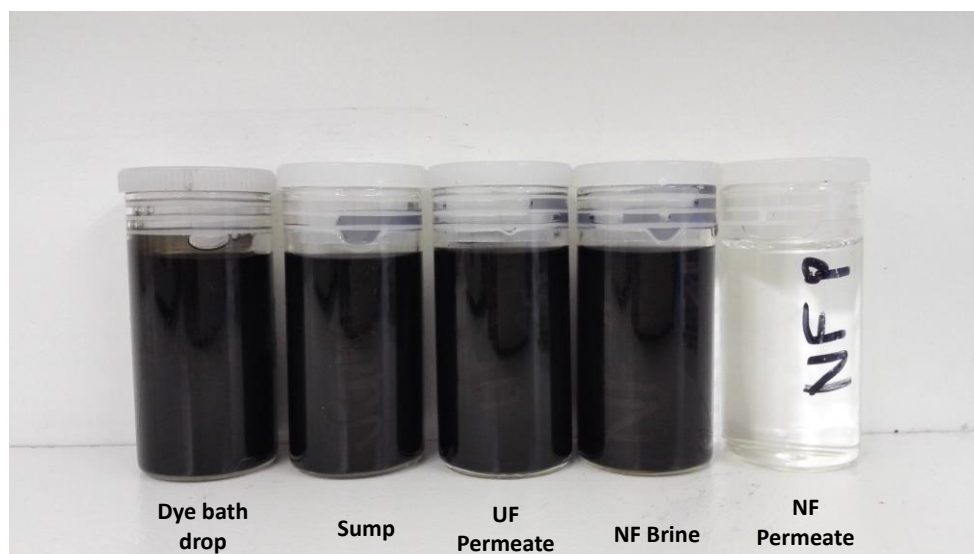


Figure 8.9 Cotton reactive Black pre-treatment UF and NF mass balances.

Volumetric recoveries in the UF/NF pilot plant were low, ranging from 11.6–26.7% for pre-treatment and UF to 13.5–31% for NF. Conversely, colour retention (i.e. dye fractionation) was almost 100% effective (refer to Figure 8.10) indicating that the process model was effective albeit with low volumetric efficiencies. The NF brine fraction was subsequently treated downstream using nanophotocatalytic TiO<sub>2</sub> for colour degradation.



**Figure 8.10 Representative dye fraction at various pre- and post-treatment stages indicating complete colour retention by NF treatment.**

Currently accepted volumetric productivities for NF range between 40 to 55% in terms of recovery efficiencies. However, during the operation of the pilot plant, differential pressure increases across the pre-treatment resins indicated a progressive degree of fouling, primarily because automated CIP (cleaning in place) was not within the design scope of the pilot plant. As a consequence of intermittent pilot plant operation (which was a function of Falke's manufacturing schedule which shifted continuously based on client demand), insufficient manual CIP events were scheduled. However, from a process design perspective, the principle of using NF as a final barrier treatment to fractionate the dye-containing stages which would subsequently be treated using nanophotocatalytic TiO<sub>2</sub> was effectively demonstrated.

## 8.6 NANOFILTER BRINE TREATMENT USING PHOTOCATALYSIS

The brine obtained from the NF was treated using photocatalysis. The slurry system was used with  $\beta$ -FeOOH/TiO<sub>2</sub>Anatase. The optimum conditions obtained during preparation of the catalyst, as documented in Chapter 4, i.e. catalyst concentration (800 mg/L), H<sub>2</sub>O<sub>2</sub> addition (50 ml/L) and a pH of 4.4, was used without further optimisation. The NF brine was treated in the 200 ml jacketed reactor with a 500 W tungsten light source. The wavelength scan of the brine and treated brine was conducted over a wavelength range of 200 nm to 800 nm. Each colour consisted of two to three dyestuffs at various concentrations. The three effluents tested were from the flowing dye bath drops:

**Olive:** Synozol Red K-3BS. Synozol Yellow K-3RS. Synozol Navy KBF

**Black:** Synozol Ultra Black. Synozol Red K-3BS

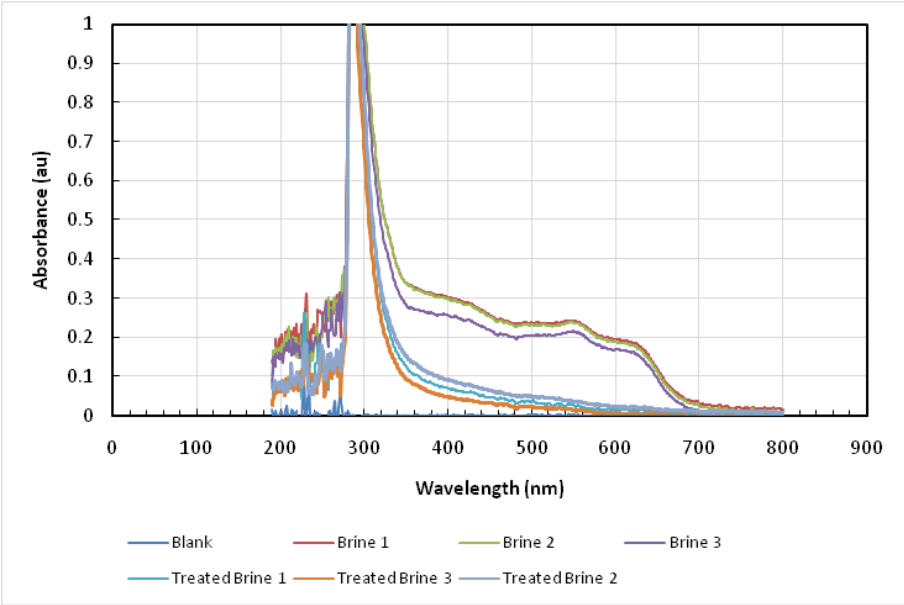
**Bell Blue:** Synozol Red K-3BS. Synozol Yellow K-3RS. Synozol Brilliant Blue R

A 100 mg/L of each dye was prepared and a wavelength scan conducted for each colour. The maximum wavelength ( $\lambda_{\max}$ ) was found to be 418.5 nm for Synozol Yellow, 541.4 nm for Synozol Red, 614.4 nm for Synozol Navy, 592.6 nm for Synozol Ultra Black and 593.9 for Synozol Brilliant Blue over a scan range of 200 nm to 800 nm. Thereafter, a mixed standard was prepared consisting of equal proportions of the two or three dyes at 100 mg/L. These were diluted to construct a calibration curve. The same samples were used, but at the appropriate wavelength for each colour as determined. A sample was withdrawn from the reactor every 15 minutes. The objective of this work was to evaluate if it was possible to remove all colour from the

brine using photocatalysis. More work should be done to determine the reaction rates. Three samples of NF brine were collected during the trial run on the UF/NF pilot plant and used for degradation studies.

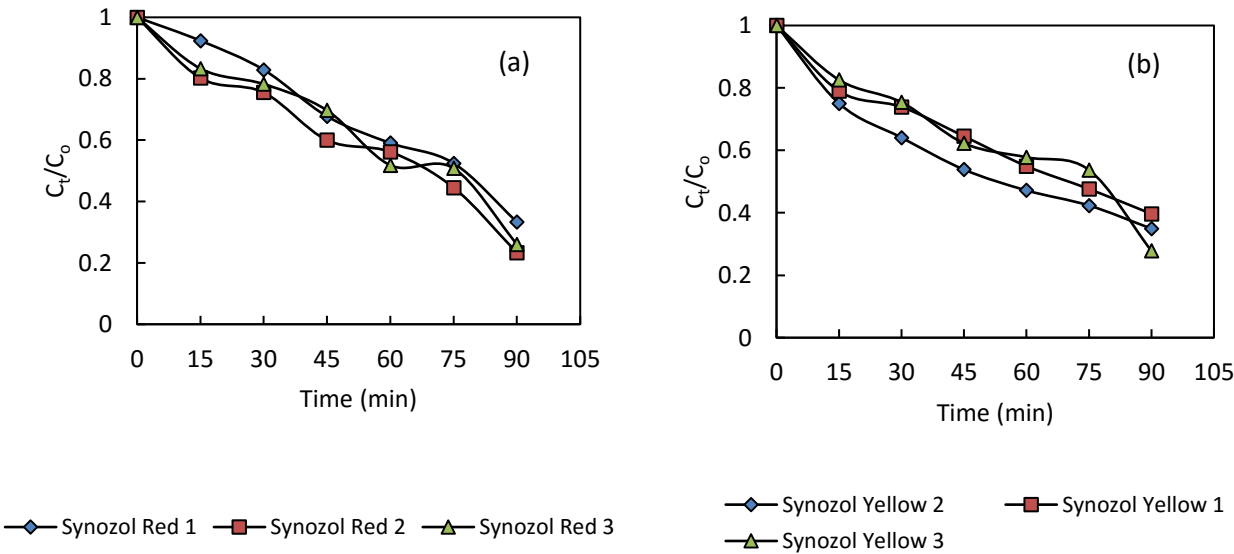
### 8.6.1 Olive effluent

**Figure 8.11** clearly shows the disappearance of the characteristic peaks for Synozol Yellow, Red and Navy indicating the degradation of dye molecules during photocatalysis. However, the high absorbance peaks in the UV range are indicative of the aromatic intermediates formed during the reaction.



**Figure 8.11 UV-Vis spectra for NF brine and treated NF brine**

Figure 8.12 (a), (b) and (c) show the degradation curves of the Olive NF brine at each  $\lambda_{max}$ . Each sample was repeated three times. Figure 8.12 (d) and (e) show a comparison of the degradation of Olive NF brine at each of the  $\lambda_{max}$ , clearly indicating that Synozol Navy degraded the fastest. The final degradation percentage for Olive colour at 90 minutes for Synozol Navy was  $81 \pm 3\%$ , for Synosol Red was  $72 \pm 5\%$  and for Synoset Yellow was  $66 \pm 6\%$ . The degradation kinetics for the Red and Yellow were essentially the same.





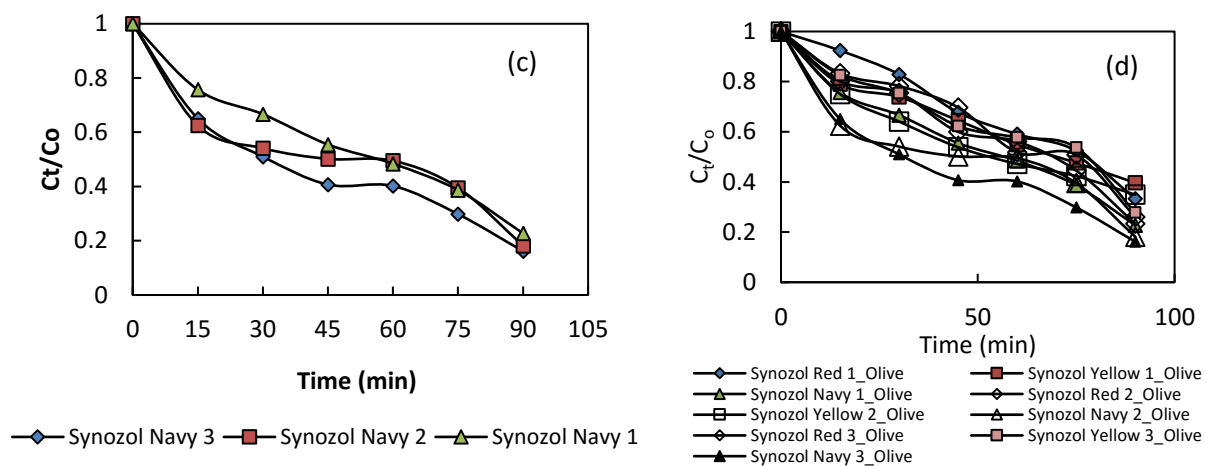


**Figure 8.12 Photodegradation of Olive NF Brine at  $\lambda_{\max}$  of 418.5 nm for Synozol Yellow, 541.4 nm for Synozol Red and 614.4 nm for Synozol Navy**

### 8.6.2 Black effluent

The black dyebath consisted of Synozol Ultra Black and Synozol Red. Repeatable results were obtained for the three samples obtained from the NF, apart from Ultra Black sample 1. Figure 8.13 (a) and (b) show a comparison of the individual samples of Ultra Black and Synozol Red. Degradation of up to 98% was obtained within 120 minutes of treatment for the Synozol Ultra Black, but for Synozol Red, treatment had to continue to more than 200 minutes to obtain similar results, as shown in Figure 8.13 (c) and (d).

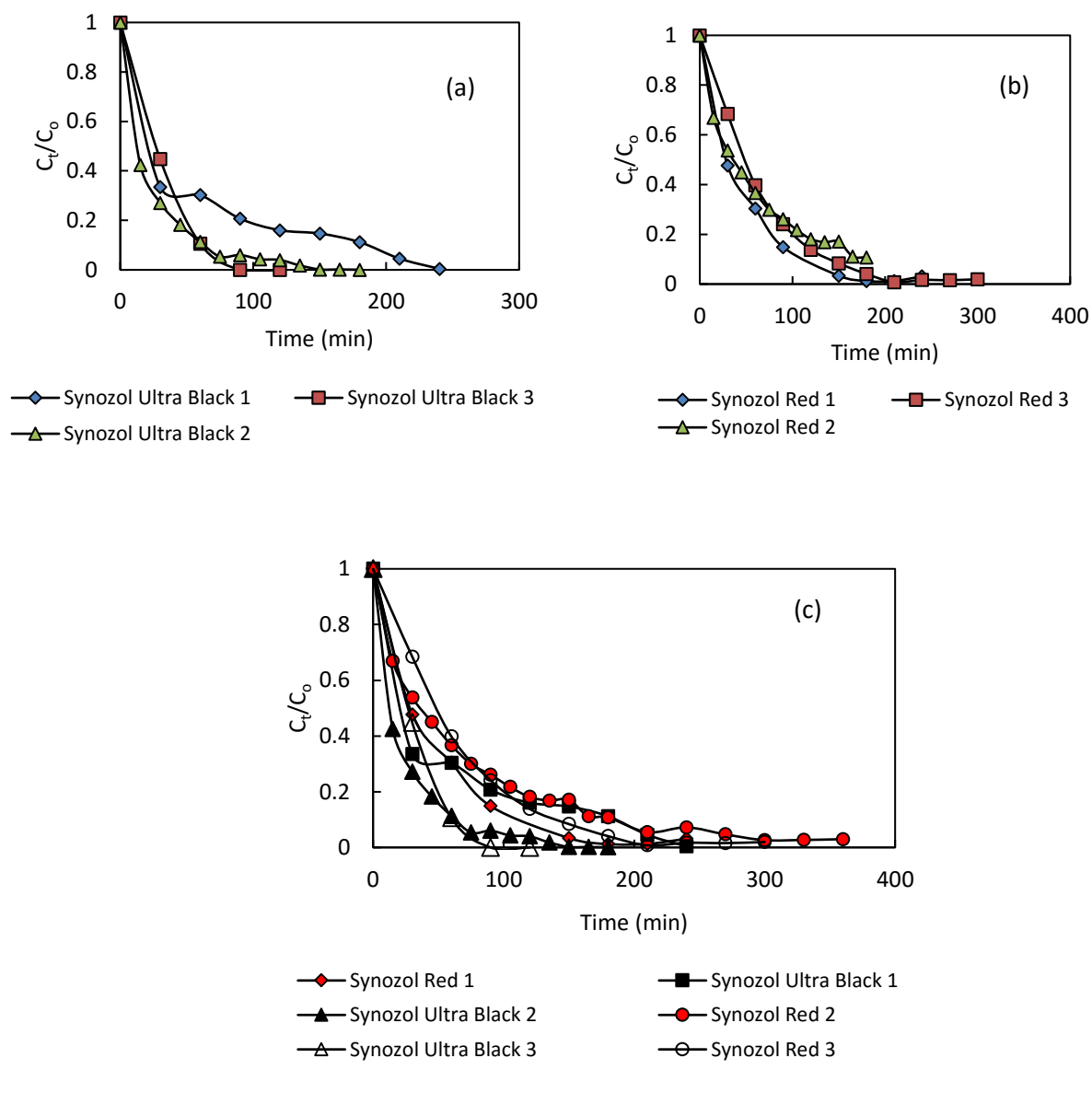
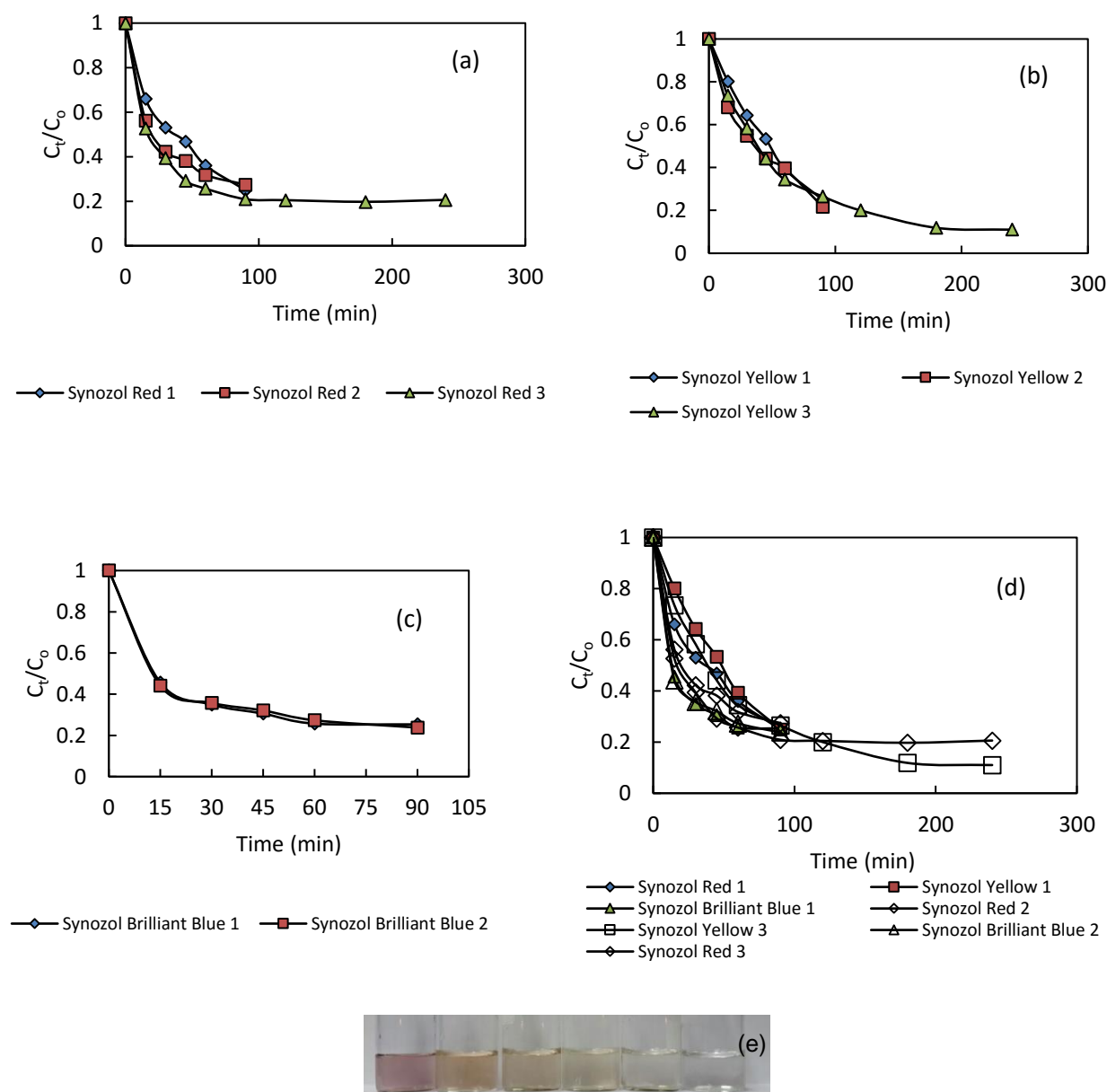


Figure 8.13 Photodegradation of Black NF brine

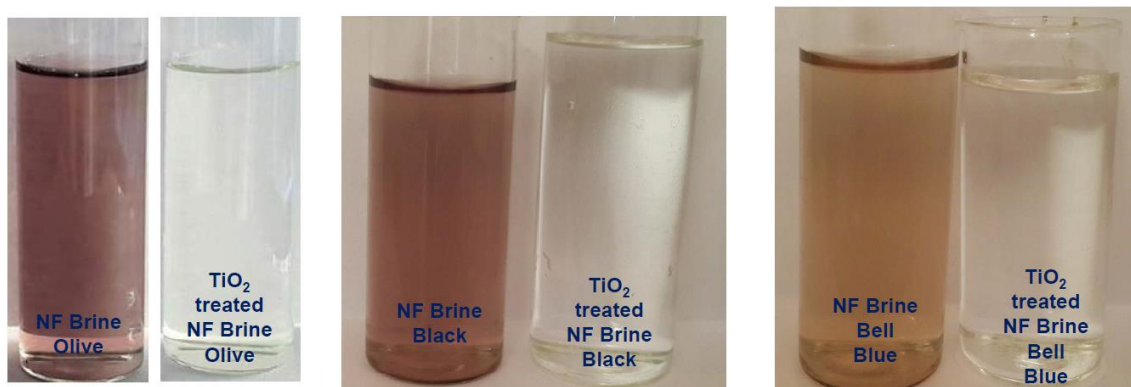
### 8.6.3 Bell Blue effluent

The Bell Blue dyebath consisted of Synozol Red, Yellow and Brilliant Blue. The Yellow was most difficult to degrade, followed by Red and then Brilliant Blue as shown in Figure 8.14 (a) to (d). All visible colours were only removed after a treatment time of more than 400 minutes (Figure 8.14 (e)). It is important that more tests be conducted to ascertain the detailed reaction kinetics.



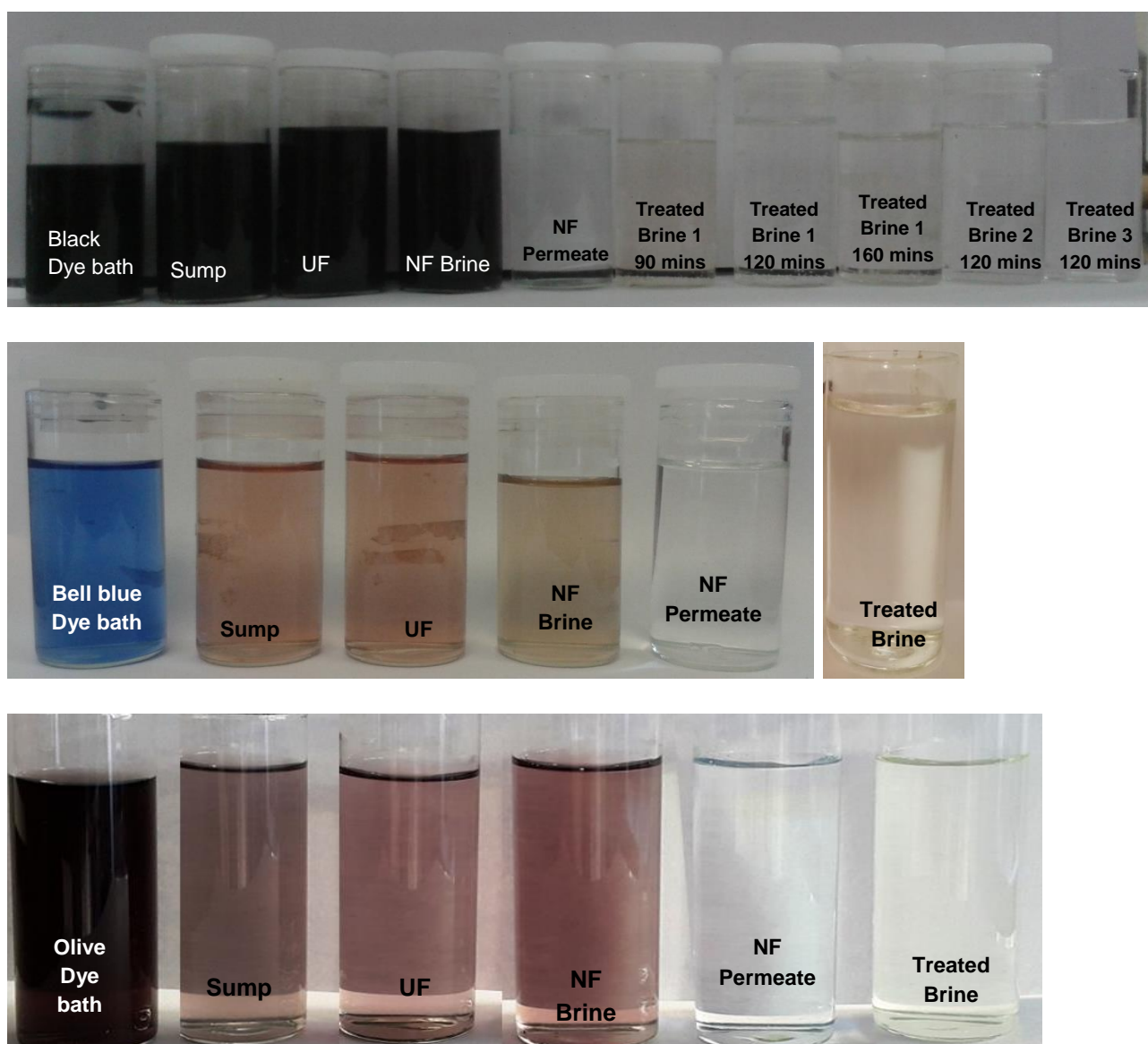
**Figure 8.14 Photodegradation of Bell Blue NF brine**

Figure 8.15 shows a comparison of the colour of brine and treated brine samples. In all cases a colourless product was obtained after 400 minutes of treatment with the locally developed  $\beta$ -FeOOH/TiO<sub>2</sub>Anatase photocatalyst in a slurry reactor under tungsten light.



**Figure 8.15 Colour comparison of brine and treated brine of Olive. Black and Bell Blue effluents**

Figure 8.16 shows the visual colour changes of effluent from Black, Bell Blue and Olive dye baths, sump, ultrafiltration, nanofiltration brine and permeate, as well as for  $\text{TiO}_2$  treated brine.



**Figure 8.16 Colour comparison of effluent from dye bath to final treated product**

# 8.7 CHARACTERISTICS OF FALKE EFFLUENT BEFORE AND AFTER TREATMENT

Effluent samples were collected from the dye drop, as follows: before reaching the sump, sump, after UF, NF brine and permeate. The NF brine was then treated by photocatalysis. All these effluent samples were analysed for pH (Figure 8.17), conductivity (Figure 8.18), total dissolved solids (TDS) (Figure 8.19), total organic carbon (TOC) (Figure 8.20), sulphate (Figure 8.21), phosphates and/or sulphates (Figure 8.22).

The pH of the NF permeate ranged between 9 and 10 except for the sump for the black dye drop. The pH of the treated NF brine was between 4 and 5 due to the fact that the catalyst performs better in an acidic medium, as was found during tests conducted in the development of the  $\beta$ -FeOOH/TiO<sub>2</sub> catalyst. This can easily be adjusted after treatment to meet disposal or reuse standards.

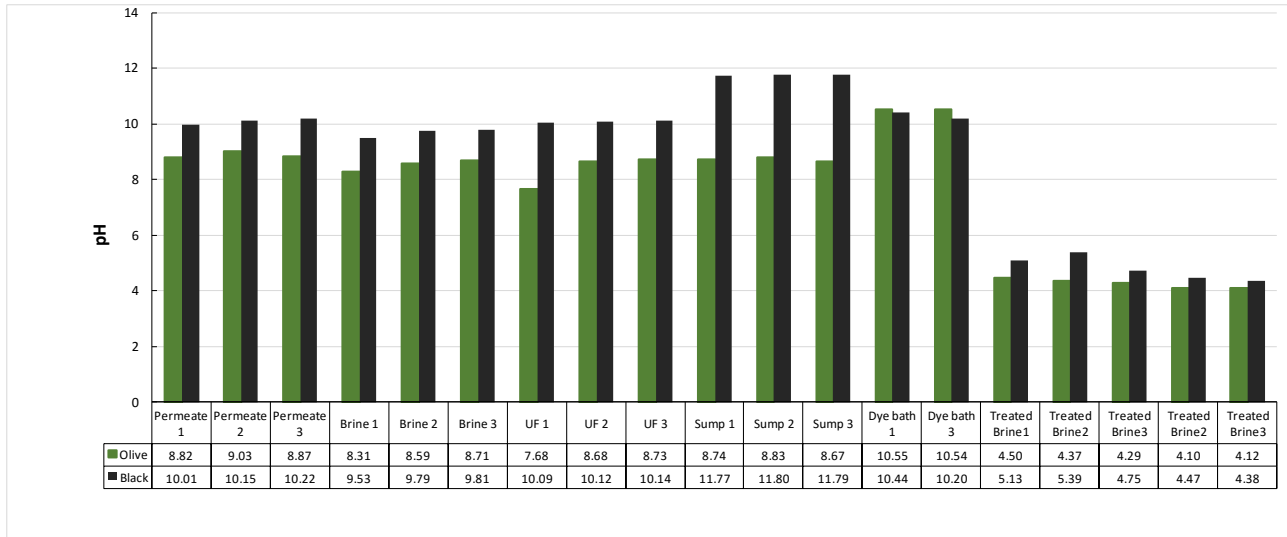


Figure 8.17 pH

The conductivity remained essentially unchanged for all treatment processes, apart from a significant reduction during NF when the permeate reached values as low as 0.05 mS/cm. It should be noted that the high values for the sump for the black effluent are not displayed graphically although the values of over 100 mS/cm are shown in the table below the graph. Although sampling of the sump took place as soon as the effluent was dropped, it contains more than one effluent at any point and time. The conductivity of the black was generally higher than that of the olive. Similar results were obtained for TDS.

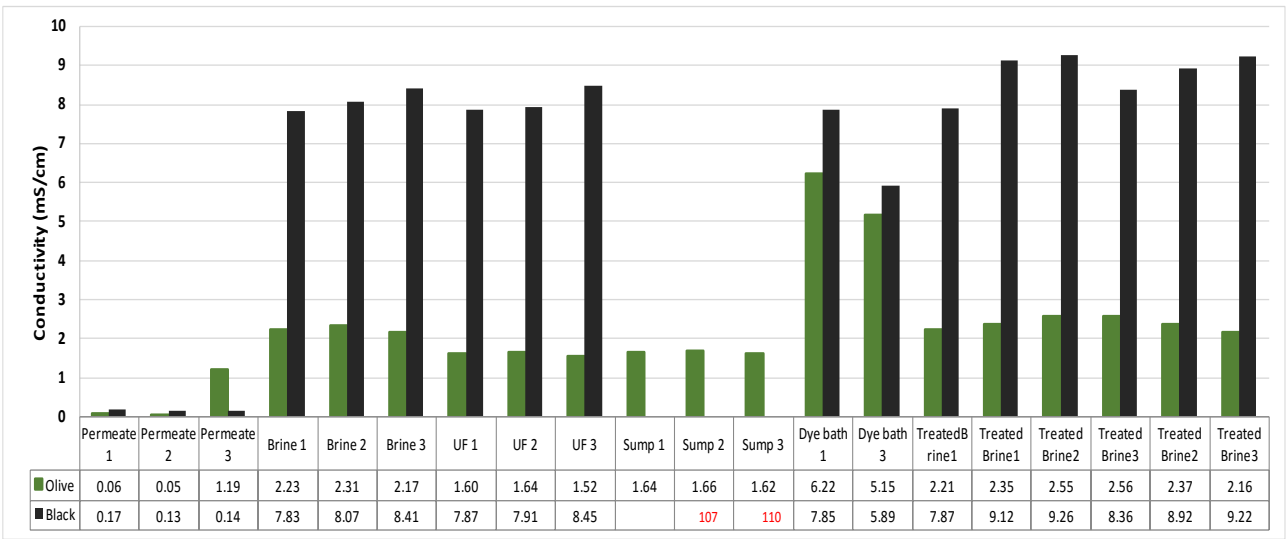
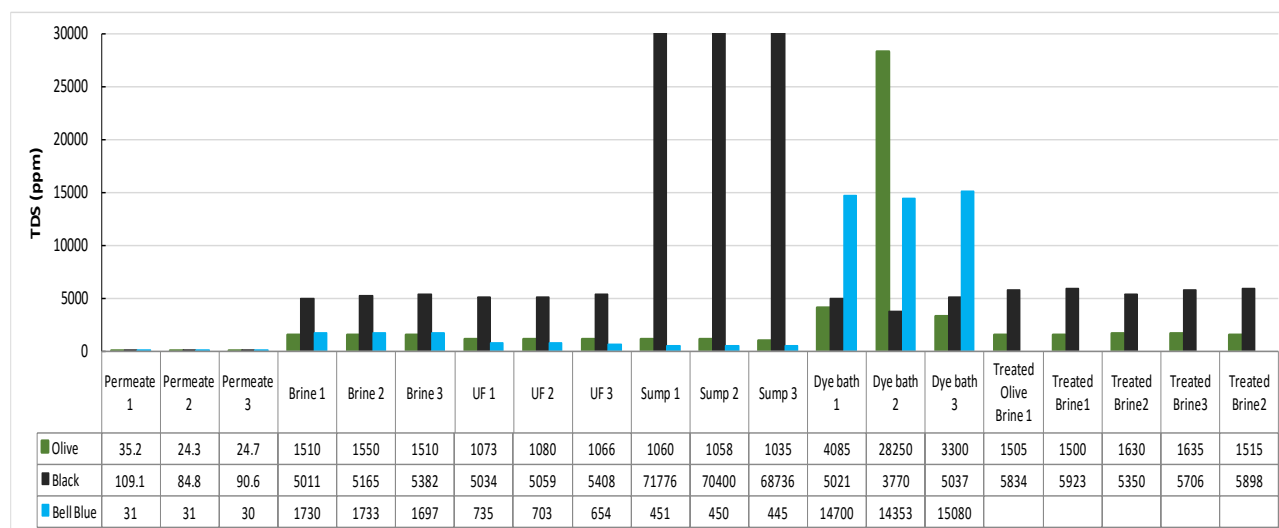


Figure 8.18 Conductivity



**Figure 8.19 TDS**

The TDS of the NF permeate was ~25 ppm. The TDS of the NF brine increased by 25% to 1500 ppm compared to 1100 ppm from effluent in the sump. The TDS of the treated NF brine remained similar to that of the NF brine.

Figure 8.20 shows a reduction in TOC of 60% to 72% between the NF brine and the treated brine for all the effluents evaluated in this work. Further mineralisation could possibly be achieved if treatment time during photocatalysis is extended, and this should be investigated further.

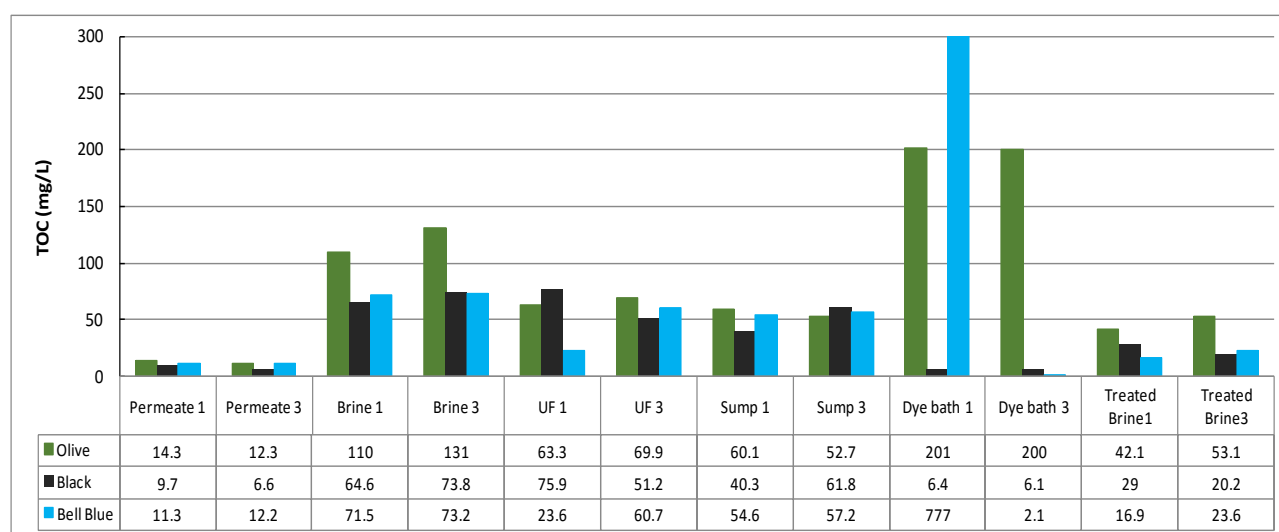


**Figure 8.20 TOC**

Nanofiltration was efficient in reducing the sulphate and phosphate content. The treated NF brine had high anion content as expected. During photocatalysis the dye is degraded and organic intermediates are formed, which, under continued treatment, will mineralise into CO<sub>2</sub>, H<sub>2</sub>O and the inorganic ions according to the structure of the dye.

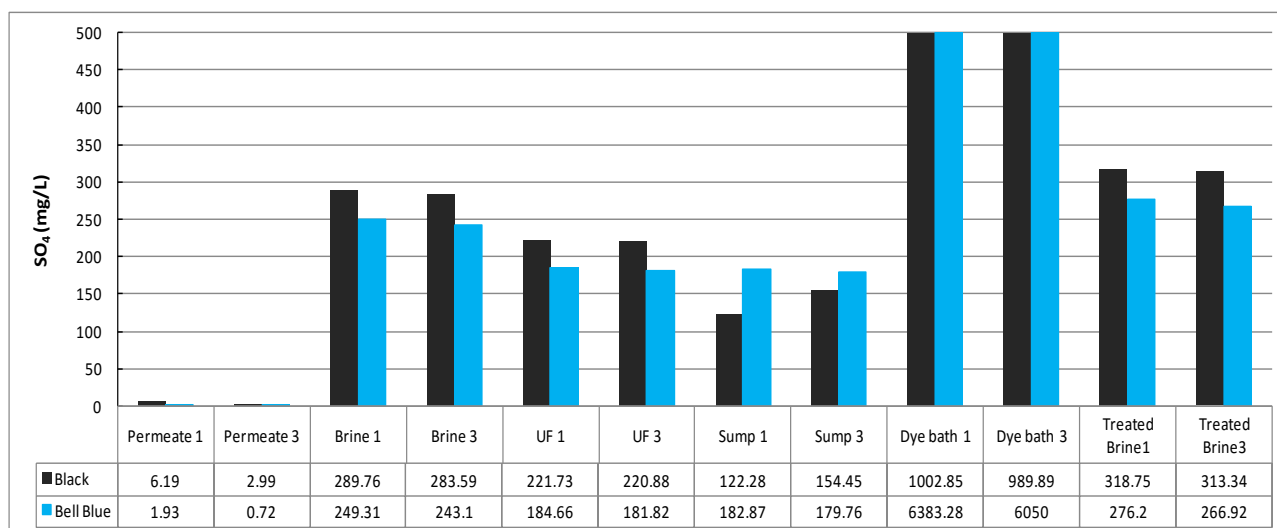


Figure 8.21 Sulphate

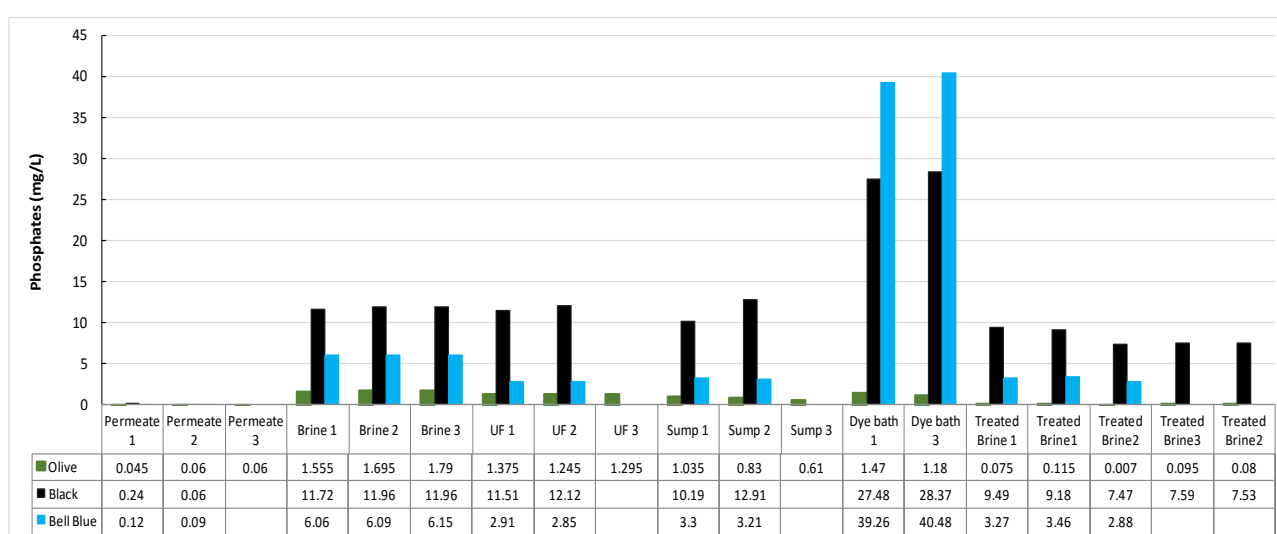


Figure 8.22 Phosphates

## 8.8 CONCLUSIONS

An UF/NF pilot plant was designed and installed at the Falke factory to treat the effluent from the sump. Unfortunately, the effluent from the dye drop could not be pumped directly to the UF/NF pilot plant because it would require significant changes. Under the current conditions, 50% of water could be recovered as the nanofiltration permeate.

The colour was successfully removed from the NF brine during treatment using standard conditions, as determined during the development of a visible light active  $\beta$ -FeOOH/TiO<sub>2</sub> nanophotocatalyst. If the treatment time is increased, further reduction of TOC could be achieved. The amounts of inorganic ions present in the treated brine can be recovered during a further treatment step.

## CHAPTER 9: CONCLUSIONS AND RECOMMENDATIONS

---

### 9.1 CONCLUSIONS

A stream segregation scoping assessment for cleaner effluent production was conducted at Falke Eurosocks factory. It is proposed that the main process effluent streams are segregated based on composition and effluent strength as opposed to an end-of-pipe strategy where all effluent streams are mixed.

The study has shown that the high-volume dye-free effluent streams can be separated and treated using UF to remove particulates and suspended solids. The filtered product stream can be treated using GAC to remove any residual colour and then reused as process water.

The main dye-containing effluent streams (dye-containing drops) can be treated using UF and NF to remove and concentrate the dye fraction of the segregated stream. The NF retentate (NF brine) can then be treated using nanoparticles and then dewatered for solid waste removal. The NF dye-free permeate as well as the treated NF brine can then be desalinated using RO to remove the high salt content which is then evaporated for reuse in specific dye house processes.

Strategies for the controlled synthesis of TiO<sub>2</sub> nanophotocatalysts were developed. For the sol-gel process it was demonstrated that using acid concentration as a means of polymorph manipulation is only effective at gel formation times of less than 72 hours, enabling the synthesis of rutile-rich, brookite-rich or equal amounts of brookite and rutile with equal percentage of not more than 15% anatase. The shape of TiO<sub>2</sub> nanoparticles changed from rod to elliptical particles for shortened gel formation time, irrespective of HCl concentration. An increase in photocatalytic activity efficiency is observed when using a mixed-phase photocatalyst, with an increasing brookite percentage and decreased APS.

Titanium dioxide nanoparticles were also synthesised using a CHS route to enable local large-scale production of photocatalytic nanopowders. Temperature was found to have a major increasing effect on the APS, with a minor influence on PSD and PY, while pressure seemed to have a negligible effect on the entire system. The addition of nitric acid was the most influential on the system, as it not only had a strong reducing effect on the APS, which increases the area and potentially the photocatalytic effect, but also majorly increased PY. Therefore, adding acid can possibly make the CHS process commercially viable by producing small particles with a narrow size distribution at a high yield. We were unable to change the particle shape and also the percentage of anatase, brookite and rutile which remained at approximately 62 to 68%, 25 to 29% and 5 to 9% respectively over the entire range of conditions. An important outcome of the work was that particle size can be controlled between 4 nm to 8 nm which is well within the specification of sub 10 nm TiO<sub>2</sub> particles with a large amount of anatase. Pure anatase was also produced using the CHS system for comparison with commercial anatase. To reduce the band gap of anatase TiO<sub>2</sub>, ultra-small, rod-like  $\beta$ -FeOOH particles were combined with pristine anatase through a heterojunction structure. It showed higher photocatalytic performance than anatase and P25 TiO<sub>2</sub> alone during degradation studies of methyl orange and acid black, with more than 90% colour degradation in 60 minutes.

Technology was developed to remove organic contaminants from textile effluents using nanophotocatalysts based on TiO<sub>2</sub> and doped TiO<sub>2</sub> catalysts immobilised in and on stabilised and carbonised ES PAN under daylight, UVB and UVC in a TBR.

The stabilisation and carbonisation of ES PAN supports was developed and described as being challenging. The best results were obtained with an 8% PAN/DMSO stabilised at 240°C with P25 and titanium precursors in the spinning dope. The type and concentration of additives such as P25 and titanium precursors affects the required optimum conditions for the stabilisation and carbonisation of ES PAN scaffolds. The optimum conditions for the stabilisation of ES PAN, with and without additives, was determined to be a temperature of 240°C with a dwell time of two hours on a mesh in a loose frame (to prevent curling). The optimum conditions



for carbonisation of the stabilised fibres were determined to be 700°C in a quartz tube furnace under nitrogen at a heating rate of 2°C per minute from 240°C. Higher carbonisation temperatures resulted in brittle and cracked mats. Treatment of textile effluents from Falke using the prepared mats in the TBR showed optimum removal of 80 to 100% after 6 to 12 hours with an acid black and reactive navy-blue dyestuff from model dyes and the Falke sump.

PAN nanofibres were prepared by the electrospinning technique and modified with EDTA-EDA chelating agents. The textural and chemical characterisation of the nanofibres was carried out by analysis of the specific surface area (Brauner Emmet and Teller), thermogravimetric analyses, scanning electron microscopy, Fourier transform infrared spectroscopy and X-ray photoelectron spectroscopy. Substantial changes were observed after chemical incorporation of the impregnants to the external surface and inner pore walls of PAN nanofibres. The noticeable improvement in the removal efficiencies of neat and modified nanofibres against the target dye molecules is attributed to changes in the fibres' surface chemistry. This indication was evinced by the maximum adsorption capacity for MB, MO and RR determined at 298 K, that was 62.50, 100.0 and 125.0 mg g<sup>-1</sup>, respectively.

After the chelation of Ti<sup>4+</sup> ions with surface carboxylic and amine groups of the EDTA-EDA chemically immobilised on PAN nanofibres (following self-growth of TiO<sub>2</sub> nanoparticles during the incubation process), additional changes to the properties of the modified PAN nanofibres were observed. The composite nanofibre was annealed under N<sub>2</sub> gas to simultaneously crystallise the TiO<sub>2</sub> nanoparticles and enhance the robustness of the PAN nanofibres as cyclisation reactions and the cross-linking of adjacent nitrile groups (–C=N–C=N–) usually takes place at temperatures above 200°C. The fabricated composite nanofibres exhibited the combined advantages of the two-phase materials, such as unique catalytic and optical properties of TiO<sub>2</sub> nanoparticles, along with the excellent thermal stability, chemical inertness and high mechanical strength of PAN nanofibres. The nanomaterial was applied in the photodegradation of MB, MO and RR from synthetic water samples. Results showed higher photodegradation efficiency in removing model dyes as compared to the commercial P25 TiO<sub>2</sub> nanoparticles.

An UF/NF pilot plant was designed and installed at the Falke factory to treat the effluent from the sump. Unfortunately, the effluent from the dye drop could not be pumped directly to the UF/NF pilot plant because it would require significant changes. Under the current conditions, 50% of water could be recovered as the NF permeate. The colour was successfully removed from the NF brine during treatment using standard conditions as determined during the development of a visible light active β-FeOOH/TiO<sub>2</sub> nanophotocatalyst. The sample was only treated for 90 minutes; if treatment time is increased, further reduction of TOC could be achieved. The amounts of inorganic ions can be recovered during a further treatment step.

## 9.2 RECOMMENDATIONS

Based on the successful treatment of the effluent with a 50% recovery of high quality permeate at pilot plant scale, and the subsequent removal of colour from NF brine at laboratory scale, it is recommended that:

- The effluent system pipeline is fitted to allow dye drop effluent to be directly fed to the UF/NF pilot plant to facilitate easy redirection of the reactive dye drops to the UF/NF pilot plant sump. The drops happened mainly in the early morning hours, making it very difficult for the research team to collect samples for testing.
- The industrial potential for the utilisation of the TiO<sub>2</sub> immobilisation techniques developed in this work is great since there is a nanofibre spinning company in Cape Town (Stellenbosch Nanofibre Company) that is able to produce mats of up to 2-metres wide. These larger mats should be incorporated in a multistage, thin-film, fixed-bed photocatalytic reactor for upscaling of the process, using artificial and/or natural sunlight.
- The intermediate complex organic compounds formed during degradation of the dyes should be monitored using HPLC coupled with a diode array detector followed by mass spectrometry (HPLC-DAD-MS). This is an extremely important part of the degradation study as it was shown in previous studies in the literature that over-treatment could lead to more toxic clear water than the actual dyestuff in the original effluent.

- The actual cost and saving of the proposed two-phase strategy treatment be conducted based on larger scale treatment trials to confirm the current projection that it will lead to lower CAPEX investment requirements and the ability to recycle a larger volume of effluent once treated.
- Future studies should focus on the stability of the fabricated composite nanofibres in order to reduce the self-degradation of the support nanopolymer and consequently minimise the leaching of the metal oxide.

## CHAPTER 10: REFERENCES

---

- AAL AA, BARAKAT MA and MOHAMED RM (2008) Electrophoretic Zn-TiO<sub>2</sub>-ZnO nanocomposite coating films for photocatalytic degradation of 2-chlorophenol. *Journal of Applied Surface Science* **254** 4577–4583.
- AFFAM AC and CHAUDHURI M (2013) Degradation of pesticides chlorpyrifos, cypermethrin and chlorothalonil in aqueous solution by TiO<sub>2</sub> photocatalysis. *Journal of Environmental Management* **130** 160–165.
- AHMADI N, NEMATI A and SOLATI-HASHJIN M (2014) Synthesis and characterization of co-doped TiO<sub>2</sub> thin films on glass-ceramic. *Materials Science in Semiconductor Processing* **26** 41–48.
- AHMED S, RASUL MG, BROWN R and HASHIB MA (2011) Influence of parameters on the heterogeneous photocatalytic degradation of pesticides and phenolic contaminants in wastewater: A short review. *Journal of Environmental Management* **92** 311–330.
- AKPAN UG and HAMEED BH (2009) Parameters affecting the photocatalytic degradation of dyes using TiO<sub>2</sub>-based photocatalysts: A review. *Journal of Hazardous Materials* **170** 520–529.
- AKPAN UG and HAMEED BH (2010) The advancements in sol–gel method of doped-TiO<sub>2</sub> photocatalysts. *Appl Catal A* **375** (1) 1–11.
- ALBERICI RM, NOGUEIRA RP, CANELA MC, GUIMARAES JR and JARDIM WF (n.d.) Advanced oxidation processes applied to the treatment of organic and inorganic contaminants. 1-10.
- AMINE K, YASUDA H and YAMACHI M (1999)  $\beta$ -FeOOH, a new positive electrode material for lithium secondary batteries. *Journal of Power Sources* **81** 221–223.
- AMOTH A, MILLER J and HICKMAN G (1992) Treatment technologies for the reduction of colour. AOX, resin and fatty acids. TAPPI environmental conference 339-346.
- ANDERSSON M, ÖSTERLUND LL, JUNGSTROEM S and PALMQVIST A (2002) Preparation of nanosize anatase and rutile TiO<sub>2</sub> by hydrothermal treatment of microemulsions and their activity for photocatalytic wet oxidation of phenol. *Journal of Physical Chemistry B*, **106** (41) 10 674–10 679.
- ARSANA P, BUBPA C and SAND-AROON W (2012) Photocatalytic Activity under Solar Irradiation of Silver and Copper Doped Zinc oxide: Photodeposition versus Liquid Impregnation Methods *Journal of Applied Sciences* **12** (17) 1809–1816.
- ASTM E2535 (2007) Standard Guide for Handling Unbound Engineered Nanoscale Particles in Occupational Settings
- ATHANASEKOU CP, ROMANOS GE, KATSAROS FK, KORDATOS K, LIKODIMOS V and FALARAS P (2012) Very efficient composite titania membranes in hybrid ultrafiltration/photocatalysis water treatment processes. *Journal of Membrane Science* 392–393 192–203.
- AZIZ AA, YONG KS, IBRAHIM S and PICHIAH S (2012) Enhanced magnetic separation and photocatalytic activity of nitrogen doped titania photocatalyst supported on strontium ferrite. *Journal of Hazardous Materials* **199–200** 143–150.
- BAHNEMANN D (2004) Photocatalytic water treatment: solar energy applications. *Solar Energy* **77** 445-459.
- BAI H, LIU L, LIU Z and SUN DD (2012) Hierarchical 3D dendritic TiO<sub>2</sub> nanospheres building with ultralong 1D nanoribbon/wires for high performance concurrent photocatalytic membrane water purification *Journal of Water Research* **47** (12) 4126–4138
- BAI HW, LIU ZY, LIU L, and SUN DD (2013) Large-scale production of hierarchical TiO<sub>2</sub> nanorod spheres for photocatalytic elimination of contaminants and killing bacteria. *Chem. Eur. J.* **19** 3061 – 3070.
- BANDARA J, KLEHM U and KIWI J (2007) Raschig rings-Fe<sub>2</sub>O<sub>3</sub> composite photocatalyst activate in the degradation of 4-chlorophenol and Orange II under daylight irradiation. *Applied Catalysis B: Environmental* **76** 73-81.
- BANDAS (RATIA) C, LAZAU C, DABICI A, FIRLOAGA PS, VASZILCSIN N, GROZESU I and TIPONUT V (2011) Microwave-assisted hydrothermal method for synthesis of nanocrystalline anatase TiO<sub>2</sub>. *Chemical Bulletin* **56** (70) 2 81-84.

- BARAKAT MA, CHEN YT and HUANG CP (2004) Removal of toxic cyanide and Cu (II) Ions from water by illuminated TiO<sub>2</sub> catalyst *Journal of Applied catalysis: Environmental* **53** (1) 13–20
- BARCLAY SJ and BUCKLEY CA (2002) *Waste Minisation Guide for the Textile Industry. A Step Towards Cleaner Production*. Report no TT 139/00. Water Research Commission. Pretoria. South Africa.
- BARCLAY SJ and BUCKLEY CA (1990) *Water management and effluent treatment in the textile industry: scouring and bleaching effluents*. Report no 122/1/90. Water Research Commission. Pretoria. South Africa.
- BARCLAY SJ and BUCKLEY CA (2004) *The regional treatment of textile and industrial effluents*. Report no 456/1/04. Water Research Commission. Pretoria. South Africa.
- BAUER R, WALDNER G, FALLMANN H, HAGER S, KLARE M, KRUTZLER B, MALATO S and MALETZKY P (1999) The photo-fenton reaction and the TiO<sub>2</sub>/UV process for waste water treatment – novel developments *Journal of Catalysis Today* **53** (1) 131–144.
- BAVYKIN DV and WALSH FC (2010) Titanate and titania nanotubes: Synthesis, properties and applications. Royal Society of Chemistry.
- BEHNAJADY MA, MODIRSHAHLA N, DANESHVAR N and RABBANI M (2007) Photocatalytic degradation of an azo dye in a tubular continuous-flow photoreactor with immobilized TiO<sub>2</sub> on glass plates. *Chemical Engineering Journal* **127** 167–176.
- BHARATHI KS and RAMESH ST (2013) Removal of dyes using agricultural waste as low-cost adsorbents: a review. *Applied Water Science* **3** (4) 773–790
- BINDA M, GOUNDER P, BUCKLEY CA and BROUCKAERT BM (2008) *Promotion of biodegradable chemicals in the textile industry*. Research report no 1363/1/08. Water Research Commission. Pretoria. South Africa
- BISCHOFF BL and ANDERSON MA (1995) Peptization process in the sol-gel preparation of porous Anatase (TiO<sub>2</sub>). *Chemistry of materials* **7** 1772–1778.
- BREZOVÁ V, BLAZKOVA A, BOROŠOVÁ E, CEPPAN M and FIALA R (1995) The influence of dissolved metal ions on the photocatalytic degradation of phenol in aqueous TiO<sub>2</sub> suspensions *J. Mol Catalysis A* **98** 109–166
- BRYDSON RM and HAMMOND C (2005) Generic methodologies for nanotechnology: classification and fabrication. In: Kelsall RW, Hamley IW and Geoghegan M (eds) *Nanoscale science and technology*. John Wiley and Sons Ltd. West Sussex. England.
- BYRAPPA K, LOKANATHA RAI KM and YOSHIMURA M (2000) Hydrothermal preparation of TiO<sub>2</sub> and photocatalytic degradation of hexachlorocyclohexane and dichlorodiphenyltrichloromethane. *Environmental Technology* **21** (10) 1085.
- CHEN D, JIANG Z, GENG J, WANG Q and YANG D (2007) Carbon and nitrogen co-doped TiO<sub>2</sub> with enhanced visible-light photocatalytic activity. *Ind Eng Chem Res* **46** (9) 2741–2746.
- CHEN D, SIVAKHUMAR and RAY AK (2000) Heterogeneous Photocatalysis on environmental remediation. Development of Chemical Engineering Mineral Process **8** 505–550.
- CHEN H, SU C, CHEN J, YANG T HSU N and LI WR (2011) Preparation and Characterization of Pure Rutile TiO<sub>2</sub> Nanoparticles for Photocatalytic Study and Thin Films for Dye-Sensitized Solar Cells *Journal of Nanoparticles* 1–8.
- CHEN H, SU C, CHEN JL, YANG TY, HSU NM and LI WR (2011) Preparation and characterization of pure rutile TiO<sub>2</sub> nanoparticles for photocatalytic study and thin films for dye-sensitized solar cells. *Nanomaterials* 1–8.
- CHENG X, YU X and XING Z (2012) One-step synthesis of visible active C-N-S-tridoped TiO<sub>2</sub> photocatalyst from biomolecule cystine. *Applied Surface Science* **258** 7644–7650.
- CHOI H, ANTONIOU MG, PELAEZ M, DE LA CRUZ AA, SHOEMAKER JA and DIONYSIOU DD (2007) Mesoporous nitrogen-doped TiO<sub>2</sub> for the photocatalytic destruction of the cyanobacterial toxin microcystin-LR under visible light irradiation. *Environ. Sci. Technol.* **41** 7530–7535.
- CHOI WY, TERMIN A and HOFFMAN (1994) The Role of metal Ion Dopants in Quantum –sized TiO<sub>2</sub>. Correlation between Photoreactivity and charge carrier Recombination Dynamics. *Physical Chemistry* **98** 13669–13679.

- CHONG MN, JIN B, CHOW CWK and SAINT C (2010) Recent developments in photocatalytic water treatment technology: A review. *Water Research* **44** 2997–3027.
- CHOUCAIR M, THORDARSON P and STRIDE JA (2008) Gram-scale production of graphene based on Solvothermal synthesis and sonication. *Nature Nanotechnology* **4** (1) 30–33.
- CHOWDHURY M, NTIRIBINYANGE M, NYAMAYARO K and FESTER V (2015) Photocatalytic activities of ultra-small  $\beta$ -FeOOH and TiO<sub>2</sub> heterojunction structure under simulated solar irradiation. *Materials Research Bulletin* **68**. 133–141.
- CHRONAKIS IS (2005) Novel nanocomposites and nanoceramics based on polymer nanofibres using electrospinning process-A review. *Materials Processing Technology* **167** 283–293.
- CLARK M (2011) *Handbook of Textile and Industrial Dyeing: Principles. Processes and Types of Dyes*. Elsevier
- CLASSENS H (2004) The current status of the South African Textile Industry. *Textiles Unlimited*: 3.
- CLOETE TE, De KWAADSTENIET M, BOTES M and LOPES-ROMERO JM (2010) *Nanotechnology in water treatment applications* Caister Academic Press. 200 pages.
- COZZOLI PD, KORNOWSKI A and WELLER H (2003) Low-temperature synthesis of soluble and processable organic-capped anatase TiO<sub>2</sub> nanorods. *Journal of the American Chemical Society*, 14539–14548.
- CRINI G (2006) Non-conventional low-cost absorbents for dye removal: a review. *Bioresour technol.* **97** (9) 1061–1085
- CRONJE M, BAKER PGL, KNOETZE JH, SANDERSON RD and CROUCH AM (2005) *Removal of organic components and bacteria from water by electrochemical combustion*. Report no 1196/1/04. Water Research Commission. Pretoria. South Africa.
- DAGHRIR R, DROGUI P and ROBERT D (2013) Modified TiO<sub>2</sub> for environmental photocatalytic applications: a review. *Ind. Eng. Chem. Res.* **52** 3581–3599.
- DAI G, LIU S, LIANG Y, LIU H and ZHONG Z (2013) A simple preparation of carbon and nitrogen co-doped nanoscaled TiO<sub>2</sub> with exposed {0 0 1} facets for enhanced visible-light photocatalytic activity. *Journal of Molecular Catalysis A: Chemical* **368–369** 38–42.
- DAI J, HE R, YUAN Y, WANG W and FANGA D (2014) TiO<sub>2</sub> nanoparticles: low temperature hydrothermal synthesis in ionic liquids/ water and the photocatalytic degradation of O- nitrophenol. *Environmental Technology* (1-4) 203–208.
- DANESHVAR N, RABBANI M, MODIRSHAHLA N and BEHNAJADY MA (2004) Critical effect of hydrogen peroxide concentration in photochemical oxidative degradation of C.I. Acid Red 27 (AR27). *Chemosphere*. **56** 895–900.
- DE JAGER D, SHELDON MS and EDWARDS W (2012) Membrane bioreactor application within the treatment of high-strength textile effluent. *Water Science and Technology* **25** (5) 907–914.
- DEA (2014) National Guideline for the Discharge of Effluent from Land-based Sources into the Coastal Environment. Department of Environmental Affairs, Pretoria. South Africa.
- DI PAOLA A, GARCÍA-LÓPEZ E, MARCÌ G and PALMISANO L (2012) A survey of photocatalytic materials for environmental remediation. *Journal of Hazardous Materials*. **211–212** 3–29.
- DI PAOLA A, BELLARDITA M and PALMISANO L (2013) Brookite. the Least Known TiO<sub>2</sub> Photocatalyst. *Catalysts* 2013. 3(1). 36–73.
- DIALLO M, DUNCAN J, SAVAGE N, STREET A and SUSTICH R (2009) *Nanotechnology Applications for Clean Water. Solutions for Improving Water Quality* Elsevier. 700 pages.
- DINGA H, SUNA H and SHAN Y (2005) Preparation and characterization of mesoporous SBA-15 supported dye-sensitized TiO<sub>2</sub> photocatalyst. *Journal of Photochemistry and Photobiology A: Chemistry* **169** 101–107.
- DJAFER L, AYRAL A and OUAGUED A (2010) Robust synthesis and performance of a titania-based ultrafiltration membrane with photocatalytic properties. *Separation and Purification Technology* **75** 198–203.

DOBKIN D and ZURAW MK (2003) *Principles of Chemical Vapor Deposition* 2003 ed. Kluwer academic Publishers. US.

DOLAT D, QUICI N, KUSIAK-NEJMAN E, MORAWSKI AW and PUMA GL (2012) One-step. hydrothermal synthesis of nitrogen, carbon co-doped titanium dioxide (N,C TiO<sub>2</sub>) photocatalysts. Effect of alcohol degree and chain length as carbon dopant precursors on photocatalytic activity and catalyst deactivation. *Applied Catalysis B: Environmental* **115–116** 81–89.

DONG F, WANG H and WU Z (2009) One-Step “Green” synthetic approach for mesoporous C-doped titanium dioxide with efficient visible light photocatalytic activity. *J Phys Chem C* **113** (38) 16717–16723.

DONG HAO, ZHENMING YANG, CHUNHAI JIANG and JINSONG ZHANG (2013) Photocatalytic activities of TiO<sub>2</sub>–coated different semi conductive SiC foam supports. *Journal of Materials Science and Technology* **29** (11) 1074–1078.

DORFMAN LM and ADAMS GE (1973) Reactivity of the Hydroxyl Radical in Aqueous Solutions. US Department of Commerce National Bureau of Standards. June 1973.

DOSHI J and RENEKER DH (1995) Electrospinning process and applications of electrospun fibres. *Journal of Electrostatics* **35** 151–160.

EDE S, HAFNER L, DUNLOP P, BYRNE J and GEOFFREY W (2012) Photocatalytic disinfection of bacterial pollutants using suspended and immobilised TiO<sub>2</sub> powders. *Journal of Photochemistry and Photobiology* **88** (3) 728–735.

EINARSRUD M-A and GRANDE T (2014) 1D Nanostructures from Chemical Solutions **43** 2187-2199.

FACCINI M, BORJA G, BOERRIGTER M, MARTÍN DM, CRESPIERA SM, VÁZQUEZ-CAMPOS S, AUBOUY L and AMANTIA D (2015) Electrospun carbon nanofibre membranes for filtration of nanoparticles from water. *Journal of Nanomaterials* **2015** 1–9.

FALAH H and THEKRA A (2010) Photocatalytic treatment of textile industrial wastewater. *International Journal of Chemistry Science* 1353–1364.

FAN JJ, ZHAO L, YU J and LIU G (2012) The effect of calcination temperature on the microstructure and photocatalytic activity of TiO<sub>2</sub>–based composite nanotubes prepared by an in situ template dissolution and method. *Nanoscale* **4** 6597–6603.

FEITZ AJ, BOYDEN BH and WAITE TD (2000) Evaluation of two solar pilot fixed-bed photocatalytic reactors. *Water Research* **34** (16) 3927–3932.

FERNANDEZ A, LASSALETTA G and JIMENEZ V (1995) Preparation and characterisation of TiO<sub>2</sub> photocatalysts supported on various rigid supports (glass, quartz and stainless steel) comparative studies of photocatalytic activity in water purification. *Applied Catalysts B: Environmental* **7** 49–63

FERNÁNDEZ-GARCÍA M, WANG X, BELVER C, HANSON JC and RODRIGUEZ JA (2007) Anatase-TiO<sub>2</sub> nanomaterials: Morphological/size dependence of the crystallization and phase behavior phenomena. *The Journal of Physical Chemistry C* **111** 674–682.

FORGACS E, CSERHATI T and OROS G (2004) Removal of synthetic dyes from wastewaters: a review. *Environment international* **30** (7) 953–971

FROST and SULLIVAN Research Service (2006) Impact of Nanotechnology in Water and Wastewater Treatment (Technical Insights). <http://www.frost.com/prod/servlet/report-brochure.pag?id=D09D-01-00-00-00> (Accessed 5 September 2014).

FUJISHIMA A, ZHANG X and TRYK DA (2008) TiO<sub>2</sub> photocatalysis and related surface phenomena. *Surface Science Reports* **63** (12) 515–582.

GE M, GUO C, ZHU X, MA L, HAN Z, HU W and WANG Y (2009) Photocatalytic degradation of methyl orange using ZnO/TiO<sub>2</sub> composites *Journal of Front Environmental Science Engineering China* **3** (3) 271–280.

GERISCHER H and HELLER A (1991) The role of oxygen in the photooxidation of organic molecules on semiconductor particles. *Journal of Physical Chemistry* **95** (13) 5261–5267.

GHOREISHIAN SM, BADII K, NOROUZI M, RASHIDI A, MONTAZER M, SADEGHI M and VAFAEE M (2014) Decolorization and mineralization of an azo reactive dye using loaded nano-photocatalysts on spacer

- fabric: Kinetic study and operational factors. *Journal of the Taiwan Institute of Chemical Engineers*. **45** 2436–2446.
- GIUANLUCA LP, BONO A, KRISHNAIAH D and COLLIN JG (2008) Preparation of titanium dioxide photocatalyst loaded onto activated carbon support using Chemical Vapour Deposition. *Hazardous Materials* **7747** 1–11.
- GU DE, LU Y, YANG BC and HU YD (2008) Facile preparation of micromesoporous carbon-doped TiO<sub>2</sub> photocatalysts with anatase crystalline walls under template-free condition. *Chem Commun* (**21**) 2453–545.
- GULUMIAN M (2011) Health and Safety of Nanotechnology: Ensuring a Sustainable Development of Nanotechnologies.
- GUPTA SM and TRIPATHI M (2011) A review of TiO<sub>2</sub> nanoparticles. *Chinese Science Bulletin*, **56**(16) 1639–1657.
- GUPTA SM and TRIPATHI M (2012) A review on the synthesis of TiO<sub>2</sub> nanoparticles by solution route. *Central European Journal of Chemistry*, **10**(2) 279–294.
- GUPTA VK and SUHAS (2009) Application of low-cost adsorbents for dye removal- A review. *Journal of Environmental Management* **90** (8) 2313–2342.
- HABIB A, SHADAT T, BAHADUR NM, ISMAIL IM and MAHMOOD AJ (2013) Synthesis and characterisation of ZnO-TiO<sub>2</sub> nanocomposites and their application as photocatalysts. *Journal of International Nano Letters* **3** (5) 1–8.
- HAN R, ZHANG S, ZHAO W, LI X, and JIAN X (2009) Treating sulphur black dye wastewater with quaternized poly(phthalazinone ether sulphone ketone) nanofiltration membranes. *Separation and Purification Technology*. Vol. 67. 26–30.
- HAN Z, CHANG VWC, ZHANG L, TSE MS and TAN OK (2012) Preparation of TiO<sub>2</sub>-coated Polyester fibre filter by spray coating and its photocatalytic degradation of gaseous Formaldehyde. *Aerosol and Air Quality Research* **12**. 1327–1335.
- HASHIMOTO K, IRIE H and FUJISHIMA A (2005) TiO<sub>2</sub> photocatalysis: a historical overview and future prospects. *Jpn J Appl Phys* **44** (12) 8269–8285.
- HENDERSON MA (2011) A surface science perspective on TiO<sub>2</sub> photocatalysis. *Surface Science Reports* **66** (6-7) 185–297.
- HERRMANN J-M (1999) Heterogeneous photocatalysis: fundamentals and applications to the removal of various types of aqueous pollutants. *Catalysis Today* **53** (1) 115–129.
- HILLE T, MUNASINGHE M, HLOPE M and DERANIYAGALA, Y (2006) *Nanotechnology, water and development*. Meridian Institute
- HOFFMANN MR, MARTIN ST, CHOI W, and BAHNEMANN DW (1995) Environmental applications of semiconductor photocatalysis. *Chem. Rev.* **95** 69–96
- HSU JP and NACU A (2003) On the factors influencing the preparation of nanosized titania sols. *Langmuir*, **19**(10) 4448–4454.
- HUANG T, LIN X, XING J, WANG W, SHAN Z and HUANG F (2007) Photocatalytic activities of hetero-junction semiconductors WO<sub>3</sub>/SrNb<sub>2</sub>O<sub>6</sub>. *Materials Science and Engineering: B* **141**(1–2) 49–54.
- HUDLIKAR M, JOGLEKAR S, DHAYGUDE M and KODAN K (2012) Green synthesis of TiO<sub>2</sub> nanoparticles using aqueous extracts of *Jatropha curcas* L. latex. *Material Letters* **75** 196–199.
- HUSSIEN FH and ABASS TA (2010) Photocatalytical treatment of textile industrial wastewater *Journal of Int. J. Chem. Sci.* **8** (3) 1353–1364.
- JAIN T and SANDHU A (2009) *Quantitative Methods*. New Delhi, India: V.K Publications.
- JANG HD, KIM S-K, Kim SJ (2001) Effect of particle size and phase composition of titanium dioxide nanoparticles on the photocatalytic properties. *Journal of Nanoparticle Research* **3**(2-3) 141–147.
- JAYASEELAN C, RAHUMAN AA, ROOPAN SM, KIRTHI AV, VENKATESAN J, KIM SK, IYAPPAN M and SIVA C (2013) Biological approach to synthesize TiO<sub>2</sub> nanoparticles using *Aeromonas hydrophila* and its bacteriological activity. *Spectrochimica Acta Part A Molecular and Biomolecular Spectroscopy* **107** 82–89.

- JIANG Y, SUN Y, LIU H, ZHU F and YIN H (2007) Solar photocatalytic decolorization of C.I Basic Blue 41 in an aqueous suspension of TiO<sub>2</sub>-ZnO *Journal of Dyes and Pigments* **78** 77–83.
- JIAO X, CHEN D and XIAO L (2003) The effects on organic additives on hydrothermal zirconia nanocrystallites. *Journal of Crystal Growth* **258** (1-2) 158–162.
- JIEMSIRILERS S, JINAWATH S, KALAMBAHETI C, KASHIMA DP and LIWSIRISAENG P (2011) Photocatalytic degradation of phenolic compounds by TiO<sub>2</sub> powder: 18th International Conference On Composite Materials. Jeju. Korea. August 21–26. 1-5.
- JIN XC, LIU GQ, XU ZH and TAO WY (2007) Decolorization of a dye industry effluent by *Aspergillus fumigatus* XC6. *Applied Microbiology and Biotechnology*. **74** (1). 239–243.
- JONI IM, OGI T, IWAKI T and OKUYAMA K (2013) Synthesis of a colorless suspension of TiO<sub>2</sub> nanoparticles by nitrogen doping and the bead-mill dispersion process. *Ind. Eng. Chem. Res.* **52** 547–555.
- JOO J, KWON SG, YU T, CHO M, LEE J, YOON J et al. (2005). Large-scale synthesis of TiO<sub>2</sub> nanorods via nonhydrolytic sol-gel ester elimination reaction and their application to photocatalytic inactivation of E.coli. *J. Phys. Chem. B* **109** 15297–15302.
- JOSHI M, BANSAL R and PURWAR R (2004) Colour removal from textile effluents. *Indian Journal of Fibre and Textile Research* **29** 239–259.
- JOSSET S, TARANTO J, KELLER N, KELLER V, LETT M, LEDOUX M, BONNET V and ROUGEAN S (2007) UV- A photocatalytic treatment of high flow rate air contaminated with *Legionella pneumophila*. *Catalysis* **129** 215.
- KANDIEL TA, ROBBEN L, ALKAIM A and BAHNMANN D (2013) Brookite versus anatase TiO<sub>2</sub> photocatalysts: phase transformations and photocatalytic activities. *Photochemical and Photobiological Sciences* **12** (4) 602–609.
- KASPRZYK-HORDERN B, ZIĄŁEK M and NAWROCKI J (2003) Catalytic ozonation and methods of enhancing molecular ozone reactions in water treatment. *Applied Catalysis B: Environmental* **46** 639–669.
- KATOH R, FURUBE A, YAMANAKA K and MORIKAWA T (2010) Charge separation and trapping in N-Doped TiO<sub>2</sub> photocatalysts: A time-resolved microwave conductivity study. *J. Phys. Chem. Lett.* **1** 3261–3265.
- KAWASAKI S-I, XIUYI Y, SUE K and HAKUTA Y et al. (2009) Continuous supercritical hydrothermal synthesis of controlled size and highly crystalline anatase TiO<sub>2</sub> nanoparticles. *The Journal of Supercritical Fluids* **50** 276–282.
- KAWASAKI S-I, XIUYI Y, SUEB K, HAKUTAA Y, SUZUKIA A and ARAIA K (2009) Continuous supercritical hydrothermal synthesis of controlled size and highly crystalline anatase TiO<sub>2</sub> nanoparticles. *The Journal of Supercritical Fluids* **50** (3) 276–282.
- KERNANI R, MAMERI N and LOUNICI H (2014) The use of TiO<sub>2</sub> as catalyst in thin film fixed bed reactor for the treatment of landfill water. *Mediterranean Journal of Chemistry* **3** (1) 780–788.
- KHATAEE AR, PONS MN and ZAHRAA O (2009) Photocatalytic degradation of three azo dyes using immobilised TiO<sub>2</sub> nanoparticles on glass plates activated by UV light irradiation: Influence of dye molecular structure. *Journal of Hazardous Materials* **168** 451–457.
- KIM CH, KIM B-H and LEE KS (2008) TiO<sub>2</sub> nanoparticles loaded on graphene/carbon composite nanofibres by electrospinning for increased photocatalysis. *Journal of SciVerse ScienceDirect* **50** 2472–2481.
- KIM JH, NOH BH, LEE GD and HONG SS (2005) Hydrothermal synthesis of titanium dioxide using acid peptizing agents and their photocatalytic activity. *Korean Chemical Engineering* **22** 370–374.
- KIM M, KIM K-D, TAI W, SEO H, LUO Y, KIM Y et al. (2010) Enhancement of photocatalytic activity of TiO<sub>2</sub> by high energy electron-beam treatment under atmospheric pressure. *Catal Lett* **135** (1) 57–61.
- KIM YJ, GAO B, HAN SY, JUNG MH, CHAKRABORTY AK, KO T, LEE C and LEE WI (2009) Heterojunction of FeTiO<sub>3</sub> nanodisc and TiO<sub>2</sub> nanoparticle for a novel visible light photocatalyst. *The Journal of Physical Chemistry C* **113** (44) 19179–19184.



- KODOM T, DOUGNA A, TCHAKALA I, GNAZOU M-ED, DJANEYE-BOUNDJOU G and BAWA ML (2013) TiO<sub>2</sub> PC500 coated on non woven paper with SiO<sub>2</sub> as a binder-assisted photocatalytic degradation of reactive black 5 in aqueous solution. *Water Resource and Protection* **5** 1227–1234.
- KONGSUEBCHART W, PRASETHDAM P, PANPRANOT J, SIRISUK A, SUPPHASRIRONGJAROEN P and SATAYAPRASERT C (2006) Effect of crystallite size on the surface defect of nanoTiO<sub>2</sub> prepared by solvothermal synthesis. *Crystal Growth* **297** 234.
- KRIVEC M, SEGUNDO RA, FARIA JL, SILVA AMT and DRAŽIĆ G (2013) Low-temperature synthesis and characterization of rutile nanoparticles with amorphous surface layer for photocatalytic degradation of caffeine. *Applied Catalysis B: Environmental* **140** 19–15.
- KUMAR J AND BANSAL A (2011) Photodegradation of amaranth in aqueous catalysed by immobilised nanoparticles of titanium dioxide. *Journal of Environmental Science and Technology* **9** 479–484.
- KUO CS, TSENG YH, HUANG CH and LI YY (2007) Carbon-containing nano-titania prepared by chemical vapor deposition and its visible-light-responsive photocatalytic activity. *Journal of Molecular Catalysis A: Chemical* **270** (1–2) 93–100.
- LACHHEB H, PUZENAT E, HOUAS A, KSIBI M, ELALOUI E, GUILLARD C and HERRMANN JM (2002) Photocatalytic degradation of various types of dyes (Alizarin S, Crocein Orange G, Methyl Red, Congo Red, Methylene Blue) in water by UV-irradiated titania. *Applied Catalysis B: Environmental*, **39** (1) 75-90.
- LAZAR M, VARGHESE S and NAIR S (2012) Photocatalytic water treatment by titanium dioxide: recent updates. *Catalysts* **2** 572–601.
- LEARY R and WESTWOOD A (2011) Carbonaceous nanomaterials for the enhancement of TiO<sub>2</sub> photocatalysis – Review. *CARBON* **49** 741–772.
- LEE SY and PARK SJ (2013) TiO<sub>2</sub> photocatalyst for water treatment applications. *Journal of Industrial and Engineering Chemistry* 1–9.
- LEONG KH, MONASH P, IBRAHIM S and SARAVANAN P (2014) Solar photocatalytic activity of anatase TiO<sub>2</sub> nanocrystals synthesized by non-hydrolitic sol–gel method. *Solar Energy* **101** 321–332.
- LI J-G, ISHIGAKI T et al. (2007) Anatase, brookite, and rutile nanocrystals via redox reactions under mild hydrothermal conditions: phase-selective synthesis and physicochemical properties. *The Journal of Physical Chemistry C*, **111**, 4969–4976.
- LI JZ, ZHONG JB, HU W, LU Y, ZENG J and SHEN YC (2013) Fabrication of tin-doped zinc oxide by parallel flow co-precipitation with enhanced photocatalytic performance. *Journal of Materials Science in Semiconductor Processing* **16** 143–148
- LI Q, XIE R, LI YW, MINTZ EA and SHANG JK (2007) Enhanced visible light-induced photocatalytic disinfection of *E. coli* by carbon sensitized nitrogen-doped titanium oxide. *Environ Sci Technol* **41** (14) 5050–5056.
- LIAO D and LIAO B (2007) Shape, size and photocatalytic activity control of TiO<sub>2</sub> nanoparticles with surfactants. *Journal of Photochemistry and Photobiology A: Chemistry* **187**(2-3) 363–369.
- LITTER MI (1999) Heterogeneous Photocatalysis: transition metal ions in photocatalytic systems. *Applied Catalyst B: Environmental* **23** 89–114.
- LIU SH and SYU HR (2013) High visible-light photocatalytic hydrogen evolution of C,N-codoped mesoporous TiO<sub>2</sub> nanoparticles prepared via an ionic-liquid template approach *International journal of hydrogen energy* **38** 13856–13865.
- MANU B and CHAUDHARI S (2002) Anaerobic decolourisation of simulated textile wastewater containing azo dyes. *Bioresource Technology* **82** (3) 225–231.
- MATSUNAGA T and INAGAKI M (2006) Carbon-coated anatase for oxidation of methylene blue and NO. *Appl Catal B* **64** (1–2) 9–12.
- MCGANN JP, ZHONG M, KIM EK, NATESAKHAWAT S, JARONIEC M, WHITACRE JF, MATYJASZEWSKI K and KOWALEWSKI T (2012) Block copolymer templating as a path to porous nanostructured carbons with highly accessible nitrogens for enhanced (electro)chemical performance. *Macromolecular Chemistry and Physics* **213** (10-11) 1078–1090

- MERRSEWS AN and ISRAEL J (1976) The crystallization of anatase and rutile from amorphous titanium dioxide under hydrothermal conditions. *American Mineralogist* **61** 419–424.
- MILLS A, DAVIES RH and WORSLEY D (1993) Water purification by semiconductor photocatalysis. *Chemical Society Reviews* **22** 417–425.
- MINERO C, PILEZZETTI E, PICHAT P, SEGA M and VINCENTI M (1995) Formation of condensation products in advanced oxidation technologies: The photocatalytic degradation of diclorophenols on TiO<sub>2</sub>. *Environmental Science and Technology* **29** 2226–2234.
- MINGSHAN Z, PENGLEI C and MINGHUA L (2011) Sunlight-driven plasmonic photocatalysts based on Ag/AgCl nanostructures synthesised via an oil in water medium: enhanced catalytic performance by morphology selection. *Materials Chemistry* **21** 16413–16419.
- MITORAJ D, JACZYK, AGNIESZKA, STRUS, MAGADALENA, KISCH, HORST, STOCHEL, GRAYNA, HECZKO, PIOTR, MACYK and WOJCIECH (2007) Visible light inactivation of bacteria and fungi by modified titanium dioxide. *Photochemical and Photobiological Sciences* **6** (6) 642–8.
- MONTI D, PONROUCH A, ESTRUGA, PALACIN MR, AYLLON JA and ROIG A (2013) Microwaves as a synthetic route for preparing electrochemically active TiO<sub>2</sub> nanoparticles. *Journal of Materials Research* **28** (3) 340–347.
- MUJTABA A, ALI M and KOHLI K (2014) Statistical optimization and characterization of pH-independent extended release drug delivery of cefpodoxime proxetil using Box-Behnken design. *Chemical Engineering Research and Design* **92** 156–165.
- MUSEE N (2010) Nanotechnology: Understanding potential risks and the adoption of proactive paradigm. Water Research Commission Media Breakfast: Nanotechnology. 15th March 2010.
- MUTAMBANENGWE C, OYEKOLA O, TOGO C, WHITELEY, CG and DU PLESSIS (2008) *Production of enzymes for industrial wastewater treatment: Proof of concept and application to the dye industry*. WRC Report no 1541/1/08. Water Research Commission. Pretoria. South Africa.
- NGUYEN TA and JUANG RS (2013) Treatment of waters and wastewaters containing sulphur dyes: A review. *Chemical Engineering Journal* **219** 109–117.
- NI M, LEUNG MKH, LEUNG DYK and SUMATHY K (2007) A review and recent developments in photocatalytic water-splitting using TiO<sub>2</sub> for hydrogen production. *Renewable Sustainable Energy Rev* **11** (3) 401–425.
- NIGAM P, BANAT IP, SINGH D and MARCHANT R (1996) Microbial process for the decolourization of textile effluent containing azo, diazo and reactive dyes. *Process Biochem* **31** 435–442.
- NIU H and LIN T (2012) Review article: Fibre generators in needleless electrospinning. *Journal of Nanomaterials* 1–13.
- NOORJAHAN M, REDDY MP, KUMARI VD, LAVEDRINE B, BOULE P and SUBRAHMANYAM M (2003) Photocatalytic degradation of H-acid over a novel TiO<sub>2</sub> thin film fixed bed reactor and in aqueous suspensions. *Photochemistry and Photobiology A: Chemistry* **156** 179–187.
- NYAMUKAMBA P, TICHAGWA L and GREYLING C (2012) The influence of carbon doping on TiO<sub>2</sub> nanoparticle size, surface area, anatase to rutile phase transformation and photocatalytic activity. *Materials Science Forum*. **712** 49–63.
- OCHIAI T, NAKATA K, MURAKAMI T, FUJISHIMA A, YAO Y, TRYK DA and KUBOTA Y (2009) Development of solar-driven electrochemical and photocatalytic water treatment system using a boron-doped diamond electrode and TiO<sub>2</sub> photocatalyst. *Journal of Water Research* **44** (3) 904–910
- ORDENES- AENISHANSLINS NA, SAONA LA, DURAN-TORO VM, MONRAS JP, BRAVO DM AND PEREZ-DONOSO JM (2014) Use of titanium dioxide nanoparticles biosynthesized by bacillus mycoides in quantum dot sensitized solar cells. *Microbial Cell Factories* **13** 90.
- PAN G-T, HUANG CM, CHEN L-C and SHIU W-T (2006) Immobilization of TiO<sub>2</sub> onto Nonwoven Fibre Textile by Silica sol: Photocatalytic activity and durability studies. *Journal of Environmental Engineering and Management* **16** (6) 413–420.
- PEARCE CI, LLOYD and GUTHRIE JT (2003) Removal of colour from textile water using whole bacterial cells: A review. *Dyes and Pigments* **58** (3) 179–196.

- PEKAKIS PA, XEKOUKOULOTAKIS NP and MANTZAVINOS D (2006) Treatment of textile dyehouse wastewater by TiO<sub>2</sub> photocatalysis. *Water Research* **40** (6) 1276–1286.
- PERAL J and DOMENECH X (1992) Photocatalytic cyanide oxidation from aqueous copper cyanide solutions over TiO<sub>2</sub> and ZnO. *Journal of Chemical Technology and Biotechnology* **53** 93–96.
- PERALTA-ZAMORA P, GOMES DE MORAES S, PELEGRINI R et al. (1998) Evaluation of ZnO, TiO<sub>2</sub> and supported ZnO on the photoassisted remediation of black liquor, cellulose and textile mill effluents. *Journal of Chemosphere* **36** (9) 2119–2133.
- PEREZ MARIANO J, LAU KH, SANJURJO A, CARO J, PRADO JM and COLOMINAS C (2006) Multilayer coatings by chemical vapour deposition in a fluidised bed reactor at atmospheric pressure (P/FBR-CVD): TiN/taN and TiN/W. *Surface Coatings Technology* **201** 2174–2180.
- PETRIK L and NDUNGU P (2012) *Nanotechnology In Water Treatment*. Research report no 1897/1/12. Water Research Commission. Pretoria. South Africa.
- PRAHSARN C, KLINSUKHON W and ROUNGPAISAN N (2011) Electrospinning of PAN/DMSO/H<sub>2</sub>O containing TiO<sub>2</sub> and photocatalytic activity of their webs. *Journal of Material Letters* **65** 2498–2501.
- PRESTI LL, CEOTTO M, SPADAVECCHIA F, CAPPELLETTI G, MERONI D, ACRES RG and ARDIZZONE S (2014) Role of the nitrogen source in determining structure and morphology of N-Doped nanocrystalline TiO<sub>2</sub>. *J. Phys. Chem. C* **118** 4797–4807.
- QI D, XING M and ZHANG J (2014) Hydrophobic carbon-doped TiO<sub>2</sub>/MCF/F composite as a high performance photocatalyst. *J. Phys. Chem. C* **118** 7329–7336.
- QIAN Y, CHEN Q, FAN C and ZHOU J (1993) *Material Chemistry* **3** 203.
- QU Q, GENG H, PENG R, CUI Q, GU X, LI F and WANG M (2010) Chemically binding carboxylic acids onto TiO<sub>2</sub> nanoparticles with adjustable coverage by solvothermal strategy. *Langmuir* **26** (12) 9539–9546.
- QURESHI U, BLACKMAN C, HEYTT G and PARKIN IP (2007) Tungsten oxide and tungsten oxide –titania thin films prepared by aerosol-assisted deposition – use of preformed solid nanoparticles. *Inorganic Chemistry* **10** 1415–2142.
- RADOVIC MD, MITROVIC JZ, BOJIC DV, ANTONIJEVIC MD, KOSTIC MM, BAOSIC RM and BOJIC AL (2014) Effects of system parameters and inorganic salts on the photodecolourisation of textile dye Reactive blue 19 by UV/H<sub>2</sub>O<sub>2</sub> process. *Water SA* **40** (3) 570–557.
- RAHAMAN MS, ISMAIL AF and MUSTAFA A (2007) A review of heat treatment on polyacrylonitrile fibre. *Polymer Degradation and Stability* **92** 1421–1432.
- RAUF MA, SHEHADI IA, HASSAN WW (2007) Studies on the removal of neutral red on sand from aqueous solution and its kinetic behaviour. *Dyes Pig.* **75** 723–726.
- RAWAL SB (2011) Photocatalytic Reaction: An efficient method for mineralizing environmental pollution. *SONSIK JOURNAL* **3** 38–46.
- RAWAL SB, CHAKRABORTY AK and LEE WI (2009) Heterojunction of FeOOH and TiO<sub>2</sub> for the formation of visible light photocatalyst. *Bull. Korean Chem. Soc.* **30** (11) 2613.
- REN W, AI Z, JIA F, ZHANG L, FAN X and ZOU Z (2007) Low temperature preparation and visible light photocatalytic activity of mesoporous carbon-doped crystalline TiO<sub>2</sub>. *Applied Catalysis B: Environmental* **69** (3–4) 138–144.
- REYES-CORONADO D, RODRIGUEZ-GATTORNO G, ESPINOSA-PESQUEIRA ME, CAB C, DE COSS R and OSKAM G (2008) Phase-pure TiO<sub>2</sub> nanoparticles: anatase, brookite and rutile. *Nanotechnology* **19** 10.
- RIU J, BARCELO D and RAFOLS C (1997) Determination of sulphonated azo dyes in water and wastewater. *Trends in Analytical Chemistry* **16** (7) 405–419.
- ROY SC, VARGHESE OK, PAULOSE M and GRIMES CA (2010) Toward solar fuels: photocatalytic conversion of carbon dioxide to hydrocarbons. *American Chemical Society* **4** (3) 1259–1278.
- RYU J and CHOI W (2007) Substrate-Specific Photocatalytic Activities of TiO<sub>2</sub> and Multiactivity Test for Water Treatment Application: *Environ. Sci. Technol.* **42** (1) 294–300.

- SAIEN J, ASGARI M, SOLEYMANI AR and TAGHAVINIA N (2009) Photocatalytic decomposition of direct red 16 and kinetics analysis in a conic body packed bed reactor with nanostructure titania coated Raschig rings. *Chemical Engineering Journal* **151** 295–301.
- SAJJAD AK, SHAMAI S, TIAN B, CHEN F and ZHANG J (2010) Comparative studies of operational parameters of degradation of azo dyes in visible light by highly efficient  $\text{WO}_x/\text{TiO}_2$  photocatalyst. *Hazardous Materials* **177** (1-3) 781–791.
- SAMPAIO M-J, SILVA C-G, SILVA AMT, VILAR VJP, BOAVENTURA RAR and FARIA JL (2013) Photocatalytic activity of  $\text{TiO}_2$ -coated glass raschig rings on the degradation of phenolic derivatives under simulated solar light irradiation. *Chemical Engineering Journal* **224** (0) 32–38.
- SARAVANAN P, PAKSHIRAJAN K and SAHA P (2009) Degradation of phenol by  $\text{TiO}_2$ -based heterogeneous photocatalysts in presence of sunlight. *Journal of Hydro-environment Research* **3** 45–50.
- SATHISH M, VISWANATHAN B, VISWANATH RP and GOPINATH CS (2005) Synthesis, characterization, electronic structure and photocatalytic activity of nitrogen-doped  $\text{TiO}_2$  nanocatalyst. *Chem. Mater.* **17** 634–6353.
- SAVIN II and BUTNARU R (2008) Wastewater characteristics in textile finishing mills. *Environmental Engineering and Management Journal* **7** 859–64.
- SCANLON DO, DUNNILL CW, BUCKERIDGE J, SHEVLIN SA, LOGSDAIL AJ, WOODLEY SM, CATLOW CRA, POWELL MJ, PALGRAVE RG, PARKIN IP, WATSON GW, KEAL TW, SHERWOOD P, WALSH A and SOKOL AA (2013) Band alignment of rutile and anatase  $\text{TiO}_2$ . *Nature Materials* **12** (9) 798–801.
- SCHROPP REI, STANNOWSKI B, BROCKHOFF AM, VAN VEENENDAAL PATT and RATH JK (2000) Hot wire CVD of heterogeneous and polycrystalline silicon semi conducting thin films for application in thin film transistors and solar cells. *Materials Physics and Mechanics* **1** (2) 73–82.
- SCHUTTE CF and FOCKE W (2007) *Evaluation of nanotechnology for application in water and wastewater treatment and related aspects in South Africa*. WRC Report No: KV 195/07.
- SHAO GS, LIU L, MA TY, WANG FY, REN TZ and YUAN ZY (2010) Synthesis and characterization of carbon-modified titania photocatalysts with a hierarchical meso-/macroporous structure. *Chemical Engineering Journal* **160** (1) 370–377.
- SHAO H-F, QIAN X-F, YIN J and ZHU Z-K (2005) Controlled morphology synthesis of  $\beta\text{-FeOOH}$  and the phase transition to  $\text{Fe}_2\text{O}_3$ . *Journal of Solid State Chemistry* **178** (10) 3130–3136.
- SHI H, MAGAYE R, CASTRANOVA V and ZHAO J (2013) Titanium dioxide nanoparticles: a review of current toxicological data. *Particle and Fibre Toxicology* **10** 15.
- SHON HK, PHUNTSO S, CHAUDHARY DS, VIGNESWARAN S and CHO J (2013) Nanofiltration for water and waste water treatment- a mini review. *Drinking Water Engineering and Science* **6** 47–53.
- SIERRA-PALLARES J, MARCHISIO DL, ALONSO E and PARRA-SANTOS MT et al. (2011) Quantification of mixing efficiency in turbulent supercritical water hydrothermal reactors. *Chemical Engineering Science* **66** 1576–1589.
- SIMONSEN ME, SØGAARD EG (2010) Sol-gel reactions of titanium alkoxides and water: influence of pH and alkoxy group on cluster formation and properties of the resulting products *Journal of Sol-Gel Science and Technology* **53** (3) 485–497.
- SINGH K and ARORA S (2011) Removal of synthetic textile dyes from wastewaters: A critical review on the present treatment technologies. *Environmental Science and Technology* **40** (9) 807–878.
- SLATER K (2003) *Environmental Impact of Textiles: Production. Process and Protection*. 1<sup>st</sup> ed. Woodhead. Cambridge. England.
- SMITH DI (1995) *Thin film Deposition: Principles and Practices*. McGraw-Hill. New York.
- SO WW, PARK SB, KIM KJ and MOON SJ (1997) Phase transformation behavior at low temperature in hydrothermal treatment of stable and unstable titania sol. *Journal of Colloid and Interface Science* **191** 398–406.
- STONE V, NOWACK B, BAUN A, VAN DEN BRINK N, VON DER KAMMER F, DUSINSKA M, HANDY R, HANKIN S, HASSELLO VM, JONER E and FERNANDES TF (2010) Nanomaterials for environmental

studies: Classification. reference material issues. and strategies for physico-chemical characterisation. *Science of the Total Environment* **408** 1745–1754.

STYLIDI M, KONDARIDES DI and VERYKIOS XE (2004) Visible light induced photocatalytic degradation of Acid Orange 7 in aqueous TiO<sub>2</sub> suspensions. *J. Appl Catal B* **47** (3) 189–201.

SU C, TONG Y, ZHANG M, ZHANG Y and SHAO C (2013) TiO<sub>2</sub> nanoparticles immobilization on polyacrylonitrile nanofibres mats: a flexible and recyclable photocatalyst for phenol degradation. *Journal of RSC Advanced* **3** 7503–7512.

SU C, TSENG CM, CHEN LF, YOU BH, HSU BC and CHEN SS (2006) Sol-hydrothermal preparation and photocatalysis of titanium oxide. *Thin Solid Films* **498** (1-2):259–265.

SUBASH B, KRISHNARKUMAR B, SWAMINATHAN M and SHANTHI M (2012) Highly efficient. solar active and reusable photocatalyst: Zr-loaded Ag-ZnO for reactive red 120 dye degradation with synergistic effect and dye-sensitized mechanism **29** (3) 939–949.

SUN C, LI H, ZHANG H, WANG Z and CHEN L (2005) Controlled synthesis of CeO<sub>2</sub> nanorods by a solvothermal method. *Nanotechnology* **16** (9) 1454.

SUN L, ZHAO X, CHENG X, SUN H, LI Y, LI P and FAN W (2012) Synergistic effects in La/N Codoped TiO<sub>2</sub> Anatase (101) surface correlated with enhanced visible-light photocatalytic activity. *Langmuir* **28** 5882–5891.

SWARTZ CD, MORRISON IR, THEBE T, ENGELBRECHT WJ, CLOETE VB, KNOTT M, LOEWENTHAL RE and KRUGER P (2004) *Characterisation and chemical removal of organic matter in South Africa coloured surface*. Report no 924/1/03. Water Research Commission. Pretoria. South Africa.

TACHIKAWA T, TOJO S, KAWAI K, ENDO M, FUJITSUKA M and OHNO T (2004) Photocatalytic oxidation reactivity of holes in the sulphur- and carbon-doped TiO<sub>2</sub> powders studied by time-resolved diffuse reflectance spectroscopy. *J Phys Chem B* **108** (50) 19299–306.

TAKAHASHI M, CHIBA K and LI P (2007) Formation of hydroxyl radicals by collapsing ozone microbubbles under strongly acidic conditions. *J Phys Chem B*. **111** (39) 11443–11446.

TAO J, YANG M, CHAI JW, PAN JS, FENG YP and WANG SJ (2014) Atomic N modified rutile TiO<sub>2</sub> (110) surface layer with significant visible light photoactivity. *J. Phys. Chem. C* **118** 994–1000.

TARABARA VV (2009) Multi-functional nanomaterial-enabled membranes for water treatment. Chapter 5 of DIALLO M, STREET A, SUSTICH R, DUNCAN J, SAVAGE N (eds) *Nanotechnology Applications for Clean Water. Solutions for Improving Water Quality*. William Andrew Inc. 59–75.

TAYADE RJ, KULKANI RG and JASRA RV (2006) Transition Metal Ion Impregnated Mesoporous TiO<sub>2</sub> for Photocatalytic Degradation of Organic Contaminants in Water. *Industrial and Engineering Chemistry Research* **45**. 5231–5238.

TENG D, YU Y, YANG X and RYU S (2007) Activation of electrospun titanate/polyacrylonitrile nanofibres with H<sub>3</sub>PO<sub>4</sub>. Seattle.

TESTINO A, BELLOBONO IR, BUSCAGLIA V, CANEVALI C, D'ARIENZO M, POLIZZI S, SCOTTI R and MORAZZONI F (2007) Optimizing the photocatalytic properties of hydrothermal TiO<sub>2</sub> by the control of phase composition and particle morphology. A systematic approach. *Journal of the American Chemical Society*, **129** (12) 3564–3575.

THERON J, WALKER JA and CLOETE TE (2008) Nanotechnology and Water Treatment: Applications and Emerging Opportunities. *Critical Reviews in Microbiology* **34** 43–69.

TORIMOTO T, FOX III RJ and FOX MA (1996) Photoelectrochemical doping of TiO<sub>2</sub> particles and the effect of charge carrier density on the photoactivity of microporous semiconductor electrode films. *J. Electrochem. Soc* **143** (11) 3712–3717.

TOSIK R (2005) Dyes Color Removal by Ozone and Hydrogen Peroxide: Some Aspects and Problems. *Ozone: Science and Engineering* **27** 265–272.

TRESCHÉV SY, CHOU PW, TSENG YH, WANG JB, PEREVEDENTSEVA EV and CHENG CL (2008) Photoactivities of the visible-light-activated mixed-phase carbon-containing titanium dioxide: The effect of carbon incorporation. *Applied Catalysis B: Environmental* **79** (1) 8–16.

- TSUZUKI T (2009) Commercial scale production of inorganic nanoparticles. *Int. J. Nanotechnol.* **6** (5/6) 567–578.
- VELHAL SG, KULKARNI SD and JAYBHAYE RG (2012) Novel nanoparticles for water and waste water treatment. *Research Journal of Chemistry and Environment.* **16** (2) 95–103
- VERMA A, POONAM and DIXIT D (2012) Photocatalytic degradability of insecticide Chlorpyrifos over UV irradiated Titanium dioxide in aqueous phase. *International Journal of Environmental Sciences* **3** (2) 743–755.
- VOHRA MS and DAVIS AP (1997) Adsorption of Pb(II). NTA. and Pb(II)-NTA onto TiO<sub>2</sub>. *J Colloid Interface Sci.* **194** (1) 59–67.
- VORKAPIC D and MATSOUKAS T (1998) Effect of temperature and alcohols in the preparation of titania nanoparticles from alkoxides. *Journal of the American Ceramic Society* **81**(11) 2815–2820.
- WANG G, WANG Z, ZHANG Y, FENG G and ZHANG L (2004) Controlled synthesis and characterisation of large scale uniform DY(OH)(3) and DY<sub>2</sub>O<sub>3</sub> single crystal nanorods by a hydrothermal method. *Nanotechnology* **15** 1307.
- WANG P, ZHOU T, WANG R and LIM TT (2011) Carbon-sensitized and nitrogen-doped TiO<sub>2</sub> for photocatalytic degradation of sulphanilamide under visible-light irradiation. *Water Research* **45** 5015–5026.
- WANG YM, LIU WS, XIU Z, JIAO XB, CUX P and PAN J (2006) Preparation and photocatalytic properties of silica gel-supported TiO<sub>2</sub>. *Materials Letters* **60** (7) 974–978.
- White A (1990) Heterogeneous electrochemical reactions associated with oxidation of ferrous oxide and silicate surfaces. *Reviews in Mineralogy and Geochemistry* **23** 467–509.
- WILKE K AND BREUER HD (1999) The influence of transition metal doping on the physical and photocatalytic properties of titania. *Journal of Photochemistry and Photobiology A: Chemistry* **121** (1) 49–53
- WOLD A (1993) Photocatalytic properties of TiO<sub>2</sub>. *Chemistry of Materials* **5** 280–283.
- WU M, LIN G, CHEN D, WANG G, HE D, FENG S and XU R (2002) Sol-hydrothermal synthesis and hydrothermal structural evolution of nanocrystal titanium dioxide. *Chemistry material* 1974–1980.
- WU N, WANG J, TAFEN DN, WANG H, ZHENG J-G, LEWIS JP, LIU X, LEONARD SS and MANIVANNAN A (2010) Shape-enhanced photocatalytic activity of single-crystalline anatase TiO<sub>2</sub> (101) nanobelts. *Journal of the American Chemical Society* **132** (19) 6679–6685.
- WU Y, XING M and ZHANG J (2011) Gel-hydrothermal synthesis of carbon and boron co-doped TiO<sub>2</sub> and evaluating its photocatalytic activity. *Journal of Hazardous Materials* **192** 368–373.
- XIE T, SHI L, ZHANG J and ZHANG D (2014) Immobilizing Ni nanoparticles to mesoporous silica with size and location control via a polyol-assisted route for coking- and sintering-resistant dry reforming of methane. *Journal of The Royal Society of Chemistry* **50** 7250–7253.
- XIE R-C and SHANG JK (2007) Morphological Control in Solvothermal Synthesis of Titanium dioxide. *Material Science* **42** (16) 6583.
- XU Z, MING Z, JINGYU W, JIANRU L, LIXINAG Z and BO L (2013) Visible light degradation of azo dye methyl orange using TiO<sub>2</sub>/β-FeOOH as heterogeneous photo Fenton like catalyst. *Water Science and Technology*
- XUEJING W, SHUWEN Y and XIAOBO L (2009) Sol-gel Preparation of CNT/ZnO Nanocomposite and Its photocatalytic property. *Chinese Journal of Chemistry* **27** 1317–1320.
- YANG K, DAI Y, HUANG B and WHANGBO MH (2009) Density Functional Characterization of the Visible-Light Absorption in Substitutional C-Anion- and C-Cation-Doped TiO<sub>2</sub>. *J. Phys. Chem. C* **113** 2624–2629.
- YANG X, CAO C, ERICKSON L, KEITH H, MAGHIRANG R and KLABUNDE K (2008) Synthesis of visible-light-active TiO<sub>2</sub>-based photocatalysts by carbon and nitrogen doping. *Journal of Catalysis* **260** (1) 128–133.
- YOSHIMURA M and BYRAPPA K (2008) Hydrothermal processing of materials: past. present and future. *Journal of Materials Science* **43** (7) 2085–2103.
- YUN J, JIN D, LEE Y and KIM H (2010) Photocatalytic treatment of acidic waste water by electrospun composite nanofibres of pH-sensitive hydrogel and TiO<sub>2</sub> *Journal of Materials Letters* **64** 2431–2434

- YURDAKAL S, LODDO V, AUGUGLIANO V, BERBER H, PALMISANO G and PALMISANO L (2007) Photodegradation of pharmaceutical drugs in aqueous TiO<sub>2</sub> suspensions: Mechanisms and Kinetics. *Catalysis Today* **129** 9.
- ZAYANI G, BOUSSELM I L, MHENNI F and GHRABI A (2009) Solar Photocatalytic degradation of commercial textile azo dye: Performance of pilot plant scale thin film fixed-bed reactor. *Desalination* **248** 23–31.
- ZHANG D and ZENG F (2012) Visible light-activated cadmium-doped ZnO nanostructured photocatalyst for the treatment of methylene blue dye: *Journal of Material Science* **47** 2155–2161.
- ZHANG H and BANFIELD JF (2005) Size dependence of the kinetic rate constant for phase transformation in TiO<sub>2</sub> nanoparticles. *Chemistry of Materials* **17** 3421–3425.
- ZHANG K, KEMP C and CHANDRA V (2012) Homogeneous anchoring of TiO<sub>2</sub> nanoparticles on graphene sheets for waste water treatment *Journal of Materials Letters* **81** 127–130.
- ZHANG M, XU Z, LIANG J, ZHOU L and ZHANG C (2015) Potential application of novel TiO<sub>2</sub>/β-FeOOH composites for photocatalytic reduction of Cr(VI) with an analysis of statistical approach. *International Journal of Environmental Science and Technology*. **68** (10)
- ZHANG W (2005) Nanotechnology for Water Purification and Waste Treatment. Frontiers in Nanotechnology. US EPA Millennium Lecture Series from LeHigh University. July 18. 2005. Washington D.C.
- ZHANG Y, CHENG K, FENGZHU L, HUANGA H, FEI B, HE Y, YEC Z and SHEN B (2014) Photocatalytic treatment of 2,4,6-trinitrotoluene in red water by multi-doped TiO<sub>2</sub> with enhanced visible light photocatalytic activity. *Colloids and Surfaces A: Physicochem. Eng. Aspects* **452** 103–108.
- ZHANG Z, BROWN S, GOODALL JBM and WENG X et al. (2008). Direct continuous hydrothermal synthesis of high surface area nanosized titania. *Journal of Alloys and Compounds* **476** 451–456.
- ZHU K AND HU G (2014) Supercritical hydrothermal synthesis of TiO<sub>2</sub> nanostructures with controlled phase and morphology. **94** 165–173.
- ZHU M, WANG J, OUTLAW RA, HOU K, MANOS DM and HOLLOWAY BC (2007) Synthesis of carbon nanosheets and carbon nanotubes by radio frequency plasma enhanced chemical vapour deposition. *Diamonds Related Materials* **16** 196–201.
- ZIELINSKA-JUREK A, WALICKA M, TADAJEWSKA A, LACKA I, GAZDA M and ZALESKA A (2010) Preparation of Ag/Cu-doped titanium (IV) Oxide nanoparticles in W/O microemulsion. *Physicochemical Problems in Mineral Processing* **45** 113–126.